The Pennsylvania State University

The Graduate School

College of Engineering

WIND TURBINE DESIGN USING A FREE-WAKE VORTEX METHOD WITH WINGLET APPLICATION

A Dissertation in

Aerospace Engineering

by

David Maniaci

Submitted in Partial Fulfillment
of the Requirements
for the Degree of

Doctor of Philosophy

May 2013

The dissertation of David Maniaci was reviewed and approved* by the following:

Mark D. Maughmer
Professor of Aerospace Engineering
Dissertation Advisor
Chair of Committee

Barnes W. McCormick, Jr.
Professor of Aerospace Engineering

Dennis K. McLaughlin
Professor of Aerospace Engineering

Kenneth S. Brentner
Professor of Aerospace Engineering

Sue Ellen Haupt
Adjunct Professor of Meteorology

Sven Schmitz
Assistant Professor of Aerospace Engineering

George A. Lesieutre
Professor of Aerospace Engineering
Head of the Department of Aerospace Engineering

*Signatures are on file in the Graduate School

ABSTRACT

Wind turbine blades are traditionally designed with blade element momentum theory (BEMT). This method is incapable of accurately analyzing non-conventional or non-planar blade planforms. Modern wind turbine blade design thus requires non-standard modeling that can effectively analyze the effects of a non-planar blade, such as a blade with a winglet. The free-wake, distributed vorticity element (FW-DVE) method meets these analysis goals. Previous work applied the FW-DVE method to wind turbines, but did not include the influence of profile forces and did not include any design applications. The present research focused on developing the FW-DVE method into a design tool for wind turbine design applications and on the validation of this tool.

In the research presented in this thesis, the FW-DVE method was modified to include the effect of airfoil profile drag and to account for the effects of stall and a non-linear lift-curve. A design tool was created to aid in using the WindDVE analysis code for trade space exploration. The method was used to analyze and design a winglet for a small-scale wind turbine, which was tested in a wind tunnel at the University of Waterloo where it exhibited a 9% increase in the maximum coefficient of power of the rotor. The performance results from this test have been used to validate the FW-DVE method for wind turbine design, along with an analysis of the National Renewable Energy Laboratory's Unsteady Aerodynamics Experiment Phase VI wind turbine.

TABLE OF CONTENTS

LIST OF FIGURES

LIST OF TABLES

NOMENCLATURE

AOA = angle-of-attack, angle between V_{Rel} and local chord vector
c = chord
c_d = blade section drag coefficient
c_l = blade section lift coefficient
c_m = blade section moment coefficient about the quarter-chord
c_{mid} = chord at the panel mid-span
eD = freestream drag vector, parallel to kinematic velocity (V_{Kin})
eD_p = profile drag vector, parallel to relative velocity (V_{Rel})
eL = freestream lift vector, normal to kinematic velocity (V_{Kin})
eL_p = profile lift vector, normal to relative velocity (V_{Rel})
F_{ind} = induced force, = Γ x w_{ind}
F_{IP_ind} = in-plane component of induced force, produces torque and power, = Γ x w_{A_ind}
F_{OP_ind} = out-of-plane component of induced force, produces thrust, = Γ x w_{T_ind}
LFA = local flow angle, angle between (V_{Rel} + W_{ind_surf}) and the local chord vector
R = rotor radius (m)
r = local radius of blade section
S_{Ref} = reference area of a spanwise blade element
TSR = tip-speed ratio
V_{Body} = body velocity of a blade element sans blade rotation, typically due to structural dynamics
V_{Kin} = kinetmatic velocity = V_{Wind} + Ωr + V_{Body}(freestream velocity for fixed wing)
V_{Rel} = relative velocity vector = V_{Kin} +W_{ind_Wake}
V_{Wind} = Wind velocity
w_{A_ind} = axial component of induced velocity
w_{T_ind} = tangential component of induced velocity
W_{ind} = induced velocity of the vortex wake (also called W_{ind_wake})
W_{ind_surf} = induced velocity of the lifting surface
ZLL = zero lift line
α = angle of attack, relative to the chord line
α_{ind} = induced angle of attack
α_{ZLL} = angle of attack of the zero-lift line
$\alpha_{\emptyset L}$ = angle of attack for zero-lift of the airfoil (also called $\Delta\alpha_{ZL}$)
β = twist angle of blade section chord line
β_{ZLL} = twist angle of blade section zero lift line
Γ = circulation, line integral around a closed loop of the velocity of the fluid tangent to the loop
φ = relative velocity flow angle
φ_0 = local kinematic velocity flow angle
Ω = rotor rotational rate,(radians/second)

ACKNOWLEDGEMENTS

Thank you to my committee for their focus and guidance during the progression of this dissertation. I owe much appreciation to my academic advisor, Dr. Mark Maughmer, for his time, energy, friendship, and support over the years. Thank you to the faculty, staff, and fellow students of the Aerospace Engineering Department who have been a very supportive community of colleagues and friends. Specific thanks to my office mates for sharing so many ideas (and good food).

Götz Bramesfeld, the developer of FreeWake, provided a considerable amount of help throughout the research. I am very grateful for his advice and for helping to guide me toward my first job after graduate school. Blair Basom, who originally developed WindDVE, provided a considerable amount of information and consultation during the course of this research and has always been a supportive friend.

I am very appreciative for the mentorship of Marshall Buhl and Ye Li during my internships at NREL and for the funding from the Ocean Energy Modeling group which helped to support a portion of the modeling tool development.

I am also thankful to Drew Gertz, who designed the baseline wind turbine blade, and built and tested my winglet design as part of his M.S. thesis research at the University of Waterloo.

Thank you to my friends, family, and my girlfriend Cynthia for being who you are. You have provided the balance and motivation that has fed this work (and me).

Chapter 1

Introduction

Advanced wind turbine blade design requires non-standard modeling tools. Blade element momentum theory (BEMT) can model conventional blade planforms quickly; however, it is incapable or limited in its ability to accurately analyze non-planar blade planforms and has relatively poor performance away from the blade design point, particularly if the blade is heavily loaded [1]. A design tool is desired that can effectively analyze the effects of a non-planar blade, such as a blade with a winglet. Free-wake vortex analysis methods meet these analysis goals.

Conventional free-wake vortex methods generally make use of vortex filaments or vortex particles to transport shed and trailing vorticity through the wake. To prevent numerical singularities from destabilizing the solution, these methods typically employ a cut-off distance from the filament singularity to eliminate excessively large induced velocity contributions that would otherwise be calculated in the vicinity of the singularity. The current research uses the distributed-vorticity-element (DVE) method described in Refs. [2,3], which is a free-wake vortex method. The free-wake distributed vorticity element (FW-DVE) method for wind turbines is called WindDVE [4]. The FW-DVE model is unique and has several advantages over conventional vortex filament models. One advantage is that it does not require the use of a cut-off radius or vortex core model in the inner part of the wake for numerical stability [1–3]. Such an addition would violate the underlying principles of the potential flow formulation and add a source of uncertainty. Another advantage of the FW-DVE method is that for a given level of fidelity, the method has a lower computational cost than other methods because of the use of higher-order elements for modeling the circulation distribution [2]. This is a strong advantage for

design work, where a large number of analysis cases may be needed during the development of a rotor design.

The free-wake DVE analysis method of Bramesfeld and Maughmer [2] was modified by Basom and Maughmer for wind turbine analysis [4], but this work did not include the influence of profile drag or stall and was not applied to any practical designs. In the research presented in this thesis, the FW-DVE method was modified to include the effect of airfoil profile drag and to account for the effects of stall and a non-linear lift-curve. The method was then used to design and analyze a winglet for a small-scale wind turbine, which was tested in a wind tunnel. The performance results from this test have been used to validate the FW-DVE method for wind turbine design. Additionally, validation has been performed using the National Renewable Energy Laboratory's Unsteady Aerodynamics Experiment Phase VI wind turbine [5].

1.1 Background and Relevance of Work

This section gives an overview of the three-dimensional flow field about a lifting surface and how the FW-DVE methd models it. Relatively high aspect ratio lifting surfaces with attached flow can be modeled using a three-dimensional, potential flow field with a simplified lifting surface representation and boundary conditions to define the surface circulation distribution. The lift on a wing section is typically defined by applying a flow tangency condition to control points on the lifting surface, by assuming a relationship between the angle-of-attack and lift, or by using airfoil data tables combined with blade element theory to influence the forces that the potential flow solution produce. Lift is a function of the change in pressure across a surface due to its curvature, which is defined as an airfoil profile being placed along a reference chord line. For a finite wing, the lift must go to zero at the wing tips, which results in a variation of lift along the span. Spanwise pressure gradients also exist due to the change in lift along the span. The

spanwise pressure gradients cause spanwise flow, which can interact with the chordwise pressure gradients. This spanwise flow is shed into the wake of the lifting surface and creates an interacting field of pressure and velocity, which in turn influences the lift produced by the lifting surface. The pressure-velocity field that makes up the wake of a wind turbine can be effectively modeled using a distribution of potential vorticies. In modeling terms, it is refererred to as the vortex wake.

It is typically assumed that the influence of the spanwise flow on the lifting surface is limited to an effective velocity induced by the vortex wake; however, this is not always the case. This assumption implies that the spanwise flow does not directly interfere with the chordwise pressure gradients, and allows the effect of the spanwise pressure gradient and chordwise pressure gradient to be separated into two individual solutions whose interaction can be found through iteration. This assumption is adequate only for attached flow conditions. When relevant amounts of separated flow are present, strong interactions between spanwise and chordwise pressure gradients result in an increased stall angle relative to an airfoil in two-dimensional flow. This effect is known as stall delay, and it is an important phenomenon to consider for stall-regulated wind turbines. It is not so important for the performance analysis of most pitch regulated wind turbines. Stall delay can be modeled by adjusting the airfoil profile force data at various spanwise stations, which is the method used in some of the analysis cases presented in Chapters 5 and 6.

The effect of a vortex wake on a lifting surface is often referred to as an induced velocity field because of the use of potential vortices to model it, although “induction” is a misnomer that comes from the use of potential fields to model the relationship between electricity and magnetism [6]. In a fluid, force can only be transferred through pressure, momentum, and shear stress; there is no physical induction, although the relationship of pressure and velocity can be modeled as a vortex system.

A lifting surface can be modeled by a bound vortex element, typically a vortex filament. The term "lifting line" refers to the line vortex element used to model the surface circulation. For an airfoil with a sharp trailing edge, the circulation on the lifting line must be set to satisfy the Kutta condition, which states that there must be smooth flow off of the trailing edge. One method used to determine the surface circulation distribution is to enforce a flow tangency condition at a point on the lifting surface. The more control points there are along the surface, the more accurately one can determine the chordwise circulation distribution; however, for each control point there must be a lifting line. The simplest model is one that uses a single lifting line and one control point. Weissinger's approximation places the lifting line at the quarter-chord point and the control point at the three-quarter chord point [7]. The wing can be divided into individual vortex elements in the spanwise directions, creating an equation system where the circulation for all lifting line elements must be solved such that there is no flow through any of the control points. The vortex lattice method models a three-dimensional lifting surface by placing similar vortex elements along both the chord and span directions.

The resultant flow through each control point has a contribution of induced velocity from each surface lifting line, as well as the freestream flow component of velocity normal to the control point (which accounts for angle-of-attack), a contribution due to body motion (such as blade rotation, flapping, or torsion), and the total induced velocity contribution from the wake. In planar, fixed-wing analyses the induced velocity contribution from the wake can be modeled by semi-infinite trailing vortices shed from the edges of the lifting line of each surface vortex element. If there are multiple lifting lines, each lifting line will have semi-infinite vortex filaments emanating from its edges. The equivalent wake shape for a rotating wing would be semi-infinite vortex filaments following a helix. Analytic solutions exist for such semi-infinite helicoidal filaments, but they are either limited to lightly loaded rotors or are prohibitively complex to solve for practical problems [4,8]. The wake can also be modeled by semi-infinite

vortex cylinders, which correspond to the rotor being modeled as having an infinite number of blades, but this is inaccurate for typical rotors. The wake can also be modeled by setting its shape to fall along pre-defined functions, which come from either experimental data or through a less physically-constrained analysis. Such a method is typically referred to as a fixed-wake analysis and can offer fast computational results, but it cannot inherently model the effect of the wake shape due to changes of the lifting surface geometry or due to interactions with other lifting surfaces.

In a free-wake method, the wake shape is computed in-between computations of the lifting surface circulation distribution by solving for the velocities on the wake surface and relaxing the wake. The wake must be force-free such that it produces no spurious forces, since it has no physical surface to support a force without acceleration. The force-free condition is obtained when the trailing vortex elements are aligned with the local flow direction. Relaxing the wake at each timestep assures that the force-free condition is met at each timestep. Although this implies nothing for what happens between timesteps, it is typically a good assumption to assume that the wake vorticity distribution fairs smoothly between wake control points such that the discretization error is small. Since the method uses temporal relaxation, an unsteady solution depends on the temporal relaxation scheme and time-step sizes. If a steady, or quasi-steady, solution exists, then the method should be accurate as long as the timestep size allows a proper wake shape to develop, since the timestep size determines the azimuthal size of each wake DVE. Truly unsteady solutions must also select a proper timestep size to capture the unsteady aerodynamic effects that are to be modeled and must also account for the unsteady Kutta condition. A hybrid solution could be developed that would model certain effects during each temporal timestep, and then spatially relax the wake in-between each timestep. When modeling a wing behind a propeller, for example, the wing and propeller would be moved during each

temporal timestep, and the wake of both lifting surfaces would be relaxed in-between each timestep.

The method of solution of the lifting surface circulation distribution is the same for fixed-wake and free-wake methods, rotating or non-rotating. The difference between the two methods is that the free-wake method must be relaxed during each timestep, which involves computing the total induced velocity on each wake element control point and then moving (or relaxing) each wake element by a proportional amount, and maintaining any geometric constraints on the wake shape.

Typically, the lifting-line vortex filaments of each surface vortex element have constant strength, such as with a vortex lattice method. Modeling the change in circulation along the lifting surface span requires multiple vortex elements, with the model accuracy controlled by the number of spanwise elements. Horstmann [9] developed lifting surface vortex elements with parabolic distributions, which can model the spanwise circulation distribution to a given accuracy with fewer spanwise elements than by using constant strength vortex elements [2,10].

The parabolic surface vortex elements of Horstmann have been shown to have additional advantages when applied to free-wake methods. For constant strength vortex elements, a change in circulation across the lifting surface is modeled by a jump in circulation between neighboring spanwise elements. This jump in circulation causes discontinuities in the distribution of shed vorticity in the wake. The discontinuities cause issues in solving free-wake methods; if the control point of a wake vortex element is close to the vortex filament of another wake element, then the induced velocities on that control point can become very large, causing unrealistic wake vortex element displacements. The parabolic circulation distributions of the Horstmann method result in sheets of shed vorticity with linear distributions that are continuous in the magnitude of vorticity [2]. Due to the continuity in shed vorticity, the velocity fields modeled by each wake element are finite, and the tangentially induced velocity in the plane of the sheet is undetermined.

The finite induced velocity of the wake elements eliminates numerical stability issues caused by the wakes of conventional methods with singularities in the wake (vortex filament and particle methods), giving this method a distinct advantage in terms of numerical stability compared to the conventional methods.

Bramesfeld and Maughmer [2] aimed to combine the accuracy of Hortstmann's parabolic vortex elements with the improved modeling accuracy promised by a free-wake method. A vortex element was created that could be used to model the wake by combining an upstream element with semi-infinite trailing vorticies and a downstream element in the same plane as the upstream element, as shown in Figure 1-1. The trailing vorticies of the downstream element are equal in strength, but of opposite direction as the trailing vortices of the upstream element, so that the total induced velocity of the trailing vorticies is zero. This leaves behind only the contribution of the upstream element, the downstream element, and the vortices connecting the two. By adding many of what have been termed "distributed vorticity elements", or DVEs, together, the wake can be modeled with the ability to relax and deform to a force-free wake shape.

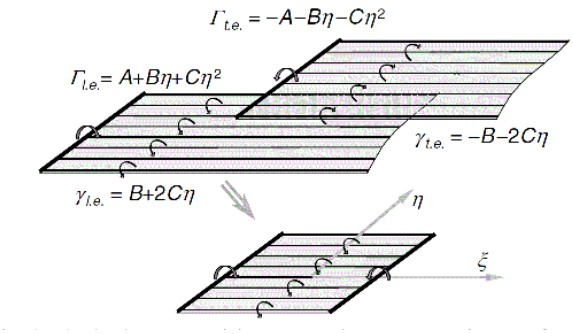

Figure 1-1 A distributed vorticity element (DVE) is composed of vortex filaments with parabolic voriticy distributions along the DVE leading and trailing edges and of two semi-infinite vortex sheets [2].

Figure 1-2 shows the vorticity distribution of two example DVEs and the resulting induced velocities. The two elements alone would have logarithmic singularities at their side-

edges, but when placed next to each other on the same plane, the singularities cancel, resulting in a finite total velocity (labeled w2 total) [3]. Although the ultimate side-edges have singularities, they are logarithmic and are less likely to cause numerical issues than the pole singularities of conventional discrete vortex methods.

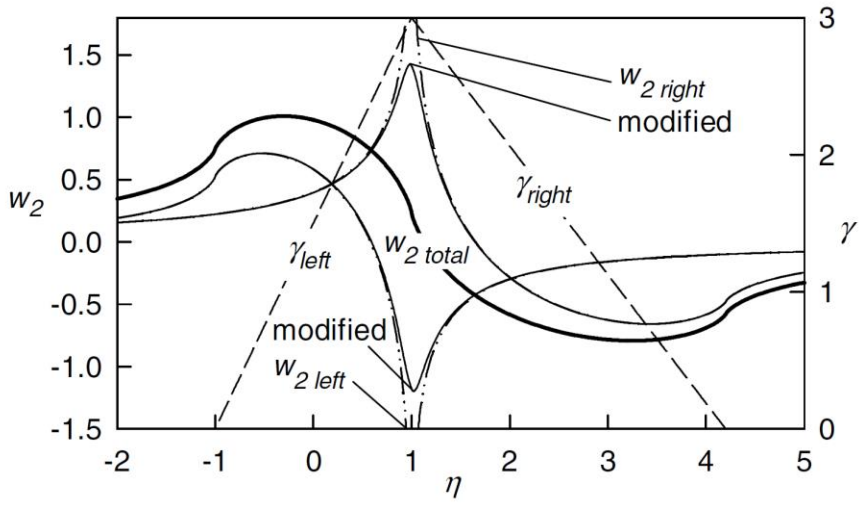

Figure 1-2 The spanwise distribution of the normal velocity induced in the plane of two semi-infinite vortex sheets. Dashed line indicates the spanwise vorticity distribution and the solid lines indicate the induced velocity. The two vortex sheets span from η = -1 to 4.2 and meet at η = 1. Figure from Bramesfeld [3].

To reduce the possibility of numerical issues caused by the side-edge logarithmic singularities, in WindDVE the induced velocity at the side-edges of the wake are computed slightly inboard of the actual side-edge of each DVE, which reduces the local induced velocity [1,4]. Although the solution is affected by the selection of the control point, the effect is minimized by the limited strength of the logarithmic singularity.

An additional modification to the method was introduced in Ref. [1,4] to aid the computation of the induced velocity when two elements are significantly out of plane with each other. The original method presented no numerical issues when there were moderate deflections

in dihedral between two spanwise adjacent DVEs; however, if the angles were larger, such as occurs in the roll-up of the tip vortex, then numerical issues could arise. Although the solution still converges and is well behaved, it oscillates between timesteps. A method called "DVE splitting" was added to WindDVE to reduce this effect [4]. The method takes two spanwise adjacent DVEs and computes the induced velocity near the juncture as though a DVE has been introduced across the juncture between them.

The work in Ref. [4] also describes the force computation for rotating (specifically wind turbine) systems, a wake extrapolation routine, a steady-wake relaxation routine, and a method which allows for variable timestep sizes.

1.2 Design Tool Development

The current research aims to further develop the method into a design tool and to exercise it with a wind turbine case study. This requires the addition of profile drag, stall modeling, improvements in wake modeling, and some additional pre- and post-processing capabilities. The tool will then be used to design a winglet for a wind turbine, and the procedure validated using data from a small wind turbine tested at the University of Waterloo. The results from this test are used to validate the new DVE method, code, and the design method used for the winglet.

1.2.1 Viscous Effects on the Lifting Surface

Vortex methods are potential flow solutions and do not include viscous effects. Viscous effects must be applied within the model, typically through boundary conditions or by adjusting the solution to match the forces predicted by a blade-element solution. Blade-element theory is used to calculate the forces on a blade section based on results of two-dimensional airfoil section test data, or from some other source, such as an unsteady aerodynamics model.

1.2.1.1 Profile Drag

The effect of profile drag on lifting surface forces was added to WindDVE as part of this research. The method uses the effective angle-of-attack or section lift coefficient and local chordwise Reynolds number based on the total local flow velocity to calculate the local profile drag coefficient. The local profile drag coefficient is incorporated into the analysis by utilizing a table lookup and linear interpolation routine that is applied to data from airfoil tables of angle-of-attack, lift coefficient and drag coefficient.

The viscous drag on the airfoil creates a wake of reduced flow velocity behind the airfoil; this velocity deficit is often measured during a wind tunnel airfoil test using a traversing pitot-static probe and is used to compute the profile drag (viscous and pressure drag) acting on the airfoil. The effect of this velocity deficit on the advection of the vortex wake is typically ignored in free-wake vortex methods. This effect is most likely minor, although it has not been clearly quantified. Profile drag force can be added to the total blade forces independently of the potential flow solution, unless the force contribution of the profile drag is included in the momentum of the wake. A discussion of whether or not to include profile drag in the momentum balance of BEMT solutions is given in Ref. [11]. In WindDVE, profile drag can optionally be included in the shed wake vorticity, but the influence of this effect has not been investigated.

1.2.1.2 Stall Modeling

One of the boundary conditions used to define the circulation distribution along the lifting surface is that no flow is allowed through the control point of each lifting surface DVE. This boundary condition is referred to as the kinematic flow condition or as flow tangency. An iterative method was implemented in the analysis code that allows the incorporation of airfoil lift

forces. This method allows the incorporation of viscous effects on lift into the three dimensional potential flow solution. The viscous lift effects include a non-linear and non-ideal lift curve slope, airfoil stall, and stall delay modeling. All three of these effects are accounted for in airfoil profile lift and drag tables. The forces that the rotor can produce are calculated via a blade element method using these tables. The incorporation of these data into the solution of the free wake potential flow distributed vorticity element method solution requires iteration between the blade element solution and the potential flow solution.

1.2.2 Wake Modeling Parameters

A detailed study of the effect of the wake modeling parameters on the analysis results of the FW-DVE method was undertaken and is presented in Chapter 4. The wake modeling parameters must be selected correctly for the type of analysis (steady or unsteady) and for the tip-speed ratio. Analysis cases for low values of tip-speed ratio showed very little sensitivity to wake modeling parameters beyond a certain set of values, but high tip-speed ratio cases showed a noticeable sensitivity.

In order to further speed up certain analysis cases, a special wake relaxation process was applied to steady wake cases, referred to as the steady relaxation method [4]. The steady relaxation method replaces the time history of the relaxation process of a wake DVE control point with the current timestep relaxation velocities from upstream wake DVEs that have the same azimuth and spanwise station. The steady relaxation process can greatly speed up the convergence time of a solution, but does not apply to unsteady wake cases and can give non-realistic wake shapes for high tip-speed ratio cases.

An extrapolation method has also been applied to the wake. This method extrapolates the wake shape based on the last fully relaxed wake row [4]. The extrapolation distance determines the length of the wake downstream of the rotor that is fully relaxed; beyond the wake

extrapolation distance, the wake shape is extrapolated based on the pitch of the last row of relaxed wake DVEs. The wake extrapolation method does not speed up convergence as much as the steady relaxation method, but it can be applied to unsteady analysis cases to speed up convergence of the solution.

1.2.3 Trade Space Exploration Tool

To enhance the ability to explore the design space of a wind turbine using the free-wake vortex method analysis code WindDVE, a specific trade-space tool was created. This tool reads a wind turbine blade geometry definition file similar to that of blade-element momentum theory.

At each stage of the model development, the code needs to be run using several different example cases. Creating input files is currently very time consuming; it can take anywhere from half an hour to several hours to create the input files necessary to generate one power-output curve for an example wind turbine. The input file tool automates many of the steps necessary for creating these various input files. It is standard practice to assess the dependence of the results of the DVE code on input file grid geometry and spacing. In order to facilitate such studies, the input file tool is able to automatically generate different surface panel spacings. A separate section of the tool collects the results from all of the WindDVE analysis cases, and once collected, the data are used for plotting or further data analysis.

1.2.4 Design Application: Winglets for Wind Turbines

Winglets offer a performance benefit for lifting surfaces, including for wind turbines. A model of the effects of the wake downstream of the wind turbine is required to accurately analyze the effect of the winglet. Blade element momentum theory (BEMT) is not applicable to the analysis of a winglet due to the assumptions of radial independence and the use of a tip-loss model to account for wake effects. A vortex method, whether it is a free wake or prescribed wake

type, will model the effect of the wake vorticity on the lifting line and hence is able to capture the effects of a winglet. A free-wake model will theoretically give more accurate results than a prescribed wake model due to capturing effects of the roll-up of the wake, albeit at larger computational cost and complexity than a prescribed wake model.

Chapter 6 of this document presents the design and analysis of a winglet for a small-scale wind turbine using the free-wake distributed vorticity element method.

1.3 Review of Analysis Methods for Wind Turbine Design

This section give a summary of analysis methods for HAWTs (horizontal-axis wind turbines), followed by a review of various free-wake vortex methods (FWVM). Additionally, a summary of the inclusion of viscous effects in FWVM solutions is included.

1.3.1 Comparison of Analysis Methods

Several different methods are available for the aerodynamic analysis of wind turbines. These include the blade element momentum theory, the general dynamic wake theory, prescribed wake vortex methods, free wake vortex methods, and computational fluid dynamics solutions of full Navier-Stokes analysis. These methods are contrasted in this section of the paper, with an overview of vortex methods given in the next section.

1.3.1.1 Blade Element Momentum Theory

The most commonly used analysis method for wind and water (tidal-current) turbines is the blade element momentum theory (BEMT), which is thoroughly explained in several references [11–17]. This method assumes that the force produced by a blade element is the sole mechanism responsible for the rate of change of momentum passing through the annulus created

by the rotation of that blade element. It also assumes that radial stations do not interfere with each other. Typical implementations use the Prandtl tip and hub loss models to model induced velocity effects near the tip and hub of the wind turbine rotor. The effect of the rotor blade planform on induced velocity is not directly modeled in BEMT, meaning that it cannot accurately model the induced power effects of dihedral (winglets), sweep, partial span lift augmentation devices (flaps), or blade tip geometry. BEMT also does not model time-dependent behavior of the wind turbine wake, commonly referred to as the dynamic wake effect [18].

Figure 1-3 shows a comparison between predictions of the coefficient of power using a BEMT analysis and predictions using a free-wake vortex method (FWVM), entitled "BEM" and "DVE Relaxed Wake", respectively, in the figure. The results presented in the figure are for a modified version of the 17 meter blade from Chapter 3_10 of the *Wind Energy Handbook* [11]; these results were originally presented in Ref. [1,4].

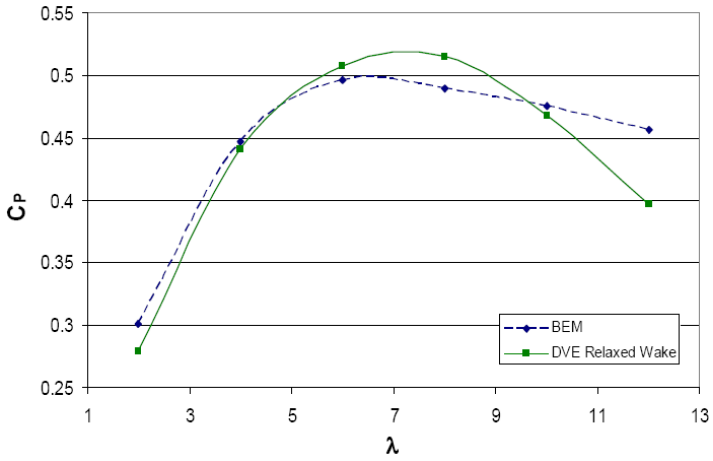

Figure 1-3 Comparison of power coefficient vs. tip-speed ratio predicted by a BEMT analysis and a fully relaxed-wake vortex method analysis [1].

The FWVM analysis was performed using WindDVE, which models the performance of the blade using the free-wake, distributed vorticity element (FW-DVE) vortex model [1–4]. In order to better match the inviscid FW-DVE analysis results, Basom used a symmetric airfoil with the

profile drag equal to zero, a the lift-curve slope equal to 2π, and blade twist values presented in Table 6.1 of Ref. [4]. The BEMT analysis was performed using the National Renewable Energy Laboratory's analysis tool WT_Perf [1,4,19]. At the design TSR of 6, the BEMT analysis predicts a Cp 2.3% less than the FW-DVE model, which is in sufficient agreement to consider that the two methods are comparable at the design TSR [1]. This result is consistent with the circulation distributions at the design TSR predicted from the two analysis methods, corresponding to the "λ=6" plot in Figure 1-4.

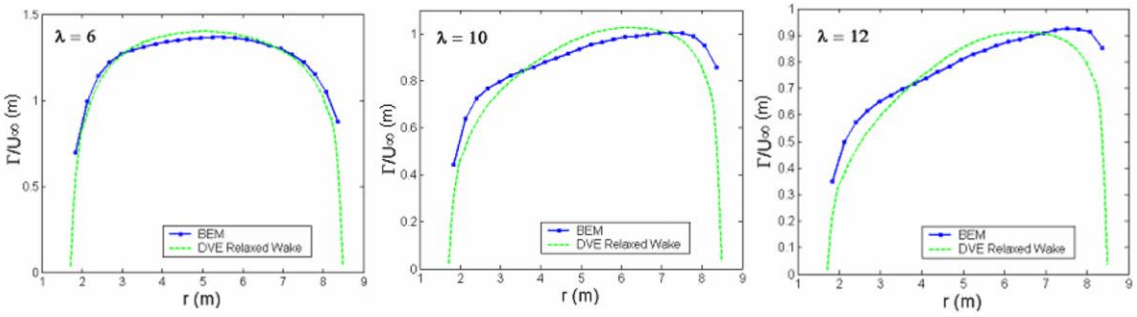

Figure 1-4 Circulation distribution for two of the cases from Figure 1 [1].

At a TSR of 12 the circulation distributions predicted by the two analysis methods are very different, which is reflected in the difference in the predicted power coefficients at this TSR, as shown in Figure 1-3. At a TSR of 10 the predicted circulation distributions of the two methods follow trends similar to the distributions at a TSR of 12; however, at a TSR of 10, the predicted power coefficients from the two methods are similar. For this case, the increased circulation in the middle of the blade predicted by the FW-DVE method is made up for by the decreased circulation at the hub and tip regions of the blade relative to the predictions using the BEMT tip-loss model [1]. The circulation distributions can have a profound effect on the final design of the blade [1]. A final blade design might be influenced by the higher, off-design TSRs, in which case

the BEMT and FWVM models used in this particular study would produce significantly different blade geometries. If one assumes the FWVM to be the most accurate representation of actual flow conditions, then the BEMT predictions would be good for design and analysis purposes near the design TSR, but could cause significant errors at off-design conditions.

A similar study was performed by Gupta and Leishman that compared the analysis results of a FWVM and BEMT [20]. The power and thrust prediction results were comparable between the two methods for tip-speed ratios below 6; however, at higher tip-speed ratios, the BEMT model failed to give good results due to high wake induction factors near the region of the tip. The study also showed that the FWVM could accurately model the aerodynamic response of a rotor operating with large yaw angles, where BEMT theory would fail without corrections. Figure 1-5 illustrates modeling results of the axial induction factor over a rotor disc for several yaw angles using the FWVM (referred to as FVM) and BEMT with a Coleman inflow correction [20]. This figure illustrates that, relative to the FWVM model, the BEMT model is significantly over-predicting the axial induction factor at the rotor blade tips for the yawed cases, which results in a relative over-prediction of rotor power output and loads.

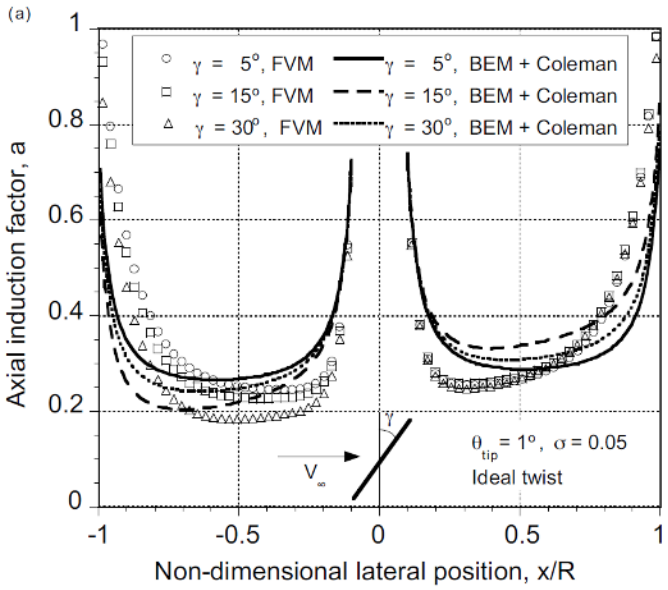

Figure 1-5 Axial induction factor vs lateral position of a rotor for various yaw angles [21].

1.3.1.2 General Dynamic Wake and Unsteady Wake Modeling

There is a time-dependent relationship between changes in the rotor forces and the corresponding changes in the rotor induced velocity distribution, which is termed the dynamic wake effect. This effect is typically modeled by letting the Kutta condition be applied instantaneously during a time-step, making it a quasi-steady method. Unsteady aerodynamic modeling requires the modeling of the time-delay of the response of the Kutta condition on a lifting surface, which is typically modeled using an unsteady aerodynamic model, such as that of Leishman-Beddoes [21].

The dynamic wake effect can be modeled in BEMT by adding a time dependent filter on the induced velocity used in the BEMT solution [14]. The resulting method is similar to the general dynamic wake (GDW) theory, which models the dynamic wake effect by equating the pressure distribution along the rotor disc with the time history of the forces produced by the rotor disc [18,22–25]. One example of an aerodynamic analysis tool that uses GDW theory is AeroDyn, which is part of the structural dynamics analysis tool FAST, both of which are

maintained by the National Renewable Energy Laboratory (NREL) [18,26]. The GDW theory has the same limitations in modeling induced power effects as BEMT. Both methods require tuning of the time dependent induced velocity parameters, typically using experimental data or models with fewer physical assumptions [24,25]. For example, during the development of the GDW model for wind turbines, the coefficients that control the time-dependent aspects of the aerodynamic solution were tuned to the Tjaereborg 2MW wind turbine [22].

1.3.1.3 Navier-Stokes CFD

Analysis methods with fewer physical assumptions than BEMT and GDW include full-potential solutions (including compressibility), vortex methods, and computational solutions of the Navier-Stokes equations, such as Reynolds averaged Navier-Stokes (RANS) computational fluid dynamics (CFD) solutions.

RANS CFD analyses, however, are too computationally expensive for practical analysis and design problems. Vortex methods offer a balance, in that they can be applied to a wider range of geometries and flow conditions without as many tuning parameters as BEMT and GDW models and with a much lower computational cost than RANS-CFD. For example, a wind turbine study using a free-wake vortex method (FWVM) showed a half-hour computation time for 30 wake revolutions downstream, while a similar study using a CFD simulation required 42 hours to compute 2 wake revolutions on multiple processors, the results of which are summarized in Table 1-1 [27,28]. Studies have also been performed using a hybrid between two or more methods, such as using an actuator line model of the turbine blades along with a large eddy simulation of the wake [29,30]. Another hybrid approach is to use CFD to analyze the local area of the rotor blade, and a vortex model of the wake; this method has the advantage over full CFD analysis of limiting artificial dissipation of vorticity and reducing computational time [31–35].

Table 1-1 Computation time comparison for wind turbine analysis.

Method	Processor	Wake Revolutions	Computation Time
BEMT [28]	Single Core 2.27 GHz	--	10 s
FVM [28]	Single Core 2.27 GHz	30	0.5 hrs
CFD [27,28]	128 x Dual Core 3.2 GHz	2	42 hrs

1.3.2 Vortex Methods

A variety of vortex method solutions are available, some of which are illustrated in Figure 1-6. Some analytical solutions are available, although numerical solutions offer more analysis flexibility. Numerical solutions typically use a singularity solution of Laplace's equation. These methods can be split into models used for the lifting surfaces and models used for the corresponding wakes. Some methods use a hybrid analytical solution, for example, a prescribed wake method might use a vortex lattice representation of the lifting surface and an analytical model of the helical wake. Different lifting surface models include the lifting line model, the vortex lattice model, panel methods, and distributed vorticity elements (DVE) [3,36].

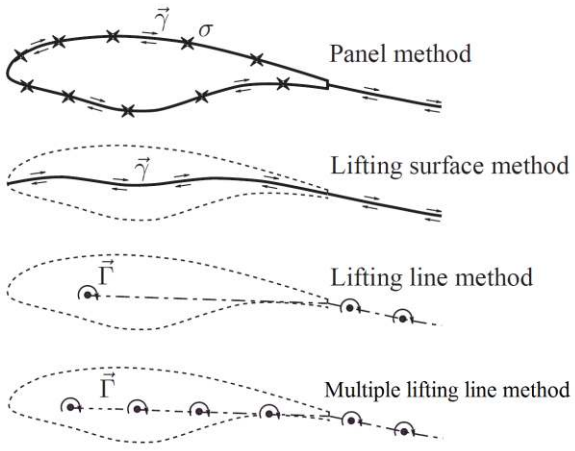

Figure 1-6 Methods used to model a lifting surface with vortex elements [44-modified].

A lifting line representation of a wind turbine blade models the lift of the blade as a single spanwise distribution of circulation, ignoring chordwise effects of circulation. This works well for long, slender blades, but can produce significant errors when analyzing blades with relatively low aspect ratios or other chordwise variations in circulation due to spanwise effects. A lifting surface representation models both the spanwise and streamwise distributions of circulation, examples of which are the multiple lifting-line method, the vortex lattice method, and panel methods. Lifting-line and vortex lattice methods ignore thickness effects of the lifting surface; panel methods model the effect of the thickness of the lifting surface. The DVE method is an extension of Horstmann's multiple lifting line method (MLL), which uses multiple lifting lines to represent the chordwise distribution of the lifting surface circulation [1–3]. In a panel method, the induced drag can be determined by integrating the pressure forces around the blade surface; however, this method is very sensitive to the panel density, requiring a large number of surface panels in both the spanwise and streamwise directions [38]. Palmiter and Katz [39] used a panel method to analyze a wind turbine and Baltazar and Campos [40] used a panel method to analyze a marine current turbine. Wake modeling is captured by several methods, including vortex filaments, quadrilateral filament vortex elements, vortex particles, and distributed vorticity elements [3,41]. Vortex filaments can be straight or curved (helical); an application of curved vortex filaments to a wind turbine analysis was performed by Gupta and Leishman [42,43].

1.3.2.1 Wake Modeling Using Vortex Elements

As mentioned earlier in this chapter, spanwise pressure gradients along a wing cause spanwise velocity. The spanwise velocity of the upper surface will tend to be from the wing (or blade) tip toward the wing centerline, as pressures are lower near the centerline (corresponding to increased lift and circulation there). The strength of the spanwise flow depends on the local spanwise pressure gradient, which is typically strongest near the wing tips. The upper surface

will tend to have larger spanwise pressure gradients than the lower surface for a wing producing positive lift. The larger upper surface pressure gradients also cause a larger magnitude of spanwise flow, so that there is a difference in spanwise flow between the upper surface and lower surface of the wing at the wing's trailing edge. This difference in flow direction produces vorticity, which is shed in the wake behind the wing. The wake of the wing includes the momentum of the entire flow field created by the spanwise pressure gradients and the associated spanwise flow. This momentum also has an associated pressure field, which influences the entire flow field, including the lifting surface and the wake itself. The momentum and pressure field can be modeled by applying a distribution of vorticity along the wake shear layer. The distribution of vorticity in the wake can be discretized and modeled using vortex filaments, sheets, or a combination of them, as illustrated in Figure 1-7.

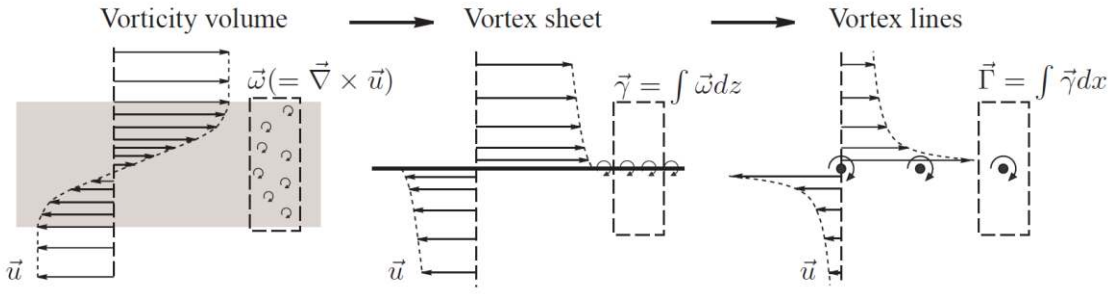

Figure 1-7 Representation of the wake velocity and pressure field with discretized potential vortex elements. View toward upstream from behind the wing [37].

1.3.2.2 Analytical Solutions of Vortex Models

Several analytical solutions of vortex models of wind turbines have been found [8,44–47]. Although these solutions typically offer fast computation time, they have a limited range of applicability. The Goldstein solution offers an analytic solution of the induced velocity due to a helical vortex wake sheet [8]. This solution is the exact solution for a lightly loaded rotors; its usefulness is limited since wind turbine rotors are typically not lightly loaded. The solution by

Theodorsen can be applied to heavily loaded rotors, but the implementation is complicated and is limited by its use of an approximate relationship between the properties of the near-wake and the far-wake [1,4,46].

1.3.2.3 Prescribed and Free-Wake Vortex Methods

The shape of the pressure and velocity field of the wind turbine wake has an impact on how the wake affects the velocities and loads on the wind turbine blade. The wake shape is more important for a rotating wing than for a fixed wing aircraft because it stays in close proximity to the lifting surface due to the rotation of the rotor blades. A prescribed wake method uses empirical data and prescription functions to prescribe its shape; in contrast, a free wake method physically models the shape of the wake by computing the local induced velocities on the wake. Prescribed wake methods are faster and simpler to develop than free wake analysis methods and require much less computational time, but require *a priori* knowledge of the wake shape. For low rotor disc loading, the details of the wake shape have less of an influence on blade loads than when the rotor disc has high loading, so a prescribed wake method is more applicable to low disc loading analysis cases. The wake shape and roll-up can be especially important in calculating loads near the blade tip, which have a large influence on the total loads of the rotor blade. Analysis cases where the loads and induced velocity near the rotor blade tip are important may see a noticeable difference in predictions from a free-wake analysis relative to a prescribed wake analysis.

The prescribed wake wind turbine modeling method by Kocurek is illustrated in Figure 1-8 [48–52]. A recent wind turbine analysis of NREL's Unsteady Aerodynamics Experiment (UAE) Phase VI wind turbine was performed using this code, which was referred to as the Lifting Surface Wind Turbine (LSWT) code [53,54]. The prescribed wake model in the code was modified in order to make use of measurements of the wake of a small model wind

turbine [55]. The analysis of the NREL-UAE Phase VI turbine showed good correlation at low wind speeds to the experimental data available from the test, but at higher wind speeds strong deviations occurred on the inner half of the blade near the rotor hub [54]. These deviations could be due to limitations of the prescribed wake model in capturing the effects of a wake shape that differs from the empirical wake shape model, although further research would be necessary to prove this claim.

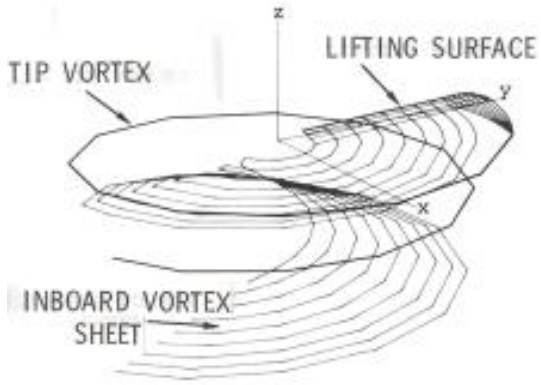

Figure 1-8 Vortex model used by Kocurek [50].

A hybrid semi-relaxed wake model was developed by Basom et al., which uses an assumed wake shape for each spanwise row of the vortex wake [4]. The pitch of the wake row is determined by a single induced velocity computation at the middle of the wake row, considerably reducing the number of induced velocity computations required in the vortex wake. The resulting wake shapes using the semi-relaxed wake model are shown in (c) and (d) of Figure 1-9 [4]. The results from the hybrid, semi-relaxed wake method indicated unacceptable errors in the coefficient of power when compared to the fully-relaxed (free) wake computation [1,4]. These errors are most likely caused by the vorticity in the wake not being stretched toward the center and edges of the wake, as occurs in the free-wake model.

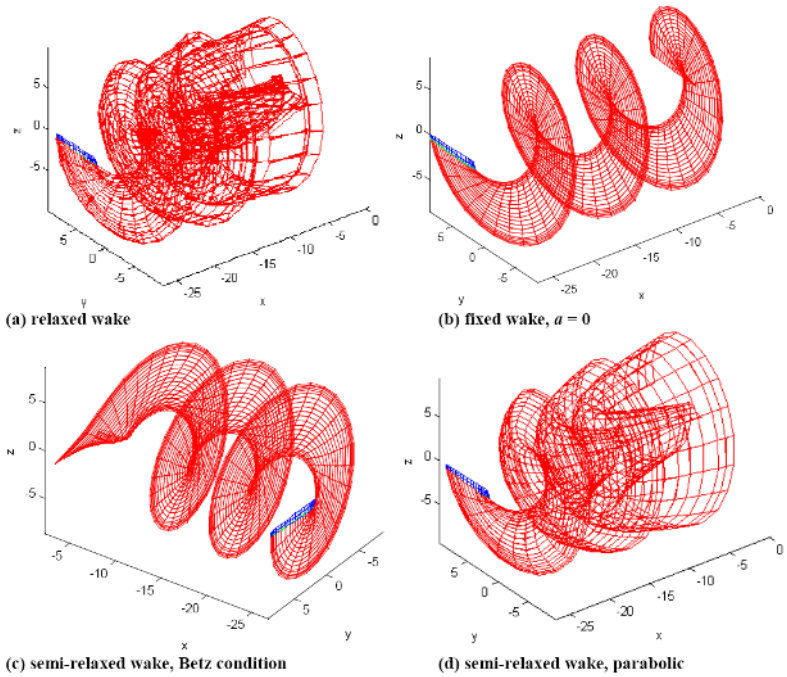

Figure 1-9 Comparison of various methods for wake shape computation, 3 wake revolutions, $\lambda = 6$ [4].

In 1999 Coton and Currin [56] published work performed to validate an unsteady prescribed wake model for the analysis of horizontal-axis wind turbines (HAWTs). This model was later coupled with the structural dynamics analysis tool FAST in order to provide full aeroelastic analysis capabilities of HAWTs (FAST is maintained by the National Renewable Energy Laboratory) [57]. The prescribed wake method was added to the aerodynamic analysis code AeroDyn, which is integrated with FAST [58–60]. A prescribed wake method was chosen over a free-wake method due to the decreased computational time of the prescribed wake method [56]. The method uses a vortex core model, but the model was not fully described in the paper. The trailing wake vortices are equal to the step-wise radial changes in the lifting surface bound vorticity. The wake prescription functions were developed based on empirical data of a HAWT operating in axial flow; the same prescription functions were later found to be applicable to a yawed rotor [56,57]. The empirical prescription functions describe wake axial flow velocities as a function of the axial induction factor of a spanwise blade, the freestream wind velocity, and the

local blade radius. These functions are calculated at three points downstream of the rotor and the velocities in-between are interpolated. The radial wake expansion is modeled by setting the radial wake velocity equal to the radial velocity computed at the rotor blade and assuming that the radial velocity transitions to zero at the far-wake. The wake vortex position depends on the blade element axial induction at the time that the wake vortex was generated. For steady-state operation, the entire downstream series of vortex filaments are updated based on the trailing and shed vorticity at the lifting surface for that time-step. For unsteady aerodynamic analysis, the wake geometry prescription function for each vortex filament is based on the axial induction factor of the blade element that shed the filament for the time-step when the filament was shed. The method also uses the Leishman-Beddoes unsteady aerodynamics model that is included in AeroDyn [56].

The results of the method match the experimental results of the NREL Phase VI wind turbine used to validate the prescribed wake analysis method fairly well for steady-state operation. The prescribed wake analysis results were comparable to the results from BEMT, but the GDW results differed significantly at the blade root and tip (most likely due to the lack of a tip-loss model in GDW) [57]. For the unsteady loads analysis, the yaw cases seemed to match the experimental data well; however, the cases of step-pitch change had significant errors [57]. One of the sources of error with this method is the condition that the wake filament prescription function does not change with time or with downstream location. This relates to the additional error source that is that the method is iterating on steady-state prescribed wake geometries. The authors of the paper believe that the total effect of these limitations is small, but offer no proof or data to indicate the magnitude of the effect of these limitations. A free-wake method avoids these errors by computing the local wake shape at each time-step, although this can require relatively small time-step size, which increases the required computational time.

If the wake shape is known, or if detailed performance results are not a priority, then the prescribed wake method can offer fast results with improved modeling capability than the BEMT

or GDW models for some analysis cases. Detailed design work can require modeling accuracy beyond what the prescribed wake method can offer (without knowledge of the wake shape). A prescribed wake method cannot capture the effects of interacting rotors, and would give significant errors for design cases such as a tandem rotor configuration or when modeling turbine-turbine interaction. For such cases, a free-wake vortex method would likely produce more physically accurate results.

1.3.3 Vorticity Elements used in Free-Wake Vortex Methods

Free wake methods model non-linear wake relaxation by iterating a potential flow model. The lifting surface and its shed wake are modeled with a potential flow solution and might include corrections for viscous forces and effects. The potential flow model of the lifting surface and wake is discretized in order to enable numerical modeling [3]. The locations of the trailing filaments are not known *a priori*, as with a prescribed wake method. Instead, they are moved with the local velocity that is computed at control points located on the filaments. The mathematical singularity at the center of each control point results in unrealistic induced velocities near that point. If a control point moves within close proximity of another filament, the unrealistic induced velocities at the control point can cause errors in the movement of the wake filament the control point is associated with.

1.3.3.1 Wake Relaxation

The relaxation of the wake elements can be performed through temporal iteration or through spatial relaxation. Methods that perform wake relaxation through spatial iteration include Clark and Leiper (1970), Rosen and Grabe (1988), Felker et al. (1988), Bagai and Lesihman (1995), Mortara and Maughmer (1993), and Emdad and Nikseresht (2003) [38,61–66]. Methods that perform time-marching (temporal) relaxation include Scully (1975), Baron and

Boffadossi (1993), Bramesfeld, and Maughmer (2007), and Basom and Maughmer (2010) [1,3,42,67,68].

The first calculation that demonstrated the utility of the representation of the vortex sheet by discrete line vortices was by Westwater in 1935 [69,70]. The eventual use of digital computers enabled the extension of the discrete vortex free-wake model to the evaluation of the three-dimensional vortex wake. As mentioned earlier, the use of discrete vortex filaments to represent the continuous vorticity of the vortex wake sheet causes numerical stability issues due to the pole-type singularity in tangential induced velocity at the center of the vortex filament. If a control point moves too close to the filament, non-realistic deformations of the wake can arise, causing erratic and numerically unstable behavior including: crossover of the vortex lines, shooting out of the vortex line from within the ordered sheet of the rolled-up tip vortex (Figure 1-10), and irregular oscillations in the positions of vortices in the rolled-up wake sheet [70]. The oscillations of the wake shape can become apparent in the calculation of the coefficient of pressure (CP), as shown in Figure 1-11.

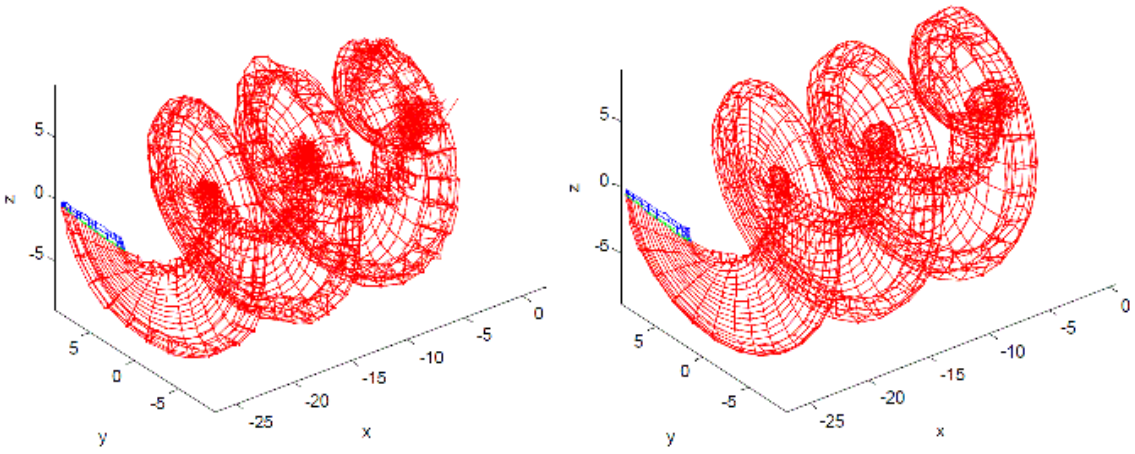

Figure 1-10 Oscillations in the convergence of the wake shape caused by numerical instabilities during wake relaxation (left) and a numerically stable solution (right) [4].

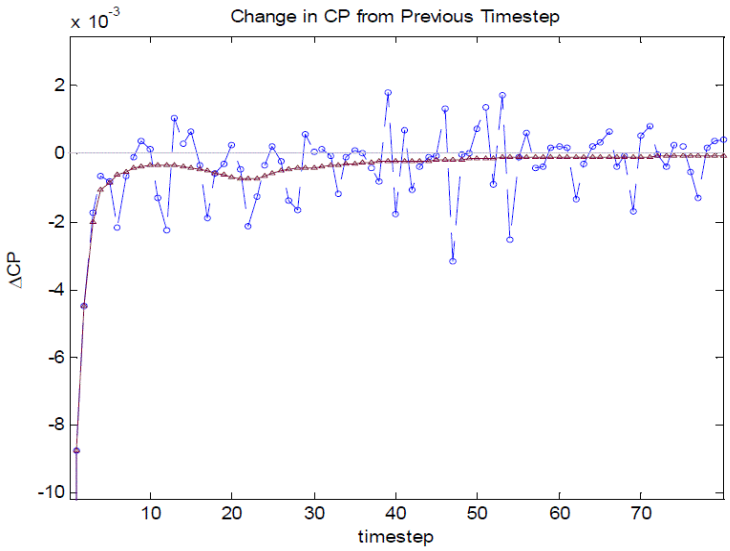

Figure 1-11 Oscillations in the convergence of the power coefficient caused by numerical instabilities during wake relaxation [4].

It was found by Hackett and Evens [71] that some of the numerical issues associated with the singularities of the discrete vortices could be removed by using vortices of equal spacing but of varying strength. Alternatively, the numerical issues can be avoided by moving the control points away from the influence of the singularity [4]. A more commonly used method to remove wake relaxation issues is the addition of a "cut-off" distance around the vortex filaments of the wake model. Numerical stability issues of the wake roll-up near the wake edge are also avoided by the use of an amalgamation technique, where vortex lines merge into a single line when the distance between two vortices drops below a certain distance [72].

A relaxed wake model is shown in the top of Figure 1-12, the bottom of Figure 1-12 shows the same relaxed wake model, but with a cutoff distance method applied, represented by the circles on the edges of the wake. Vortex core models can also be used to avoid numerical issues caused by the cores of the discrete vortices; these models are discussed in the next section.

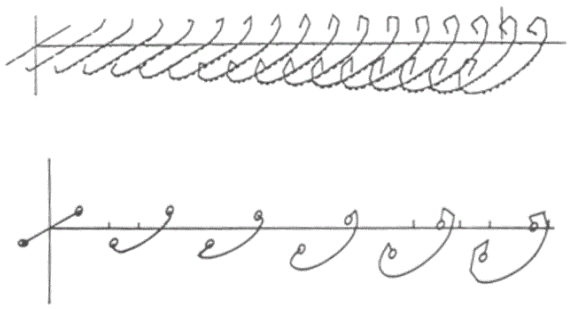

Figure 1-12 Relaxed wake using discrete vortex lines without a tip-core cutoff distance (top) and with a tip-core cutoff distance (bottom) [70].

1.3.3.2 Vortex Filaments and Lines

A geometric representation of vortex filaments (also called vortex lines) is shown in Figure 1-13. A vortex wake model is created by attaching many filaments together to model the shed and trailing vorticity. Curved vortex filaments can offer a better geometric approximation of the helical form of the wake behind a wind turbine, although they are slightly more complicated to implement than straight-line vortex filaments [42,43].

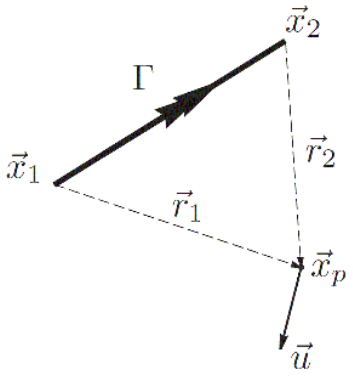

Figure 1-13 Geometric representation of the parameters used to calculate the induced velocity via Equations 1-1 and 1-2 [37].

By applying the Biot-Savart law, the tangential induced velocity of a straight vortex line vortex filament with constant vortex strength Γ is given by:

$$\overrightarrow{u_\Gamma}(\overrightarrow{x_p}) = \frac{\Gamma}{4\pi}\frac{(r_1+r_2)(\overrightarrow{r_1}\times\overrightarrow{r_2})}{r_1 r_2(r_1 r_2+\overrightarrow{r_1}\cdot\overrightarrow{r_2})} \quad (1\text{-}1)$$

where $\overrightarrow{x_p}$ is the evaluation point (also called influenced point, control point, or collocation point), $\overrightarrow{r_1}$ and $\overrightarrow{r_2}$ are vectors from the endpoints of the influencing vortex filament to the evaluation point, and r1 and r2 are the lengths of $\overrightarrow{r_1}$ and $\overrightarrow{r_2}$; these parameters are illustrated in Figure 1-13 [37]. The application of the "cut-off radius" parameter, δ, results in:

$$\overrightarrow{u_\Gamma}(\overrightarrow{x_p}) = \frac{\Gamma}{4\pi}\frac{(r_1+r_2)(\overrightarrow{r_1}\times\overrightarrow{r_2})}{r_1 r_2(r_1 r_2+\overrightarrow{r_1}\cdot\overrightarrow{r_2})+(\delta l_0)^2} \quad (1\text{-}2)$$

In Equation 1-2, the parameter delta (δ) is a function of the length of the vortex line filament (l_0), and is typically reported as a percentage [37].

The van Garrel smooth-transition method (given in Equation 1-2) and the cut-off radius methods modify the tangential induced velocities of vortices and are used to improve numerical stability of the vortex method solutions; the tangential induced velocity results from the smooth-transition model are shown in Figure 1-14. The central region of a vortex structure (referred to as the vortex core) is influence by viscous effects. One model of the viscous core region is the Rankine model; in this model, the velocity peaks at r^* and then linearly transitions to zero induced velocity at a radius of zero (which implies that r_1 and r_2 goto zero in Equation 1-2 and that β and γ go to zero in Equation 1-3). The tangential induced velocity given by the Rankine model is shown in Figure 1-15 for comparison to the induced velocities from the smooth-transition model of van Garrel, shown in Figure 1-14.

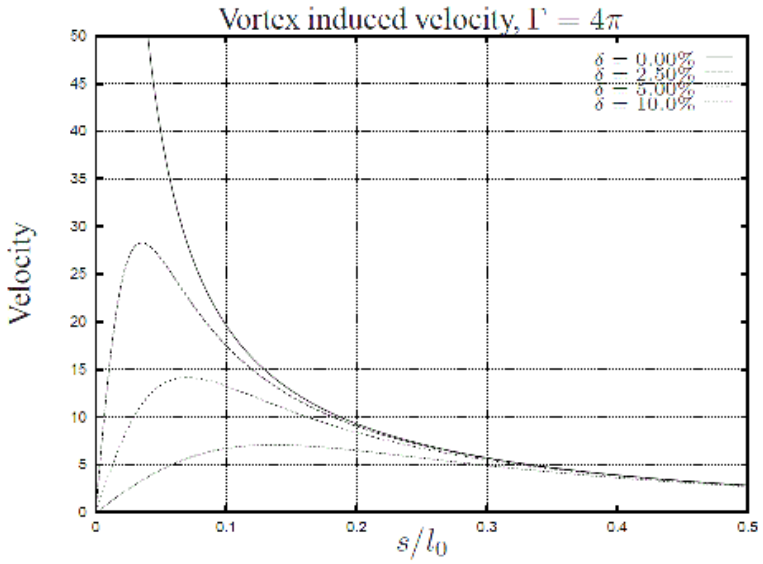

Figure 1-14 Tangential induced velocity using a smooth transition cut-off radius [37].

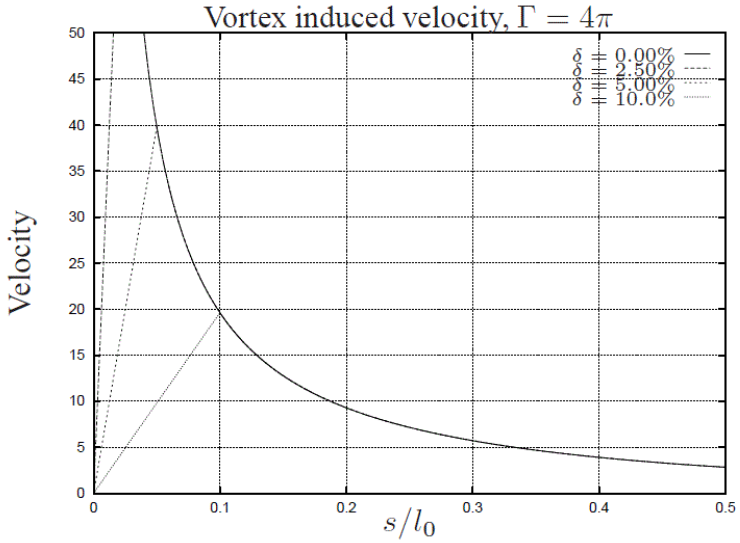

Figure 1-15 Tangential induced velocity using a Rankine core cut-off radius [37].

The rate and shape of the wake roll-up is influenced by the selection of the cutoff distance, which Rom [70] states should be found through numerical experimentation in order to prevent numerical stability issues. The free-wake method by van Garrel [37] used a value of $\delta = 0.01$ throughout the vortex wake, although reported that values could range from 1 to 10% and a value of 0.01% could be used on the bound vortices [37,73]. The free-wake vortex method

of Kloosterman [73] initially used a smaller value for δ, but increased to δ = 0.01 in order the match the theoretical circulation distribution of an elliptic fixed wing.

The fixed value for δ used by van Garrel and Kloosterman is easy and quick to implement; however, Rom [70] reported that by varying the size of the cut-off radius or vortex-core parameter with the local flow conditions at a given timestep, numerical stability could be improved [70]. The geometric properties of the cutoff distance method of vortex core modification used by Rom are shown in Figure 1-16 [70].

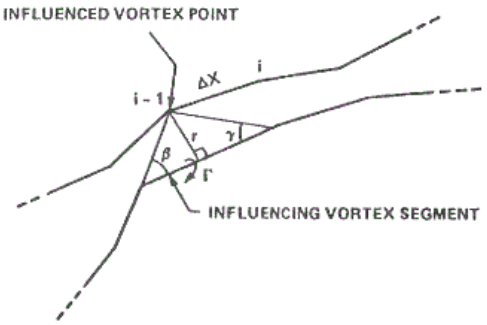

Figure 1-16 Geometric representation of the parameters used to calculate the cutoff distance in Equation 1-3 [70].

The vortex core cut-off radius as a function of the time-dependent geometric properties of the vortex filament are given by:

$$r^* = \left[\frac{\Gamma\,\Delta x\,(\cos\beta+\cos\gamma)}{4\pi V_\infty}\right]^{1/2} \tag{1-3}$$

where the parameters are defined in Figure 1-16 [70,74]. The cutoff distance in Equation 1-3 is dependent on the length (Δx) of the vortex line segment on which the induced velocity is being calculated and on the length (represented by angles β and γ) and circulation strength (Γ) of the influencing vortex; these values change with each filament and each timestep [70]. The resulting cut-off radius found in Equation 1-3 can replace the ($\delta^* l_0$) parameter in Equation 1-2 or can be used in a Rankine vortex core type model. Almosnino [74] reports that letting the cut-off distance vary based on Equation 1-3 yielded faster convergence times due to 10-20%, required

fewer iterations and allowed some cases to converge that did not converge when a fixed value for r^* (or δ) was used.

1.3.3.3 Vortex Blobs

A vortex blob is created by making a smooth approximation of a point vortex [75]; this approximation is made by applying a cut-off radius to a point vortex (also called a vortex particle), which creates a spherical vortex core [72]. The method has the advantage that the vortex blobs are free to move independently of each other, which can be helpful when modeling complex flow-fields that are not readily modeled by vortex sheets or lines. A position vector and a strength vector are used to track each vortex blob, which can be thought of as a vortex filament with no length [68]. The strength vector experiences strain based on the local velocity gradient [68]. One disadvantage of the use of vortex blobs, relative to vortex filaments, is that both the vortex particle location and the circulation strength (each of which is a three component vector) must be calculated and stored at each time step [72]. Stretching does not have to be specially accounted for in a filament method, since it is accounted for through the advection of the control points at the ends of the vortex filament [72]. Only one control point vector and a scalar of the circulation strength need to be calculated and stored for each time-step of the filament method, giving it a lower computational cost than a vortex blob method. The initial strength of a vortex blob is equal to the local vorticity shed at the corresponding span-wise element on the lifting surface multiplied by the grid spacing between elements to the third power [72].

Vortex particle methods have been used to analyze complicated water flow, helicopter wakes, and wind turbines [68,76,77]. Any of the vortex core models can be applied to the vortex blobs, although linear transitions through the vortex core are common, similar to a Rankine vortex core model. An analysis of vortex wake roll-up in the Trefftz plane was undertaken by Krasney [75] using a vortex blob model. The method was able to effectively model the tight roll-

up of the vortex wake tip vortex. The work by Krasney [75] included a thorough investigation of the effect of time-step size, number of elements, and of round-off errors. Round-off errors were found to be particularly important in regions of the wake influenced by numerical instabilities [75]. An illustration of the initial wake roll-up is shown in Figure 1-17. The left-side of the figure shows the vortex blob positions and the right-side shows an interpolated curve through these points.

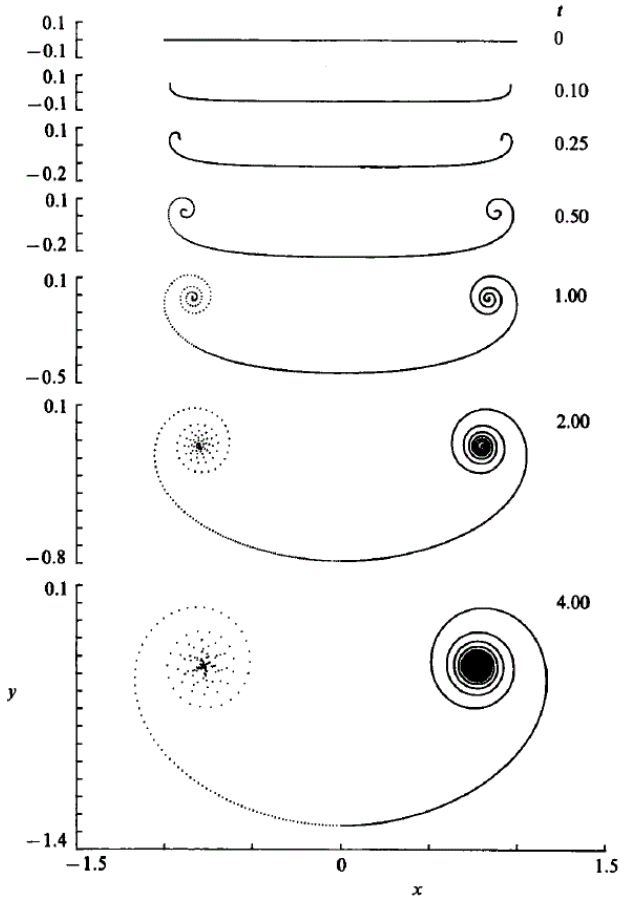

Figure 1-17 Vortex wake roll-up analysis using vortex blobs. The left side of the image shows the vortex blob positions and the right side shows interpolated curve through these points [75].

Lee and Na [68] used a free vortex blob method to model the initial transients of a helicopter rotor as it begins to hover. It was found that initial instabilities in the wake solution could be limited by slowly starting the rotor rather than impulsively starting it, the latter of which

is done by most methods [68]. The wake solution for a rotor in hover is shown in Figure 1-18, where the "cloud" of vortex blobs in the bottom of the image is caused by the startup transients [68].

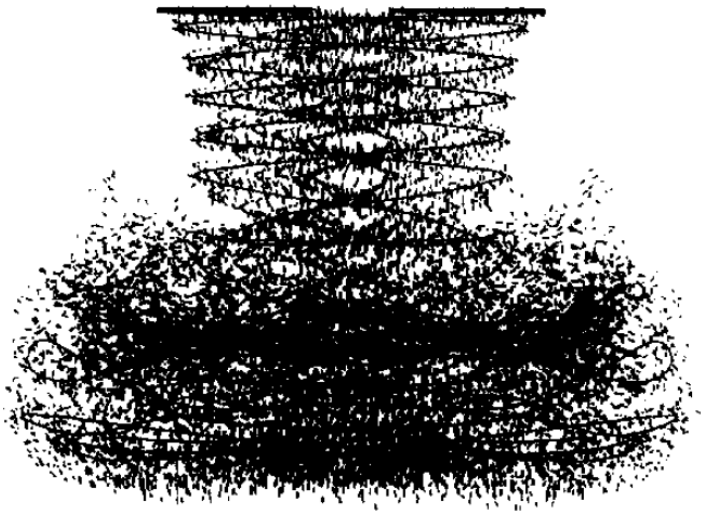

Figure 1-18 Vortex blob representation of 12 revolutions of the wake of a hovering helicopter [68].

1.3.3.4 Distributed Vorticity Elements

One issue with the use of all of the above mentioned methods is that the solution of the wake shape and the induced velocity and loads on the main wind turbine become dependent on the cut-off distance or vortex core model, which must be either determined using empirical data of the tip-vortex core or through trial and error experimentation with the numerical stability of an analysis code. The DVE method of Bramesfeld and Maughmer uses distributed sheets of vorticity to model the wake [2,3]. These sheets only have singularities at the side-edges of the wake. The singularities are logarithmic, and are thus considerably weaker than the pole-type singularities of a vortex filament. The DVEs will be discussed more in the next chapter.

1.3.4 Viscous Effects in the Wake

Viscous effects on the wake were not included in the development of WindDVE, but could be added as a future addition to the method, so a brief description of such models is given in this section. Potential flow solutions, which include vortex methods, provide good modeling tools of the lifting surface and its interdependent relationship with the wake. Viscous effects are not included in a potential flow solution, but can be added to analysis tools in the form of viscous effect models.

In potential flow solutions, the wake is often modeled as being thin, infinitely thin in the case of a vortex sheet or point vortex. The physical wake behind a lifting surface has thickness. Two-dimensional temporally relaxed wake sheets with thickness have been successfully modeled, as shown in Figure 1-19, but no published results have been found that apply such a model to full three dimensional models of lifting surfaces [70]. Conventional vortex wake models are based on the assumption that effects of wake thickness are negligible. In such models, the wake is modeled by zero-thickness vortex singularity elements, such as vortex sheets, vortex filaments, or vortex particles. Corrections can then be applied to the model to account for the wake thickness, such as models of the viscous vortex core. The thickness of the wake can also be modeled using multiple vortex sheet models, which Simoes and Grahm used to model the wake of a wind turbine operating near or post stall [78].

The vorticity shed from a wind turbine blade concentrates near the tip-side edge of the wake. This stronger region of vorticity is referred to as the tip vortex. Some methods model only the tip vortex and apply a vortex core model to model the measured velocities in the tip vortex core region. The vortex core model serves the purpose of preventing numerical instabilities that would be caused by the singular behavior of the Biot-Savart induced velocity calculation. Some methods also use vortex filaments to model the inner sections of the wake. A vortex core model can be used to maintain numerical stability of the induced velocity calculations in the inner wake

region, although these models are empirically tuned to experimental measurements of the induced velocity of the tip vortex region since the induced velocity in the inner wake is too low to accurately measure experimentally [73].

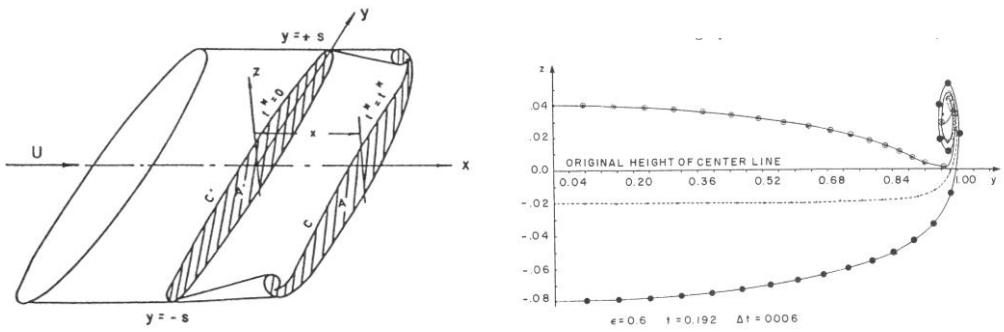

Figure 1-19 Cross section of a wake modeled with thickness. Figure from Rom, Ch. 5.3.2 [70].

For some modeling problems the vortex core model is desired to predict the viscous effects in the wake, rather than only applying a vortex core model for the sake of numerical issues. For example, if detailed induced velocities in the wake are needed to compute the effect of wake interaction on a downstream turbine for turbine-turbine interaction problems. Such effects are important for modeling "wake turbulence", particularly for the interaction of small aircraft with the wakes of much larger aircraft [7].

The representation of viscous effects in the vortex wake can be split into three physical effects: viscous diffusion; vortex stretching; and viscous dissipation [64]. Models that capture these effects are applied to the tip, vortex-core model, since this is typically the most dominant flow feature of the wake. The models of these flow feature effects are semi-empirical; however, the flow features are hard to measure, requiring hot-wire anemometer velocity measurements or particle image velocimetry (PIV) [73]. The central wake flow features are particularly hard to measure due to the smaller values of vorticity and wake-dependent (induced) velocities relative to the dominate influence of the tip-vortex, contributing to the lack of viscous effect models applicable to this flow region. Despite the lack of a proper model of viscous effects for the

central wake, the viscous effects models are sometimes applied to the central wake flow region, essentially as a replacement for the "cut-off radius" method for the avoidance of singularity issues. The free-wake DVE method has not yet been applied to the turbine-turbine interaction problem; therefore, it does not employ a vortex core model.

1.3.5 Summary

This section has given an overview of various analysis methods available for wind turbines: BEMT, GDW, PWVM, FWVM, and CFD. The blade-element momentum theory (BEMT) is applicable to the design of planar blades near their design point, but shows errors at off-design conditions and cannot properly model non-planar or swept blade designs. It cannot model unsteady wake effects unless a time delay model is added, which would make it similar in capabilities and limitations as the general dynamic wake (GDW) model. The prescribed wake vortex method (PWVM) is applicable to rotors of low disc loading or where the shape of the wake is known prior to the analysis. The free-wake vortex method (FWVM) can model the shape of the wake, and can accurately model higher rotor blade loadings without needing to know the wake shape a priori. The FWVM can use vortex filaments, vortex blobs, quadrilateral elements or DVEs. The higher-order parabolic circulation distribution of DVEs allows the use of fewer span-wise surface elements to achieve the same level of accuracy as do the constant strength surface elements used in most other vortex methods. It is common to use vortex filaments to model the discretized vortex wake, where the core of each filament contains a singularity that requires special treatment in order to avoid numerical issues resulting in unrealistic wake deformations. In the DVE method, the singularities of adjacent DVE elements cancel each other, so that special treatment to prevent numerical issues is only required at the wake ultimate side-edge and when DVEs meet at acute angles [1,3].

Chapter 2

Free-Wake DVE Method: Velocities, Angles, and Forces

The wind turbine analysis method described in this chapter uses distributed vorticity elements (DVEs) to model the pressure and velocity field of the wind turbine lifting surface and its wake. Both the lifting surface and the vortex wake are modeled using DVEs. The interaction between the lifting surface and the wake vorticity is captured by solving an equation system, the solution of which results in the distribution of circulation across the lifting surface. The shape of the wake is determined by moving each wake DVE element by the total velocity acting on it. The control point of each wake element convects with the total local flow field, and each wake element moves into alignment with the local induced velocity.

The forces on the lifting surface are computed by either applying the Kutta-Jowkowski therorem on the spanwise vortex filaments of the lifting surface DVEs, or by using the stall model that uses airfoil data look-up to determine the force on the lifting surface based on the angle of attack at each spanwise station. Profile drag can be included in either method. The relaxation of the wake shape is the most computationally time consuming process, so several options are available to improve this, including extrapolating a fixed wake shape and extrapolating wake velocities for the steady analysis cases. A description and exploration of these methods is presented in the next three chapters.

2.1 Summary of the DVE Method

The DVE method of Bramesfeld and Maughmer uses distributed sheets of vorticity to model the wake [2,3]. The distributed sheets of vorticity have singularities only at the ultimate

side-edges of the wake, and these singularities are logarithmic, which are considerably weaker than the pole-type singularities of a vortex filament [2].

The DVE method is based on the multiple lifting-line method of Horstmann, which models the circulation distribution along the lifting line as a parabolic distribution [1,2]. A distributed vorticity element (DVE) is made up of a leading edge and a trailing edge vortex filament segment with parabolic circulation distributions, equal in magnitude and opposite in orientation, as illustrated in Figure 2-1 and previously in Figure 1-1 [2]. A vortex sheet with vorticity aligned with the streamwise direction exists between the leading edge and trailing edge filaments, maintaining the total vorticity in the streamwise direction. The vortex sheet has a distribution of vorticity, which varies linearly in the spanwise direction. The lifting surface and wake are modeled by placing DVEs together to model the velocities induced by these flow features. The wake DVEs are free to move with the local induced and freestream velocities.

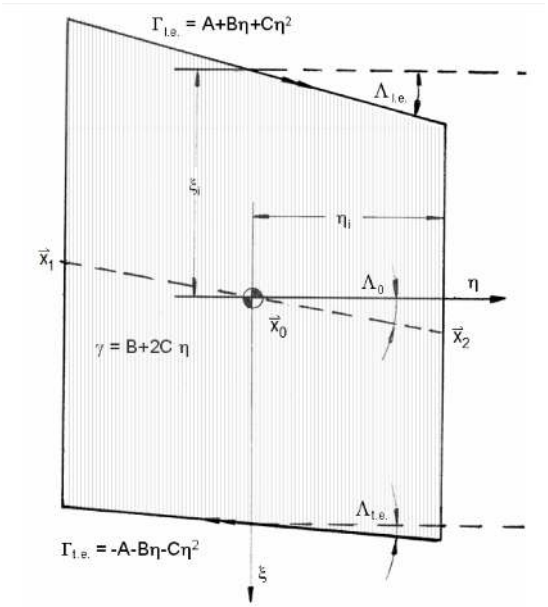

Figure 2-1 The distributed vorticity element local coordinate system and geometry [4].

In the DVE method, the circulation along the blade span is represented by lifting surface elements with a continuous parabolic circulation distribution. Many methods use a lower order,

lifting line circulation distribution model (linear or constant), which causes discretization errors [3].

The parabolic circulation distribution of the DVE surface elements is represented by three circulation coefficients: A, B, and C. The parabolic circulation distribution for one element in the local coordinate system of the element is represented by:

$$\boldsymbol{\Gamma_i(\eta) = A_i + B_i(\eta) + C_i(\eta)^2} \tag{2-1}$$

where the element has spanwise width of 2η and goes from $-\eta$ to $+\eta$. The vorticity distribution of the vortex sheet shed by a vortex filament with a parabolic circulation distribution is given by:

$$\gamma_i(\eta) = B_i + 2\eta C_i \tag{2-2}$$

A lifting surface is made of several of these spanwise elements placed together, as illustrated in Figure 2-2.

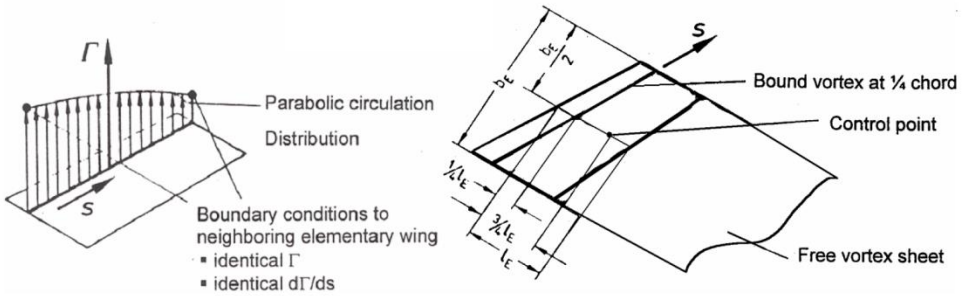

Figure 2-2 A surface is paneled with DVEs, which have a spanwise parabolic circulation distribution [9].

Three equations are needed for each element in order to solve for the three unknown coefficients (A, B, C). Two of the equations are given by the boundary condition of circulation and vorticity at the side-edge of each panel.

For n surface elements, 3n equations are needed to find a solution for the circulation coefficients. The surface element side-edge circulation and vorticity boundary conditions give 2n of the equations, while the remaining n equations come from a boundary condition defining the

magnitude of circulation along the element. The flow tangency condition is applied at control points on the surface DVEs, as illustrated in Figure 2-3. The boundary conditions can be thought of as defining the shape of the spanwise circulation distribution, while the final equation defines the magnitude of the circulation (truly all define the final shape).

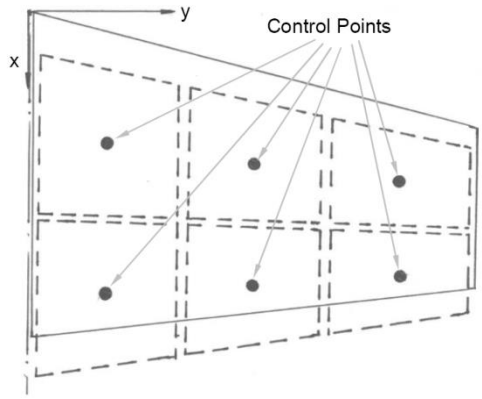

Figure 2-3 Paneling of a lifting surface (solid lines) using distributed vorticity elements (dashed lines) [2].

For an analysis case of a circulation distribution on the lifting surface that does not vary with time, it can be assumed that all leading edge and trailing edge vortex filaments of the wake DVEs cancel each other. For an unsteady analysis case, where the lifting surface circulation changes with time, the wake DVE vorticity will vary in the streamwise (along the wake helix) direction. Steady and unsteady analysis cases will be discussed in the section on the equation system solution and in the section on wake modeling.

2.2 Reference Frames

2.2.1 Global Reference Frame

The wind turbine rotor and blades are defined in a stationary global reference frame [4]. This global reference frame is represented by a Cartesian coordinate system with X, Y, and Z axes and also by a cylindrical coordinate system with an X-axis, a radial axis, and a tangential

axis. The global reference frame and coordinate systems are illustrated in Figure 2-4. The Cartesian coordinate system is referred to as the global XYZ coordinate system and the cylindrical coordinate system is referred to as the ART coordinate system (axial-radial-tangential). The X-axis is equivalent in both coordinate systems and lies along the rotor's axis of rotation; the X-axis defines the axial direction and the downstream (or positive wind speed) direction. Positive rotor rotation of a speed Ω follows right-hand rotation about the X-axis. The Z-axis points away from the center of the Earth, or along the axis of a vertical wind turbine tower. The Y-axis points right when looking upstream.

Some revisions of the WindDVE code have an option to either keep the rotor stationary along the X-axis and move the wake downstream by the wind speed or to only move the wake by the induced velocities and march the rotor upstream to simulate the wind speed. For cases when the rotor moves axially to simulate the wind speed, the rotor is marched upstream along the negative X-axis.

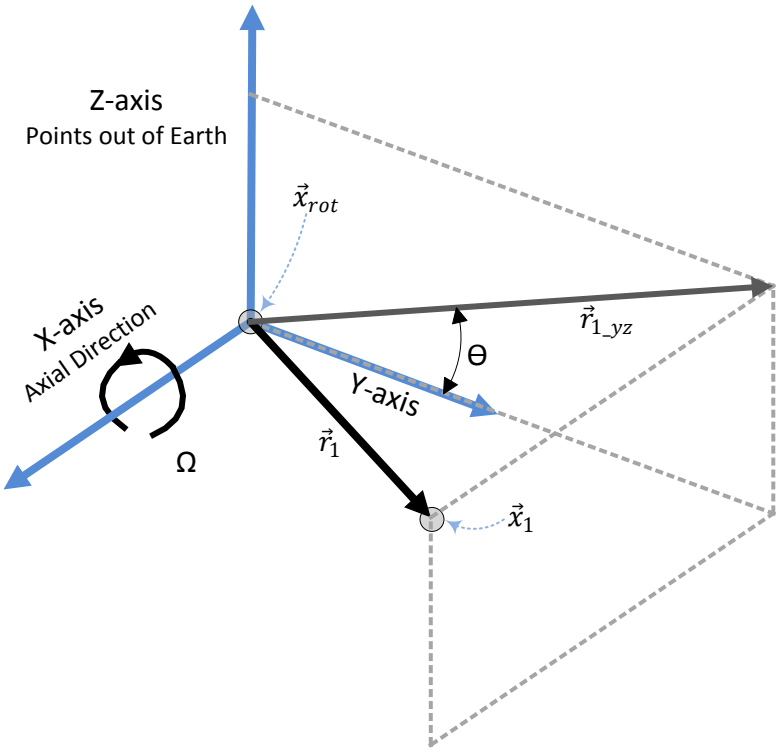

Figure 2-4 Major axes of the Global Coordinate Reference Frame (XYZ Coordinate System).

The rotor rotates in the Y-Z plane; the radial direction of the cylindrical reference frame is also in the Y-Z plane. The center of rotation of the rotor is at the point $\vec{x}_{rot}$. For a point $\vec{x}_1$ along the rotor blade, the vector to the center of rotation is $\vec{r}_1$, as shown in:

$$\vec{r}_1 = \vec{x}_1 - \vec{x}_{rot} \tag{2-3}$$

The projection of $\vec{r}_1$ onto the Y-Z plane is represented by $\vec{r}_{1\_yz}$.

The angle θ is positive for right-hand rotation about the X-axis, with θ being measured between the Y-axis and the radial direction, represented by $\vec{r}_{1\_yz}$. The cylindrical and Cartesian coordinate systems are related by:

$$x = x; y = r\cos\theta; z = r\sin\theta \tag{2-4}$$

2.2.2 Local DVE Reference Frame

The local forces and velocities of a DVE are given in a local element-fixed reference frame. The DVE reference frame is represented by the Cartesian ξ-η-ζ (xi-eta-zeta) coordinate system, as shown previously in Figure 2-1. The ξ-axis is aligned with the local flow direction, which is defined as the local tangential vector of the rotor. The vorticity of the sheet is aligned with the ξ-axis and the vortex sheet of the DVE is in the ξ-η (or chord-span plane of the DVE). The η-axis lies along the span of the element and is perpendicular to the local flow direction. The ζ-axis is normal to the plane of the DVE, defined by the ξ and η axes. The origin of the local DVE reference frame is located at its geometric center and is designated by the reference point $\vec{x}_0$ in the global reference frame. The point $\vec{x}_0$ is also the control point of the DVE, where the kinematic boundary condition is imposed in the surface circulation equation system solution [2,4].

The leading edge and trailing edge vortex filament of the DVE intersect lines parallel to the η-axis at the sweep angles $\Lambda_{l.e.}$ and $\Lambda_{t.e.}$. The side-edges of the DVE are parallel to the ξ–

axis, which is also the local flow direction. The span of the DVE is parallel to the η–axis and is equal to $2\eta_i$. The chord runs between the midpoint of the leading edge filament and the midpoint of the trailing edge filament; the chord length is $2\xi_i$. The DVE mid-chord line runs between the mid-chord of the left and right DVE side-edges. The mid-chord points in the local coordinate system of the left and right side-edges can be found given the mid-chord sweep angle (Λ_0) and the span of the DVE (η_i), as shown by:

$$\overrightarrow{x_1} = \begin{bmatrix} -\eta_i \tan \Lambda_0 \\ -\eta_i \\ 0 \end{bmatrix} \qquad \overrightarrow{x_2} = \begin{bmatrix} \eta_i \tan \Lambda_0 \\ \eta_i \\ 0 \end{bmatrix} \tag{2-5}$$

The orientation of a DVE is defined by three orientation angles: dihedral (υ), incidence (ϵ), and yaw (ψ). A vector in the global reference frame can be transformed to the local DVE reference frame through three steps relative to the three orientation angles. Positive rotation direction follows the right-hand rule [4].

1.) Dihedral: Intermediate axis's x'-y'-z' formed by rotation of angle υ about the X-axis.
2.) Incidence: Intermediate axis's x"-y"-z" formed by rotation of angle ϵ about the y'-axis.
3.) Yaw: Local DVE axis' ξ-η-ζ formed by rotation of angle ψ about the z"-axis.

The full matrices used to transform between these two reference frames are listed in Ref. [4].

2.3 Blade Section Angles and Velocities

The relevant aerodynamic angles of a blade element section are shown in Figure 2-5. The angle-of-attack of the airfoil zero lift line ($\alpha_{\emptyset L}$) shown in Figure 2-5 is positive, which corresponds to an airfoil with negative camber. Figure 2-6 shows the blade section angles for a positively cambered airfoil, which typically has a negative value of $\alpha_{\emptyset L}$.

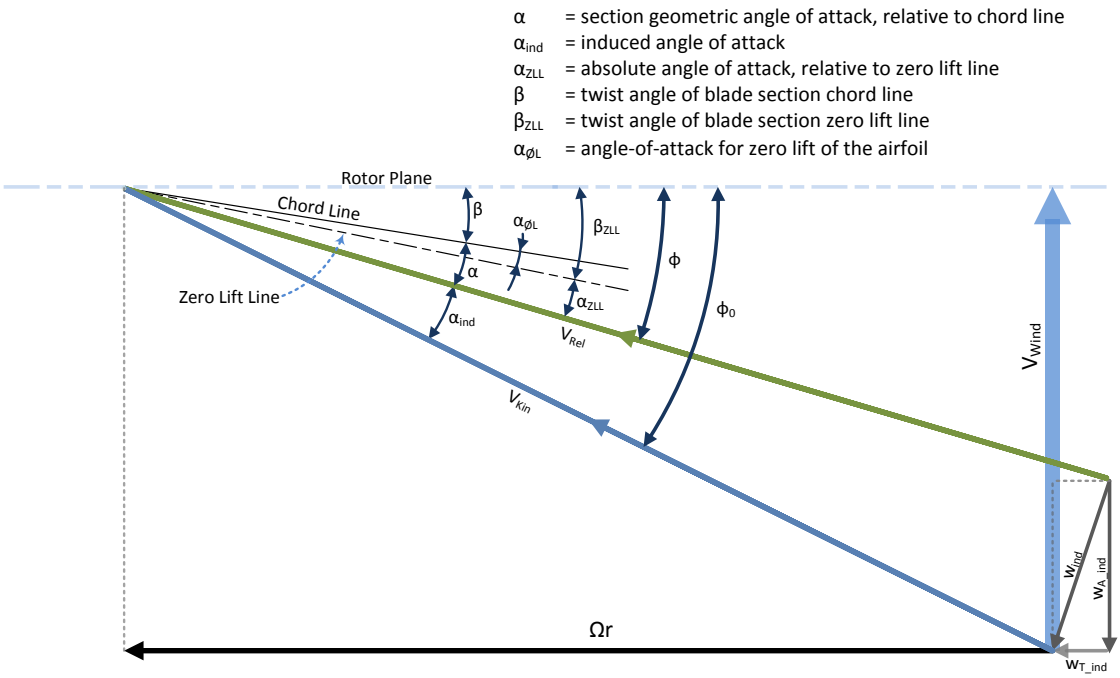

Figure 2-5 Blade section angles used in WindDVE. The angle-of-attack for zero lift ($\alpha_{\emptyset L}$) is shown with a positive value, which corresponds to a negatively cambered airfoil.

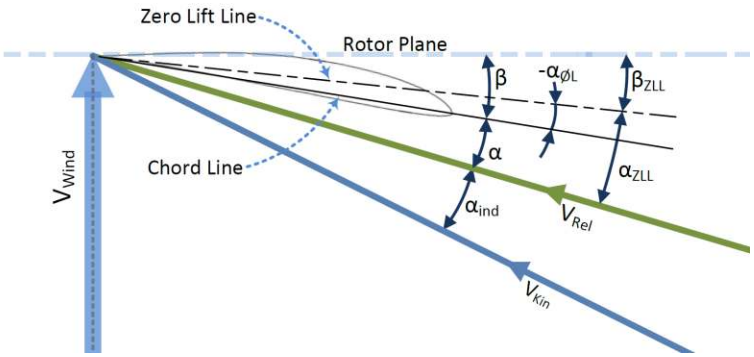

Figure 2-6 Blade section angles used in WindDVE. A positively cambered airfoil is shown, which corresponds to a negative value of angle-of-attack for zero lift ($\alpha_{\emptyset L}$).

Reference is made throughout this section to the freestream velocity and the freestream force on the lifting surface. What is referred to as the freestream velocity is actually the combination of the body velocities and the wind velocity. For a wind turbine, the body velocities include the effect of rotor rotation and any velocity due to blade or rotor deflection. Dynamic blade and rotor deflections have not been modeled in the present research, although the

WindDVE code has been modified to account for additional body velocities that could be prescribed by a structural dynamics analysis method. The freestream velocity is also referred to as the kinematic velocity and is found from:

$$\vec{V}_{Kin} = \vec{V}_{Wind} + \Omega r \tag{2-6}$$

where r is the local radial distance in the plane of the rotor. The freestream force magnitude is dependent on $\vec{V}_{Kin}$, the freestream force is normal to $\vec{V}_{Kin}$.

The induced velocity of the entire wake system on the lifting surface is represented by the term $\vec{w}_{ind}$, which has components normal and tangential to the rotor plane. The vector sum of the induced wake velocity and $\vec{V}_{Kin}$ results in the total velocity:

$$\vec{V}_{tot} = \vec{V}_{Kin} + \vec{w}_{ind} \tag{2-7}$$

The profile forces of a blade element section are relative to the component of $\vec{V}tot$ in the plane of the blade element section chord unit vector ($\hat{e}_{chord}$) and normal unit vector ($\hat{e}_{normal}$). The terms "V_{Kin}" in Figure 2-5 and Figure 2-6 and "w_{ind}" in Figure 2-5 refer to the components of $\vec{V}_{Kin}$ and $\vec{w}_{ind}$, respectively, that are in the $\hat{e}_{chord}$ and $\hat{e}_{normal}$ plane. As illustrated in Figure 2-5, the relative velocity ($\vec{V}_{Rel}$) is the sum of the components of $\vec{V}_{Kin}$ and $\vec{w}_{ind}$ that are in the $\hat{e}_{chord}$ and $\hat{e}_{normal}$ plane. The relative velocity can also be found from the component of the total velocity in the plane of $\hat{e}_{chord}$ and $\hat{e}_{normal}$:

$$\vec{V}tot_{Norm\_Chord} = \left(\vec{V}tot \cdot \hat{e}_{chord}\right) + \left(\vec{V}tot \cdot \hat{e}_{normal}\right) \tag{2-8}$$

$$\vec{V}_{Rel} = \vec{V}tot_{Norm\_Chord} \tag{2-9}$$

If there is no local element spanwise flow, then the total and relative velocities are equivalent. The relative velocity is used to compute the profile forces on the blade element section; the profile drag is along the relative velocity vector and the profile lift is normal to it.

2.4 Lifting Surface Geometry and Paneling

2.4.1 Panel Definition

An example wind turbine blade created by WindDVE is shown in Figure 2-7.

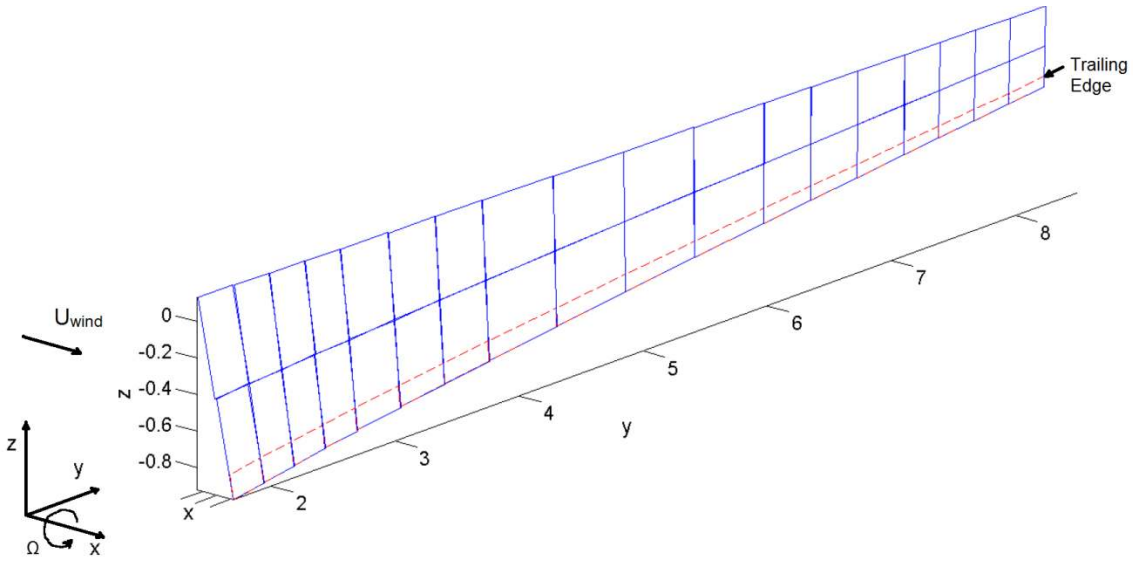

Figure 2-7 Blade represented by surface DVEs in WindDVE. Surface DVEs are the blue, solid lines and trailing-edge DVEs are the red, dashed lines [5-modified].

The wind turbine blade lifting surface is made up of surface panels, one of which is shown in Figure 2-8. The panel "right-side" and "left-side" are defined with the blade root on the left and the blade tip on the right when the blade is viewed from above. The left side-edge is referred to as the inner side-edge (subscript "i") and the right side-edge is referred to as the outer side-edge (subscript "o"). Each panel is defined along its quarter-chord line by an inner point (**X1** or $\vec{x}_1$) and an outer point (**X2** or $\vec{x}_2$), both of which are coordinates in the X-Y-Z global coordinate system.

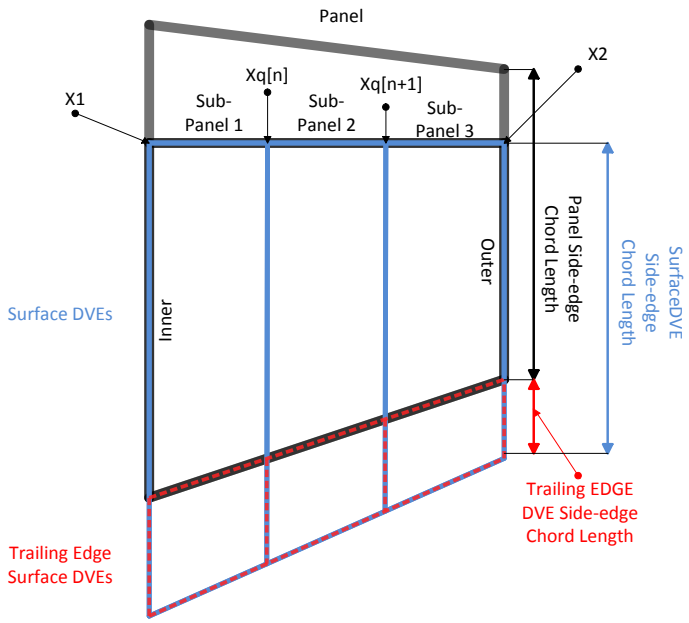

Figure 2-8 Surface panel (black lines) represented by surface DVEs (blue lines) and trailing-edge DVEs (dashed, red lines).

A planar blade will only have input geometry in the Y-axis. For zero sweep and dihedral, a quarter chord line with no sweep or dihedral lies along the positive Y-axis. Sweep is accounted for by adding to the panel Z-axis quarter-chord line definition; positive sweep angle requires deflecting the quarter-chord line in the negative Z-axis direction. Dihedral is accounted for through changes in the blade X-axis, which is aligned with the axis of rotation, with positive pointing downwind. For example, a suction-side winglet will point downwind on an upwind (of the tower) wind turbine, which will require adding positive deflection to the X-axis coordinate of the tip-edge of the winglet panel. The definition of the blade geometry in relation to the global reference frame in WindDVE is different from the blade geometry definition in the multiple lifting-line method of Horstmann [9] and the DVE based code FreeWake2007 [2], as illustrated in Figure 2-9. The WindDVE blade planform definition is equivalent to the planform definition of Horstmann and FreeWake2007 with a twist of ninety degrees, which places an untwisted blade in the Y-Z plane and aligns the component of wind normal to the rotor with the X-axis.

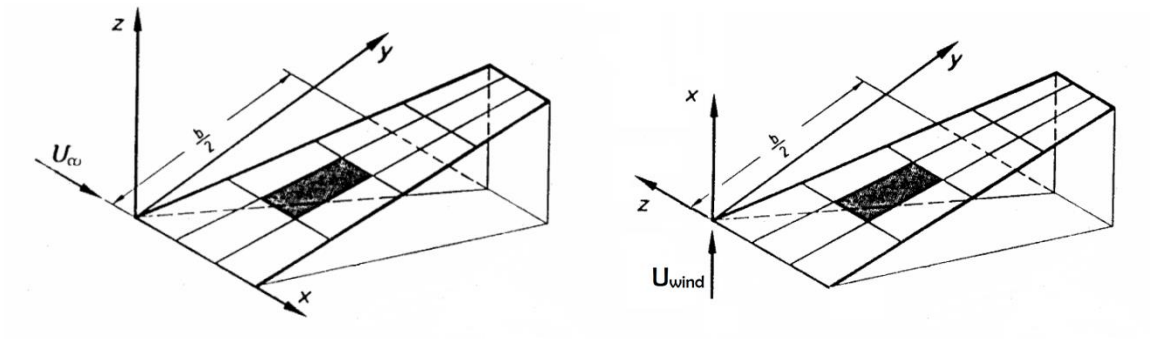

Horstmann and FreeWake2007 **WindDVE**

Figure 2-9 Lifting surface orientation of Horstmann [9] and FreeWake2007 [2] compared to the orientation of WindDVE [4]. Original image from Ref. [9].

Each panel can be divided into "n" span-wise sub-panels of equal span. The sub-panels are referred to as "elementary wings" in previous papers on DVEs [2,3,9]. If there is more than one sub-panel (n > 1), then the sweep of each sub-panel follows a gradual transition from the sweep of the inner subpanel to the outer sub-panel. The sub-panels are defined along their mid-span and mid-chord lines as an average of the corner points that define them. The side-edges of the sub-panel DVEs are parallel to each other and to the mid-span line, which is also the chord line of the DVE. The untwisted chord line of each DVE is defined such that it is aligned with the local tangential direction. The average chord length is defined along the mid-span line, as well as the xi (ξ) axis of the DVE.

A row of DVEs is applied along the trailing edge of the surface panels. The leading edge of this row of DVEs is continuous, which can alleviate issues caused by the gaps at the trailing edge of surface panels due to pitch or dihedral changes. A more detailed overview of trailing edge surface DVEs can be found in Ref. [4].

If more than one lifting line is used to model the lifting surface, as shown in Figure 2-10, then an equal number of chord-wise surface DVEs are applied to the surface and the leading-edge

of the row of DVEs closest to the panel leading edge is no longer aligned with the quarter-chord line.

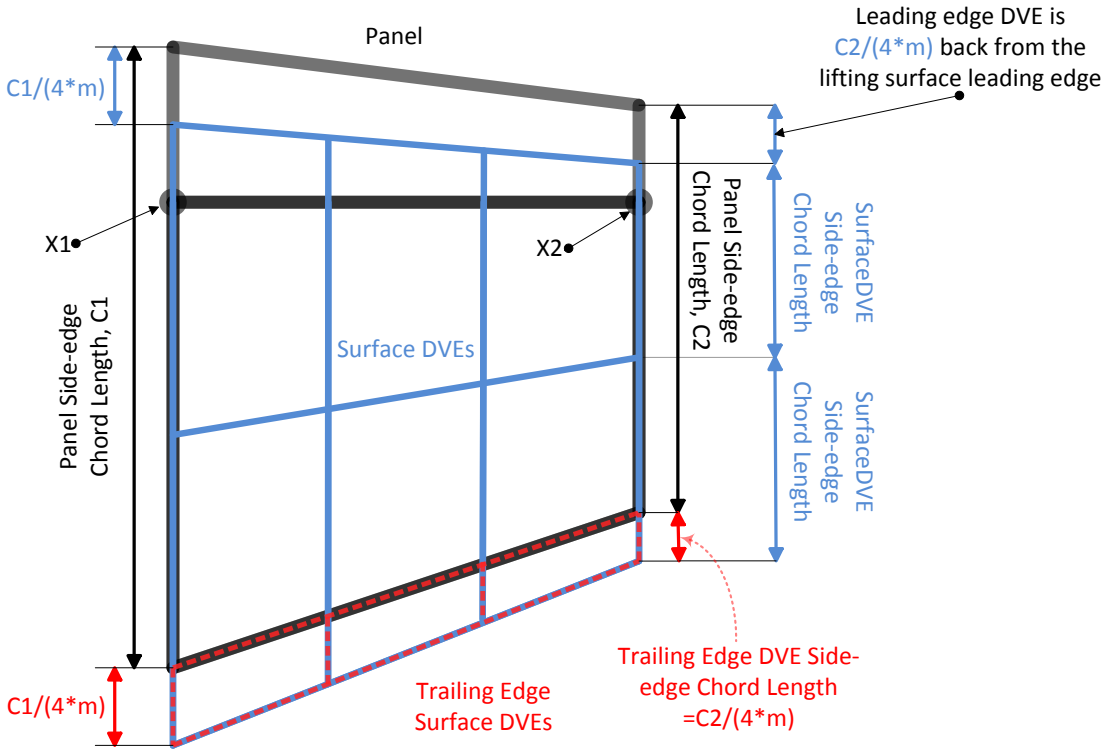

Figure 2-10 Surface paneling using DVEs with two chordwise lifting-lines. The surface panel (black lines) is represented by surface DVEs (blue lines) and trailing-edge DVEs (dashed, red lines).

For the two lifting lines shown in Figure 2-10, there are two DVEs in the chordwise direction. There are also three spanwise sub-panels, for a total of six DVEs to model the surface of this one panel. The six surface DVEs are shown in blue and the three trailing-edge DVEs are shown as red, dashed lines. The trailing edge overlap of the last row of surface DVEs has an overlap of c/(4*m), where m is the number of lifting lines and c is the chord length. This overlap allows the control point of the aft row of surface DVEs to be close to the trailing edge of the blade surface panels. The foremost leading edge DVE is c/(4m) behind the lifting surface leading edge. The length c/(4m) corresponds to the quarter chord length for each surface DVE of a given spanwise segment.

In addition to the quarter-chord side-edge points, each panel side-edge geometry is also defined by a chord length (c) and pitch angle (β). The pitch angle (in degrees) defines the chord line of the panel and subsequently also defines the pitch angle of the surface DVEs when the zero-lift angle-of-attack of the surface panel is added. Twist is performed about the local span axis, $\hat{e}_b$, which is defined in the next section [4].

The panel airfoil aerodynamic properties are defined in a file containing airfoil polar data. An example airfoil polar data file and WindDVE input file is included in the Appendix, and an example panel definition from the WindDVE input file is shown in Table 2-1. The airfoil polar data file for a specific surface panel is defined in the WindDVE input file by the number in "airfoil no. = 1", which corresponds to file: "airfoil1.dat". The WindDVE code can currently accept up to 15 airfoil definitions, although this limit can easily be increased by allocating more memory for airfoil files.

Table 2-1 Example panel geometry definition from the WindDVE input file.

```
panel #:1              number of spanwise elements: n = 4      airfoil no. = 1
Alpha_zl = -5.00
neighboring panels (0 for none)      left:0  right:2
azimuth angle of panel Y'=axis:      azi = 0.
  Xin     Y'in     Z'in     chord    pitch     Bound.Cond.
  0.000   0.200    0.000    0.40     7.00      100
  Xout    Y'out    Z'out    chord    pitch     Bound.Cond.
  0.000   0.600    -0.050   0.30     4.00      220

panel #:2              number of spanwise elements: n = 4      airfoil no. = 2
Alpha_zl = -4.00
neighboring panels (0 for none)      left:1  right:0
azimuth angle of panel Y'=axis:      azi = 0.
  Xin     Y'in     Z'in     chord    pitch     Bound.Cond.
  0.000   0.600    0.050    0.30     4.00      220
  Xout    Y'out    Z'out    chord    pitch     Bound.Cond.
  0.000   1.000    -0.100   0.20     1.00      100
```

The airfoil data file contains lines of the airfoil angle of attack (AOA or α), lift coefficient (c_l), drag coefficient (c_d) and aerodynamic moment about the airfoil quarter-chord point (c_{m25}); all of which can be given for various Reynolds numbers. The airfoil data angle-of-attack and panel twist in the WindDVE input file is relative to the airfoil chord line, whereas the panel geometry

twist within the potential flow analysis of the WindDVE code is defined relative to the zero-lift line. The angle-of-attack of the airfoil at zero-lift ("Alpha_zl") must also be included in the panel definition in the input file so that the twist of the zero-lift-line can be set within the code. The zero-lift angle-of-attack of the airfoil depends on the camber of the airfoil. It can also be a function of Reynolds number, but only changes noticeably for relatively low values of Reynolds number. The effect of the change in Reynolds number on the zero-lift angle-of-attack is typically high enough to be negligible during a single wind turbine analysis case, so it is held constant for each panel rather than being calculated within the WindDVE code. The zero-lift angle-of-attack of each panel may need to be changed as the wind speed is changed in the input file, depending on the Reynolds number range.

2.4.2 Blade Angles

The twist angle of the chordline (β_1 and β_2) at each panel side-edge and the airfoil zero lift line ($\alpha_{\emptyset L}$) at the panel mid-span is set in the WindDVE input file. The relationship between these angles is shown in Figure 2-5 and Figure 2-6. There is also a collective pitch angle for all rotor blades of the analysis case. Immediately after reading these values, WindDVE stores β_{ZLL} for each panel side-edge as a function of β, $\beta_{Collective}$ and $\alpha_{\emptyset L}$ as:

$$\beta_{ZLL} = \beta + \alpha_{\emptyset L} + \beta_{Collective} \tag{2-10}$$

where β represents the pitch angle from the input file for each panel side-edge (β_1 or β_2) and $\beta_{Collective}$ is an increment on pitch added collectively to all sections of the blade. In Figure 2-5 and Figure 2-6, $\beta_{Collective}$ is not shown; if it were included it would be an increment between the rotor plane and both β and β_{ZLL}.

The surface DVEs are created relative to β_{ZLL}. The potential flow solution is referenced to the zero lift line (ZLL), since the surface DVEs have no camber along the chord-wise sections. The surface DVEs are referenced to the zero lift line angle of attack (α_{ZLL}) and twist angle (β_{ZLL}).

The twist angle of the zero lift line of each panel side-edge (β_{ZLL_1} and β_{ZLL_2}) are used to compute the twist of the surface DVEs. If the Reynolds number range is relatively low, then one could modify this method so that $\alpha_{\emptyset L}$ accounts for changes due to Reynolds number during analysis. If blade section twist due to structural deflection is to be included in the model, it can be added as an increment to the blade section twist angle ($\Delta\beta$) and the surface DVE geometry must be recalculated during a timestep to account for such a deflection.

The forces and moments of the airfoil of a blade section are referenced to the chord line twist (β) and chord line angle-of-attack (α). Profile force calculation is achieved by performing a table lookup of airfoil profile force and moment coefficient data, which contains angle-of-attack relative to the chord line, lift coefficient, drag coefficient, and moment coefficient relative to the quarter-chord of the airfoil section. The angle-of-attack for airfoil data is adjusted using:

$$\alpha = \alpha_{ZLL} + \alpha_{\emptyset L} \tag{2-11}$$

where $\alpha_{\emptyset L}$ is typically negative for a positively cambered airfoil, as shown in Figure 2-6.

2.4.3 Surface DVE Generation

As mentioned earlier, the panel quarter-chord line is defined by an inner point ($\vec{x}_1$) and an outer point ($\vec{x}_2$). The vectors and angles used to define a surface sub-panel are illustrated in Figure 2-11. The vector $\vec{v}_q$ is the local trajectory of the quarter chord line for a panel and is defined by:

$$\vec{v}_q = (\vec{x}_2 - \vec{x}_1) \tag{2-12}$$

The unit vector $\hat{e}_q$ is defined along $\vec{v}_{qn}$, as shown in:

$$\hat{e}_q = \frac{\vec{v}_{qn}}{\|\vec{v}_{qn}\|} \tag{2-13}$$

The quarter-chord line of all sub-panels of a panel will fall along unit vector $\hat{e}_q$ [4]. The quarter-chord vector of the first sub-panel of a panel with "n" sub-panels is defined using:

$$\vec{v}_{qn} = (\vec{x}_2 - \vec{x}_1)\frac{1}{n} \quad 2\text{-}14$$

The side-edge of each panel and sub-panel are aligned with the local tangential direction unit vector, which results in the side-edge lines of adjacent sub-panels not being parallel when there is a change in sweep across a panel. The side-edges of each sub-panel DVEs are parallel to each other and to the mid-span line. The average chord length is defined along the mid-span line, as well as the xi (ξ) axis of the DVE.

Positive rotation about the x-axis and zero twist result in the chord line aligned with the tangential direction unit vector ($\hat{e}_T$), which is opposite the local rotational direction unit vector ($\hat{e}_\theta$):

$$\hat{e}_T = -\hat{e}_\theta \quad 2\text{-}15$$

The local span axis is defined relative to the zero-twist surface normal vector. The unit vector normal to a surface sub-panel with zero twist is given by:.

$$\hat{e}_{n0} = \frac{\hat{e}_T \times \hat{e}_q}{|\hat{e}_\theta \times \hat{e}_q|} \quad 2\text{-}16$$

The local span axis unit vector $\hat{e}_b$ is found by taking the cross product of the zero-twist sub-panel normal vector and the sub-panel tangential unit vector:

$$\hat{e}_b = \hat{e}_{n0} \times \hat{e}_T \quad 2\text{-}17$$

The chord-wise unit vector for a sub-panel is a function of the local tangential unit vector, the local zero-twist normal unit vector, and the section twist angle beta:

$$\hat{e}_C = (\cos\beta)\,\hat{e}_T + (\sin\beta)\,\hat{e}_{n0} \quad 2\text{-}18$$

The unit normal vector of a sub-panel is defined from the chord vector and the span axis:

$$\hat{e}_N = \hat{e}_C \times \hat{e}_b \quad 2\text{-}19$$

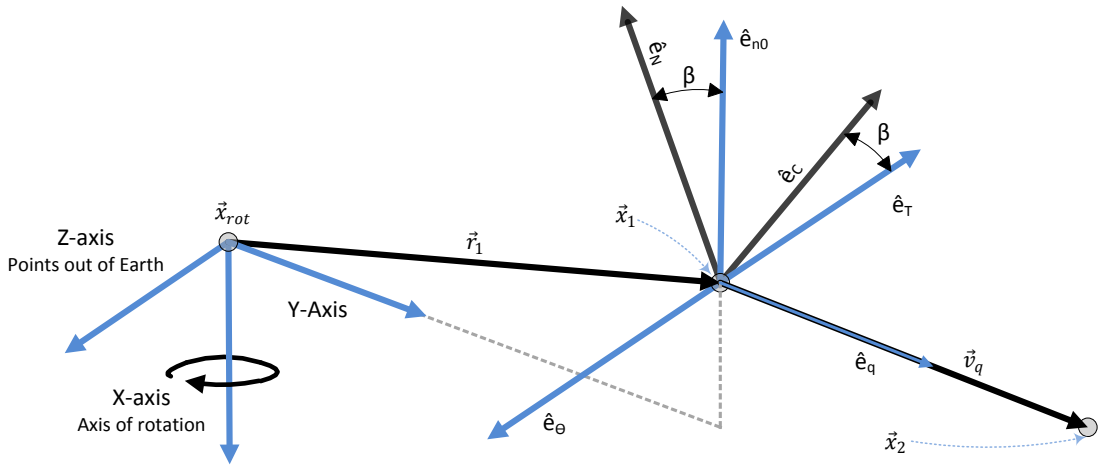

Figure 2-11 Vectors and points used to determine DVE surface geometry and orientation.

2.4.3.1 Surface Gaps

The derivation of the induced velocity of a DVE assumes that it is planar. The method described above for defining the surface geometry of the lifting surface results in gaps when there is a difference in dihedral angle between two adjacent surface panels and/or at least one of the panels is twisted, since only the DVE mid-chord is forced to attach to the neighboring element. Forcing a DVE to attach at more than one point would violate its planar nature. A break in sweep or twist between two adjacent panels can also cause a surface gap. The effect of the gaps is negligible if a sufficient number of spanwise panels are used [2,3]. The number of panels required depends on how much the geometry changes in the spanwise direction, and a sensitivity study should be performed as a first step in an analysis case. A more detailed discussion of the effect of surface gaps is given in the Appendix along with the example WindDVE input file.

2.5 Induced Velocity Computation of a DVE

The calculation of the velocity induced by the circulation and vorticity of a DVE is required for the computation of induced force, local velocity for wake relaxation, angle-of-attack, and the local flow angle. The induced velocity of a DVE is obtained by integrating across its span. The circulation distribution of the leading edge vortex filament of a DVE of index "i" is given by:

$$\boldsymbol{\Gamma_{i\_LE}(\eta_i) = A_{i\_LE} + \eta_i B_{i\_LE} + (\eta_i)^2 C_{i\_LE}} \tag{2-20}$$

The strength of the circulation distribution of the trailing edge element is of equal magnitude and distribution, but has the opposite orientation as the leading edge vortex filament. The circulation distribution of the trailing edge filament is given by:

$$\boldsymbol{\Gamma_{i\_TE}(\eta_i) = -A_{i\_TE} - \eta_i B_{i_{TE}} - (\eta_i)^2 C_{i\_TE}} \tag{2-21}$$

In order to comply with the Helmholtz vortex theorem, a vortex sheet is shed from the leading edge vortex filament of strength given by:

$$\boldsymbol{\gamma_{i\_LE}(\eta_i) = B_{i\_LE} + 2\eta_i C_{i\_LE}} \tag{2-22}$$

The vorticity shed from the trailing edge filament is also of opposite orientation, but is in the plane of the shed vorticity from the leading edge element; the vorticity of the vortex sheet shed b the trailing edge filament is given by:

$$\boldsymbol{\gamma_{i\_TE}(\eta_i) = -B_{i\_TE} - 2\eta_i C_{i\_TE}} \tag{2-23}$$

Referring to Figure 2-1, the shed vorticity of the leading edge and trailing edge filaments cancel each other out, so that the induced velocity contribution of the vortex sheets can be ignored downstream of the trailing edge.

The Biot-Savart law can be used to calculate the induced velocity at a point due to a vorticity distribution in an incompressible flow. The total induced velocity of a DVE induced on

a point is found by integrating the vortex elements of a DVE over its span. Following the convention of Basom, positive circulation is defined by the component of the vorticity in the η– direction being positive; the direction of the induced velocity follows the right-hand convention [4]. This is distinct from the definition by Horstmann [9], who uses a left-hand convention for the induced velocity of a vorticity vector that is positive in the η–direction; this distinction results in the opposite signs for the following equations (see equations 20 and 26 of Horstmann [9]). The induced velocity of a vortex filament with a parabolic circulation distribution is given by:

$$\vec{w}_{filament}(\xi_A, \eta_A, \zeta_A) = \int_{-\eta_i}^{\eta_i} \frac{\Gamma}{4\pi {r_1}^3} \begin{bmatrix} \zeta_A \\ -\zeta_A \tan \Lambda \\ -\xi_A + \eta_A \tan \Lambda \end{bmatrix} d\eta \tag{2-24}$$

where $P_A(\xi_A, \eta_A, \zeta_A)$ is the point at which the induced velocity is being calculated [1,4]. The induced velocity of the corresponding wake sheet is given by:

$$\vec{w}_{sheet}(\xi_A, \eta_A, \zeta_A) = \int_{-\eta_i}^{\eta_i} \frac{\gamma}{4\pi} \frac{1}{(\eta_A - \eta)^2 + {\zeta_A}^2} \left\{ \frac{\xi_A - \eta \tan \Lambda}{r_1} + 1 \right\} \begin{bmatrix} 0 \\ \zeta_A \\ -\eta_A + \eta \end{bmatrix} d\eta \tag{2-25}$$

where

$$r_1 = \sqrt{(\xi_A - \eta \tan \Lambda)^2 + (\eta_A - \eta)^2 + {\zeta_A}^2} \tag{2-26}$$

The analytical solution of the velocities induced by the bound vortex filament and its shed wake are presented in Ref. [2,4,9]. The induced velocity contribution of each of the four components of a DVE (the leading edge and trailing edge sheets and filaments) are summed to give the total induced velocity at point $\vec{P}_A(\xi_A, \eta_A, \zeta_A)$ due to a DVE:

$$\vec{w}_{P_A} = \vec{w}_{filament\_LE} + \vec{w}_{sheet\_LE} + \vec{w}_{filament\_TE} + \vec{w}_{sheet\_TE} \tag{2-27}$$

The induced velocity is found in the local DVE reference frame and then transformed to the global reference frame using the transformation described in section 2.2.2 of this document.

When operating in steady, uniform operating conditions, the wake modeled with DVEs is filament free [4]. If an unsteady analysis case is analyzed with rapid changes in streamwise

vorticity, then spanwise vortex filaments can be added to the vortex wake; however, most analysis cases for design work can be considered steady or quasi-steady.

2.5.1 Special Consideration Near Singularities

The solution of the DVE induced velocity, which includes the influence of the DVE vortex filaments and sheets, contains singularities that can cause numerical issues; however, these issues are much less prevalent than in conventional filament-based vortex methods. The reduced occurrence of singularity issues is because the effects of the singularities of two neighboring, planar DVEs cancel each other out, so that issues only arise when a DVE control point is in very close proximity to ultimate side-edge of a spanwise row of wake DVEs or when two adjacent DVEs meet at acute angles. The singularity at the ultimate side-edge of a row of wake DVEs has logarithmic strength. The logarithmic singularity strength is weaker than the pole-type singularity of conventional filament vortex methods, which also contributes to the reduced effect of singularities in the DVE method [4].

Despite the weaker strength of the logarithmic singularity, the side-edge singularities still require special treatment to avoid numerical issues. Wake DVEs are connected at the side-edge mid-points, which is also where the induced velocity is computed during the relaxation process. Two methods are used to avoid numerical issues associated with the singularities at the wake side-edges [2,4]. The method by Bramesfeld adds an additional singularity at the edge of the vortex sheet. This singularity is summed with the logarithmic singularity of the sheet, which results in a finite value of the side-edge self-induced velocity [2–4]. The method added by Basom [4] computes the induced velocity for the wake side-edge control points at a location slightly inboard of the side-edge, thus avoiding computation issues at the exact side-edge. Basom [4] also introduced the "DVE-splitting" algorithm, which avoids issues associated with overly acute angles between wake DVEs due to roll-up in the region of tip vorticity. The method works

by replacing the corner where two DVEs meet with a single, equivalent DVE during induced velocity calculations [1,4].

2.6 Force Computation on the Lifting Surface

The computation of forces on the lifting surface is split into three parts: the force due to the freestream velocity acting on the surface circulation, the force of the induced velocity acting on the surface circulation, and the profile force. The total force acting on a blade element is equal to the sum of these three forces. The freestream and induced forces are found by applying the Kutta-Joukowski theorem to the surface DVE vortex filaments. The freestream forces are computed relative to the surface vortex filaments, while the induced forces can either be computed on the surface vortex filaments or at the vortex filaments of the surface trailing edge DVEs. If the stall modeling option is utilized, then the lift and drag forces used to determine the rotor loads are computed based on the airfoil lift and drag coefficients. For cases when stall modeling is not utilized, the freestream and induced forces are computed as described above and profile drag is optionally added to them.

For each of the three force components, four forces are calculated using vector components: the total force, the lift force, the drag force, and the side force; each of these four force components are calculated in the global coordinate system (XYZ) and also in the axial-radial-tangential coordinate system (ART).

The most relevant velocities and forces of a blade element section are shown in Figure 2-12. As mentioned earlier, the kinematic velocity (V_{Kin}) is the equivalent of the freestream velocity for a fixed wing. For a wind turbine it is the sum of the freestream wind velocity (V_{wind}) at the evaluation point of the blade element, the onset velocity due to blade rotation (Ωr), and the body velocity (V_{Body}) due to structural or mechanical deflection of the blade element.

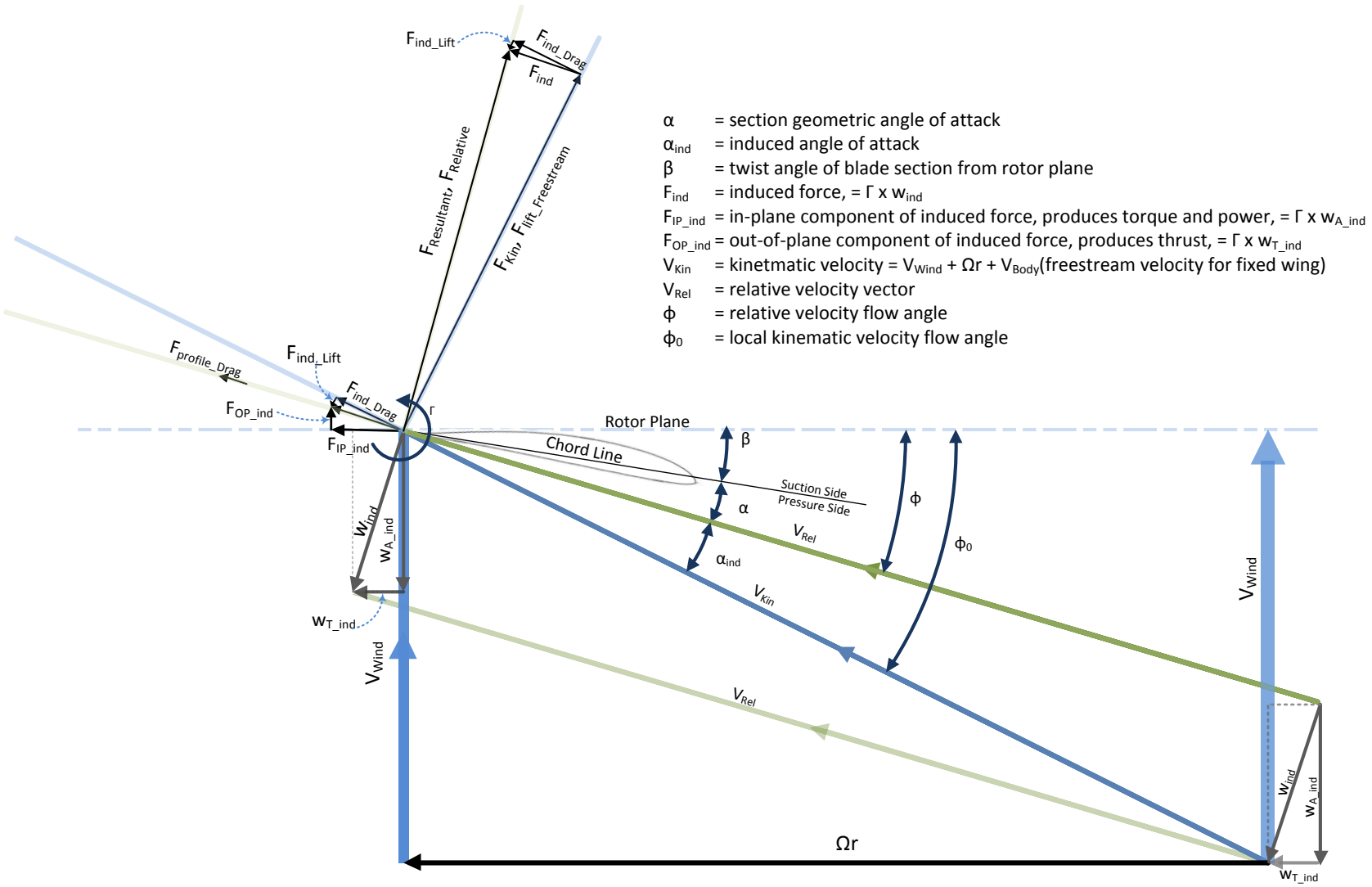

Figure 2-12 Velocities and forces of a blade element section.

A larger version of the force and velocity vectors is shown in Figure 2-13.

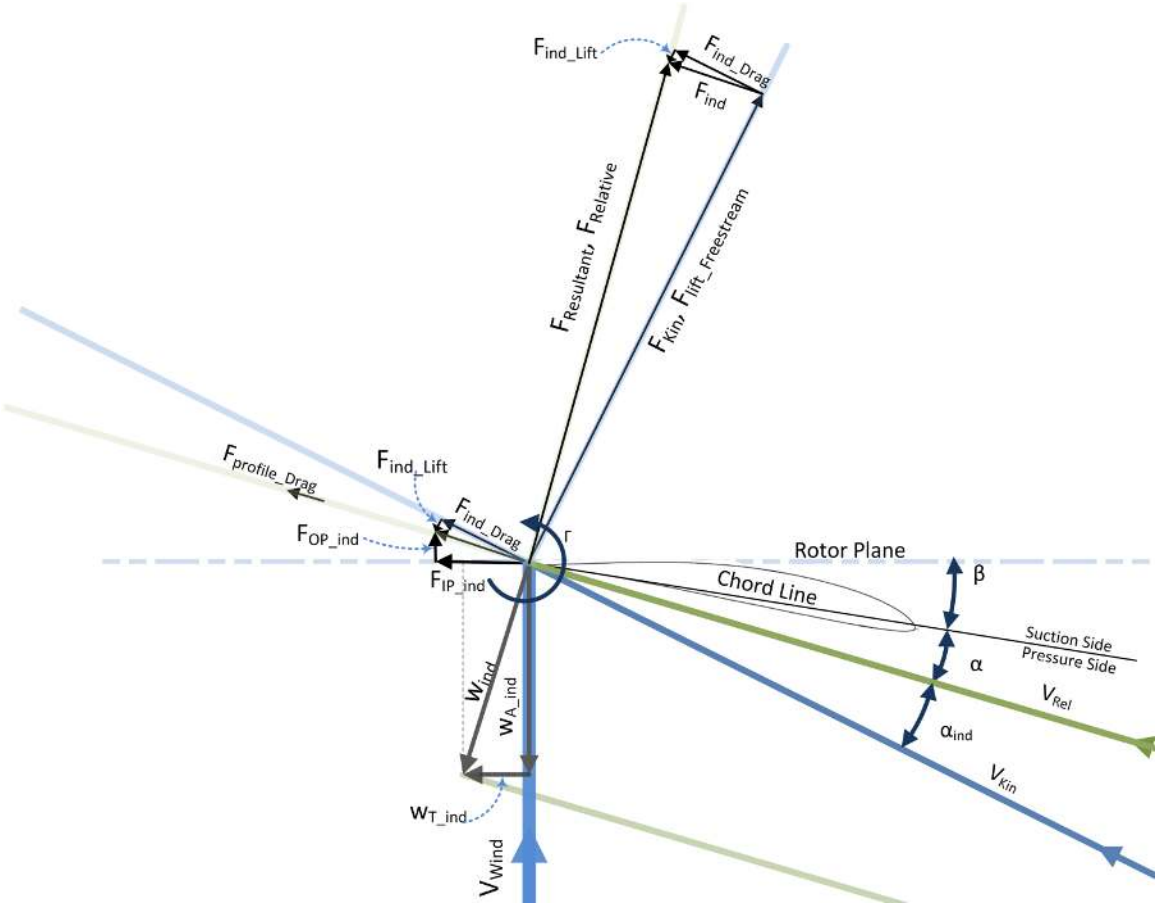

Figure 2-13 Forces and velocities on a blade section.

2.6.1 Forces and Moments Produced by a DVE Filament

The forces produced by the lifting surface are modeled by applying the Kutta-Joukowski Theorem to individual vortex filaments. The circulation (Γ) is given by the line integral around a closed loop of the velocity of the fluid tangent to the loop. The circulation can be found through:

$$\Gamma = \oint_C \vec{u} \cdot d\vec{\boldsymbol{l}} = \int_S \left(\vec{\nabla} \times \vec{u}\right) d\vec{\boldsymbol{S}} \tag{2-28}$$

which applies Stokes theorem for an area S that is enclosed by the curve C [79].

A representation of the circulation is shown in Figure 2-14. The curvature of the airfoil in the left side of the figure causes a velocity and pressure gradiant along the upper and lower surface of the airfoil lifting surface. The right side of the image shows how this system of pressure and velocity can be represented by a potential vortex.

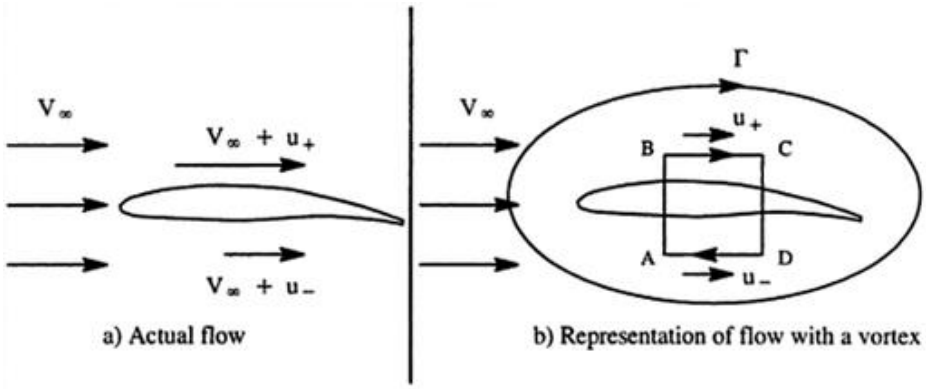

Figure 2-14 Representation of a flowfield with a potential vortex. Modified from Ref. [79].

The circulation about a lifting surface can be related to the force produced by that surface. The freestream force is calculated using the Kutta-Joukowski theorem, which relates the generation of lift on a lifting surface to the circulation of the surface in a uniform flow. For this application, the flow is assumed uniform for a blade section, but can vary between blade sections and through time. For a simple lifting surface, the lift per unit length can be expressed as:

$$L' = \rho V_\infty \Gamma \tag{2-29}$$

More generally, a vortex filament enclosed by the curve C in velocity field $\vec{v}$ produces a force $\overrightarrow{F'}$ per unit length:

$$\overrightarrow{F'} = \int_c \rho \vec{v} \times d\vec{\Gamma} \tag{2-30}$$

The force produced by a DVE vortex filament is given by [4]:

$$\vec{F} = \int_{-\eta_i}^{\eta_i} \rho \Gamma(\eta) \vec{v}(\eta) \times \vec{S} d\eta \tag{2-31}$$

The total moment of the DVE filament about the center of rotation is found by integrating the moment of the differential force vector about the center of rotation [4], as shown in:

$$\vec{Q} = \int_{-\eta_i}^{\eta_i} \rho\Gamma(\eta)\vec{r}(\eta) \times \left[\vec{v}(\eta) \times \vec{S}\right] d\eta \tag{2-32}$$

2.6.2 Lift, Drag, and Side Force

In addition to a total force vector, all forces are computed in the local lift, drag, and side force directions (LDS). The lift unit vector is defined as being the direction of the local freestream velocity crossed with the local unit vector of the lifting line that forces are being computed on. This definition of the lift unit vector is different from the work of Basom, where lift was defined as being normal to the local radial unit vector [4]. The drag unit vector is defined as being along the local freestream velocity. The side force unit vector is defined as being along the vector defined by the cross-product of the lift and drag unit vectors. This definition of the LDS forces results in the freestream force having no drag or side force components; however, the induced force will typically produce force in all three directions. The profile forces are referenced to the relative velocity, so this chapter's definition of lift, drag, and side-forces are only relevant to the freestream and induced forces.

2.6.3 Freestream Force Computation

The vortex filaments at the leading edge of each surface DVE create a system of lifting lines. The freestream force on each surface lifting line is computed by taking the cross product of the freestream velocity and the lifting line filament circulation distribution. The freestream velocity (equivalent to $\vec{V}_{Kin}$ in Figure 2-12) and the circulation distribution both change along the span of each lifting line, so the total freestream force is computed by integrating across the

filament. The analytical solution of this integral is presented in Ref. [4]. The freestream force creates no drag, so the total force is in the lift direction, which is normal to $\vec{V}_{Kin}$. This force is labeled as $F_{lift\_Freestram}$ in Figure 2-12 and Figure 2-13; it is equal to the cross-product of $\vec{V}_{Kin}$ and the surface circulation, so it is referred to as F_{kin} as well.

2.6.4 Resultant Force

The resultant force on a blade element is the sum of the freestream and induced force components. The sum of the induced and freestream velocities in the plane of the blade element section is the relative velocity ($\vec{V}_{Rel}$). The resultant force can be computed by finding the cross-product of $\rho\vec{V}_{Rel}$ and the circulation vector. The resultant force from the potential flow soltuion can also be found as a sum of the freestream lift, induced lift, and induced drag forces:

$$\vec{F}_{Res} = \vec{L}_{fs} + \vec{L}_{ind} + \vec{D}_{ind} \tag{2-33}$$

This is the preferred method since it allows the freestream force component to be computed from the analytical solution and the induced force component to be computed using Gaussian quadrature, as described in the next section.

2.6.5 Induced Force Computation

The induced force acting on the lifting surface is computed as the cross product of the induced velocity due to the entire system of surface and wake DVEs and the circulation on the DVE lifting line whose forces are being computed. The induced velocity (w_{ind}) is the sum of the induced velocity created by the vortex wake and the lifting surfaces. The induced force vectors are shown in Figure 2-15.

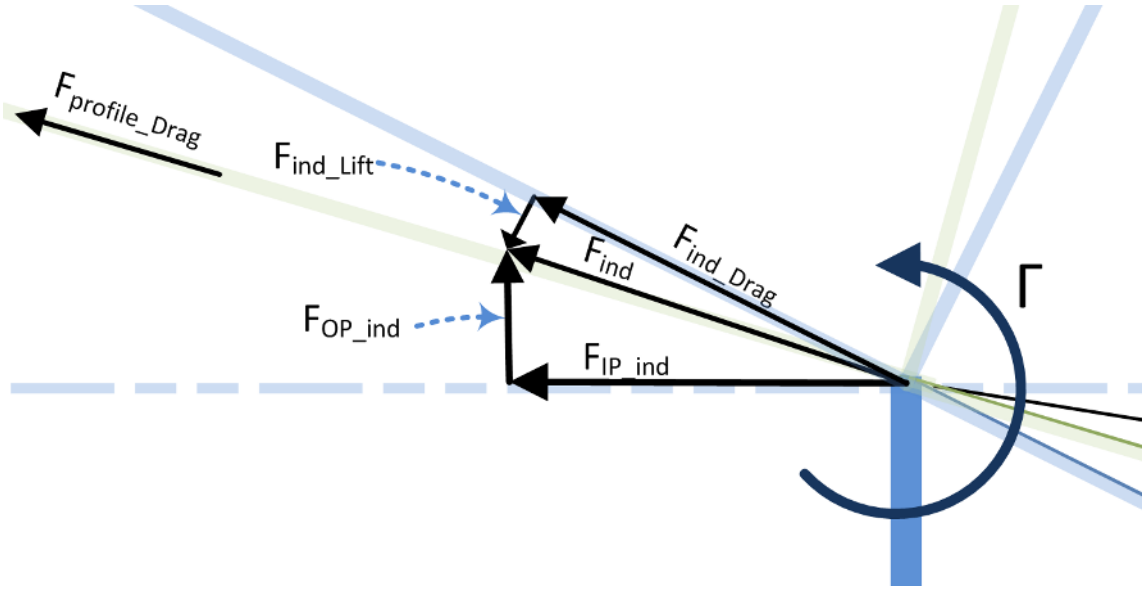

Figure 2-15 Induced force vectors and the profile drag vector for a blade section.

2.6.5.1 Induced Velocity Computation for Force Computation

The induced velocity computation is most conveniently performed in a local reference frame with the origin located at a vortex filament mid-point, rather than relative to the DVE reference frame origin point [4]. The transformation between the filament mid-point and the global coordinate system applies to either the leading edge or trailing edge lifting line of a DVE. The transformation between the local coordinate system of a DVE and the global coordinate system (described in section 2.2.2) can be applied, except that the DVE origin $\vec{x}_0$ is replaced by the mid-point of the leading edge or trailing edge filament ($\vec{x}_{mid\_LE}$ or $\vec{x}_{mid\_TE}$ respectively) [4].

The computation of induced forces requires computing induced velocities on surface filaments. The tangentially induced velocity of a vortex filament tends toward infinity as the filament is approached, as shown in Figure 1-15. The induced velocity required for force computation requires computing the induced velocity directly on the filament, where the self-induced velocity becomes zero in a Cauchy principle value sense [4]. Issues can arise due to

surface gaps between neighboring surface elements, because neighboring vortex filaments can induce an infinite velocity on each other if they meet at an angle. The infinite velocity diminishes away from the juncture. The induced force computation is performed by using quadrature points, which are significantly far enough away from the filament end point as to avoid any issues associated with the infinite induced velocities.

2.6.5.2 Location of Induced Force Computation

The induced force is computed at the trailing edge vortex filament, which is unique as many vortex methods compute the induced forces on the surface lifting lines or in the Trefftz plane [1–4]. An analysis by Basom indicated that computing the induced forces at the trailing edge more closely matched rotor power predictions from the theory by Goldstein than predictions made on the lifting lines [1,4]. A Goldstein rotor is designed using an analytical solution by Goldstein for the optimum circulation distribution of a lightly loaded rotor; it is one of the few analytical solutions available for modeling a wind turbine vortex system.

An analysis was performed to quantify the difference between induced force computations on the lifting line as compared to the trailing edge for a small-scale wind turbine with and without a winglet, as shown in Figure 2-16 and Figure 2-17. The first method computes the induced forces on the lifting lines with local de-sweeping (denoted by "LL"), the second method computes the induced forces at the trailing edge with local de-sweeping ("TE"), and the third method computes the induced forces on the trailing edge lifting line using the global de-sweeping method of Schmidt-Göller (labeled "TE_eppler") [2,4]. Results for the baseline, planar blade show very little sensitivity to the three methods for induced force computation for both the thrust (Figure 2-16) and power (Figure 2-17) predictions.

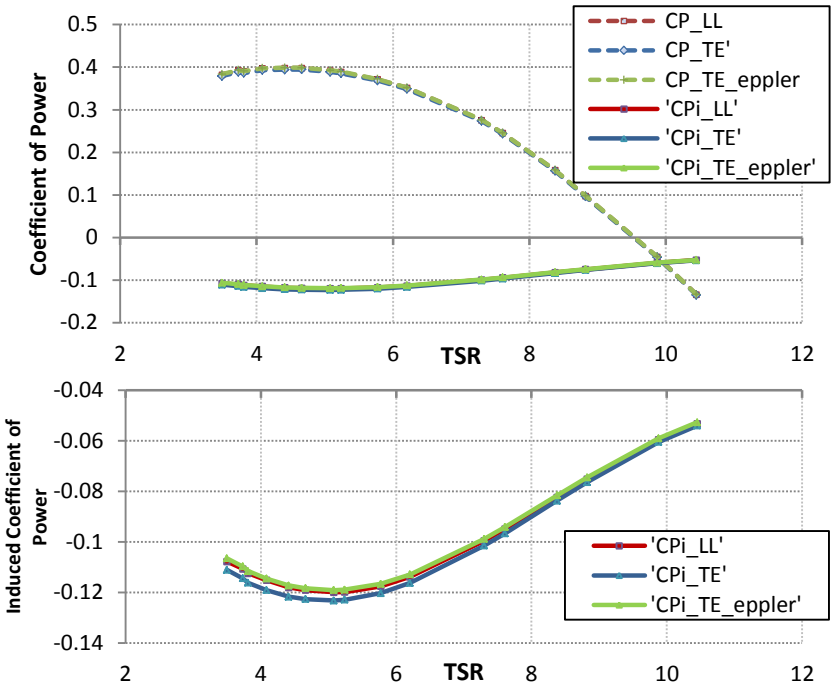

Figure 2-16 Comparison of coefficient of power computed using the three induced force computation options for the baseline, planar wind turbine described in Chapter 6 using one lifting-line.

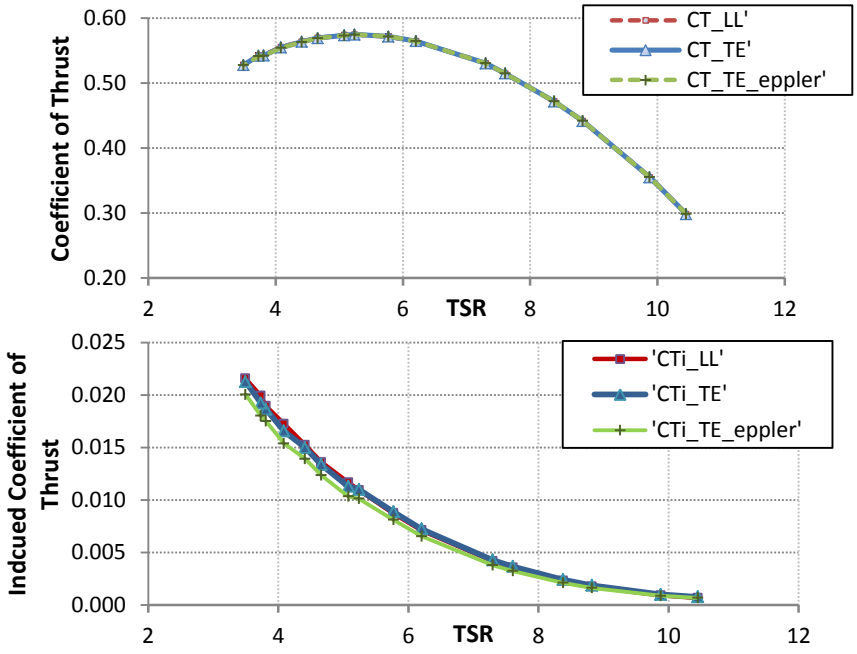

Figure 2-17 Comparison of coefficient of thrust computed using the three induced force computation options for the baseline, planar wind turbine described in Chapter 6 using one lifting-line.

Results for the blade with winglet showed an increased amount of sensitivity to the location of the induced force computation. As shown in Figure 2-18, the two trailing edge computation methods produced very similar results, but computation on the surface lifting lines predicts stronger induced power losses at higher tip-speed ratios (lower wind speed).

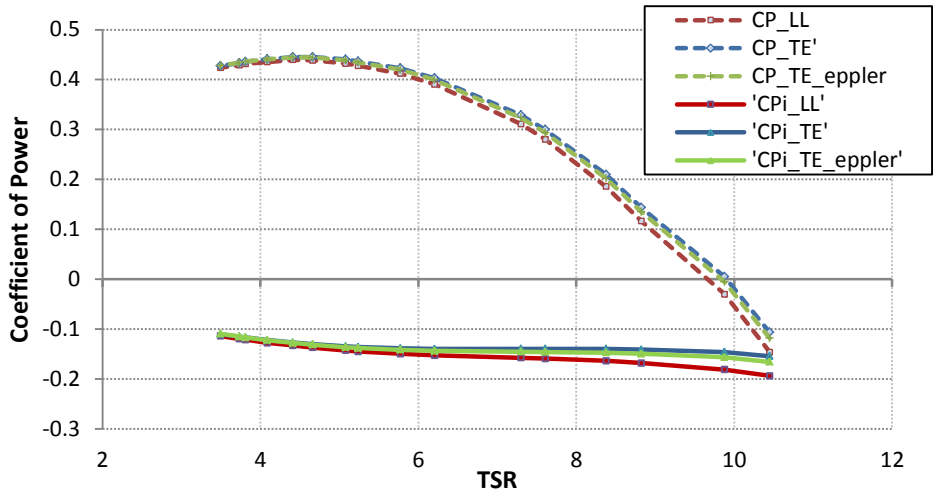

Figure 2-18 Comparison of coefficient of power computed using the three induced force computation options for the wind turbine blade with winglet described in Chapter 6 using one lifting-line.

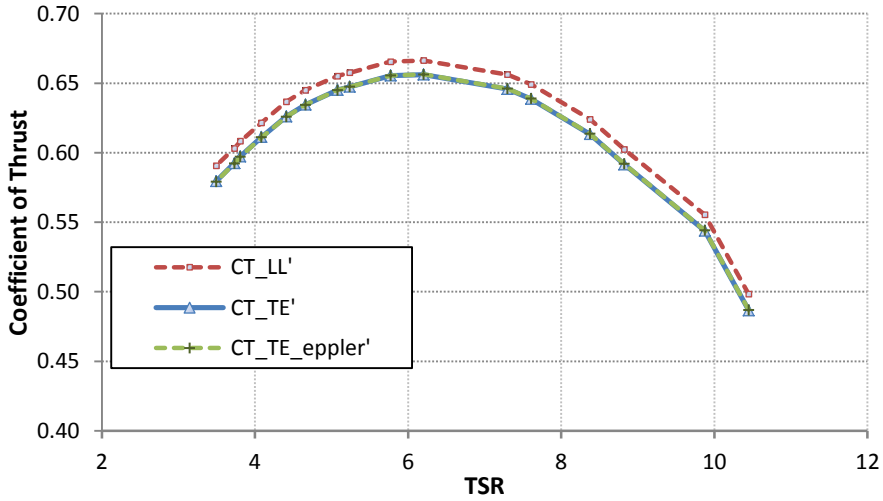

Figure 2-19 Comparison of coefficient of thrust computed using the three induced force computation options for the wind turbine blade with winglet described in Chapter 6 using one lifting-line.

The induced thrust results shown in in Figure 2-19 indicate that the lifting line calculations are 0.01 higher than the trailing edge predictions; unlike the power predictions for the winglet case, this difference is nearly constant across all tip speed ratios.

These results do not indicate which method is better, but do show that the selection of the induced force computation does make a noticeable difference for the computation of induced forces on a blade with a winglet. They also validate the "globally deswept" trailing edge induced force computation method of Basom, which produces similar results for a planar and non-planar wind turbine as the "locally deswept" predictions using the Schmidt-Göller method (labeled "_eppler" in the figures). The validation study in Chapter 5 and the winglet design case in Chapter 6 computed the induced forces at the trailing-edge using local desweeping.

2.6.5.3 Gaussian Quadrature

Unlike the freestream forces, there is not an analytic solution for the induced forces produced by a vortex filament with a parabolic circulation distribution. The induced force along a lifting surface vortex filament is computed at discrete evaluation points along the lifting surface filaments; the total force along the filament is then found by numerical integration of the force at each individual point. The numerical integration is performed using Gaussian quadrature [4].

The effect of the number of quadrature points on the total coefficient of power (CP) of a small wind turbine is displayed in Figure 2-20. These data points were taken with WindDVE for the baseline, planar small wind turbine blade having twelve spanwise panels in a cosine spacing distribution with one surface lifting line; this blade is described in detail in the final chapter of this work. Only freestream and induced forces were calculated for this figure (no profile drag or stall effects). The maximum error in CP occurred for one quadrature point, which

was located at the spanwise center of the lifting surface panels. This error was approximately 0.05% of CP relative to five quadrature points, and was 0.03% for three quadrature points. Most design cases look for changes in CP of one or two orders of magnitude larger than the maximum error for one quadrature point, but since the penalty for using more quadrature points is not significant, three quadrature points were used for the majority of the calculations presented in this paper.

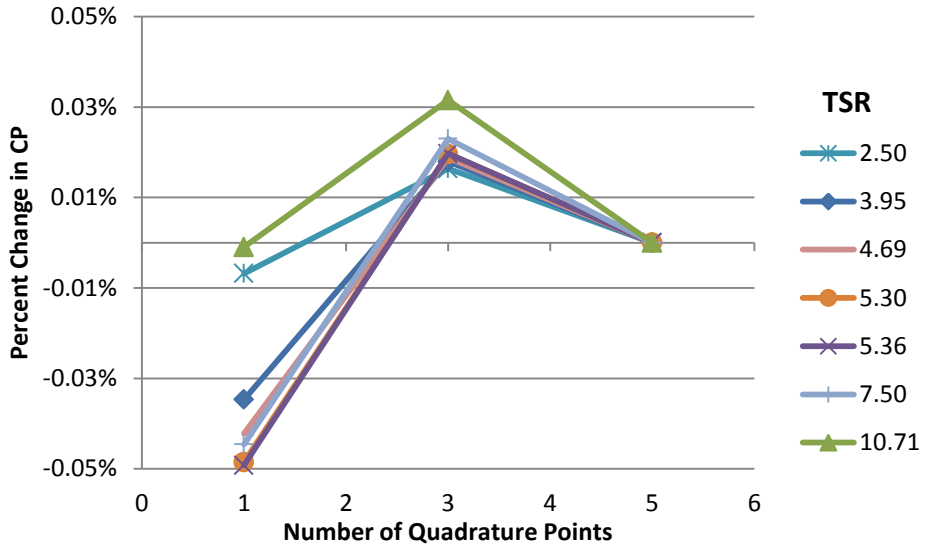

Figure 2-20 Percentage change in coefficient of power (CP) relative to 5 quadrature points for a range of tip speed ratio (TSR) for the small-scale, planar wind turbine.

2.7 Profile Force Computation

Each section of the wind turbine blade lifting surface can be thought of as an airfoil section. If the flow conditions of a blade section can be simulated in a wind tunnel, then the forces in the wind tunnel can be used to determine the forces on the wind turbine blade section, as long as the same reference conditions are matched between the rotor blade and wind tunnel. The sectional properties and flow conditions that must be matched are the angle-of-attack, Reynolds number, dynamic pressure, chord length, and Mach number. Compressibility effects are limited

for a wind turbine application, so the Mach number does not need to be matched and can assumed to be small.

2.7.1 Profile Force Coefficients

The airfoil section profile data is reported as the lift and drag coefficients, which are defined as the respective force-per-span non-dimensionalized using the local dynamic pressure and chord length, c, as shown by:

$$c_l = \frac{L'/\rho}{\frac{1}{2}\|\vec{V}_{Rel}\|^2 c} \tag{2-34}$$

$$c_d = \frac{D'/\rho}{\frac{1}{2}\|\vec{V}_{Rel}\|^2 c} \tag{2-35}$$

For some calculations, the lift and drag of a panel is calculated and the lift and drag coefficients are computed at the mid-span of the element, or as an average value for the total element force. For such cases, the coefficients are relative to the panel reference area (S_{Ref}), which is the mid-span chord length (c_{mid}) multiplied by the element span. The total element force coefficients are then given by:

$$C_l = \frac{L/\rho}{\frac{1}{2}\|\vec{V}_{Rel}\|^2 S_{Ref}} \tag{2-36}$$

$$C_d = \frac{D/\rho}{\frac{1}{2}\|\vec{V}_{Rel}\|^2 S_{Ref}} \tag{2-37}$$

Both the section lift and drag coefficient can by found from the airfoil profile data tables based on the angle-of-attack. The drag coefficient can also be looked up based on the section lift coefficient; however, this method is not common for wind turbines as search routines are typically limited to one-to-one data tables between negative and positive maximum lift

coefficients. Using the angle-of-attack for the coefficient lookup process eliminates this limitation and allows for full 360 degree data tables.

2.7.2 Reference Velocity for Profile Forces

The equivalent reference velocities used to find the airfoil profile force coefficients must be found in the vortex model. The profile force is the total force generated by an airfoil in a wind tunnel, which is theoretically equivalent to a section of a straight wing of infinite span. A straight wing of infinite span theoretically has no spanwise variation in flow conditions and the forces can be found by modeling a two-dimensional section, although two-dimensionality is arguably violated when the airfoil is fully stalled. The induced velocity due to trailing vorticity would not be included in a two-dimensional wind tunnel test since there would not be any spanwise variation in circulation. Additionally, induced velocity of the lifting surface onto itself is not included in a wind tunnel test since the wing is un-swept and planar. Because the induced velocity due to trailing vorticity and self-induced velocities is not present in a wind tunnel airfoil test, it is included in the equivalent freestream velocity of a blade section. This equivalent velocity is referred to as the relative velocity, as discussed in section 2.3. The induced velocity must be computed at a point on the lifting surface in order to compute the relative velocity. It is not immediately apparent where the induced velocity should be calculated, or even the rotational velocity, since both change along the chord length of a blade section.

A new type of surface element was created to track the geometric properties and orientation vectors of the blade spanwise stations. These elements are referred to as the blade element DVEs (BE-DVEs). A blade element DVE is defined in a similar manner as a surface DVE except that its geometry overlaps the corresponding surface panel sub-element rather than being shifted back as are the surface DVEs. The spanwise element span length is equal to the span length of the corresponding BE-DVE. The element local chord and normal unit vectors that

are used to calculate the relative velocity in Equation 2-8 and Equation 2-9 are also stored in the BE-DVE.

Once the profile drag coefficient is found from the airfoil prfile data, the magnitude of the profile drag force ($F_{profile\_Drag}$) is applied along the vector $\vec{V}_{Rel}$, which is along the profile drag unit vector ($\mathbf{e_{DP}}$). The profile lift is applied along the profile lift unit vector ($\mathbf{e_{LP}}$), which is normal to $\vec{V}_{Rel}$ and the local span axis (the span axis in this case is defined along the lifting-line unit vector).

2.7.3 Profile Lift Coefficient

There are two lift coefficients used in WindDVE. The first is the lift coefficient found from the lookup of airfoil profile data based on the angle-of-attack; this value is called the profile lift coefficient, c_{l_Prof}. The second is the lift coefficient found from the solution of the equation system, which is based on the potential flow model of the lifting surface. The second form of the lift coefficient is called the potential solution lift coefficient, c_{l_Pot}.

The potential solution lift coefficient will be derived in the 'Angle-of-Attack' section of the next chapter. This coefficient is calculated using the resultant force found on a blade element from the potential flow solution freestream and induced forces; c_{l_Pot} is then used to compute the angle-of-attack. This angle-of-attack can then be used to lookup the profile lift and drag coefficients from the airfoil profile data. The profile lift and drag are then used to compute the lifting surface forces and the rotor loads. A flow chart of the entire modified WindDVE code is shown in Figure 2-21. The profile force computation is outlined in the box labeled, "Surface Forces from airfoil data". The stall model referenced in this figure will be explained in the next chapter, as will the method for computing the angle-of-attack.

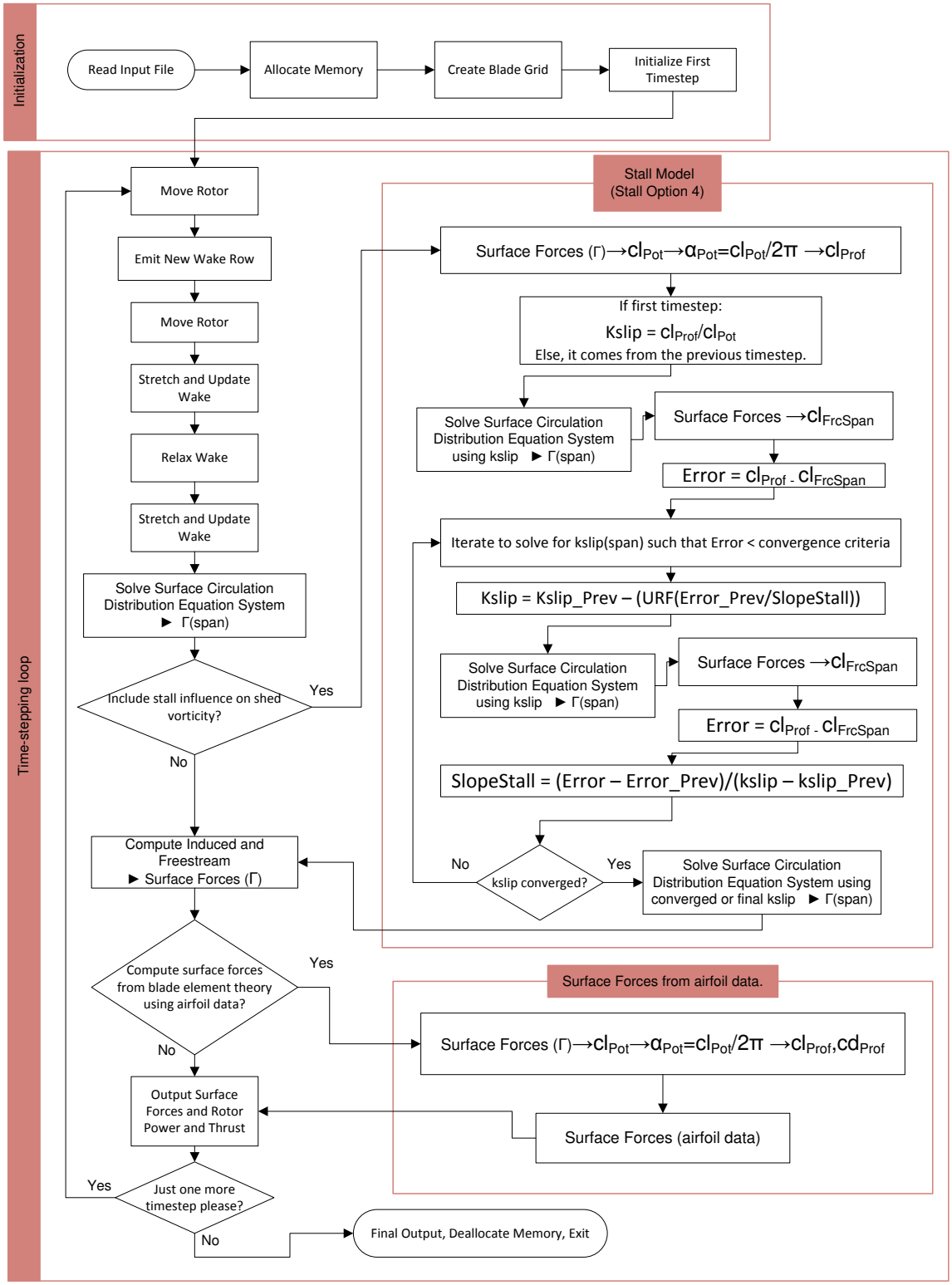

Figure 2-21 Flow chart of the WindDVE code with stall model and profile drag.

Chapter 3

Angle-of-Attack and Stall Modeling

3.1 Angle of Attack Calculation

The determination of the profile force coefficients of an airfoil is important for analysis cases when the section is stalled, or when the lift-curve of an airfoil differs from 2π. For such analysis cases, the profile force coefficients (c_l and c_d) are obtained from airfoil force data tables using the angle-of-attack. The angle-of-attack can be computed using two methods. The first method computes the angle-of-attack based on the lift coefficient solved from the equation system solution using the kinematic flow condition (c_{l_Pot}), while the second method computes the angle-of-attack directly from the flow-field velocities. The first method was found to be the preferred method for the determination of the section forces based on comparison with experimental results of the sectional normal force coefficient of the NREL UAE Phase VI wind turbine. This method of computing the angle-of-attack is similar to methods used in other free-wake codes [80]. The second method has proved to be useful for comparing the angle-of-attack with predictions from a CFD analysis as well as for comparison of the local flow angle with experimental measurements. A detailed description of the two methods is given in the next two sub-sections.

In order to validate the angle-of-attack calculation, the computed values of angle-of-attack were compared to experimental test results for the NREL UAE Phase VI wind turbine as well as to CFD analysis results for the same turbine [32,54,80,81].

3.1.1 Angle-of-Attack From Potential Flow Lift Coefficient

The first method to compute angle-of-attack is the preferred method for computing rotor blade loads. It is based on the airfoil force data, and includes the reduction in blade circulation and loads near the root and tip of the rotor blade. This method does not compute the angle-of-attack directly from the flow velocities, as it is conventionally defined, but rather computes an effective angle-of-attack based on the local spanwise force distribution.

The equation system solution obtained using the kinematic flow condition will give forces on a spanwise section that are similar to those predicted by thin airfoil theory, which predicts a lift curve slope of 2π. The lift coefficient found from thin airfoil theory is given by:

$$c_{l\_TAT} = 2\pi(\alpha - \alpha_{0L}) = 2\pi\alpha_{ZLL} \tag{3-1}$$

where α is the angle-of-attack relative to the chord line, α_{0L} is the zero-lift angle-of-attack of the airfoil, and $\alpha_{ZLL}$is the angle-of-attack relative to the zero-lift line of the airfoil.

Separation causes the lift of an airfoil to deviate from the theoretical lift curve slope of 2π as predicted by thin airfoil theory, which is why the actual airfoil profile section data (blue, solid curve in Figure 3-1) does not align with the effective lift-curve from the results for cl_{Pot} (red, dashed curve in Figure 3-1).

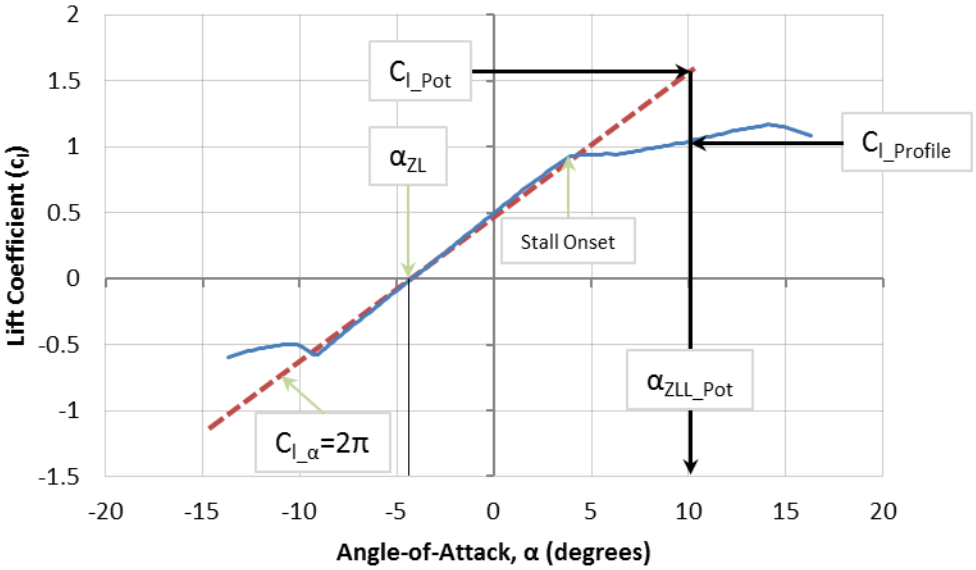

Figure 3-1 Method of computing angle-of-attack from the lift coefficient predicted with the potential flow solution. The blue line represents actual airfoil lift coefficient data and the red, dashed line represents the lift coefficient based on cl_{Pot} with a 2π lift-curve slope.

The "lift-curve" is the relationship of the lift coefficient to the angle-of-attack of the airfoil. The term "lift-curve slope" refers to the slope of the linear region of this curve, which is limited by the onset of separation at positive and negative values of angle-of-attack.

The potential resultant force (see section 2.6.4) is found using the equation system solution of the surface circulation distribution with the unmodified kinematic flow condition. The lift coefficient (c_{l_Pot}) is found from the potential resultant force:

$$c_{l\_Pot} = \frac{\frac{\|\vec{F}_{Res\_Pot}\|}{\rho}}{\frac{1}{2}\|\vec{V}_{Rel}\|^2 S_{Ref}} \tag{3-2}$$

The potential resultant force ($\vec{F}_{Res\_Pot}$) is the integrated force on a spanwise panel, and c_{l_Pot} is the average lift coefficient of the panel. The lift coefficient at a given spanwise station could be computed from the force per unit span (sectional force); however, doing so would increase the number of calls to the airfoil coefficient table lookup routine from one per panel to one per

quadrature point. For three quadrature points per panel, this would triple the number of table lookup function calls, which would increase the computational time slightly.

The effective angle of attack is referred to as α_{ZLL_Pot}, since it is obtained using the lift coefficient found from solving the potential flow solution of the surface circulation distribution along with the kinematic flow boundary condition. The angle-of-attack of the potential flow solution is always referenced to the zero-lift line and is computed by dividing cl_{Pot} by the lift-curve slope predicted by thin airfoil theory (which is 2π), as shown by:

$$\alpha_{ZLL\_Pot} = \frac{cl_{Pot}}{2\pi} \tag{3-3}$$

The angle-of-attack (α) is referenced to the chord line, and is obtained by adding the zero-lift angle-of-attack of the airfoil to α_{ZLL_Pot} as shown by:

$$\alpha_{cl\_Pot} = \alpha_{ZLL\_Pot} + \alpha_{zl} \tag{3-4}$$

The zero-lift angle-of-attack of an airfoil section (α_{zl}) is typically negative for a positively cambered airfoil. The airfoil lift and drag coefficients are then found using α_{cl_Pot}, such that:

$$(c_{l\_Profile}, c_{d\_Profile}) = \text{Table\_Lookup}(\alpha_{cl\_Pot}, \text{Reynolds Number}) \tag{3-5}$$

The angle-of-attack computed using this method is referred to as AOA_cl_Pot, as well as α_{cl_Pot}, throughout this document. The process for computing the angle-of-attack using this method is illustrated in Figure 3-1, where the cl_{Pot} lift curve has been shifted by the zero-lift angle-of-attack rather than shifting α_{ZLL_Pot}.

3.1.2 Angle-of-Attack from Local Velocities

The second method for computing the angle-of-attack makes use of the local flow velocities. In two-dimensional, wind-tunnel tests, the angle-of-attack is defined as the angle between the airfoil chord line and the freestream, which is the centerline of the wind tunnel. In the three-dimensional flowfield of a rotating lifting surface, the equivalent for the wind-tunnel

freestream flow velocity is the summation of the induced velocity due to the wake, the induced velocity due to swept and non-planar portions of the lifting surface, and the kinematic velocity (which includes both wind and rotational velocities). If all of the surface induced velocities are included and the measurement takes place away from the lifting surface, then the value becomes the local flow angle (LFA), which is the angle directly measured in experimental measurements of flow field angles.

In this method, the angle-of-attack is computed as the angle between the relative velocity vector in the plane of the section chord and normal directions ($\vec{V}_{Rel}$) and the local chord vector. The actual computation is between $\vec{V}_{Rel}$ and the local zero-lift line, with the angle-of-attack for zero lift (α_{ZL}) of the airfoil section added to the angle-of-attack of the zero-lift line, which gives the geometric angle-of-attack (relative to the chord line).

The induced velocity (and to a smaller extent the freestream velocity) varies depending on where it is calculated along the chord; the angle-of-attack will vary as well since it is directly determined from the velocities when using this method. In order to assess this effect, the angle-of-attack was computed at a number of locations on the blade surface using the small-scale wind turbine described in the last chapter. The results of this computation are shown in Figure 3-2.

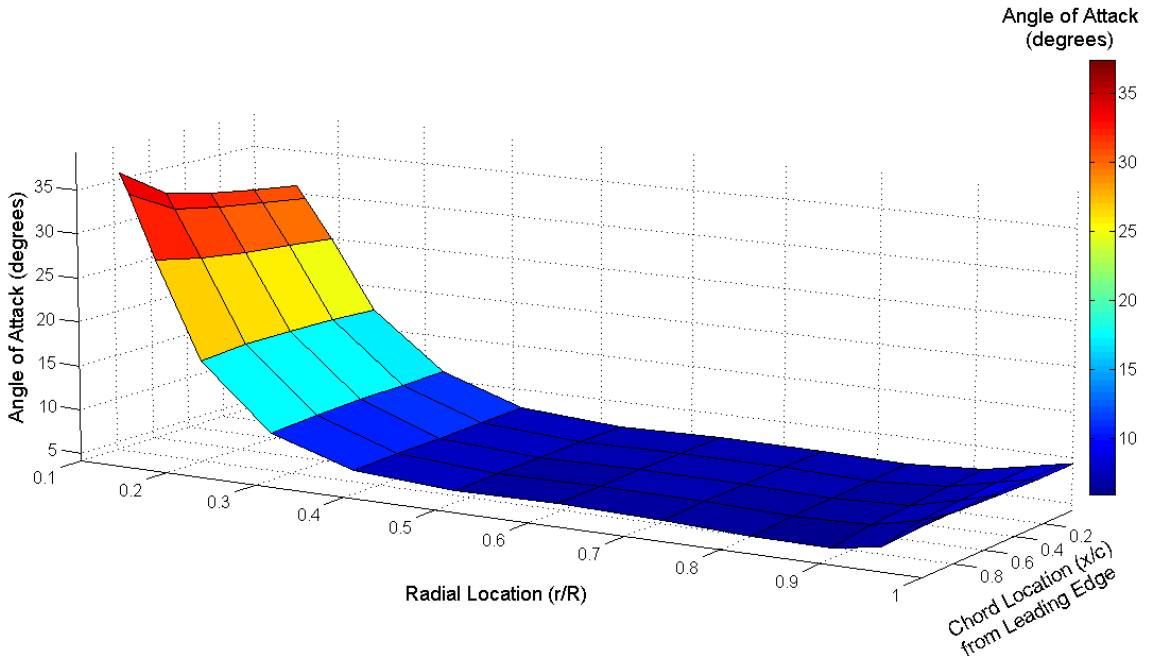

Figure 3-2 The angle-of-attack computed from the sum of the kinematic and the wake-induced velocities at a range of spanwise and chordwise locations along the blade of the baseline small-scale wind turbine described in Chapter 6; TSR 5.24, wind speed 6.4 m/s.

The angle-of-attack was computed at several locations along the chord of the blade in order to determine the dependence of the angle-of-attack on the location of velocity computation. These data points were taken for the small-scale, baseline wind turbine described in Chapter 6 at a tip-speed ratio of 5.2 and a wind speed of 6.4 m/s. The angle-of-attack at each radial location was averaged and the percentage deviation from the average is shown in Figure 3-3.

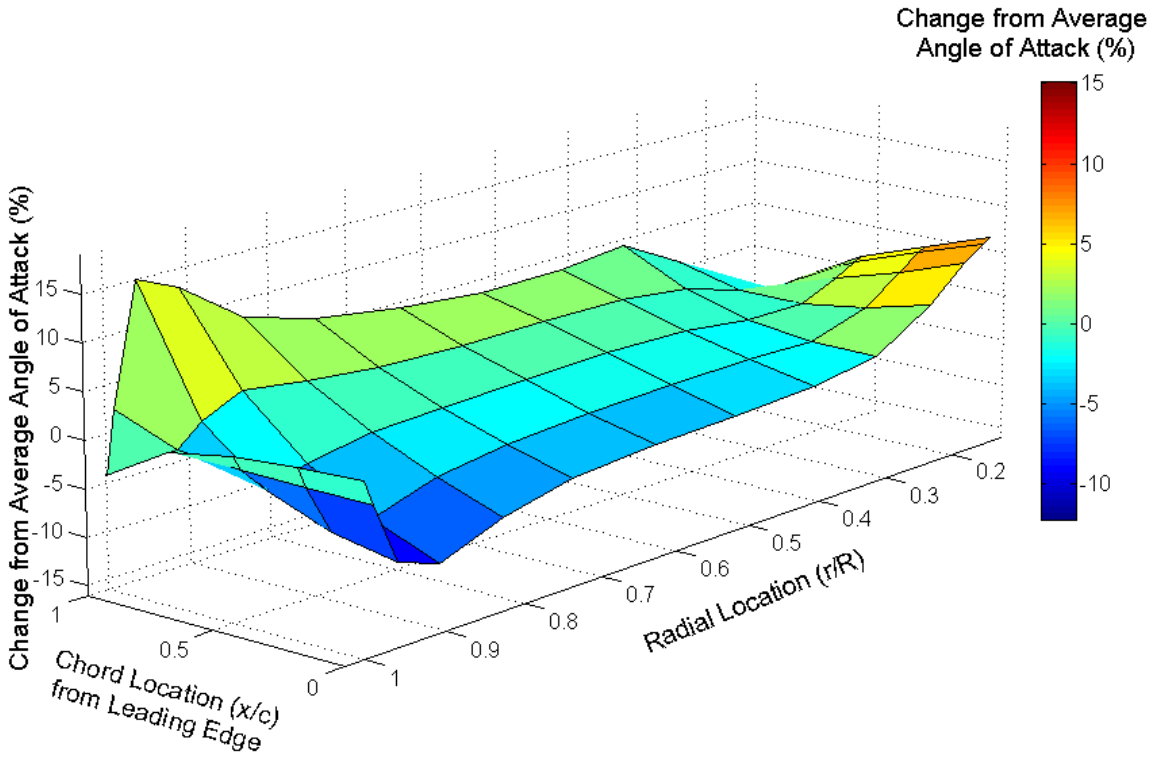

Figure 3-3 Change in percentage of angle of attack relative to the average angle-of-attack for a given spanwise (radial) location. Small-scale wind turbine, TSR 5.24, wind speed 6.4 m/s.

The spanwise center location of the blade shows a very linear rate of change in angle-of-attack along the chord. This linear rate of change means that computing the angle of attack at the blade-section mid-chord will give an exact accounting for the effective camber due to the change in angle-of-attack along the chord. The blade root and tip regions followed a more parabolic trend. A parabolic trend can be accounted for by shifting the location of where the angle-of-attack is computed. These trends can be more clearly seen in Figure 3-4. The location for the average angle-of-attack for each spanwise station was computed using the information from Figure 3-3; this location was at approximately 50% of the chord length in the center of the blade and moved closer to 75% of the blade near the blade tips. The average of this location was

appxoimately 55% of the blade chord length back from the leading edge, so this value was used for the angle-of-attack computed along the blade span.

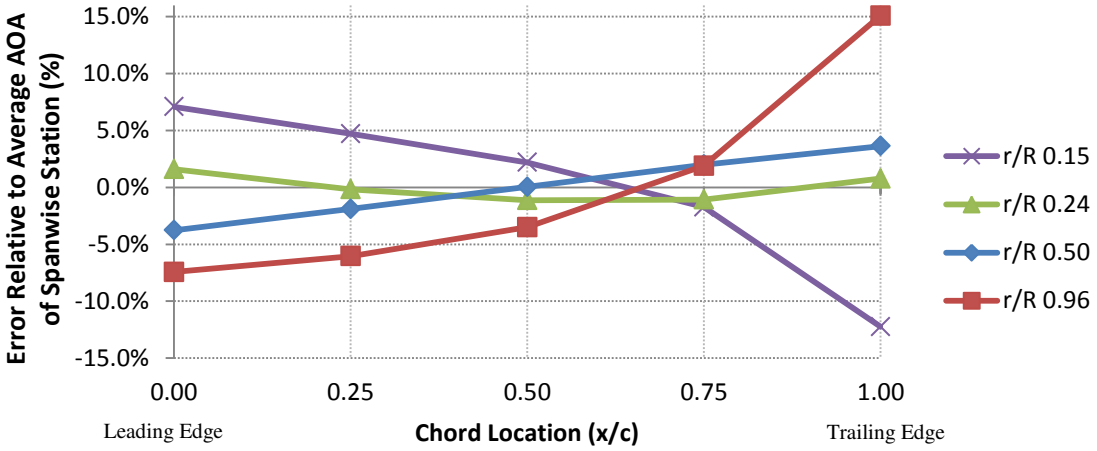

Figure 3-4 Change in percentage of angle-of-attack relative to the average angle-of-attack for a given spanwise (radial) location, results from the previous figure. Small-scale wind turbine, TSR 5.24, wind speed 6.4 m/s.

Although the computation of angle-of-attack was not used for profile force calculation, it was useful for verification and validation of the code by comparing angle-of-attack and local flow angle predictions with experimental test results and predictions from other analysis methods.

3.1.3 Angle-of-Attack Verification

The FW-DVE method was used to analyze the NREL UAE Phase VI wind turbine, which has been experimentally tested and has been analyzed in many other studies [33,53,81–84]. The angle-of-attack computation from the FW-DVE method is compared to two other methods for this turbine in Figure 3-5.

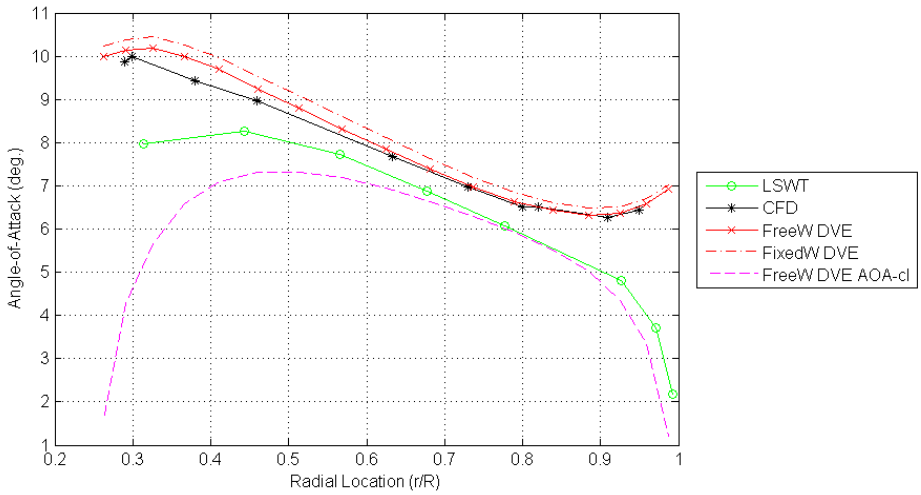

Figure 3-5 Comparison of angle-of-attack computations using the FW-DVE method with CFD[80,81] and the fixed-wake method LSWT[54]. NREL UAE Phase VI wind turbine, 7 m/s.

The "FreeW DVE AOA-cl" case in this figure shows the angle-of-attack computed with WindDVE using the method where the angle-of-attack is based on the lift coefficient from the potential flow solution. This method for computing angle-of-attack compares favorably to calculations of angle-of-attack from the prescribed wake vortex method (labeled "LSWT" for Lifting Surface Wind Turbine) of Kocurek near the blade tip. The difference between the two near the blade root is most likely caused by the region in-board of 25% of the blade radius not being modeled in the "Free W DVE" cases. The validation cases for rotor forces presented in Chapter 5 do include the blade root, but the angle-of-attack was not reinvestigated using it.

The angle-of-attack was also computed from the local flow velocities at 55% of the chord length back from the leading edge. The "FreeW DVE" case computed the angle-of-attack using a free-wake solution and the "FixedW DVE" with a fixed helical wake solution, both using the WindDVE code. Results are also shown from a RANS-CFD solution of the same rotor from Ref. [80,81]. The free-wake results from the DVE method compare very well with the CFD results near the blade tip, but there is a small difference near the blade root.

A known source of error comes from using a constant location along the blade span to compute the angle-of-attack rather than using a different value at each spanwise station. As can be seen in Figure 3-2 and Figure 3-3, near the blade root the angle-of-attack varies considerably along the chordline, producing a 3-4% error in this region of the blade when the angle-of-attack is computed at the mid-chord location. This error can partically explain the difference between the CFD results and FW-DVE predictions of angle-of-attack made using local flow velocity.

3.1.3.1 Local Flow Angle Validation

The local flow angle is the angle of the flow field measured directly in experimental conditions including the effect of the lifting surface. An illustration of the local flow angle and the angle-of-attack is shown in Figure 3-6.

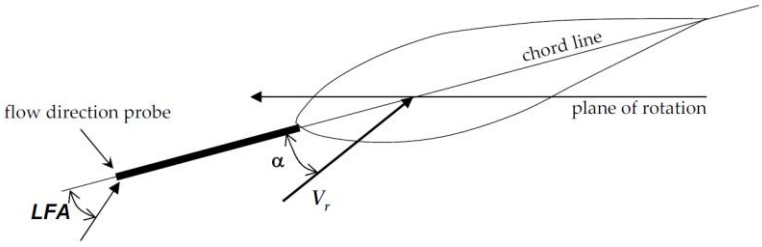

Figure 3-6 The local flow angle measured using a 5-hole pitot-static probe. Image from Sant [80].

The difference between local flow angle and angle-of-attack is that the latter is referenced to the wake induced velocity and the freestream velocity, whereas the local flow angle includes the influence of the surface bound circulation as well as the freestream and wake induced velocity. This difference is in part because the local flow angle is computed away from the airfoil surface. If the blade includes dihedral, sweep, or large amounts of twist, then the influence of the surface induced velocity due to these effects should be included in the computation of the local angle-of-attack. The reason that the angle-of-attack is used to reference airfoil profile data is that

the local flow angle is dependent on the specific airfoil being analyzed, whereas the angle-of-attack is independent of it; however, the angle-of-attack cannot be measured directly in three-dimensional wing or rotor blade systems.

The local flow angle (LFA) was also used to validate the FW-DVE method relative to experimental local flow angle measurements of the NREL UAE Phase VI wind turbine [54]; the results are shown in Figure 3-7. These results are sensitive to where the local flow angle is computed. The local flow angle was measured using a 5-hole pitot-static probe at a location 80% of the chord length in front of the leading edge and along the projection of the chord line [5]. The induced velocities were computed in the same location in the FW-DVE model.

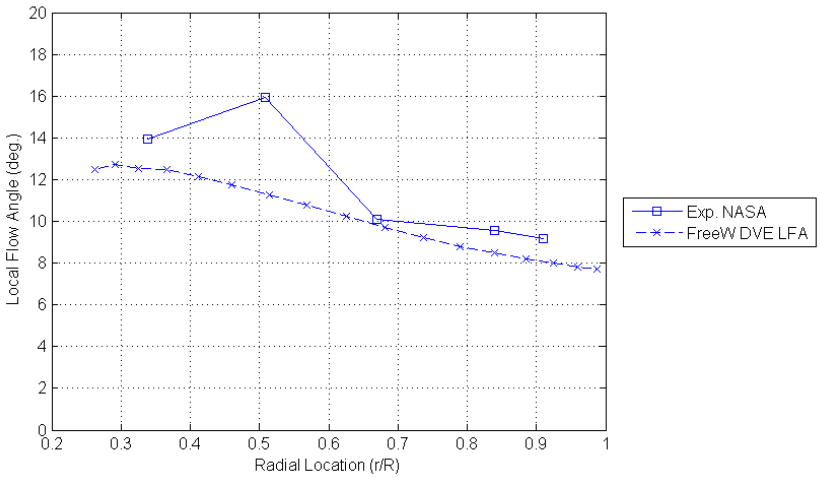

Figure 3-7 Comparison of local flow angle predictions from the FW-DVE method with experimental test results from the test of the NREL UAE Phase VI turbine at NASA Ames research center at 7 m/s. Experimental data from Ref. [54].

The comparison in Figure 3-7 provides a rough validation of the induced velocity results in the FW-DVE method. The method used to experimentally determine the local flow angle can have a considerable amount of error associated with it. The range of this error theoretically encompases the predictions from the FW-DVE method, although the exact error-bars were not

found in literature. The same error trends were seen in predictions of the local flow angle using the free-wake vortex method by Sant [80].

3.1.3.2 Effect of Angle-of-Attack Determination Method on Force Predictions

The two methods for computing the angle-of-attack were used to compute the rotor normal force coefficient (C_n), which is the component of force normal to the local chord divided by the local dynamic pressure and the local spanwise blade element reference area. In Figure 3-8 these results are compared to experimental results from the NREL UAE Phase VI wind turbine study [32], where "FW-DVE AOA_Vel" is the Cn computed from the airfoil section coefficients which were found using the angle-of-attack computed from the local flow-field velocities (the second method). This method of computing angle-of-attack overpredicts the rotor loads all along the blade, most obviously near the blade tip.

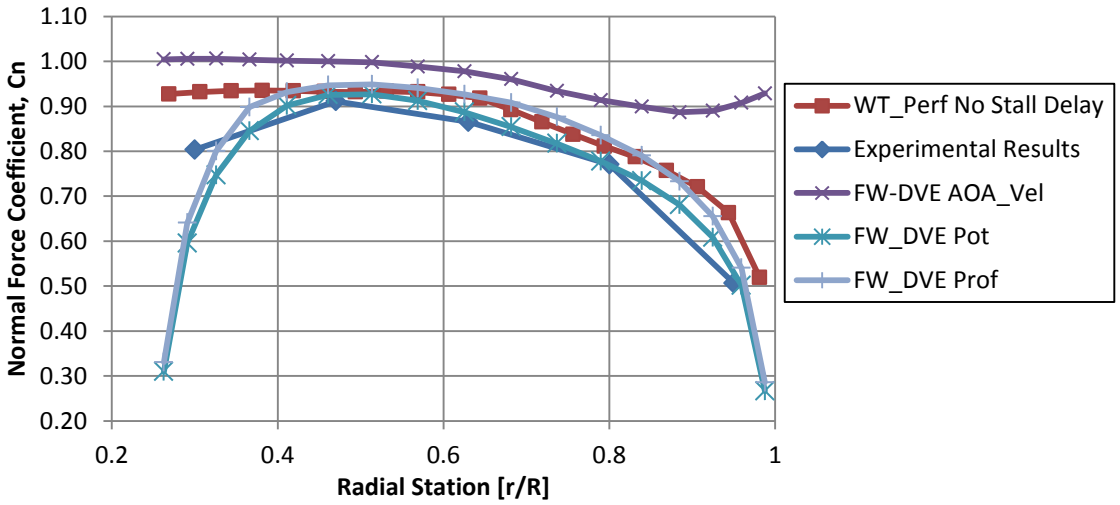

Figure 3-8 Angle of attack vs radial location for the NREL UAE Phase VI wind turbine at 7m/s wind speed. WT_Perf [19] is a blade element momentum theory based analysis code included for comparison.

The results of Cn labeled "FW_DVE Pot" were computed directly from c_{l_Pot} and from $cd_{Profile}$ found from a lookup of airfoil data based on c_{l_Pot}. This case shows the force

prediction of the free-wake method without any correction to the lift based on the actual airfoil lift-curve slope (the red, dashed curve in Figure 3-1). The results labeled "FW_DVE Prof" were created by computing Cn based on the lift coefficient and drag coefficient found from airfoil data based on the angle-of-attack computed from c_{l_Pot}, as given by Equation 3-3. The first method for angle-of-attack calculation was theorized to be the preferred method for profile force based loads calculation, as it inherently includes the reduction in blade circulation and loads near the root and tip of the rotor blade. This notion is validated by the results of Figure 3-8, showing that using the angle-of-attack from the local flow velocities to compute the rotor loads ("FW-DVE AOA_Vel") does not capture the effect of the reduction in circulation at the blade tips. These results are different from the results that would be found using lifting-line theory due to differences in where the induced forces are calculated, where along the chord the induced velocity is calculated for the effective angle-of-attack, and where the wake vorticy is shed from the lifting surface.

The "FW_DVE Prof" case should actually match the experimental results better than the ones produced in the "FW_DVE Pot" case, since the latter does not include the true lift-curve data of the airfoil. In the linear region of the airfoil lift-curve, an airfoil typically has a lift-curve slope less than the value of 2π predicted by thin airfoil theory. The airfoil data used for the above analysis actually has a lift-curve slope higher than 2π (the c_l-α data for this airfoil is plotted as the blue curve in Figure 3-1), which explains why the case using the profile data to compute the lift coefficient portion of Cn predicts higher loads than the method using the potential flow solution of the lift coefficient.

The data lableled "WT_Perf No Stall Delay" uses a similar airfoil data set, but uses the blade element momentum theory (BEMT) analysis code WT_Perf [19] for the analysis. The BEMT results from WT_Perf show similar trends as the predictions made using the FW-DVE method with cl found from the airfoil data. The over-prediciton in blade loads in the rotor tip and

root regions by WT_Perf is most likely an indication of a limit of the Prandtl tip-loss and hub-loss factors, which are used in BEMT to model the influence of the shed vorticity in the rotor wake.

The analysis results shown in Figure 3-8 could be "tuned" to match the experimental results exactly through a combination of modifing the section profile force data and the free-wake modeling parameters. Such "tuned" results are only useful for applying an anaysis method to a specific design case and have limited usefulness for validating an analysis method, especially when one considers that the experimental results always have a margin of error associated with them.

3.2 Equation System Solution of the Surface Circulation Distribution

A stall model was developed for WindDVE as part of the research presented in this dissertation and will be presented in the next section. The application of this stall model involved a significant modification to the equation system of the surface circulation distribution. This section covers a derivation of this equation system.

The lifting surface is represented by surface vorticity elements. The circulation of each surface vorticity element is solved in the lifting surface equation system by applying boundary conditions between each panel and by applying a kinematic flow condition (also referred to as the flow tangency) to a control point at each DVE. The kinematic flow condition stipulates that there must be no flow through the control point along the vector normal to the lifting surface panel.

The circulation along the blade span is represented by lifting surface elements with a continuous parabolic circulation distribution, as shown in Figure 2-2. The parabolic circulation distribution of these surface elements is represented by three circulation coefficients: A, B, C, as described in section 2.1.

The surface element side-edge circulation and vorticity boundary conditions give 2n of 3n equations required to find a solution for the circulation coefficient, where "n" is the number of surface elements. The circulation strength is equal between two elements at the side-edge. Additionally, the vorticity is equal at the side-edges of adjacent panels, which is equivalent to $d\Gamma/dy$, the slope of the circulation distribution. There are n elements and n-1 element nodes (as shown in Figure 2-8), so node number i is between elements i and i+1. The equation representing the boundary condition of matched circulation between two corresponding elements is given by:

$$A_i + B_i(\eta_i) + C_i(\eta_i)^2 - A_{i+1} - B_{i+1}(\eta_{i+1}) - C_{i+1}(\eta_{i+1})^2 = 0 \quad (3\text{-}6)$$

For element i, η_i is at the right edge of the element (typically η_i = 1), and for element i+1, η_{i+1} is at the left edge of element i+1 (typically η_{i+1} = -1). The boundary condition of matched vorticity between two corresponding elements is:

$$B_i + 2C_i(\eta_i) - B_{i+1} - 2C_{i+1}(\eta_{i+1}) = 0 \quad (3\text{-}7)$$

Each element boundary gives two equations, one representing equal circulation and one representing equal vorticity. For n surface elements, there are n-1 boundaries, giving 2*(n-1) equations. The remaining two equations come from the side-edge boundary conditions of the tip and root elements of a wind turbine blade.

For the tip and root elements (or any lifting surface edge element), the value of circulation is zero and the slope is unknown. The tip of the lifting surface is represented by the outer edge of the outermost element. For a tip element, the boundary equation for its outer edge is represented by:

$$\Gamma_{tip}(\eta) = A_{tip} + B_{tip}(\eta) + C_{tip}(\eta)^2 = 0 \quad (3\text{-}8)$$

The outer edge of the tip element is represented by $\eta = 1$ in the local coordinate system of the element.

The subscript "i" signifies the current element and "i+1" would be the next element to be computed, and "i-1" the previous element. The present method of solution works from the blade root toward the tip, so "i-1" refers to the neighboring element toward the blade root. In the local element coordinate system, the left (toward root) edge of an element is at $\eta = -1$, the right (toward tip) edge is at $\eta = +1$, and $\eta = 0$ is at the spanwise center of the element. For the root element, the inner most edge of the element represents the root (or left-side tip) of a lifting surface. The equation for the root element tip boundary condition is the same as for the outer tip element, but with the local coordinate at the element's left edge ($\eta = -1$).

3.2.1 Kinematic Flow Condition

The final *n* number of equations required to solve the surface circulation distribution equation system comes from an equation defining the magnitude of circulation. The magnitude of circulation can be defined using two methods, the kinematic flow condition method and the integrated circulation method, although only the kinematic flow condition is employed in WindDVE. The integrated circulation method may prove to be useful for other problems and so it is described in the Appendix.

The kinematic flow condition used to solve the surface circulation equation system solution requires the computation of induced velocity at the center of the DVE vortex sheet, which is the control point of the DVE. The induced velocity remains finite along the wake sheet away from its side-edges, and so the kinematic condition induced velocity computation requires no special consideration to avoid numerical issues near singularities [4]. The kinematic condition requires that the component of flow normal to the lifting surface at the surface control point be zero, such that:

$$\vec{V}_0 \cdot \vec{n}_i + \vec{w}_i \cdot \vec{n}_i = 0 \tag{3-9}$$

Where subscript "i" denotes the DVE surface element on which the kinematic condition is being applied, $\vec{n}_i$ is the local surface normal vector, $\vec{V}_0$ is the velocity vector of the kinematic velocity (incoming wind + rotational velocity), and $\vec{w}_i$ is the induced velocity vector, all of which are found at the control point of the i-th DVE. The induced velocity vector can be split into contributions from the surface elements, $\vec{w}_{i\_surface}$, and contributions from the wake elements, $\vec{w}_{i\_wake}$. The result is:

$$\vec{V}_0 \cdot \vec{n}_i + \vec{w}_{i\_surface} \cdot \vec{n}_i + \vec{w}_{i\_wake} \cdot \vec{n}_i = 0 \tag{3-10}$$

For first-order backwards time marching, the induced velocity contribution of the wake elements is taken from the previous time step. The wind velocity vector is also known, so Equation 3-10 can be re-written with the known quantities on the right hand side:

$$\vec{w}_{i\_surface} \cdot \vec{n}_i = -\vec{V}_0 \cdot \vec{n}_i - \vec{w}_{i\_wake} \cdot \vec{n}_i \tag{3-11}$$

The operation of taking the normal component of the velocity at the control point reduces the three equations for the three components of velocity into one equation for each surface DVE element. If the analysis case is assumed to be steady, then the rate of convergence of the equation system can be improved by moving the wake induced velocity to the left-hand side of Equation 3-11 [1,4]. The wake is modeled by n_{wake} DVEs; the total contribution of all the wake DVEs is given by:

$$\vec{w}_{i_{wake}}(x_0, y_0, z_0)_i = \sum_{j=1}^{n_{wake}} \vec{w}_{3j}(x_0, y_0, z_0)_i \tag{3-12}$$

The induced velocity of all of the surface DVEs is given by:

$$\vec{w}_{i_{surface}}(x_0, y_0, z_0)_i = \sum_{j=1}^{n_{surface}} \vec{w}_{3j}(x_0, y_0, z_0)_i \tag{3-13}$$

where the number of surface DVEs is represented by $n_{surface}$.

The term $\vec{\boldsymbol{w}}_{\boldsymbol{3j}}(x_0, y_0, z_0)_i$ represents the velocity that the j-th wake DVE induces on the control point of the i-th surface DVE, which is located at point $(x_0, y_0, z_0)_i$ in the global reference frame and at point $(\xi_0, \eta_0, \zeta_0)_i$ in the local DVE reference frame [2]. Included in $\vec{\boldsymbol{w}}_{\boldsymbol{3j}}$ is the combined influence of the vortex filaments and the vortex sheets of the j-th DVE; more information on solving for $\vec{\boldsymbol{w}}_{\boldsymbol{3j}}(x_0, y_0, z_0)_i$ is given in Appendix E. The induced velocity of DVE "j" can be written as a function of the coefficients that represent the quadratic distribution of circulation of the DVE (A_j, B_j, C_j) and influence coefficients, represented by the lower-case symbols in:

$$\vec{\boldsymbol{w}}_{\boldsymbol{3j}}(\xi_0, \eta_0, \zeta_0)_i = \frac{-1}{4\pi}\begin{bmatrix} A_j a_{3\xi ji} + B_j b_{3\xi ji} + C_j c_{3\xi ji} \\ A_j a_{3\eta ji} + B_j b_{3\eta ji} + C_j c_{3\eta ji} \\ A_j a_{3\zeta ji} + B_j b_{3\zeta ji} + C_j c_{3\zeta ji} \end{bmatrix} \tag{3-14}$$

For example, $a_{3\xi ji}$ represents the influence of A_j on the ξ-component of velocity at point $(\xi_0, \eta_0, \zeta_0)_i$. Equation 3-14 can alternatively be written in the form:

$$\vec{\boldsymbol{w}}_{\boldsymbol{3j}}(\xi_0, \eta_0, \zeta_0)_i = \frac{-1}{4\pi}\begin{bmatrix} a_{3\xi ji} & b_{3\xi ji} & c_{3\xi ji} \\ a_{3\eta ji} & b_{3\eta ji} & c_{3\eta ji} \\ a_{3\zeta ji} & b_{3\zeta ji} & c_{3\zeta ji} \end{bmatrix}\begin{bmatrix} A_j \\ B_j \\ C_j \end{bmatrix} \tag{3-15}$$

Using the transformation from the local DVE reference frame to the global reference frame, Equation 3-15 is transformed into:

$$\vec{\boldsymbol{w}}_{\boldsymbol{3j}}(\mathrm{x}_0, y, \mathrm{z}_0)_i = \frac{-1}{4\pi}\begin{bmatrix} a_{3\mathrm{x}ji} & b_{3\mathrm{x}ji} & c_{3\mathrm{x}ji} \\ a_{3\mathrm{y}ji} & b_{3\mathrm{y}ji} & c_{3\mathrm{y}ji} \\ a_{3\mathrm{z}ji} & b_{3\mathrm{z}ji} & c_{3\mathrm{z}ji} \end{bmatrix}\begin{bmatrix} A_j \\ B_j \\ C_j \end{bmatrix} \tag{3-16}$$

The transformation was described in section 2.2.2.

The unit vector normal to the DVE sheet at the control point of DVE "i" is represented by:

$$\vec{\boldsymbol{n}}_{\boldsymbol{i}} = \begin{bmatrix} n_{ix} \\ n_{iy} \\ n_{iz} \end{bmatrix} \tag{3-17}$$

The induced velocity component normal to the control point of DVE "i" is found by taking the normal component of Equation 3-16, resulting in:

$$\vec{\boldsymbol{w}}_{\boldsymbol{3j}}(\mathrm{x}_0, y, \mathrm{z}_0)_i \cdot \vec{\boldsymbol{n}}_{\boldsymbol{i}} = \frac{-1}{4\pi}\begin{bmatrix}\begin{bmatrix}a_{3\mathrm{x}ji}\\ a_{3\mathrm{y}ji}\\ a_{3\mathrm{z}ji}\end{bmatrix}\cdot\begin{bmatrix}n_{ix}\\ n_{iy}\\ n_{iz}\end{bmatrix} & \begin{bmatrix}b_{3\mathrm{x}ji}\\ b_{3\mathrm{y}ji}\\ b_{3\mathrm{z}ji}\end{bmatrix}\cdot\begin{bmatrix}n_{ix}\\ n_{iy}\\ n_{iz}\end{bmatrix} & \begin{bmatrix}c_{3\mathrm{x}ji}\\ c_{3\mathrm{y}ji}\\ c_{3\mathrm{z}ji}\end{bmatrix}\cdot\begin{bmatrix}n_{ix}\\ n_{iy}\\ n_{iz}\end{bmatrix}\end{bmatrix}\begin{bmatrix}A_j\\ B_j\\ C_j\end{bmatrix} \quad (3\text{-}18)$$

Each of the resulting dot products can be represented by a series of coefficients:

$$E_{a3ji} = \begin{bmatrix}a_{3\mathrm{x}ji}\\ a_{3\mathrm{y}ji}\\ a_{3\mathrm{z}ji}\end{bmatrix}\cdot\begin{bmatrix}n_{ix}\\ n_{iy}\\ n_{iz}\end{bmatrix},\ E_{b3ji} = \begin{bmatrix}b_{3\mathrm{x}ji}\\ b_{3\mathrm{y}ji}\\ b_{3\mathrm{z}ji}\end{bmatrix}\cdot\begin{bmatrix}n_{ix}\\ n_{iy}\\ n_{iz}\end{bmatrix},\ E_{c3ji} = \begin{bmatrix}c_{3\mathrm{x}ji}\\ c_{3\mathrm{y}ji}\\ c_{3\mathrm{z}ji}\end{bmatrix}\cdot\begin{bmatrix}n_{ix}\\ n_{iy}\\ n_{iz}\end{bmatrix} \quad (3\text{-}19)$$

(Equation 3-19 is equivalent to equation 43 of Horstman [9].) The coefficients of Equation 3-19 can be combined with Equation 3-11 to give the component of surface induced velocity created normal to the control point of the i-th DVE:

$$\vec{\boldsymbol{w}}_{\boldsymbol{i_{surface}}} \cdot \vec{\boldsymbol{n}}_{\boldsymbol{i}} = \sum_{j=1}^{n_{surface}} \vec{\boldsymbol{w}}_{\boldsymbol{3j}}(x_0, y_0, z_0)_i \cdot \vec{\boldsymbol{n}}_{\boldsymbol{i}} = \frac{-1}{4\pi}\sum_{j=1}^{n_{surface}} [E_{a3ji} \quad E_{b3ji} \quad E_{c3ji}]\begin{bmatrix}A_j\\ B_j\\ C_j\end{bmatrix} \quad (3\text{-}20)$$

The induced velocity of the wake DVEs is found through a similar process.

3.2.2 Matrix Form of the Surface Circulation Equation System

The 3n equations (where n is the number of surface elements) that represent the surface circulation equation system can be written and solved in matrix form, as shown by:

$$[D]\{A\} = \{R\} \quad (3\text{-}21)$$

The surface circulation coefficients (A_i, B_i, C_i) are represented by the vector $\{A\}$, which is of length 3n. The influence coefficients of the two side-edge boundary conditions and the kinematic flow condition are placed in the 3n x 3n matrix $[D]$ and the resultant vector $\{R\}$ makes up the right-hand side of the equation system and is of length 3n. An example equation system with two elements is presented in the next sequence of equations.

The tip (side-edge of the lifting surface) boundary condition is shown in matrix form as:

$$[\,1 \quad \eta_i \quad {\eta_i}^2] \cdot \begin{bmatrix} A_i \\ B_i \\ C_i \end{bmatrix} = 0 \tag{3-22}$$

and the boundary condition of matched circulation between two corresponding elements is represented by:

$$[\,1 \quad \eta_i \quad {\eta_i}^2 \quad -1 \quad -\eta_{i+1} \quad -(\eta_{i+1})^2] \cdot \begin{bmatrix} A_i \\ B_i \\ C_i \\ A_{i+1} \\ B_{i+1} \\ C_{i+1} \end{bmatrix} = [0] \tag{3-23}$$

The boundary condition of circulation magnitude is found by applying the kinematic flow condition at the control point of the i-th DVE, the influence of the surface induced velocity is represented by:

$$\vec{\boldsymbol{w}}_{\boldsymbol{i_{surface}}} \cdot \vec{\boldsymbol{n}}_{\boldsymbol{i}} = \frac{-1}{4\pi} \sum_{j=1}^{n_{surface}} [E_{a3ji} \quad E_{b3ji} \quad E_{c3ji}] \begin{bmatrix} A_j \\ B_j \\ C_j \end{bmatrix} \tag{3-24}$$

Following Equation 3-11, the sum of the surface induced velocity, the wake induced velocity, and the kinematic velocity must be zero at the surface control points. This kinematic flow condition is enforced through:

$$\frac{-1}{4\pi} \sum_{j=1}^{n_{surface}} [E_{a3ji} \quad E_{b3ji} \quad E_{c3ji}] \begin{bmatrix} A_j \\ B_j \\ C_j \end{bmatrix} = -\left(\vec{\boldsymbol{V}}_{\boldsymbol{0i}}(x_0, y_0, z_0)_i + \vec{\boldsymbol{w}}_{\boldsymbol{i_{wake}}}(x_0, y_0, z_0)_i\right) \cdot \vec{\boldsymbol{n}}_{\boldsymbol{i}} \tag{3-25}$$

The final form for the equation system solution is:

$$\sum_{j=1}^{n_{surface}} [E_{a3ji} \quad E_{b3ji} \quad E_{c3ji}] \begin{bmatrix} A_j \\ B_j \\ C_j \end{bmatrix} = 4\pi\left(\vec{\boldsymbol{V}}_{\boldsymbol{0i}}(x_0, y_0, z_0)_i + \vec{\boldsymbol{w}}_{\boldsymbol{i\_wake}}(x_0, y_0, z_0)_i\right) \cdot \vec{\boldsymbol{n}}_{\boldsymbol{i}} \tag{3-26}$$

For a two element lifting surface with one lifting-line the boundary conditions would be:

1. Side-edge, left (tip) of element 1.
2. Magnitude of Circulation (kinematic flow condition) of element 1.
3. Circulation equivalence between elements 1 and 2.
4. Vorticity equivalence between elements 1 and 2.
5. Magnitude of Circulation (kinematic flow condition) of element 2.
6. Side-edge, left (tip) of element 2.

For this case, the equation system for the two DVE element lifting surface using the kinematic flow boundary condition is represented in matrix form by:

$$\begin{bmatrix} 1 & \eta_{i1} & {\eta_{i1}}^2 & 0 & 0 & 0 \\ E_{a3j1_{i1}} & E_{b3j1_{i1}} & E_{c3j1_{i1}} & E_{c3j2_{i1}} & E_{c3j2_{i1}} & E_{c3j2_{i1}} \\ 1 & \eta_{i1} & {\eta_{i1}}^2 & -1 & -\eta_{i2} & -(\eta_{i2})^2 \\ 0 & 1 & 2\eta_{i1} & 0 & -1 & -\eta_{i2} \\ E_{c3j1_{i2}} & E_{c3j1_{i2}} & E_{c3j1_{i2}} & E_{c3j2_{i2}} & E_{c3j2_{i2}} & E_{c3j2_{i2}} \\ 0 & 0 & 0 & 1 & \eta_{i2} & {\eta_{i2}}^2 \end{bmatrix} \begin{bmatrix} A_{i1} \\ B_{i1} \\ C_{i1} \\ A_{i2} \\ B_{i2} \\ C_{i2} \end{bmatrix} = \begin{bmatrix} 0 \\ 4\pi\left(\vec{\boldsymbol{V}}_{\boldsymbol{0i}} + \vec{\boldsymbol{w}}_{\boldsymbol{i}_{\boldsymbol{wake}}}\right) \cdot \vec{\boldsymbol{n}}_{\boldsymbol{i}} \\ 0 \\ 0 \\ 4\pi\left(\vec{\boldsymbol{V}}_{\boldsymbol{0i2}} + \vec{\boldsymbol{w}}_{\boldsymbol{i2}_{\boldsymbol{wake}}}\right) \cdot \vec{\boldsymbol{n}}_{\boldsymbol{i2}} \\ 0 \end{bmatrix} \tag{3-27}$$

For an unsteady analysis case, the left-hand side of the equation system does not change after it is initialized and the equation system is solved using lower-upper decomposition. The right-hand side of the equation system (the resultant) is updated during each timestep as the wake induced velocity changes.

3.3 Stall Modeling

The condition of airfoil stall occurs when an increase in lift due to an increase in angle-of-attack is offset by the loss of lift due to separation. The equation system solution solved with the kinematic flow condition will give similar forces of a spanwise section as predicted by thin airfoil theory, which predicts a lift curve slope of 2π. Viscous effects, including separation and the influence of thickness, cause the lift of an airfoil to deviate from the theoretical lift curve slope of 2π predicted by thin airfoil theory. These effects are illustrated in Figure 3-1.

The design and analysis of a rotor for aerodynamic efficiency is typically performed for regions of operation where stall is not of significant concern, but stall may be a concern when modeling the loads of wind turbines operating at high wind speeds. A wind turbine must have some means for power regulation, since the rotor diameter is always sized to be capable of producing more power than the generator and structure can handle. A pitch regulated machine typically pitches the blade toward feather (away from stall) for power regulation. A stall regulated machine will be designed with a twist distribution such that above a certain wind speed, the root of the airfoil will begin to stall and reduce the power output of the rotor. As the wind speed increases, the stalled region of the blade increases, thus maintaining the rotor power output. A pitch-regulated machine can also pitch toward stall to limit rotor loads, although this is uncommon due to the complexity in predicting the aerodynamic response of such a machine; "pitch-regulated" commonly refers to pitch toward feather machines. Other methods of power regulation are available, but are not considered in this discussion as they are not used on any modern wind turbines in large-scale production.

For a pitch-regulated wind turbine that pitches toward feather (away from stall) for power regulation, stall is not of concern for predictions of aerodynamic performance, power regulation, and static structural loads. For a stall regulated wind turbine, including pitch toward stall machines, aerodynamic design optimization must focus on regions of operation with limited regions of separation, but aerodynamic force predictions for power regulation and structural sizing consideration will be in regions of stall. All types of wind turbines must consider stall for the analysis of dynamic load prediction, particularly for high wind speed gust conditions while yawed, which can determine the final detailed structural design of pitch regulated or stall regulated machines [11].

A stall model has been added to the FW-DVE method so that stall regulated machines can be effectively analyzed. Additionally, the incorporation of the stall model will enable the

FW-DVE method to be useful for dynamic loads prediction of cases involving wind gusts for all types of machines.

3.3.1 Stall Model Influence on the Prediction of Rotor Loads

Two possible modeling options are available with regards to stall prediction. One option includes the effect of stall on the shed wake vorticity while the other one does not. Both options predict rotor loads based on forces computed from the airfoil section lift and drag coefficients. These coefficients are determined from airfoil section coefficient data tables based on the angle-of-attack computed from cl_{Pot}, as outlined in section 2.6.4 and illustrated in Figure 2-21.

A total of six modeling options are available in WindDVE for the inclusion of airfoil section data and stall; these options are described in Table 3-1.

Table 3-1 Description of section force and stall modeling options in WindDVE.

Section Force and Stall Modeling Options	Description
SO 1	c_l from potential flow solution, c_{l_Pot}; c_d=airfoil(c_{l_Pot})
SO 2	c_l from potential flow solution, c_{l_Pot}; c_d=airfoil($\alpha_{\mathrm{cl\_Pot}}$)
SO 3	c_l and c_d = airfoil($\alpha_{\mathrm{cl\_Pot}}$); stall effect not included in wake vorticity
SO 4	c_l and c_d = airfoil($\alpha_{\mathrm{cl\_Pot}}$); stall effect included in wake vorticity
SO 5	SO 3 with c_d = 0.0
SO 6	SO 1 with c_d = 0.0

The first two options (SO1 and SO2) predict the rotor loads based on force calculations made using the equation system solution solved with the kinematic flow condition (described in section 3.2). These two methods include no effect from stall, although they do include profile drag. The option SO1 finds the drag coefficient from the airfoil data based directly on the lift

coefficient found from using the unmodified kinematic flow condition (c_{l_Pot}). The option SO2 uses α_{cl_Pot} to find the drag coefficient from the airfoil data.

The next two force computation options represent the two stall modeling options. The option SO3 computes the section forces from the lift and drag coefficients found from the airfoil data using α_{cl_Pot}, but the shed wake vorticity is based on the solution of the equation system using the unmodified kinematic flow condition, so the effect of stall is not included in the wake vorticity. The option SO4 is the same as SO3, but the effect of stall is included in the shed wake vorticity using the modified kinematic flow condition described in the next section. Stall option 4 is outlined in Figure 2-21.

The rotor forces computed using SO4 are found from the airfoil lift and drag coefficient. The lift coefficient found from the solution of the equation system and Kutta-Joukowski forces of a lifting surface section is referred to as cl_{force_span} in the WindDVE code. The difference between cl_{force_span} and cl_{Pot} is that the latter is based on the unmodified kinematic flow condition, whereas cl_{force_span} changes as the kinematic flow condition is modified during the iterative scheme of stall modeling option SO4. The iterative method of SO4 causes cl_{force_span} to approach the airfoil lift coefficient, but the values for the lift coefficient obtained from airfoil data tables are more accurate so they are used to compute the rotor forces.

The remaining two section force computation options are the same as the other options, but with the drag coefficient set to zero.

The shed wake circulation is important, as it determines the induced velocity on the lifting surface, the effect of which can drastically change rotor loads predictions. The effect of induced velocity is typically stronger for a wind turbine than for fixed wing systems, such as an aircraft. Wind turbine operating conditions without a significant influence from stall can be effectively modeled using SO2 (which does not include the effect of stall on lift). Such conditions typically apply to pitch regulated wind turbine operating conditions and to stall

regulated wind turbines operating at wind speeds well below the wind speed where the rated power of the wind turbine is reached. Wind turbines operating with limited regions of stall can be effectively modeled without the effect of stall being included on the wake vorticity (SO3), which assumes a limited influence of stall on the wake vorticity. Stall regulated wind turbines operating near the wind speed for rated power fall under this category. Modeling of wind turbines operating with large regions of stall can benefit from the inclusion of the effect of stall on the shed wake circulation (SO4); stall regulated wind turbines operating at wind speeds above the wind speed for rated power will be most accurately modeled using this option.

Pitch regulated machines experiencing dynamic stall effects caused by wind gusts may be effectively modeled using SO3. The effect of stall on wake vorticity may also be important for modeling these machines, but this depends on whether or not the circulatory term is applied in the dynamic stall model.[18,85] The application of a dynamic stall model to the FW-DVE method can be performed through modification of the stall model. Dynamic stall modeling was beyond the scope of the present research but could be a part of future work.

3.3.2 Stall Model Effect on Wake Vorticity

This section describes the method for including the effect of stall on the shed wake vorticity. The inclusion of the effect of stall on the shed wake vorticity requires modifying the lifting surface circulation distribution, since the shed vorticity is based on the change in the surface circulation at a given spanwise section. The modification of the lifting surface circulation distribution requires modifying the equation system solution, which defines the surface circulation. Without the stall model, the equation system solution is solved via the kinematic flow condition described in section 3.2.

The integrated circulation method, outlined in the Appendix, is one means for incorporating stall effects into the solution of the equation system. Several issues with the

integrated circulation method are: the convergence rate is theoretically slower than the kinematic flow condition for some cases, it is limited to one chordwise surface DVE (one lifting-line), and the influence of the total surface circulation is not included when computing the solution for each spanwise element. An alternative method would be to iteratively adjust the pitch of the surface DVEs until the desired circulation strength is met. Such a method has an advantage in that it can model multiple lifting-lines (multiple chordwise surface DVEs), but it would introduce potential numerical issues when solving for the surface forces as it would cause gaps between neighboring panels as the twist would be adjusted.

Another means for incorporating the effect of stall on the surface circulation is through the addition of a "limited slip" factor to the kinematic flow condition at the surface control points. This method has the advantage that it includes the effect of the surface induced velocity on each panel and also that it has a fairly straight-forward implementation. The main limitation is that a solution is only available for one surface lifting-line. By modifying the kinematic "no flow" condition at a control point to a "limited flow" condition, the circulation for a given spanwise station is adjusted to match a desired value. The amount of flow allowed through a control point is governed by the kinematic condition slip factor (termed "k_slip") and is applied by adjusting Equation 3- 26, which represents the kinematic flow boundary condition. The slip factor is applied to the right-hand side of Equation 3- 26, which is referred to as the *Resultant*. The slip factor was applied as a multiplier to the *Resultant*, resulting in:

$$\text{Resultant} = 4\pi * \ k_{slip} * \left(\vec{\boldsymbol{V}}_{\boldsymbol{0i}}(x_0, y_0, z_0)_i + \vec{\boldsymbol{w}}_{\boldsymbol{i\_wake}}(x_0, y_0, z_0)_i\right) \cdot \vec{\boldsymbol{n}}_{\boldsymbol{i}} \qquad (3\text{-}28)$$

The kinematic condition slip factor is initially based on the ratio of the lift coefficient found from the airfoil section data ($c_{l_{Prof}}$) and the lift coefficient from the potential flow equation system solved using the unmodified kinematic condition (c_{l_Pot}), as shown by:

$$k\_slip_{initial} = \frac{c_{l\_Prof}}{c_{l\_Pot}} \tag{3-29}$$

The slip factor for each spanwise station is then solved for iteratively using a Newton-Raphson scheme. The error (or dependent variable) in the Newton-Raphson scheme is the difference between the lift coefficient calculated from the Kutta-Joukowski forces and the lift coefficient calculated from the airfoil data. Stability of the iteration scheme required a special consideration due to the interdependence of the surface induced velocity and the circulation strength of the system of surface DVEs. The method was particularly unstable for cases with jumps in airfoil data between surface panels. Such jumps are often found for analysis cases using airfoil data corrected with a stall delay model. In order to improve the stability of the method, an under-relaxation factor of 0.2 was introduced to the Newton-Raphson scheme, and a limit of 0.2 was set for the maximum change in the slip factor for each iteration. These two additions improved stability for most cases, but added computational cost. A test case of the NREL Phase VI wind turbine at 15 m/s with stall delay corrections required 25 iterations to reach a maximum error of 0.1 in lift coefficient. The computational cost was reduced by using the value for the slip factor for each spanwise station from the previous timestep as the initial value for the current timestep. For the same test case, 10 iterations were required to reach a maximum error of 0.1 in lift coefficient and 25 iterations were required to reach an error of 0.01.

An analysis of the NREL UAE Phase VI wind turbine was performed in order to assess the influence of the different stall modeling options. Figure 3-9 shows the normal force coefficient of the NREL Phase VI turbine at 7m/s wind speed. At this wind speed there is effectively no influence of stall on the blade. The figure labels follow the same convention as in Table 3-1. The label "Prof" represents cases where forces were calculated from airfoil data, "ClPot" represents cases where forces were calculated from the Kutta-Joukousky forces with the unmodified kinematic flow condition, and "Cl_ForceSpan" represents cases where the forces

were computed from the Kutta-Joukousky forces with the kinematic flow condition modified by the stall model slip factor. The effect on the sectional normal force of the wake vorticity modified by the stall model is represented as the difference between the "SO3_Prof" and "SO4_Prof" cases.

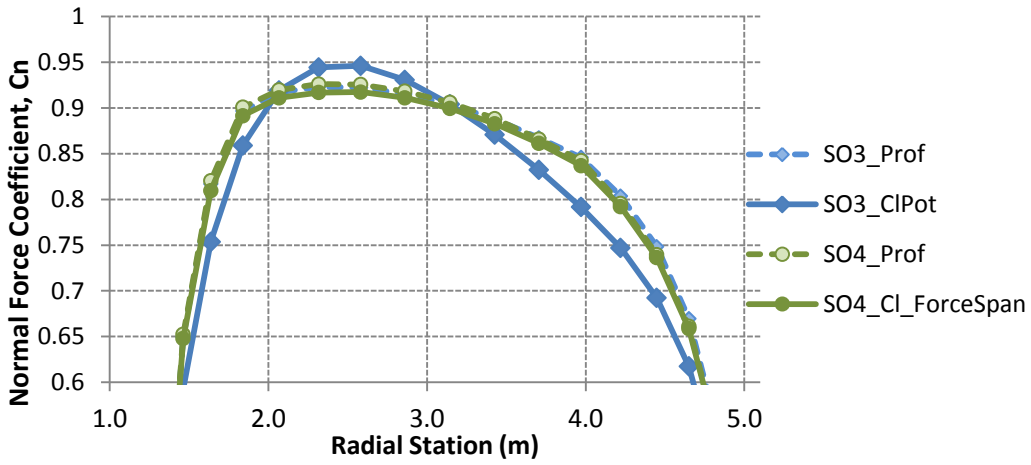

Figure 3-9 Normal force coefficient as calculated with and without the effect of stall on the surface and wake vorticity distributions. Data is for the NREL UAE Phase VI wind turbine at 7 m/s, TSR 2.53, using clean airfoil data.

The results presented in Figure 3-9 indicate that the effect of stall on the wake vorticity is negligible for the 7 m/s wind speed analysis cases, which was expected due to the lack of stall of the airfoil for this operating case. The "SO3_CLPot" case does not match the other cases because the lift curve of the airfoil for this analysis case does not match the effective lift curve found when the unmodified kinematic condition is used. A second case was analyzed at a wind speed of 15 m/s, where the blade is heavily stalled, and the results from this case are shown in Figure 3-10.

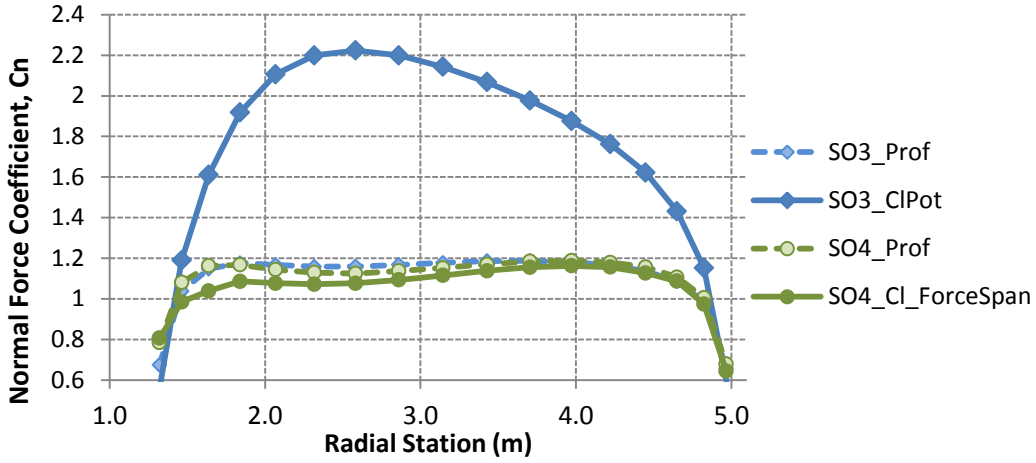

Figure 3-10 Normal force coefficient as calculated with and without the effect of stall on the surface and wake vorticity distributions. Data is for the NREL UAE Phase VI wind turbine at 15 m/s, TSR 2.53, using clean airfoil data.

The results in Figure 3-10 indicate that the inclusion of the effect of stall on the wake vorticity does have a noticeable, although minimal, effect on the rotor sectional forces. The "SO4_Cl_ForceSpan" case does not agree with the "SO4_Prof," which indicates that the iterative scheme for the kinematic condition slip factor did not entirely converge along the inner part of the blade span. This error along the inner part of the blade span is the reason why the lift and drag coefficients from the airfoil section are used to compute the rotor forces when SO4 is utilized.

There are several potential future improvements to the modified kinematic condition stall model. The first would be to investigate other iteration schemes to find ones that have improved stability and rate of convergance. A second potential improvement would be to apply the slip factor as a delta to velocity rather than a multiplier to the *Resultant* side of the kinematic condition velocity equation. This would eliminate the direct dependance of the slip factor on the wake induced velocity, which is dependant on the slip factor from the previous timestep. The method is currently limited to only one lifting line. It could potentially be improved by modifying it to work with multiple lifting lines.

The stall modeling option that does not include the effect of stall on the wake vorticity (SO3) was used to generate most of the validation results presented in Chapter 5. This is because the option SO4 did not significantly change the rotor blade forces, but it did increase the computation time and sometimes converged to non-realistic surface circulation distributions.

Chapter 4

Wake and Lifting Surface Modeling

The wake is modeled with distributed vorticity elements (DVEs), similar to the lifting surface. The main difference is that the wake DVEs can either align themselves with the local flow streamlines, or with a prescribed wake helix. This section gives an overview of the wake relaxation process and a study of the wake modeling parameters. Specific attention is given to the influence of the steady relaxation and extrapolation routines on rotor performance prediction. It also covers the influence of the surface modeling parameters on predicted rotor power. The trade space exploration tool (TSET) is presented at the end of this chapter. This tool was used for many of the analysis cases presented in this dissertation. The results from this chapter influenced the selected modeling parameters of the validation study and winglet design application presented, respectively, in the next two chapters.

4.1 Numerical Relaxation Method

During wake relaxation, the wake DVEs are moved in accordance to the local velocity impinging on them. WindDVE currently accounts for the influence of the wind speed (or freestream velocity) by moving the rotor blades upstream by a distance based on the timestep size and mean wind speed. The rotor blades are also rotated based on the rotor rotational rate. By moving the rotor upstream rather than moving the wake DVEs downstream by the wind speed, the wake DVEs only need to be relaxed by the induced velocity.

The streamwise (meaning going downstream along the wake helix) spacing of wake DVEs is determined from the timestep size of the rotor. Several time intervals can be created,

each with a different timestep size and the option of a steady or unsteady analysis [4]. A larger timestep size decreases the computation time for a given wake length or allows for a longer wake length for a given computation time. A shorter time-step size is desirable to more accurately capture the relaxed wake shape. If an unsteady analysis is undertaken then the time-step size must be made small enough to capture the dynamic wake effects of the unsteady motion. A smaller time-step size may also be required for wake stability. For a steady analysis, 10-20 timesteps are sufficient for a conventional wind turbine operating near design conditions [4]. The spanwise distribution of wake DVEs is set according to the spanwise distribution of surface DVEs.

4.2 Extrapolation

The extrapolation distance determines the length of the wake downstream of the rotor that is fully relaxed. Beyond the wake extrapolation distance, the wake shape extrapolation is based on the pitch of the last row of relaxed wake DVEs that were relaxed. Steady relaxation is turned off when a time-interval is unsteady; however, extrapolation can be used during steady or unsteady time intervals. Extrapolation helps the analysis to reach a converged solution much faster than a purely relaxed wake, reducing computation time by as much as one or two orders of magnitude. This reduction is because the computation time is a function of the number of wake timesteps to the third power [4]. It can also be useful to help the solution reach the "correct" converged value, since the chance of numerical errors increase as the number of wake elements increase and as the wake deformation increases, which corresponds to the distance downstream. Some analysis cases require reaching a steady-state, converged solution before an unsteady analysis can begin, so several steady time intervals with extrapolation can be run before the

unsteady time intervals begin. Examples of such unsteady analysis cases include a gust, a rapid change in wind direction, or a blade pitch change maneuver.

The effect of the extrapolation distance downstream of the rotor is shown in Figure 4-1. In this figure, the different cases represent various wake lengths and the x-axis indicates the extrapolation distance downstream of the rotor, where the distance is in terms of the rotor diameter. The longer wake length cases converge after about seven rotor diameters downstream, and the shorter wake length cases converge sooner. This effect is due to the interaction of the extrapolation method with the wake length. There is very little difference between the predicted power coefficients from the case with a wake of length 14.5 rotor diameters and the cases with 25.2 rotor diameters, indicating that for this tip-speed ratio, there is no reason to model a wake longer than about 14 rotor diamters. The difference between the shortest and longest wake lengths is small enough that the shortest wake length is sufficient for most analysis cases.

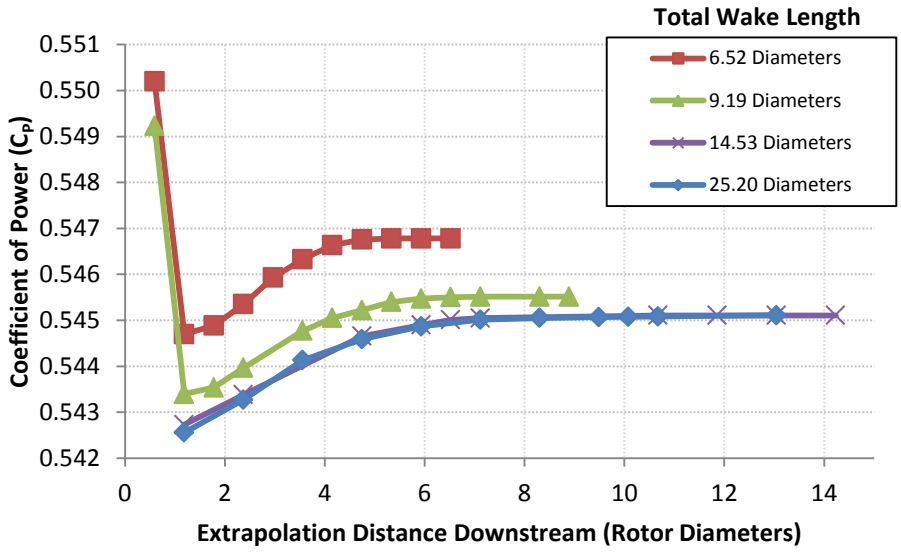

Figure 4-1 C_P vs extrapolation distance downstream for various total wake lengths. Small-scale wind turbine of Chapter 6 with winglet, TSR 5.3, 12 spanwise panels in cosine distribution.

Figure 4-2 shows the required computational time for the cases of Figure 4-1. The cases with a rotor length of 25.2 diameters take about ten times longer than the cases with a length of 9.2 diameters for the same extrapolation distance. Given the small difference in predicted coefficient of power between these two cases and the large savings in computational time for the shorter wake case, a wake model of length 6 to 9 rotor diameters is preferred for this tip-speed ratio.

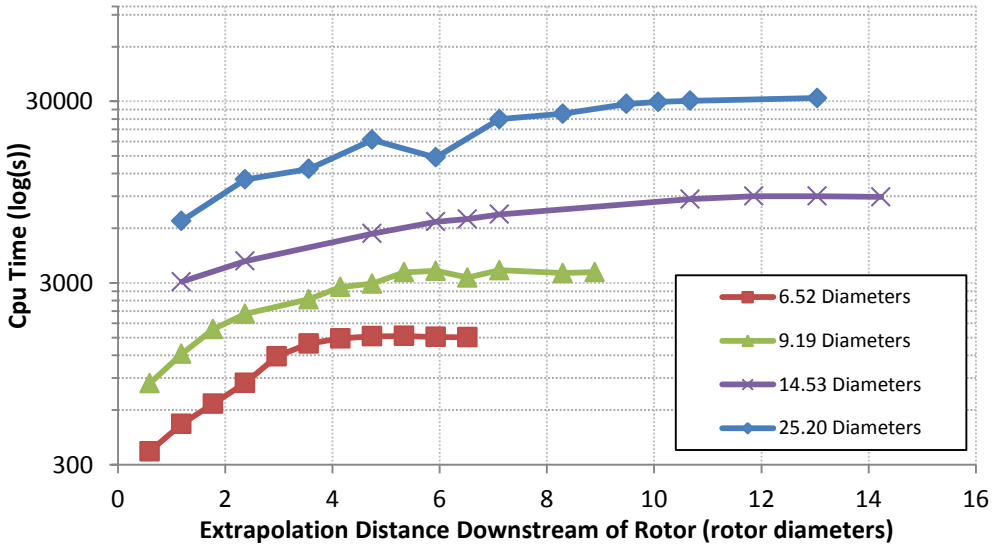

Figure 4-2 Cpu time vs Extapolation Distance Downstream for various total wake lengths. Small-scale wind turbine with winglet, TSR 5.3, 12 spanwise panels in cosine distribution.

4.2.1 Interaction of Extrapolation Distance and Tip-Speed Ratio

The influence of the extrapolation distance and total wake length on the predicted rotor power is dependent on the tip-speed ratio. In order to explore this dependence, a study was performed on the baseline planar small-scale wind turbine described in Chapter 6. The analysis cases in this study used 12 spanwise panels, a total wake length of 300 timesteps, and three time intervals: 90 timesteps at the rate of 20 steps-per-revolution, 30 timesteps as a transition interval,

and the remaining timesteps at 10 steps-per-revolution. The results shown in Figure 4-3 indicate that the extrapolation distance has little influence on the prediction of the power coefficient. After 12 revolutions, some small variations are seen, which are due to the shape of the wake changing near its end.

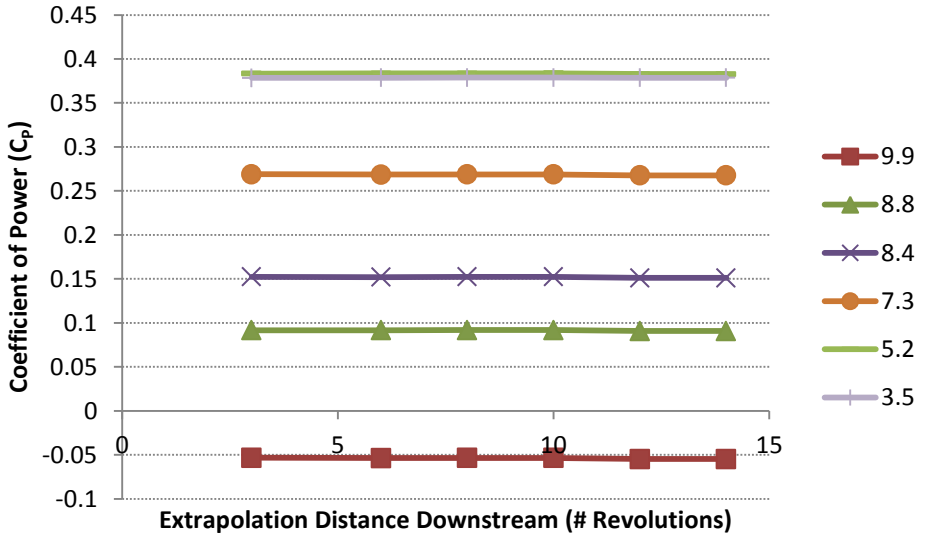

Figure 4-3 Dependence of relationship between predicted CP and the extrapolation distance downstream for various tip-speed ratios. Small-scale wind turbine, without winglet, 12 spanwise panels in cosine distribution.

The results for a blade with a winglet are shown in Figure 4-4. These results are similar to the baseline blade, except that at tip-speed ratios above about 9, the results variy considerably with extrapolation distance. The cause for the issues at high tip-speed ratio is that flow reversal near the edge of the wake causes unrealistic wake shapes because of interactions with the extrapolation routine. The presence of the unrealistic wake shapes implies that special care is needed when modeling non-planar blades at high tip-speed ratios. The tip-speed ratio that this issue arises at (9.9) corresponds to a wind speed just below the cut-in wind speed of the small-scale turbine and has no influence on the winglet design. Based on the information in these figures, the wake model for the winglet design can be extrapolated after several revolutions without a significant influence on the predicted performance.

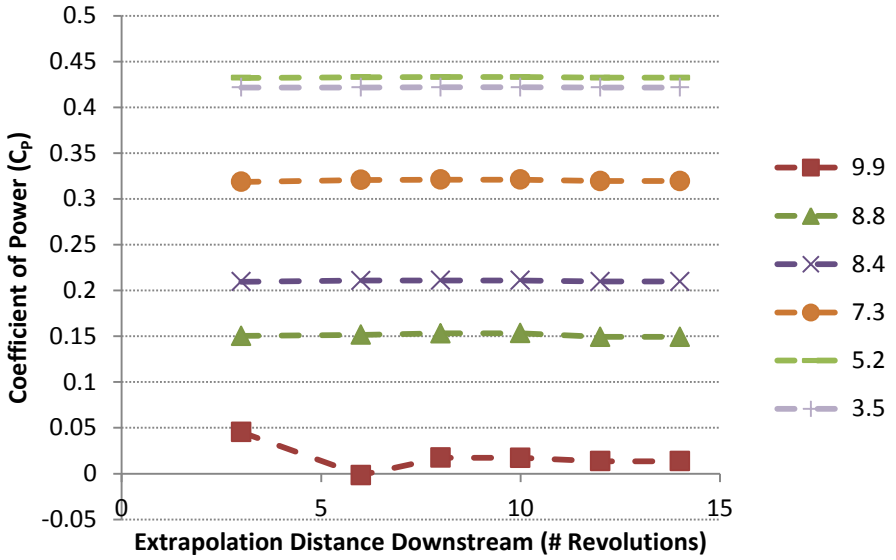

Figure 4-4 Dependence of relationship between predicted CP and the extrapolation distance downstream for various tip-speed ratios. Small-scale wind turbine, with winglet, 12 spanwise panels in cosine distribution.

4.3 Steady Analysis Versus Unsteady Analysis

The difference between the steady and unsteady analysis modes of WindDVE lie in the solution of the equation system and the wake relaxation process. The steady equation system solution method uses the most recent value of vorticity shed from the lifting surface to update the vorticity at each equivalent spanwise station throughout the wake. These wake vorticity values are what determine the influence of each wake DVE on the surface kinematic condition in the solution of the equation system. The unsteady method uses the value of vorticity for each wake panel when the panel was created. The steady method can theoretically converge faster because of its use of the most recent value of shed vorticity when solving the lifting surface equation system solution.

The circulation of each surface vorticity element is solved in the lifting surface equation system by applying boundary conditions between each panel and by applying a kinematic flow condition to a control point at each DVE. The circulation of an airfoil can also be determined through a boundary condition based on the Kutta-condition, which observes that given a proper settling time, an airfoil will produce enough circulation to create smooth flow off of its trailing edge. The application of the Kutta-condition assumes that the airfoil is not undergoing unsteady motion faster than the circulation on the airfoil can respond. The Kutta-condition is violated if the airfoil conditions are changing faster than this ratio. Unsteady aerodynamics models can be used to account for such unsteady flow conditions. The work presented in this paper is for unsteady conditions that do not require an unsteady aerodynamics model; however, the addition of such a model is a possible topic for future work.

4.4 Steady Wake Modeling

In order to further speed up certain analysis cases, a special wake relaxation process has been applied to steady wake cases and is referred to as the steady relaxation method [4]. The steady relaxation method replaces the time history of the relaxation process of a wake DVE control point with the current timestep relaxation velocities from upstream wake DVEs for the same azimuth and spanwise station. The effect of the steady relaxation method on the relaxed wake shape is illustrated in Figure 4-5. In this figure, the unsteady wake model follows the trends of the case labeled “Regular Relax” and the steady wake model follows the trends of the case labeled “Steady Relax”. The steady relaxation method can greatly speed up the convergence time of a solution, but does not apply to unsteady wake cases.

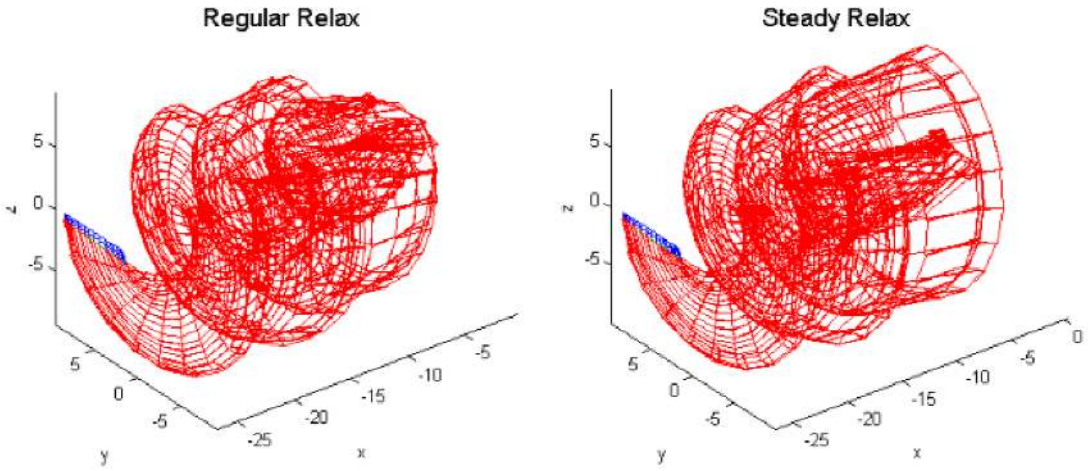

Figure 4-5 Plots of the wake shape using the regular wake relaxation method and the steady relaxation method [1].

4.5 Unsteady Wake Modeling

The results of the NREL Unsteady Aerodynamics Experiments (UAE) Phase VI Wind turbine have been used to demonstrate the unsteady modeling capabilities of the WindDVE tool and explore the effect of the wake modeling parameters on the wake relaxation process. The blade geometry of the NREL UAE Phase VI turbine used for the analysis is listed in the Appendix. A lift curve slope of 2π was used and the effect of stall and profile drag were not included in this analysis.

The results for a non-yawed case are shown in Figures 4-6 and 4-7. In these figures, the coefficient of power for the rotor is plotted against the total number of timesteps for the analysis, the total number of timesteps determining the length of the wake. Figure 4-7 focuses on a section of the same data presented in Figure 4-6. The four cases presented in each figure compare the transition from an unsteady analysis cases to a steady case (Unsteady-Steady), a purely steady solution (Steady), a case that transitions from a steady solution to an unsteady solution (Steady-Unsteady) and a purely unsteady case (Unsteady). The rotor blade conditions are the same for all

of the cases; the only difference is the equation system solution and the wake relaxation method. The steady cases use the steady relaxation process and the solution of the surface circulation distribution equation system which assumes steady-state operation.

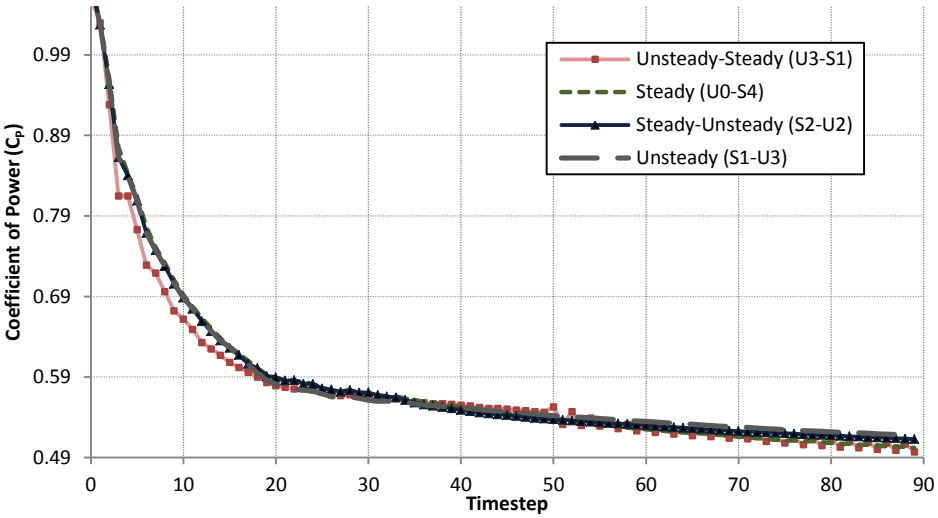

Figure 4-6 Coefficient of power vs the number of timesteps for the symmetric, non-yawed rotor, 20 timesteps per revolution. U = number of unsteady time intervals, S = number of steady time intervals. NREL UAE Phase VI wind turbine, 7 m/s wind speed.

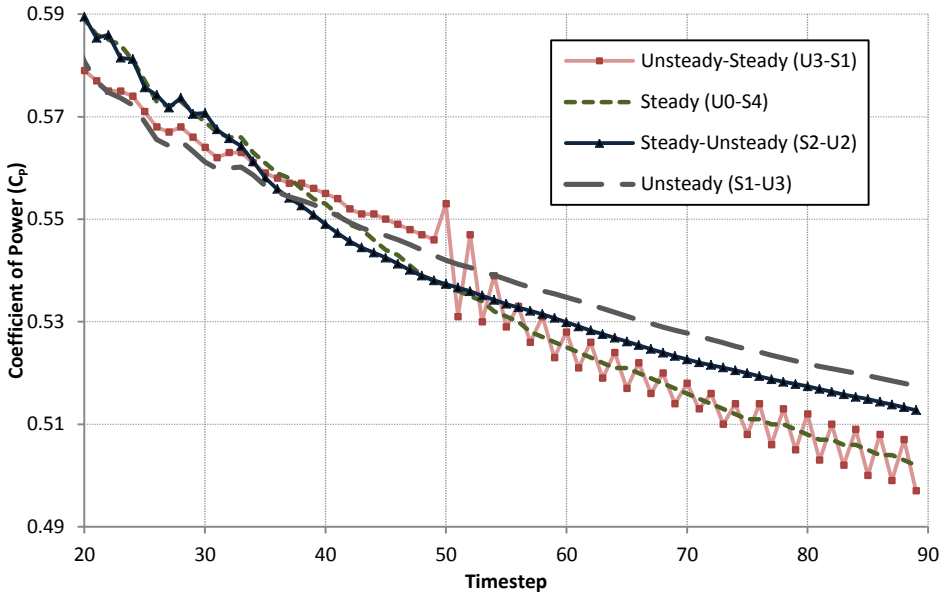

Figure 4-7 Coefficient of power vs the number of timesteps for the symmetric, non-yawed rotor, 20 timesteps per revolution. U = number of unsteady time intervals, S = number of steady time intervals. NREL UAE Phase VI wind turbine, 7 m/s wind speed.

The results of the non-yawed blade cases shown in Figures 4-6 and 4-7 indicate that, as expected, the steady case has a faster rate of convergence than the unsteady case. As explained earlier, the steady case in Figure 4-6 has a faster rate of convergence because it uses the most recent value of vorticity shed from the lifting surface to update the vorticity at each equivalent spanwise station throughout the wake. The "Unsteady-Steady" case initially follows the pure unsteady case and then transitions to eventually following the steady case, albeit with an oscillation about the pure steady case. This result is interesting as it shows that this particular case can be modeled as steady and transitioned to unsteady and the solution will approach the same average value as the purely unsteady case. It is also interesting that the "Unsteady-Steady" case displays an oscillation that neither the pure unsteady or pure steady cases exhibit. A potential source for this oscillation is that no special consideration is given when switching between the steady and unsteady analysis methods. The amplitude of the oscillation is relatively

very small and can be ignored for this case; however, it could be an issue for other cases and may warrant future attention.

The advantages of the steady relaxation method on an actual analysis case are illustrated by comparing Figures 4-8 and 4-9. Figures 4-8 shows a wind turbine rotor analyzed without the steady relaxation method; Figure 4-9 shows the same wind turbine analyzed using the steady relaxation method.

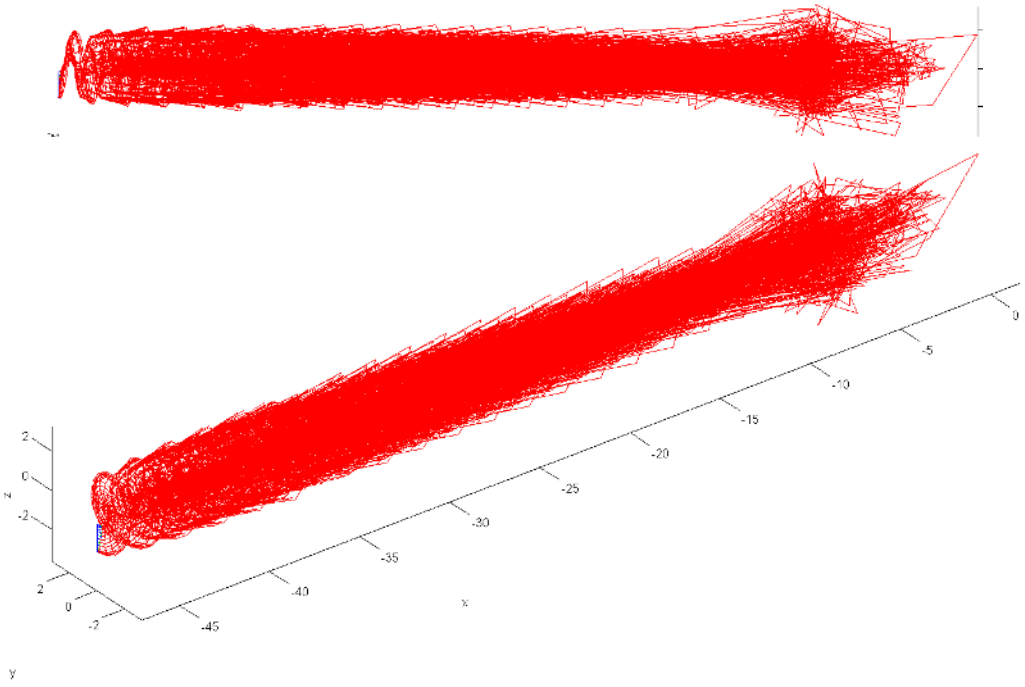

Figure 4-8 Plot of the relaxed rotor wake using the unsteady equation system solution and unsteady relaxation method.

The wake shape in Figures 4-8 contracts far downstream of the rotor because there are no downstream wake panels to create the induced velocity necessary to keep the wake from contracting. The contracting wake causes large wake deformations during the relaxation process that result in a non-realistic far downstream wake shape, indicated by the bulge of wake DVEs at

the far downstream end of the wake. The far downstream DVEs have little influence on the induced forces at the rotor, but do influence the wake shape in the far downstream region.

The wake analyzed using the steady relaxation method shown in Figure 4-9 does not have the downstream region of contraction that the unsteady relaxation method shows.

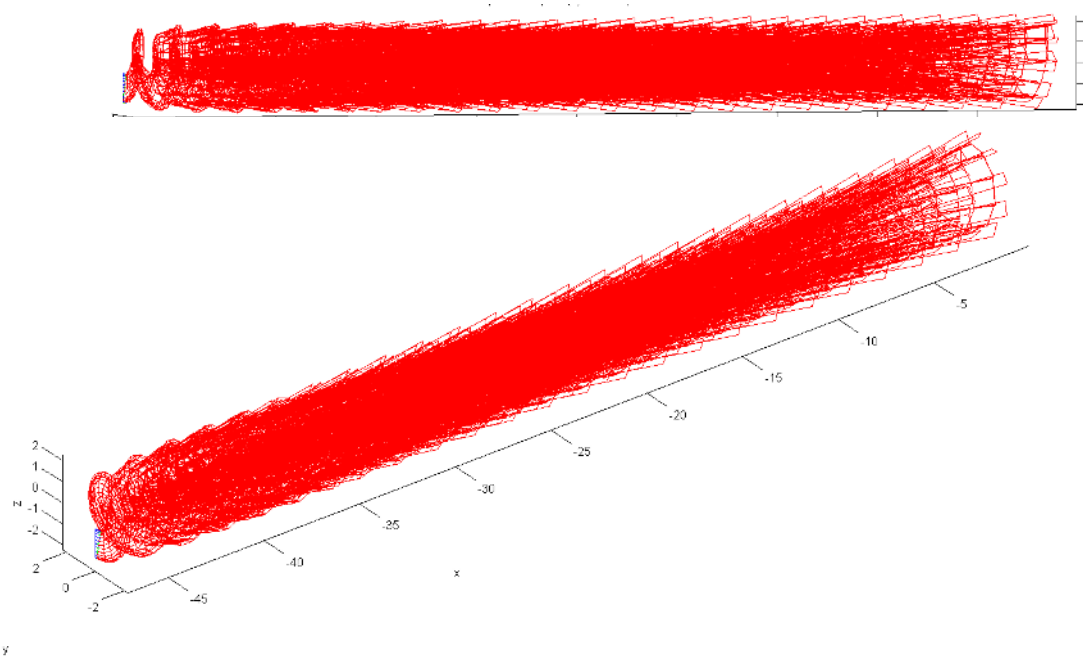

Figure 4-9 Plot of the relaxed rotor wake using the steady equation system solution and steady relaxation method.

The steady-relaxation method causes the steady wake to stay expanded throughout its length, rather than contract as the unsteady wake does at its downstream end. In a steady-state, semi-infinite wake, the induced velocity of the downstream wake supports the upstream wake and keeps it from contracting. Without the far-field, downstream wake, the local induced velocities cause the wake to contract toward its centerline. The longer the wake is modeled as fully-relaxed, the further downstream this region of contraction moves and the less effect it has on the forces computed at the rotor; however, the longer the wake the stronger the stretching and deformation

of the wake vorticity elements, increasing the chance of numerical instabilities occurring, as occurs in the unsteady wake above.

The difference in the wake shape between steady and unsteady analysis cases also influences the final force results on the rotor. The data in Figure 4-10 show the predicted coefficient of power for three analysis cases versus the location of wake shape extrapolation.

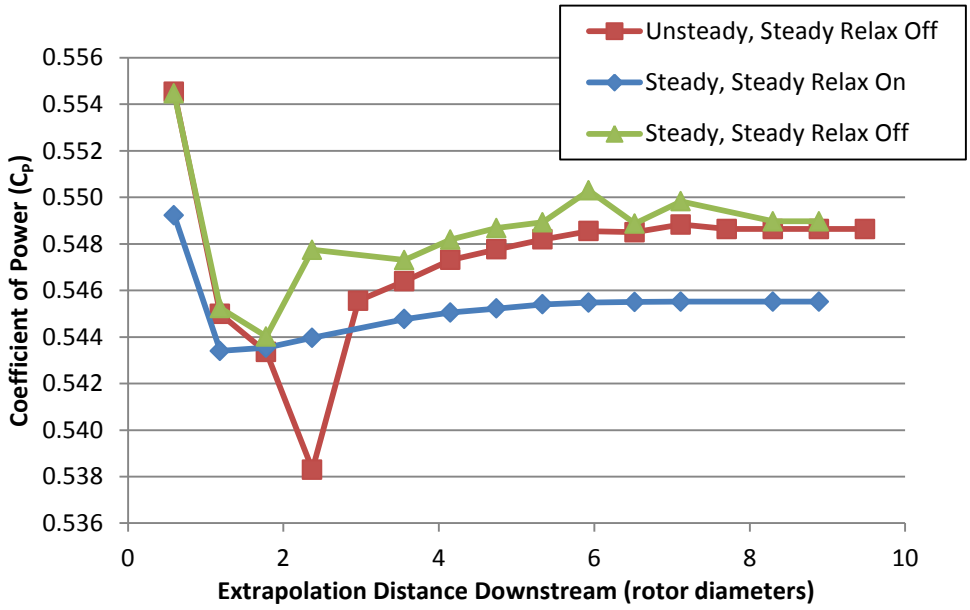

Figure 4-10 Coefficient of power vs. extrapolation distance downstream with and without the steady relaxation method. Small-scale wind turbine with winglet, TSR 5.3, 12 spanwise panels in cosine distribution, total wake length of about 15.5 revolutions, 9.2 rotor diameters.

The unsteady case uses the unsteady equation system solution, meaning that the values of vorticity of each wake DVE stays constant after each DVE is created. The steady cases use the steady equation system solution, one case with the steady relaxation method on and one case with it off. The steady relaxation method is always off for unsteady analysis cases. The steady equation system solution without the steady relaxation method does not influence the final coefficient of power value as compared to the unsteady solution. The only exception is at an extrapolation distance of 2.5 where both of the cases without the steady relaxation process show a jump in the coefficient of power. This jump is most likely caused by the extrapolation location

being near where the wake is transitioning from one time-step size to another time-step size; care must be taken to not have a wake model end near such a point. Except for the values for an extrapolation distance of 2.5, the difference between the unsteady case and the steady case without steady relaxation is less than 0.2%. The steady relaxation method makes a much larger impact than the steady equation system solution method, causing a 0.6% difference in the coefficient of power for extrapolation distances beyond about 5 diameters downstream.

The results presented in Figure 4-10 indicate that although the steady relaxation method makes a noticeable difference, it is still small enough (~0.5%) that it can be claimed that the unsteady wake solution gives approximately the same result as a steady wake solution. This verifies that the bulge in the wake DVEs in the downstream area of the wake of the unsteady case shown in Figures 4-8 does not have a significant influence on the final solution of the forces on the rotor. These results, combined with the previous figures, also show that the wake is stable without the use of the steady relaxation method. The results also indicate that the unsteady analysis case might benefit from truncating the wake DVEs beyond a certain downstream distance. The unsteady case may also benefit from starting the rotor slowly, which can prevent transient behavior during the initial wake timesteps (section 1.3.3.3 discusses this further) [68].

Now that the unsteady equation system solution and wake model have been shown to be stable and to converge to near the same result as the steady analysis case, an unsteady analysis case of a yawed rotor will be explored.

4.5.1 Yawed Rotor Modeling Results

The effect of the unsteady wake model is apparent in the results of a rotor with 30 degrees of yaw, shown in Figure 4-11. These results include a purely steady case, a purely unsteady case, and a case that is steady for several revolutions, and then switches to unsteady.

The average value of coefficient of power is approximately constant between the steady and unsteady analysis methods; however, the amplitudes are very different, with the steady case having about half the amplitude of the unsteady case. This difference is mostly due to the smoothing effect that the steady equation system solution method has on the wake vorticity distribution. The mixed case analysis had the first time interval set to steady, and then switched to unsteady. The results for the mixed case show the predicted coefficient of power initially follows the purely steady solution, and then switches to match the unsteady analysis (the switch occurs at timestep 15).

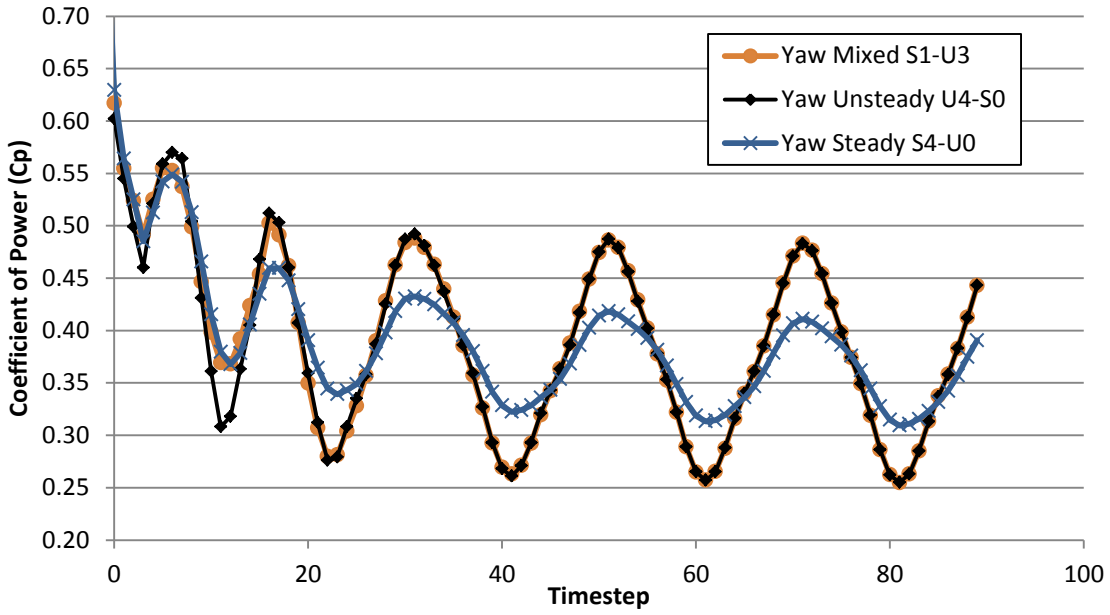

Figure 4-11 Yawed case, 30 deg., coefficient of power vs. the number of timesteps, 20 timesteps per revolution. U = # Unsteady time segments, S = # Steady time intervals. NREL UAE Phase VI wind turbine, 7 m/s wind speed. "Yaw Mixed S1-U3" switched from steady to unsteady solution at timestep 15.

The yawed rotor results illustrate the importance of using the unsteady equation system solution for unsteady analysis cases. It also shows that a steady solution can initially be used and switched to an unsteady solution without noticeably influencing the unsteady results. It is

interesting to note that switching between solution methods caused transient behavior in the mixed solution in Figure 4-7, but not in the equivalent case of the yawed analysis. Switching between steady and unsteady solutions may be explored in the future as a means to more quickly create accurate initial conditions for an unsteady solution.

4.6 Wake Length Effect of Various Wake Models

The effect of the wake length on power predictions was studied using the small-scale wind turbine that is used in the design study. The rotor was modeled with twelve spanwise panels in a cosine distribution, along with a tip-speed ratio of 5.3, and the same pattern of timestep intervals described in 4.2.1. The results of the predictions are shown in Figure 4-12. The cases labeled "Steady" were created with the steady relaxation and the steady equation system solutions. These results show very little change in coefficient of power after 400 timesteps, which corresponds to a wake of 34.5 revolutions. The difference between a wake model of 165 timesteps (11 revolutions) and 400 timesteps is less than 1% for all cases.

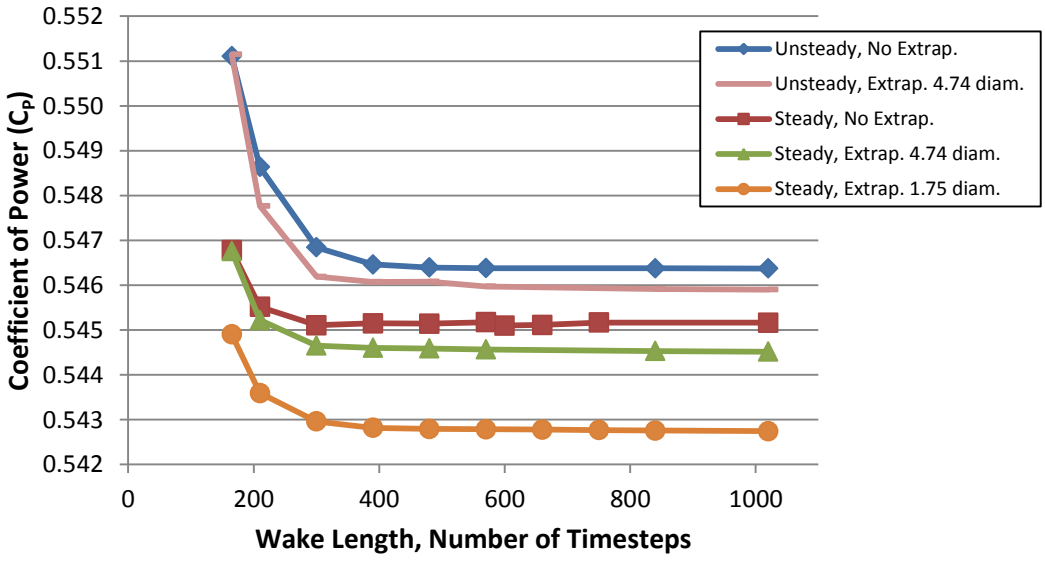

Figure 4-12 Effect of wake length of rotor power prediction. Small-scale wind turbine with winglet, TSR 5.3, 12 spanwise panels in cosine distribution.

The computation time increases exponentially as the number of timesteps increase, as is shown in Figure 4-13. The longer extrapolation distance of 4.744 rotor diameters downstream takes one quarter of the computation time as the non-extrapolated cases with a 0.1% difference in power prediction. Moving the extrapolation distance upstream to 1.75 rotor diameters downstream of the rotor reduces the computational time even more, but for a 0.5% difference in power prediction from the non-extrapolated steady analysis case.

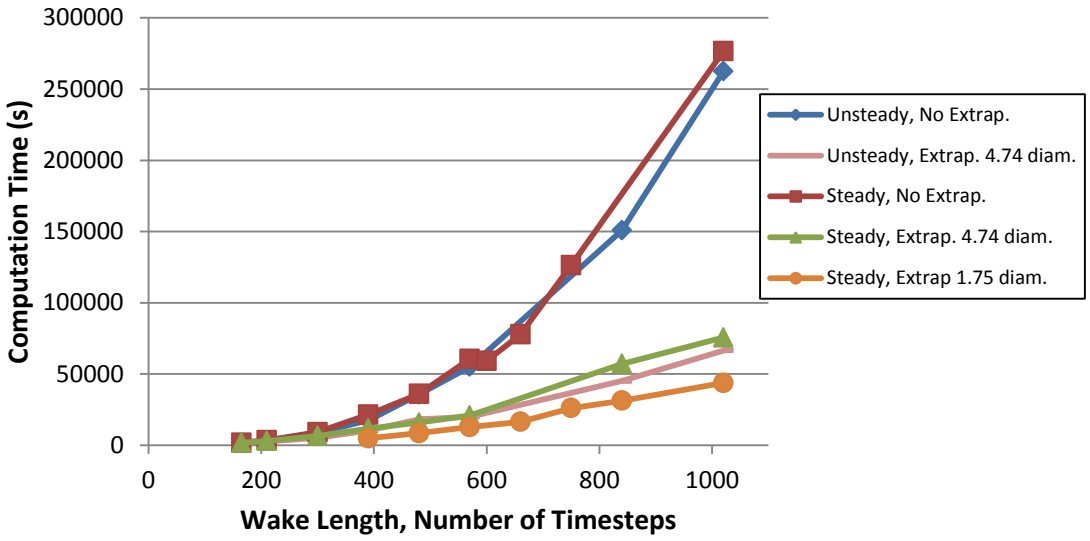

Figure 4-13 Computation time for various analysis methods versus number of timesteps. Small-scale wind turbine with winglet, TSR 5.3, 12 spanwise panels in cosine distribution.

A similar study was performed for a range of tip-speed ratios to investigate whether the effect of wake length is consistent with the predictions at one tip-speed ratio; the results of which are shown in Figure 4-14.

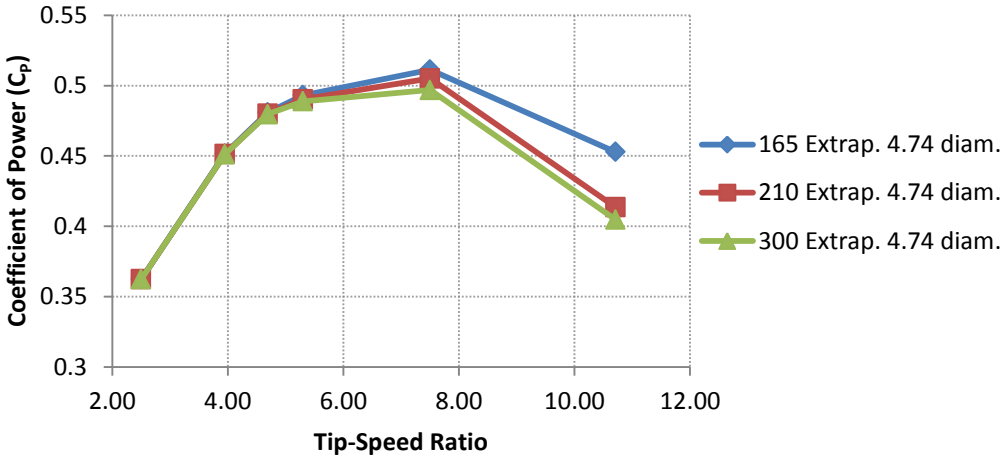

Figure 4-14 Effect of tip-speed ratio on the change in C_P with wake length. The legend refers to the wake length in number of timesteps and the extrapolation distance downstream in rotor diameters. Small-scale baseline wind turbine, 12 spanwise panels in a cosine distribution.

The results shown in Figure 4-14 indicate that the effect of wake length is not dependent on the tip-speed ratio for low values of tip-speed ratio, but there is a sensitivity to wake length at high tip-speed ratios. Just as with the extrapolation distance issues seen in Figure 4-4, this variation at high tip-speed ratio cases is due to the interaction of the extrapolation method with unrealistic wake deformation at the side-edge of the wake. The unrealistic wake deformation is most likely caused by the large amount of interaction of wake vortex sheets for high tip-speed ratio cases. Operating conditions where these issues are likely to occur are typically near the cut-in wind speed of most wind turbines and are not of critical concern for modeling since the power and loads are relatively very low.

4.7 Effect of Wake Length on Design

Figure 4-15 shows the change in C_P between the winglet and the baseline planar blades versus the number of timesteps (which determines the wake length) of the solution for a TSR of 5.3 on the baseline, planar blade. The profile drag and stall models were not used in this analysis.

These results indicate that the delta C_P from the winglet is about 10.3% for a model of 165 timesteps, 10.9% for a model of 480 timesteps, and 11% for a model of 570 timesteps. In this model, the wake shape is extrapolated after 4.74 rotor diameters downstream of the rotor, which is 8 wake revolutions for a TSR of 5.3. This shows that a wake of length 165 timesteps will get fairly close to a converged result, with 300 timesteps or more reaching the converged value.

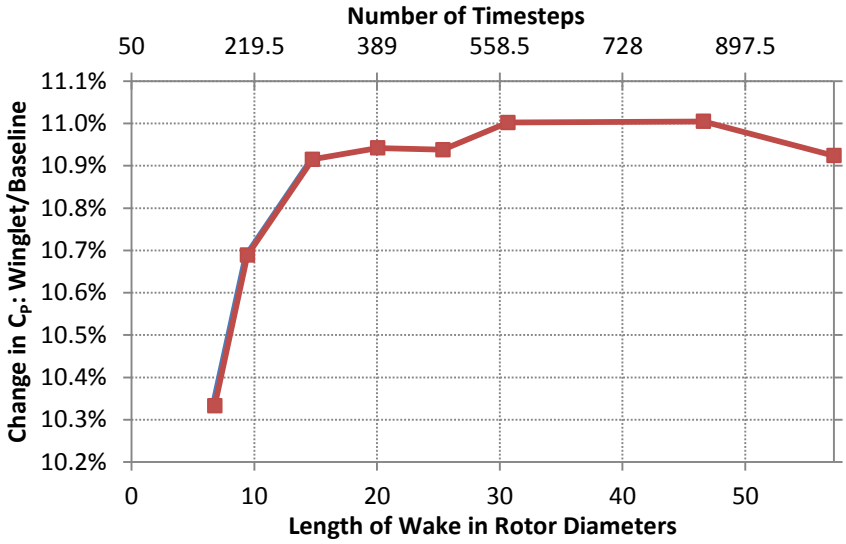

Figure 4-15 Predicted change in C_P of a winglet versus the length of the wake and the number of timesteps of the simulation. Small-scale wind turbine, TSR 5.3, 12 spanwise panels in a cosine distribution.

Figure 4-16 shows the required computation time for the results of Figure 4-15. It should be noted that the 165 timestep case took about .45 hours to finish and the 300 timestep case took 1.85 hours.

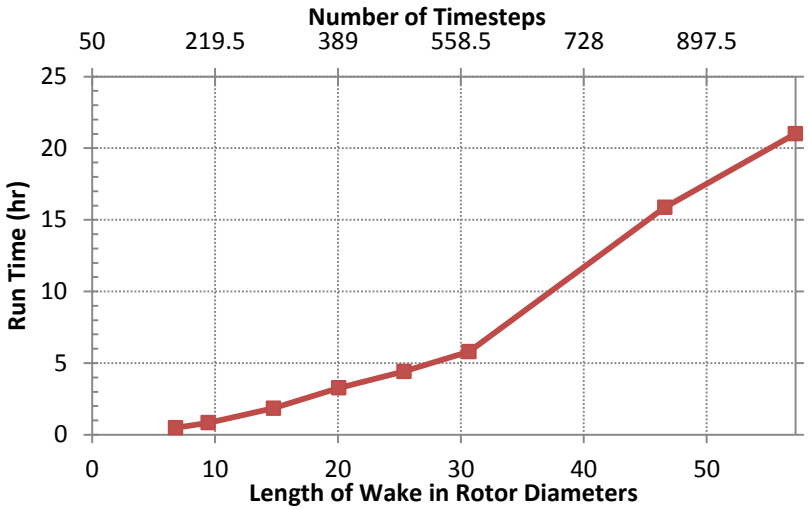

Figure 4-16 Program run-time versus length of wake. Small-scale wind turbine, TSR 5.3, 12 spanwise panels in a cosine distribution. Analysis performed on a 3.4 GHz Intel core i7-2600 processor.

The results in Figure 4-15 indicate that the design analysis is fairly insensitive to the wake length, and that shorter wakes than the ones analyzed could be used. It also indicates that beyond a wake length of 15 rotor diameters (300 timesteps for this case), there is a negligible change in the difference in predicted coefficient of power between the winglet and the baseline design cases. This analysis case showed an error of less than 0.6% between a wake length of 165 timesteps (7 diameters) and 300 timesteps (15 timesteps). In order to reduce computation time, a wake length of 165 timesteps was used for the majority of the analysis cases. Fixing the number of timesteps results in the wake length changing as the tip-speed ratio changes.

4.8 Influence of Surface Modeling Parameters on Power Prediction

The surface paneling parameters were explored in order to decide on the best values for the validation and design studies. An exploration of the effect of surface DVE paneling densities

on the power and thrust predictions of WindDVE for the 17 meter blade from Chapter 3_10 of the *Wind Energy Handbook* [11] was presented by Basom [4] and is summarized below. This wind turbine is referred to as the WEH blade; all cases are for a rotor with 3 blades, 20 timesteps per revolution, and a tip-speed ratio of 6.

Figure 4-17 shows the effect of the number of chordwise panels (which determines the number of lifting lines) and its effect on the rotor forces for the WEH blade [4]. The results of Figure 4-17 indicate that adding more than one lifting line does not have a significant impact on the power prediction. The profile drag and stall modeling routines were developed for a single lifting line; therefore, all of the validation cases model the lifting surface with one lifting line. As drawn from the results presented in Figure 4-17, for a blade of the typical aspect ratio of a wind turbine blade, the difference in the coefficient of power and the coefficient of thrust with the addition of lifting lines is negligible. For low-aspect ratio wings, the number of chordwise panels becomes more influential.

The fixed wake case in Figure 4-17 exceeds the Betz limit because the wake was only modeled for a limited number of revolutions. The predicted power coefficient decreases as the wake length increases, as shown in Figure 4-18. The fixed wake results of Figure 4-17 are for a standard fixed wake, meaning that the DVEs in each wake row are along the same spanwise (radial) line. The fixed wake model used to generate the results of Figure 4-18 placed the spanwise DVEs of each wake row along a parabola, which is why the two figures show different trends for the fixed wake cases [4]. A more detailed explanation of the differences between these two fixed wake models is given in Ref. [4] . The standard helical fixed wake model has been used to generate the fixed wake results that are presented for comparison to free wake results in other sections of this paper.

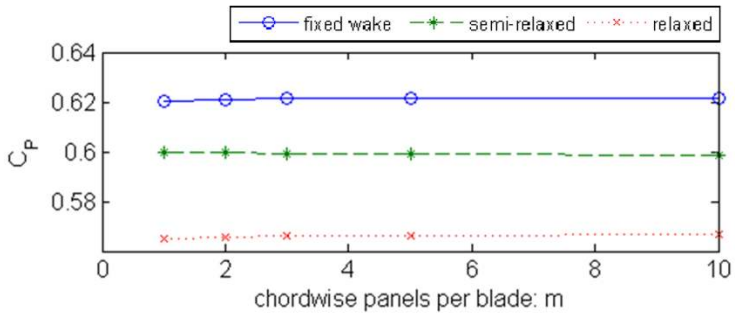

Figure 4-17 The effect of the number of chordwise panels on CP for TSR=6. WEH blade, 20 spanwise panels; fixed wake results are for 10 revolutions with standard helical wake; relaxed wake case results for 2.5 revolutions [4].

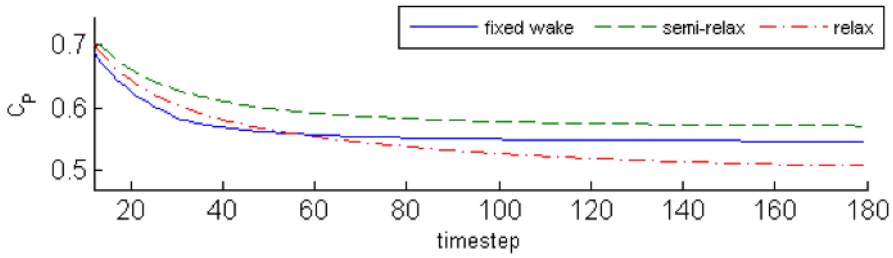

Figure 4-18 The effect of the wake length on the coefficient of power. WEH blade, TSR=6, 18 spanwise panels, 2 chordwise panels, 20 timesteps per revolution, fixed wake case uses a parabolic wake shape in the radial direction [4].

The effect of the spanwise paneling from the study of the WEH blade are shown in Figure 4-19. These results show that the predicted coefficient of power does not change much beyond ten spanwise panels, although it does continue to increase slightly as the number of spanwise panels is increased.

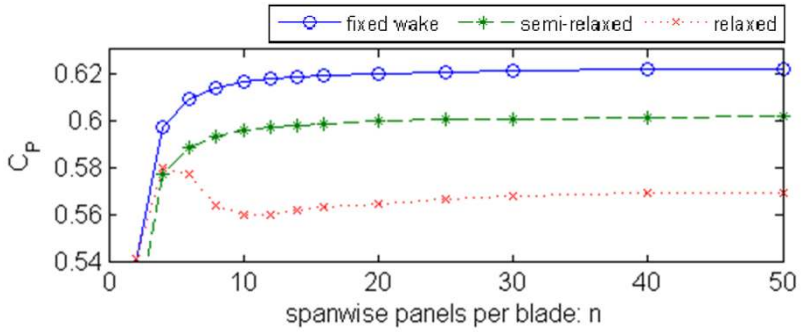

Figure 4-19 Effect of the number of spanwise panels on CP for one tip-speed ratio. WEH blade, TSR=6, 1 chordwise panel, fixed wake case results for 10 revolutions with standard helical wake, relaxed wake case results for 2.5 revolutions [4].

The study of the WEH blade presented in the previous figures only looked at one tip-speed ratio, so a similar study of the effect of spanwise paneling was performed for a range of tip-speed ratios. The small-scale wind turbine that is described in Chapter 6 was analyzed for this study so that the effect of a winglet could be included. The results, presented in Figure 4-20, were made using a blend of a linear paneling and a cosine distribution, as described in the final section of this chapter. The results indicate that the effect of the number of spanwise panels on the predication of the power coefficient is small at low tip-speed ratios and has a relatively stronger influence at higher tip-speed ratios.

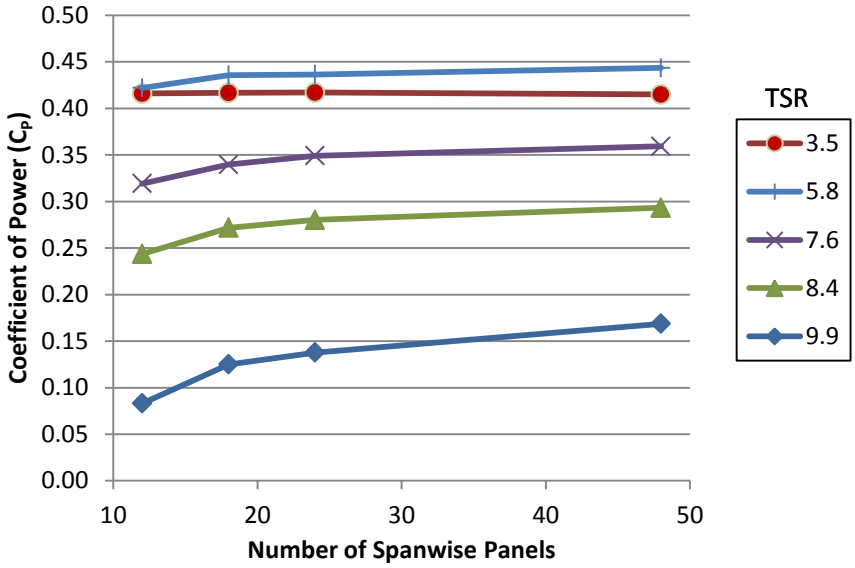

Figure 4-20 Effect of the number of spanwise panels on power prediction, baseline blade with blend of linear and cosine distribution, small-scale wind turbine, one lifting-line.

The effect of spanwise paneling on a winglet case was also performed, and the results are shown in Figure 4-21. The results show similar trends as the baseline at lower tip-speed ratios, but the behavior at the highest tip-speed ratio is not smooth with increasing number of panels. This is most likely caused by the issues with the wake shape and the extrapolation routine discussed earlier in 4.2.1 and 0. Future work could try to improve this situation, although these cases are not critical for design considerations since they correspond to very low wind speeds.

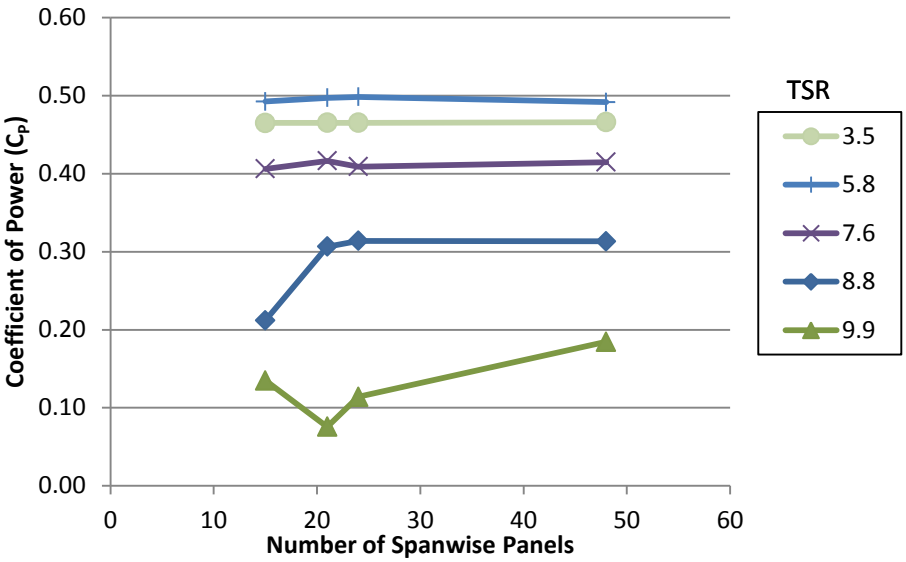

Figure 4-21 Effect of the number of total spanwise panels (main blade + winglet) on power prediction, winglet blade with blend of linear and cosine distribution, small-scale wind turbine.

Except for the highest tip-speed ratio case of the winglet blade, the trends indicate a relatively sizeable change in coefficient of power when going from 12 to 18 spanwise panels and a much smaller change when going from 18 to 24 spanwise panels. It was assumed that the NREL UAE Phase VI wind turbine will follow similar trends as the small-scale wind turbine used in Figure 4-20 and Figure 4-21. A total of 18 spanwise panels were used to model the Phase VI wind turbine during the validation analysis cases, as this value results in a balance of computation time and accuracy in the prediction of the coefficient of power.

The initial winglet design study of Chapter 6 focuses on a tip-speed ratio of 5.3. For this case, 12 spanwise panels are used on the main blade and 2 on the winglet in order to save computational time, since the results at this tip-speed ratio are fairly insensitive to an increase in the number of spanwise panels. The final results using the stall model cover the full range of operating tip-speed ratio, so 18 spanwise panels are used on the main blade and 3 along the winglet.

4.9 Trade Space Exploration Tool (TSET)

The trade-space exploration tool (TSET) is a general purpose program (referred to as a "tool") that aids in the generation of large sets of input files for WindDVE. It also has the ability to read the output of WindDVE and collect the results so that a designer or analyst can easily utilize a large number of cases. For example, the initial winglet design presented in Chapter 6 required many design cases involving exploring a range of winglet angles. Each case would take approximately three hours of user time to generate the individual input files and collect the data from the WindDVE results. The same cases take approximately thirty minutes of user time using the new tool. The TSET program did not reach a useable level of development until after the initial winglet design work was performed, since it was the design work that inspired the development of the tool. The initial winglet design presented in Chapter 6 used the spanwise panel spacing recommended at the end of this section, but only the winglet stall and trade-space analyses benefitted fully from the use of TSET.

4.9.1 Grid Generation and Input File Tool

At each stage of the model development, the code needs to be run using several different example cases. Creating input files is currently very time consuming; it can take anywhere from half an hour to several days to create the input files necessary to generate one power output curve for an example wind turbine. The input file tool automates many of the steps necessary for creating these various input files. It is standard practice to assess the dependence of the results of the DVE code on input file grid geometry and spacing, as was presented earlier in this chapter. In order to facilitate such studies, the input file tool is able to automatically generate different grid geometries and spacings.

A feature of the gridding method of the input file tool is a planform fitting feature. The results of a numerical analysis method depend on the numeric grid applied to the original blade geometry. A grid typically has a linear or cosine distribution of node points. These points do not typically lay on breaks in the blade planform geometry. Figure 4-22 shows a plot of chord length of the NREL Unsteady Aero Experiment (UAE) Phase VI rotor blade [5]. A cosine grid point distribution with 21 grid points was applied to the blade geometry and the chord length was linearly interpolated at these grid points. The interpolated blade geometry does not exactly follow the original blade geometry, causing a source of error. Standard practice is to manually adjust the grid points so that such an error can be avoided.

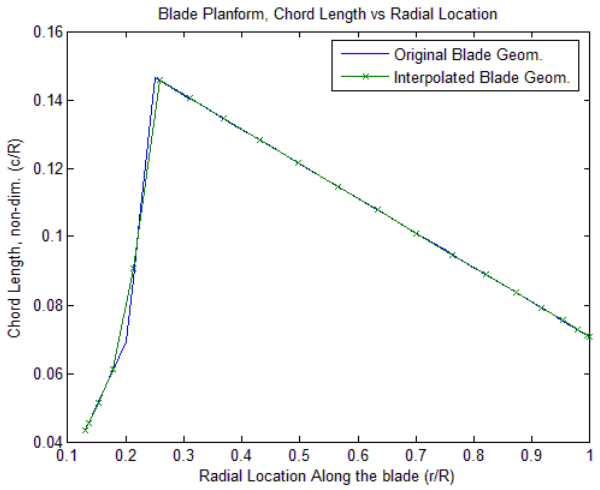

Figure 4-22 Surface paneling routine with no planform fitting.

Figure 4-8 shows the new grid with one grid point fixed, and Figure 4-24 shows the grid with two grid points fixed. The grid in Figure 4-24 follows the exact geometry of the blade.

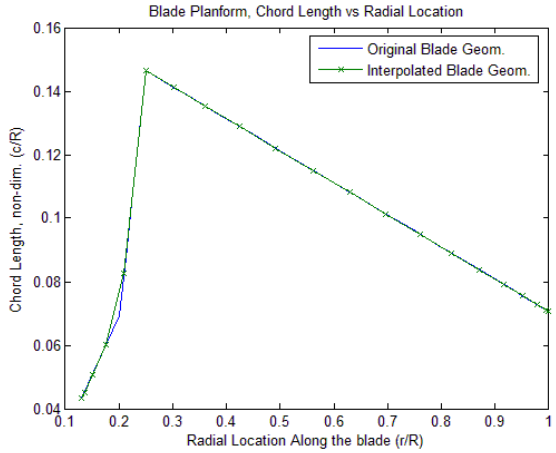

Figure 4-23 Surface paneling routine with one point planform fitting.

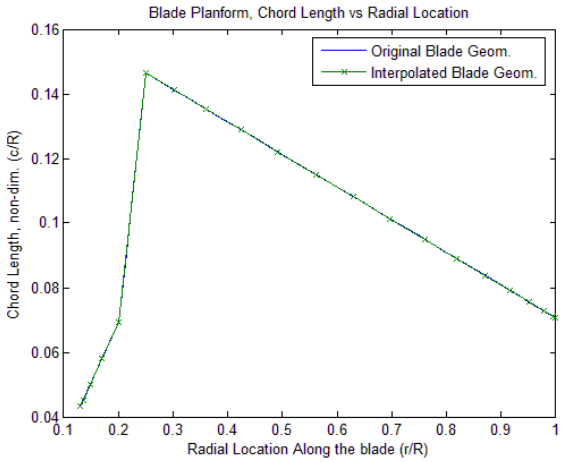

Figure 4-24 Surface paneling routine with two point planform fitting.

The new grid generation routine allows the user to fix two grid points. By automating the process of fixing these points, the user no longer has to manually adjust them every time the grid or blade geometry is adjusted. This can save a considerable amount of time, since a blade design may require a large number of geometry adjustments, each requiring a new grid to be generated.

A future potential modification to the input file generation tool would allow there to be as many forced geometry points as the user desires (rather than the current limit of two points). This modification would be useful for blade designs with multiple changes in the blade planform, although it is not required for this research.

4.9.2 Grid Spacing Factor

Experience has shown that the number of spanwise panels and their spanwise distribution can make a considerable impact on the power and thrust results of a wind turbine modeled in WindDVE. Three types of spanwise distributions have been explored: a cosine distribution, a linear distribution and an average of the two. The linear distribution has a constant spanwise width of each surface panel. The cosine distribution follows a circle from 0 to 180 degrees, where 0 is the root of the blade and 180 degrees is the tip. This distribution places more panels near the root and tip of the blade. These three distributions are shown in Figure 4-25 for a blade with 12 panels, which results in 13 geometric node points.

Preliminary results for twelve spanwise panels have shown that the cosine distribution helps some cases that will not converge when using a linear distribution. It was found that the increased panel density near the blade tips helped to improve the stability of the wake edges and roll-up region due to decreased change in circulation across each panel, but this earlier result only used 12 spanwise surface panels. A study was performed later to show the effect of the number of spanwise panels on the rotor thrust and power coefficients for a range of tip-speed ratios, as presented earlier in this chapter. It became apparent that beyond about 20 spanwise panels, non-realistic wake shapes and behavior were affecting the results, especially at high tip-speed ratios. The erroneous wake shapes were thought to be caused by the extremely thin (in the spanwise direction) wake DVEs near the edges of the wake.

In order to reduce the bunching at the blade root and tip, a new distribution was employed that is an average of a cosine distribution and a linear distribution, as shown in Figure 4-25. A new term was added to the surface paneling code called the grid spacing factor (GSF), which determines the balance between the linear and cosine distributions, with a pure linear distribution being GSF = 0, a pure cosine being GSF = 1, and GSF = 0.5 representing the average between the two.

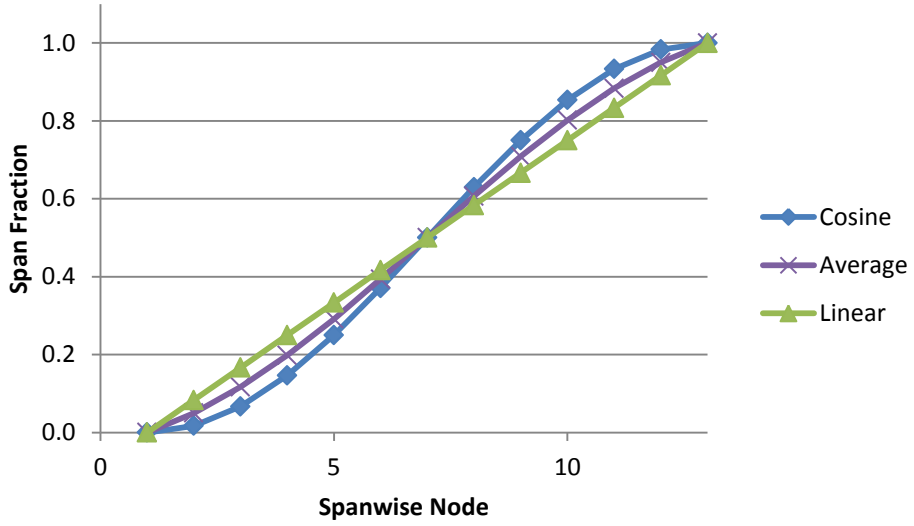

Figure 4-25 Span fraction vs. spanwise node number. A span fraction of 0.0 corresponds to the blade root and a value of 1.0 corresponds to the blade tip.

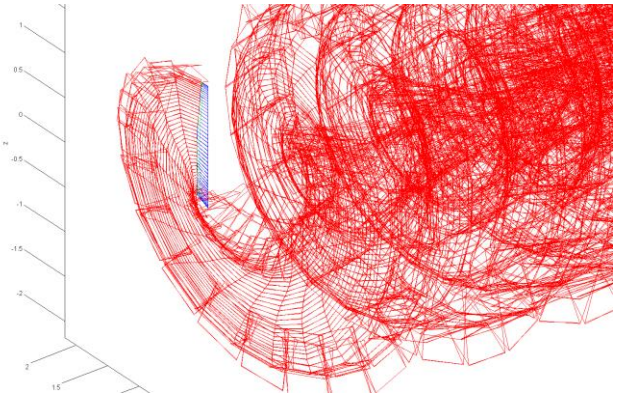

Figure 4-26 A blade modeled with 48 spanwise panels in a cosine distribution at a TSR of 10.

Figure 4-26 shows a spanwise paneling of 48 panels using a cosine distribution. Unrealistic wake shapes have formed near the tip-side edge of the wake. The panels at the edges are approximately 0.0011% of the blade span; the small panel width is the cause of the error in wake shape.

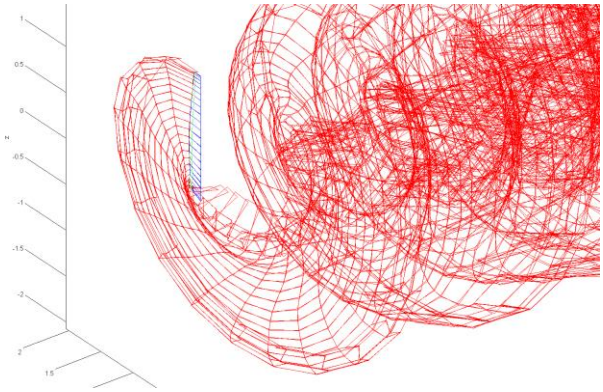

Figure 4-27 Blade modeled with 24 spanwise panels in a cosine distribution at a TSR of 10.

The error in the shape of the wake near the tip-side edge is not present for 24 spanwise panels (Figure 4-27), which for a cosine distribution result in the outer most panel having a span of 0.0043% of the rotor blade span, which is four times the span with 48 panels.

4.9.2.1 Winglet Paneling

Since the number of spanwise panels and their distribution can affect the resulting wake shape, power, and thrust, a method was created to panel the winglet in a consistent way relative to the baseline blade paneling. Some panels can be added beyond the baseline blade spanwise paneling, but if too many are added it can influence the thrust and power and any design decisions these quantities influence. The number of panels on the winglet should correspond to the relative

winglet height. It was found that for a winglet of 8% of the height of the rotor radius, three panels showed a considerable difference in power predictions relative to predictions made using two panels for cases with a tip-speed ratio greater than 6. The winglet was paneled with a linear distribution of panels (constant panel width) along the winglet height while the main blade used a blended linear-cosine distribution. The difference between three and four winglet panels was relatively small throughout the range of TSR. The analysis case with one winglet panel showed considerable difference throughout the range of TSR; therefore, for a winglet of this height the minimum paneling is two, with three or more being desirable.

It is desirable to maintain as small of a change as possible between spanwise neighboring panels in order to maintain numerical stability accuracy. Figure 4-28 shows the width of the tip-end panel on the main blade using an equally blended cosine and linear panel distribution versus the number of panels on the main blade. The width of the winglet panels is also shown for a winglet of height 8% of the rotor span with a constant panel width along the winglet span. Using the winglet and main blade panel distributions shown in Figure 4-28 results in nearly matched panel widths at the winglet-blade juncture. The widths cannot be equal due to the requirement that the number of spanwise panels be an integer.

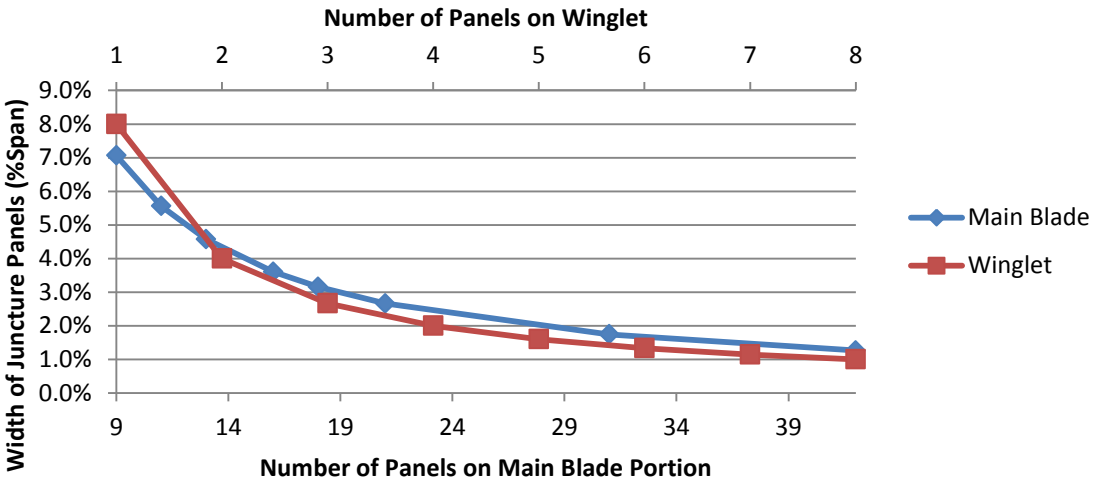

Figure 4-28 Width of the tip-end panel on the main blade versus the number of panels on the main blade using an equally blended cosine and linear panel distribution. The width of the winglet panels is shown for a winglet of height 8% of the rotor span with a constant spanwise panel width.

The winglet and main blade paneling for several values of winglet height were found by creating a plot similar to Figure 4-28; the results of which are as follows:

Table 4-1 Winglet and main blade spanwise paneling density required to minimize the change in panel width at the winglet juncture. Each winglet case has more total panels than the corresponding baseline case.

	Winglet Height:	8% Winglet		2%	4%	10%	12%
NumPanels Baseline Blade	NumPan WingletTot	NumPan Winglet	NumPanMain PortionWinglet	NumWingletPanels			
88	91	12	79	4	7	15	17
48	50	7	43	2	4	8	9
36	37	5	32	2	3	6	7
24	25	4	21	1	2	4	5
20	21	3	18	1	2	4	4
18	19	3	16	1	2	3	4
15	16	2	14	1	1	3	3
12	13	2	11	1	1	2	2
10	11	2	9	1	1	2	2

Chapter 5

Validation of the Free-wake Vortex Method

The free-wake vortex method presented in this paper was validated using comparisons from two experimental data sets. The first set used is from the National Renewable Energy Laboratory's Unsteady Aerodynamics Experiment Phase VI wind turbine, referred to as the NREL UAE Phase VI [5]. This experiment tested a 10 meter diameter wind turbine in both field and wind tunnel test conditions. The data has become a standard for the validation of wind turbine performance analysis tools. The data includes both spanwise and chordwise force and pressure data, angle-of-attack measured with a 5-hole pitot-static probe, and overall power output, in addition to a number of other relevant quantities.

The second validation case is a small wind turbine tested with and without winglets in a small-scale wind turbine testing facility at the University of Waterloo. This test is unique as it is the only available data of a winglet on a wind turbine that shows a performance benefit. The results from this test only include power output results for the entire wind turbine so a comparison cannot be made with the spanwise force distributions, as was done for the NREL UAE Phase VI turbine. The design of this winglet and the details of the small wind turbine, as well as the validation results, are presented in Chapter 6.

5.1 Modeling the NREL UAE Phase VI Wind Turbine

The NREL UAE Phase VI wind turbine wind turbine has been used for validation in many studies as the experimental test results of it have proved to be nonpareil.

The validation cases use the following modeling conditions:

Table 5-1 Lifting surface and wake modeling parameters used for the NREL Phase VI validation study.

1 lifting line
18 spanwise elements in an evenly blended linear/cosine distribution
Unsteady equation system solution
Total wake length of 4.2 revolutions over three intervals:
1.) 25 timesteps at 10 steps/rev.
2.) Transition region of 10 timesteps
3.) 20 timesteps at 20 steps/rev.

The resulting wake length is shorter than the wake length of most of the results presented in Chapter 4. The validation study of this chapter is focused on the predicted spanwise normal force of the rotor, which does not require as high a level of accuracy as the winglet design study of the next chapter. By using a shorter wake length for these validation analysis cases, the required computational time was greatly reduced.

The analysis results presented in this chapter could be "tuned" to match the experimental results exactly by modifing the section profile force. Such "tuned" results are only useful for applying an anaysis method to a specific design case and have limited usefulness for validation, especially when one considers that the experimental results always have a margin of error associated with them. Experimental results are the best that could be produced given their testing method. Similary, predictions made for validation should be the best that the analysis method can produce without correction factors that are only used for the experimental data being analyzed.

5.1.1 Stall Delay Corrections

When flow separation occurs on the lifting surface, spanwise flow develops that can have a strong interaction with the chordwise pressure gradients. This interaction causes an effect known as stall delay, since the interaction of the spanwise and chordwise pressure gradients often

causes the angle of stall to increase relative to the two-dimensional values [11]. Stall delay is typically not important for the analysis of pitch regulated wind turbines, but it is imporatant for stall regulated wind turbines such as the NREL UAE Phase VI wind turbine. It can be modeled by adjusting the airfoil profile force data at various spanwise stations; the method of adjustment is effectively the addition of a tuning factor. Adjusting this tuning factor can produce almost any result desired.

For the validation results presented in this chapter, the profile data was corrected using a standard stall delay correction tool, AirfoilPrep, which is available through the National Renewable Energy Laboratory [86,87]. The stall delay corrections were applied to the S809 airfoil data at a limited number of spanwise stations, so that the only variable needed for modifying the airfoil section data was the spanwise stations where the stall delay correction was applied. It is hoped that by applying a standard stall delay method, the strengths and weaknesses of the analysis method presented in this document will be evident in the validation studies rather than blurred over with custom correction factors.

The stall delay correction was applied at spanwise stations located at 25%, 41.88%, and 56.88% of the blade maximum radius. The section of the blade between the nacelle and the 25% radial location is referred to as the root transition region. The airfoil data for this region was not modified, as the stall delay correction grossly over-predict the loads in this region. The airfoil data files were utilized at the following locations along the blade span:

Table 5-2 Airfoil locations along the blade span, as well as the zero lift angle-of-attack of the airfoil. "SD" means that stall delay corrections were applied at the given spanwise location.

Airfoil Description	α_{0L} (deg.)	r/R Inner	r/R Outer
Cylinder	0.000	11.6%	14.1%
S809 Root Blend 33%	-7.615	14.1%	17.2%
S809 Root Blend 75%	-2.000	17.2%	25.0%
S809, SD 0.25 r/R	-1.225	25.0%	30.3%
S809, SD 0.42 r/R	-1.225	30.3%	48.4%
S809, SD 0.57 r/R	-1.225	48.4%	61.3%
S809, Clean	-1.225	61.3%	100.0%

5.1.2 Stall Modeling Options Applied to the NREL UAE Phase VI Wind Turbine

Several options for stall modeling were presented in section 3.2.2, *Stall Modeling*. Stall delay corrections are often empirically based on actual wind turbine tests or CFD analysis data and are typically implemented as corrections necessary to match blade-element theory results to the test data. Creating stall delay corrections in this way means that they inherently include the effect of stall on shed wake circulation, in which case applying stall option four ("SO4", described in section 3.2.2) would result in over accounting for this effect. The influence of stall option four is minimal, but it increases the required computation time considerably; the influence of this effect was shown in Chapter 3 for the 7 m/s and 15 m/s cases of the Phase VI wind turbine. The total effect of stall delay is much larger than the effect of including the influence of stall on the shed vorticity (stall option four); therefore, separating the influence of the latter effect has not been possible. Stall option four should be applied for analysis cases where stall delay corrections are not available, or are derived in a way where the effect of stall on shed wake vorticity is not included. Data derived in this fashion was not used for the NREL Phase VI wind turbine

validation, so stall option three ("SO3") was used to generate the validation results for this turbine since it does not include the effect of stall on the shed vorticity.

5.1.3 NREL UAE Phase VI Wind Turbine Airfoil Data

The airfoil data used for validation is presented in Figures 5-1 to 5-4. The NREL Phase VI wind turbine uses the S809 airfoil for most of the blade. The blade section of the root transition region blends between a cylinder near the nacelle and the S809 airfoil at the 25% radial location. The S809 airfoil was analyzed using XFOIL [88] with a Reynolds number of 900,000. The airfoil data for the blade station at 1/3 of the root transition region is labeled "S809 Root Blend 33%" and the airfoil data for the station at 75% of the span of the root transition region is labeled "S809 Root Blend 75%". The "S809 Root Blend 33%" airfoil was created by blending a cylinder and the S809 airfoil using the geometric blending routine in XFOIL [88]. The "S809 Root Blend 75%" airfoil data was created by blending the "S809 Root Blend 33%" airfoil data with the data of the S809 airfoil; the blending process was performed using the tool *AirfoilPrep* [86]. Cases labeled "SD" use airfoil data adjusted with the stall delay corrections, which were performed at the given spanwise location using AirfoilPrep [86].

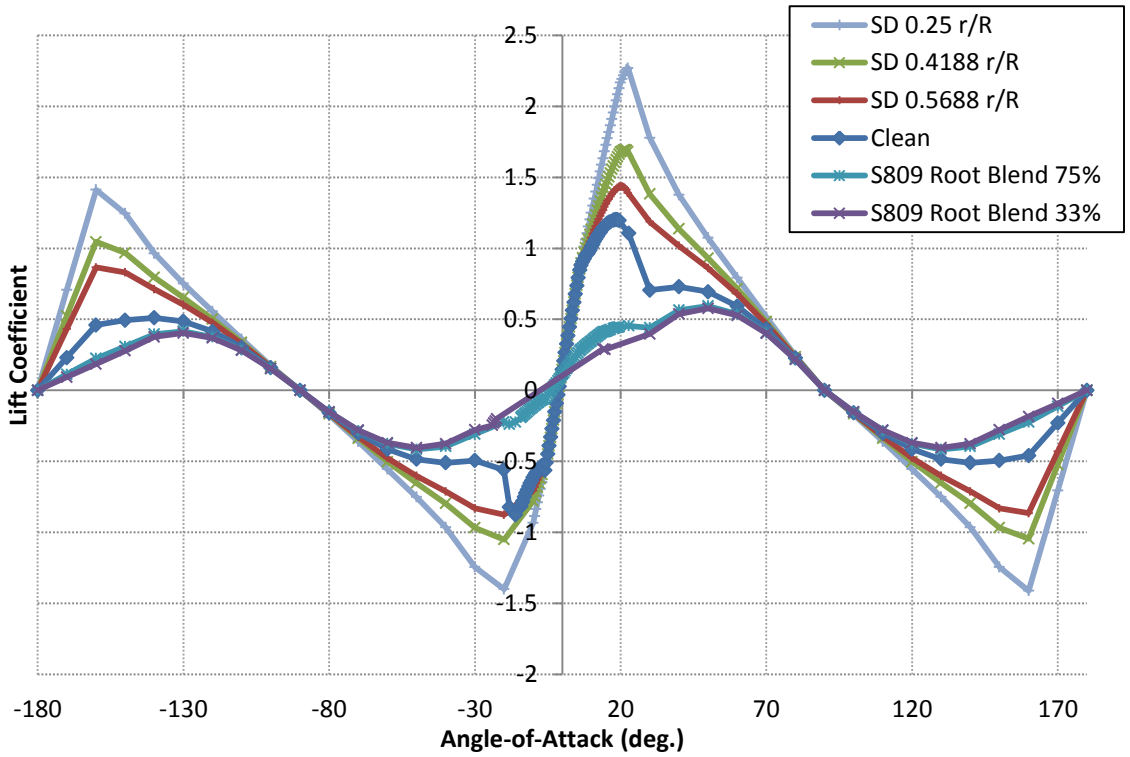

Figure 5-1 Airfoil section lift coefficient data used in the analysis of the NREL UAE Phase VI wind turbine. S809 airfoil data generated using XFOIL [88] with a Reynolds Number of 900,000. Stall delay correction performed at the given spanwise location (after "SD") using AirfoilPrep [86].

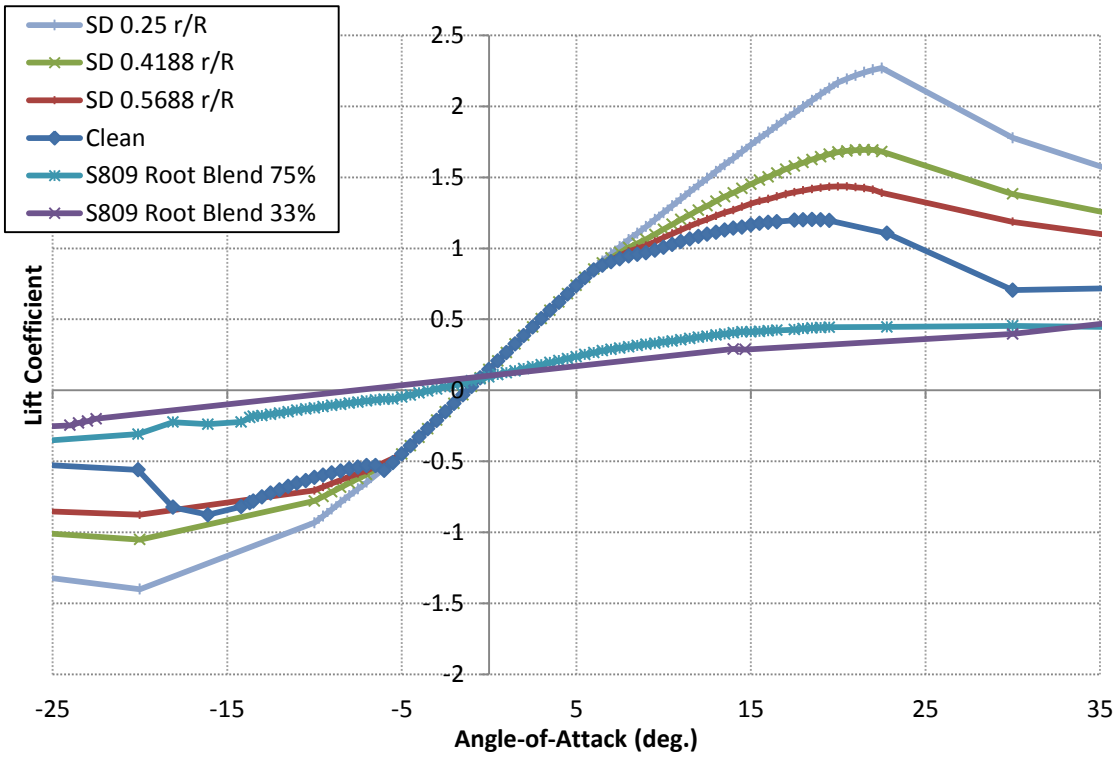

Figure 5-2 Airfoil section lift coefficient data used in the analysis of the NREL UAE Phase VI wind turbine. S809 airfoil data generated with XFOIL [88] at a Reynolds Number of 900,000. Stall delay correction performed at the given spanwise location (after "SD") using AirfoilPrep [86].

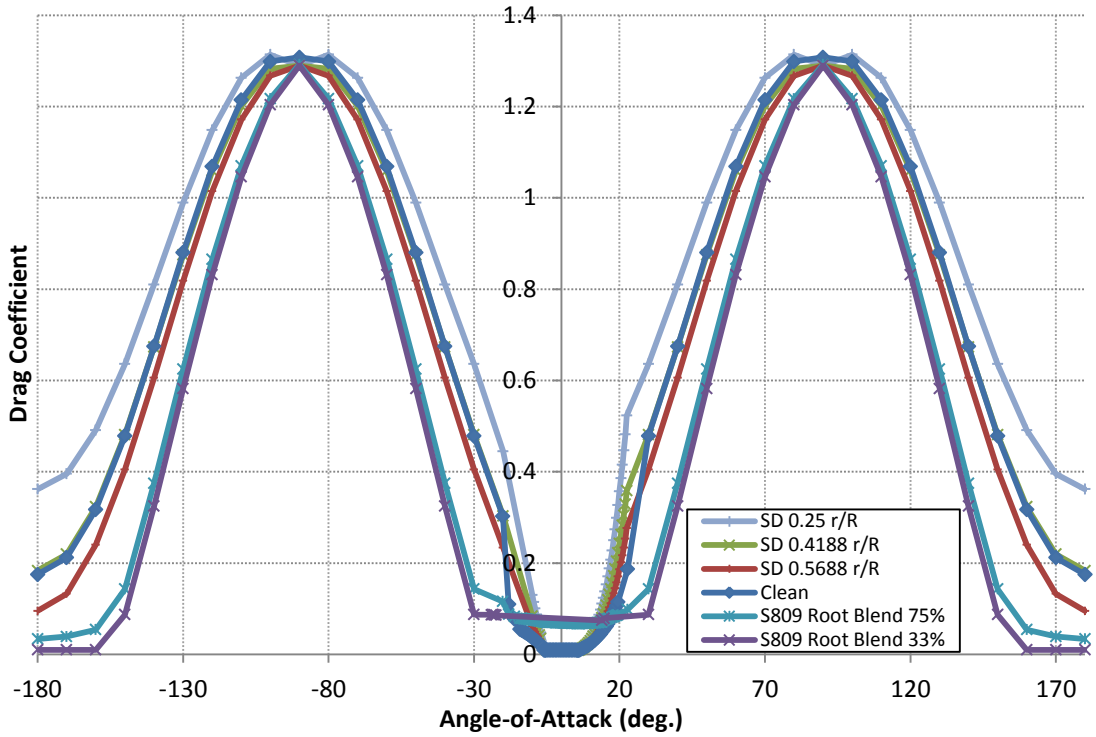

Figure 5-3 Airfoil section drag coefficient data used in the analysis of the NREL UAE Phase VI wind turbine. S809 airfoil data generated with XFOIL [88] at a Reynolds Number of 900,000. Stall delay correction performed at the given spanwise location (after "SD") using AirfoilPrep [86].

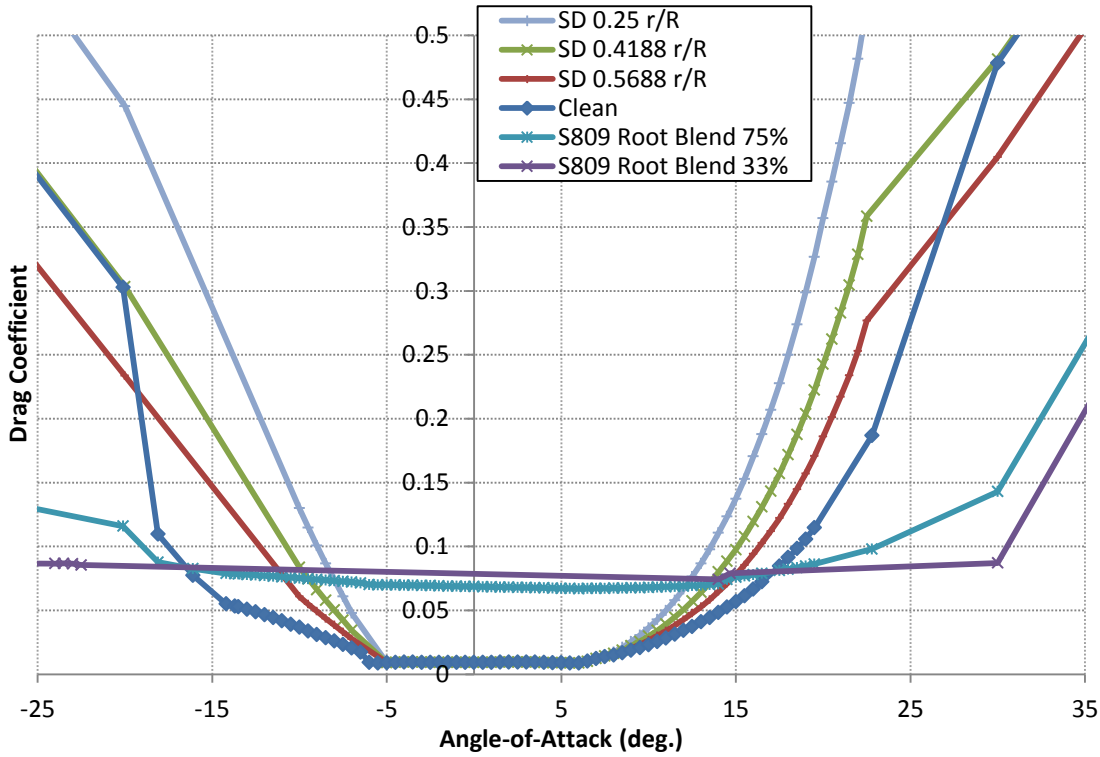

Figure 5-4 Airfoil section drag coefficient data used in the analysis of the NREL UAE Phase VI wind turbine. S809 airfoil data generated with XFOIL [88] at a Reynolds Number of 900,000. Stall delay correction performed at the given spanwise location (after "SD") using AirfoilPrep [86].

5.2 Validation Results of the NREL UAE Phase VI Wind Turbine

The experimental test of the NREL Phase VI wind turbine used pressure transducers to determine the section normal and tangential force coefficients [5]. The normal force coefficient (C_n) represents the force acting perpendicular to the airfoil chordline and the tangential force coefficient (C_t) represents the force acting parallel to the chordline. These definitions come from the NREL report on the experimental methods and results of the UAE Phase VI turbine [5]. These coefficients are related to the section lift and drag coefficients as follows:

$$C_n = c_l \cos \alpha_{Pot} + c_d \sin \alpha_{Pot} \quad 5\text{-}1$$

$$C_t = c_l \sin \alpha_{Pot} - c_d \cos \alpha_{Pot} \quad 5\text{-}2$$

The angle-of-attack (α_{Pot}) in these equations is obtained by dividing c_{l_Pot} by 2π, as outlined in Chapter 3.

The section drag coefficient is found from airfoil coefficient data based either directly on the lift coefficient obtained from the potential flow solution (c_{l_Pot}) or from α_{Pot}. The results presented below use the second method, as using c_{l_Pot} directly limits the data range to lie between positive and negative values of the maximum lift coefficient, which is exceeded on parts of the blade during almost all of the analysis cases. The lift coefficient in the above equations can either be c_{l_Pot} or can be the lift coefficient found from the airfoil section data based on α_{Pot}.

Figures 5-5 through 5-10 show a comparison of the value of the normal force coefficient (C_n) predicted from the FW-DVE method as compared to experimental results. The results from the test of the NREL UAE Phase VI wind turbine at the NASA Ames research center are labeled "Experimental" in the following figures. Cases labeled "SD" use airfoil data adjusted with the stall delay corrections. The 5 m/s and 7m/s cases shown in Figures 5-5 and 5-6 both show very good agreement for the section of the blade outside of the 40% radial station. The inner part of the blade indicates that the WindDVE predictions are over estimating the normal force relative to the experimental results. The discrpency at the inner section of the blade is most likely caused by inaccuracies with the blended airfoil data used to model the root transition region. The modeling results for the inner section of the blade could be improved by more accurately modeling this region using improved airfoil data; however, this was not deemed necessary for this study because the effect of the root region on rotor power production is minimal relative to the rest of the blade.

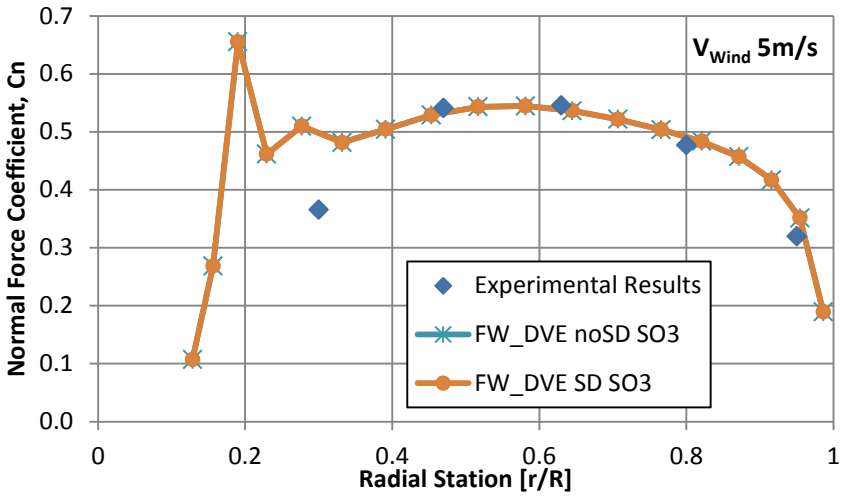

Figure 5-5 Predictions of Cn at 5m/s from the FW-DVE method with and without a stall delay model.

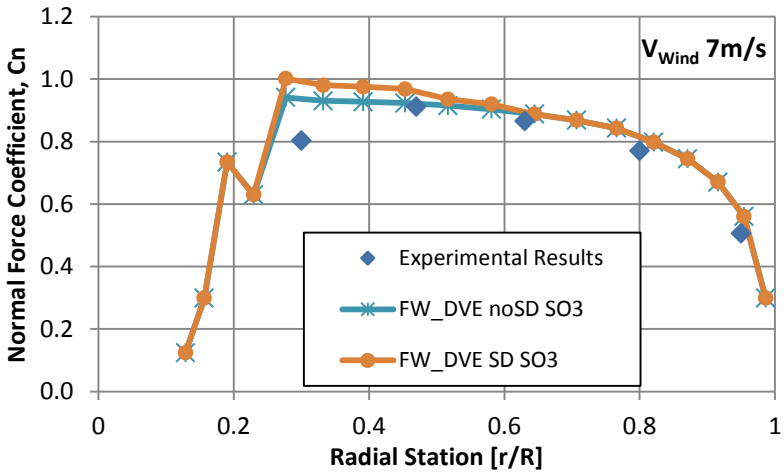

Figure 5-6 Predictions of Cn at 7m/s from the FW-DVE method with and without a stall delay model.

The agreement between the stall delay corrected results and the experimental results is very good for the 9 m/s and 10 m/s wind speed cases, shown in Figures 5-7 and 5-23. The influence of the stall delay model is obvious in all of the cases above this wind speed. The predicted tip loading is higher than the experimental results, although the predictions are within the error of the experimental data.

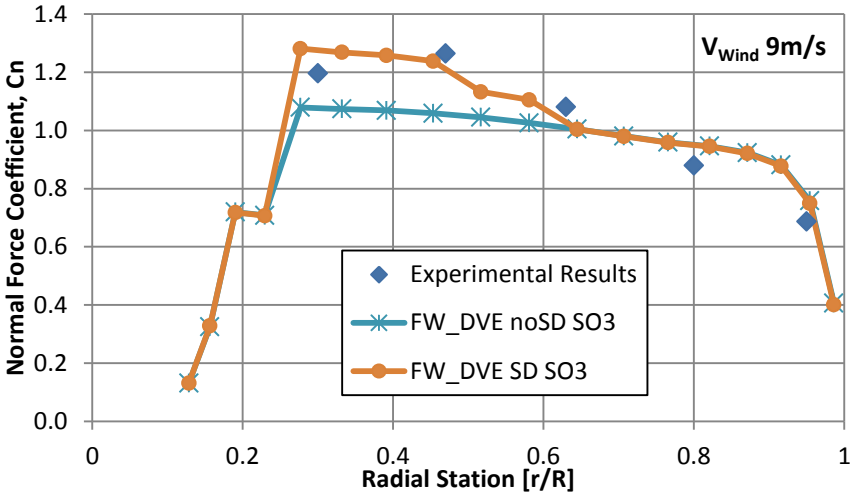

Figure 5-7 Predictions of Cn at 9m/s from the FW-DVE method with and without a stall delay model.

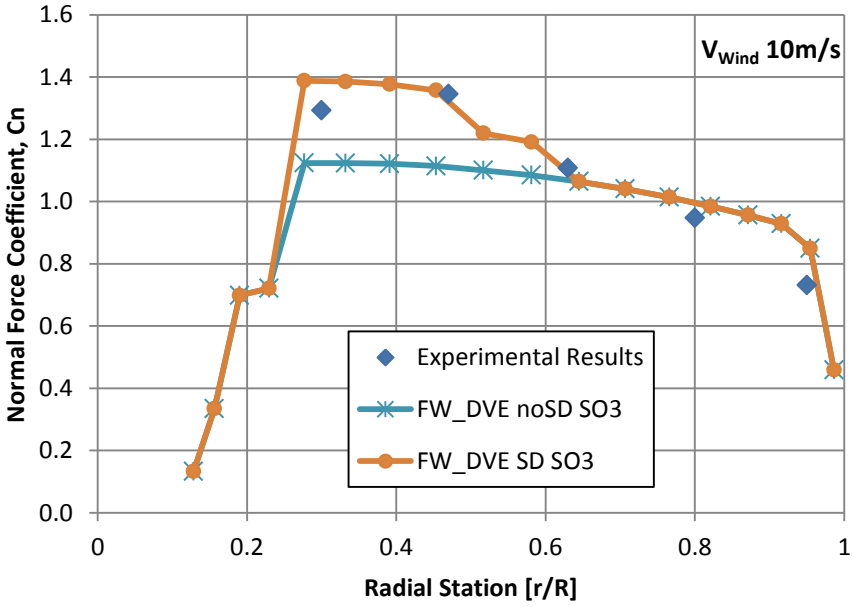

Figure 5-8 Predictions of Cn at 10m/s from the FW-DVE method with and without a stall delay model.

The 11 m/s case shown in Figure 5-9 indicates that the experimental data just outside of the 60% span location is slightly lower than the predicted values. The source of this region of decreased

normal force is unknown, although one possible source could be the presence of a strong region of trailing vorticity due to the large gradient in circulation in this region of the blade.

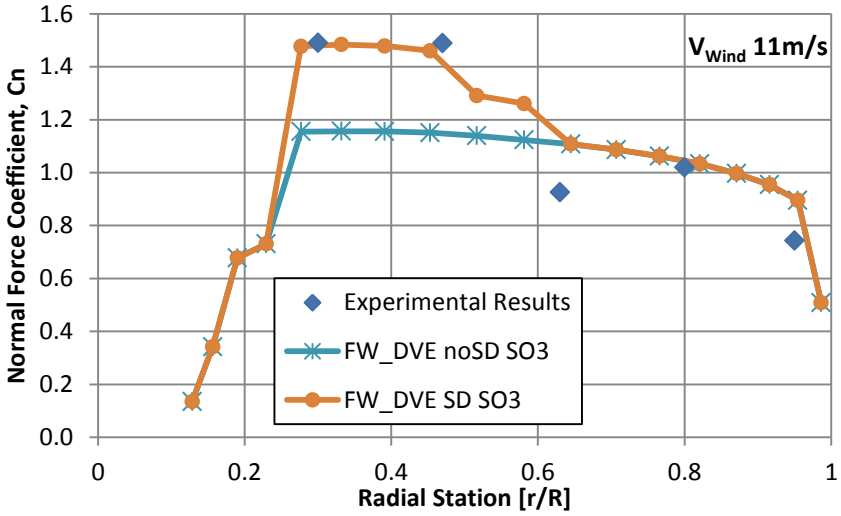

Figure 5-9 Predictions of Cn at 11m/s from the FW-DVE method with and without a stall delay model.

The predictions at a wind speed of 13 m/s are shown in Figure 5-10. These results are interesting because the experimental results indicate a more pronounced reduction in tip loading as compared to the FW-DVE predictions than in the 9 m/s and 10 m/s cases.

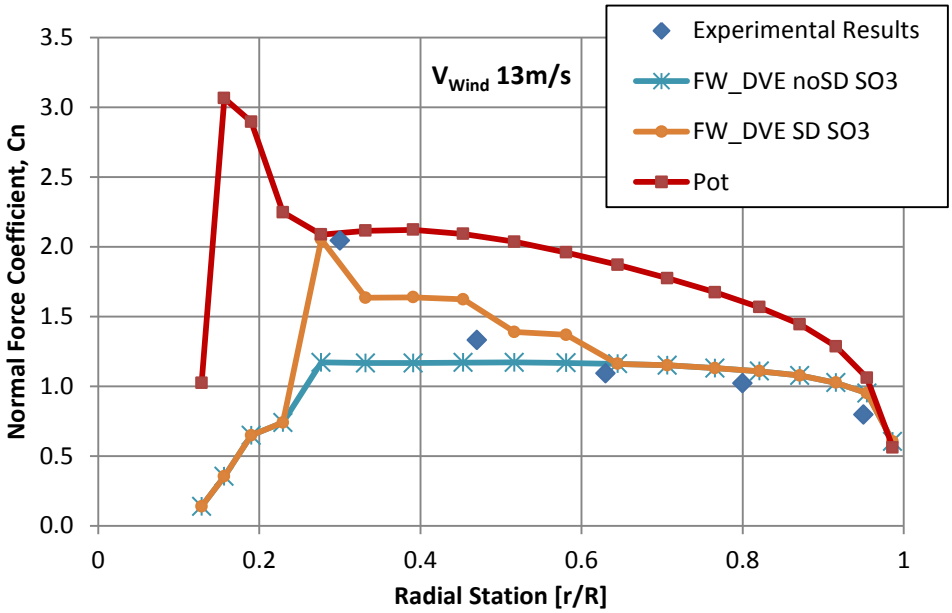

Figure 5-10 Predictions of Cn at 13m/s from the FW-DVE method with and without a stall delay model.

For the case labeled "Pot" in Figure 5-10, Cn was found by using the lift coefficient from the potential flow solution with the unmodified kinematic flow condition and the drag coefficient obtained from airfoil data based on the angle-of-attack. The forces predicted using this method over estimate Cn by a considerable amount due to the lack of the effect of stall on the lift coefficient.

The predicted normal force distribution from WindDVE shows acceptable agreement with the experimental results for the NREL Phase VI wind turbine. This agreement indicates that one can have relative confidence in the predictions made using this method.

Chapter 6

Design Applications for Wind Turbines: Winglets

This chapter describes the design process of a winglet for a small-scale wind turbine. The winglet was designed using the FW-DVE method, and tested in a small wind turbine testing facility at the University of Waterloo [89–91]. This experimental data is perhaps the first to show a performance gain of a wind turbine due to a winglet.

6.1 Winglets for Wind Turbines

6.1.1 Winglet Design and Analysis

Winglets offer a performance benefit for lifting surfaces, including for wind turbines. A model of the effects of the wake downstream of the wind turbine is required to accurately analyze the effect of the winglet. Blade Element Momentum Theory (BEMT) is not applicable to the analysis of a winglet due to the assumptions of radial independence and the standard use of a tip-loss model to account for wake effects. A vortex method, whether it is a free wake or prescribed wake type, will model the effect of the wake vorticity on the lifting line and hence is able to capture the effects of a winglet. A free-wake model will theoretically give more accurate results than a prescribed wake model due to capturing effects of the roll-up of the wake, albeit at larger computational cost and complexity than a prescribed wake model.

Winglets improve the performance of fixed wing aircraft by decreasing the rate of change of circulation along the lifting surface, which decreases the amount of vorticity trailed into the wake behind the lifting surface. Decreasing the trailing vorticity decreases the induced velocity caused by the trailing vorticity, which decreases the induced drag of the lifting surface. A winglet

on a wind turbine improves power output by increasing the amount of power that can be produced by the outer region of the wind turbine blade.

Figure 6-1 shows the effect of the winglet on the wind turbine main blade thrust force. The extra force due to the winglet is the difference between the "Axial Winglet" curve and the "Axial Baseline" curve. The data points near the tip of the winglet blade are the points on the winglet and only cover a small range of radial distance due to the winglet being vertical. The small span of radial distance of the winglet data points is due to the data points not being along the axis of twist of the winglet. Figure 6-2 shows the driving force, which produces torque and power output of the wind turbine. The effect of the winglet on driving force is the difference between the winglet and baseline curves.

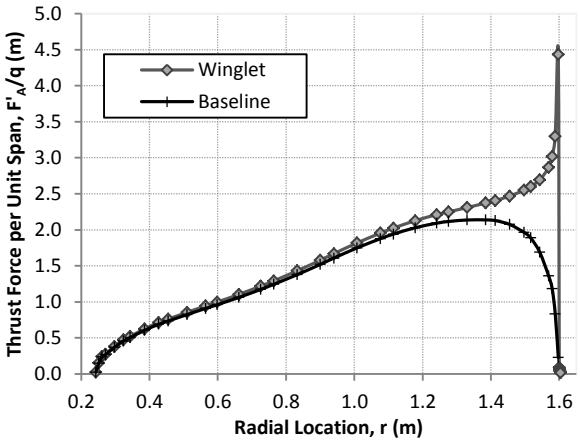

Figure 6-1 Thrust Force Distribution, Winglet vs Baseline Blade. TSR 5.3, results given as F'/q, or force per spanwise length divided by dynamic pressure.

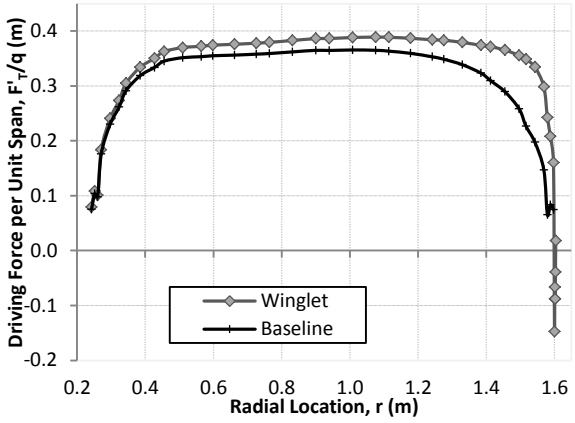

Figure 6-2 Tangential Driving Force Distribution, Winglet vs Baseline Blade. TSR 5.3, results given as F'/q, or force per spanwise length divided by dynamic pressure.

6.1.2 Prior Winglet for Wind Turbine Research

The testing of several advanced tip modifications on wind turbine performance was undertaken in the early 1980's by Gyatt and Lissaman [92]. The research utilized a vortex lattice method to analyze candidate winglet designs. The vortex lattice method used a simple fixed wake model with relatively crude spanwise panel spacing. Several tip devices were tested in the field on an experimental wind turbine as part of the research. The increase in rotor power output due to the addition of a vertical winglet with height of 5% of the rotor radius was predicted to be 7%; however, all of the designs demonstrated a decrease in performance relative to the baseline wind turbine. This degradation was attributed to the limitations of the modeling tools at the time [92].

In 1998, Imamura et al. [93] published research which involved the analysis of winglets on wind turbines. The research used a free-wake vortex lattice method with Rankine viscous core filaments to model the wake [93,94]. The paper compared the benefit of a span extension to a winglet of different cant angles, the results of which are summarized in Figure 6-3. The winglet

cant angle is the angle that the winglet makes with the plane of the main wing, so that a 90 degree cant angle is a vertical winglet and a zero degree cant angle corresponds to a main blade span extension. The results show that a winglet can achieve the same or greater increase in power output as a span extension, but with a reduced flap-wise bending moment about the blade root. A span extension of 10% of the rotor radius was predicted to give a 21% increase in maximum power output over the baseline rotor blade and a 42% increase in blade root flap-wise bending moment. A winglet of a height of 10% of the rotor radius at an 80 degree cant angle resulted in a 22% increase in power output over the baseline rotor blade and a 10% increase in the blade root flap-wise bending moment [93]. This power difference is for a tip-speed ratio of 7.2, which corresponds to maximum coefficient of power of the baseline blade. The blade root flap-wise bending moment was taken at a TSR of 4 for all of these results. The results indicate the potential of a winglet to offer the same level of power output as a baseline blade at a reduced root bending moment, which corresponds to reduced blade weight.

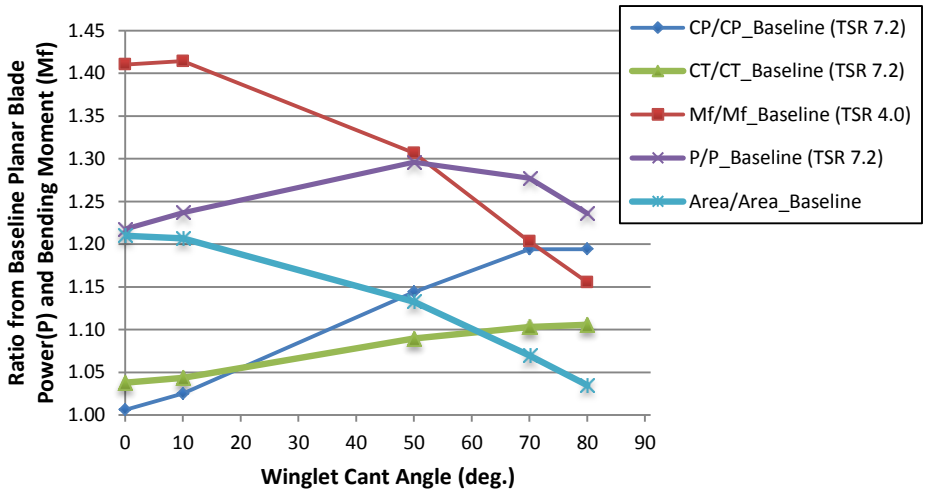

Figure 6-3 Coefficient of power (CP), coefficient of thrust (CT), power (P), area, and flapwise bending moment about the blade root (Mf) vs winglet cant angle. Ratio from baseline planar blade. Cant angle of 90 deg. is a vertical winglet, 0 deg. is a span extension [93].

Winglet research was performed more recently at Risø-DTU using a Navier-Stokes CFD analysis [95]. The initial study analyzed several combinations of winglet geometry. The winglet

for this analysis was created by stretching the outer section of the wing, then bending the tip in the downwind or upwind direction. The research showed that a downwind winglet on an upwind wind turbine (winglet on the suction side of the blade) will give a larger aerodynamic performance gain than an upwind winglet, but the gain is offset to some degree by the structural weight penalty of needing to have the winglet clear the rotor tower. The results from this study showed that an upwind winglet with height 1.5% of the rotor radius showed a 0.6-1.4% increase in C_P, depending on the twist distribution. The results also indicated that the performance effect of the winglet was not highly dependent on the twist of the tip of the winglet [95,96]. The authors found that, for a vertical winglet, a large transition radius between the main blade and the winglet hurt performance. They also found that sweeping the winglet back did not influence the mechanical power output [96]. Similar results were found in a study investing the effects of a winglet on a model wing in a wind tunnel [97]. An earlier study of winglets for sailplanes indicated that sweeping the winglet back has a similar effect as twisting the winglet [98,99].

Gaunaa and Johansen [100,101] performed an analytical vortex cylinder analysis of a wind turbine which showed that the increased power production of a winglet is due to the decrease in tip loss due to the winglet. In the same study, a FWLL (free-wake lifting line) method was developed using Rankine vortex-core filaments to model the wake. A CFD analysis (EllipSys3D) was used to verify the FWLL method [102]. The two methods compared to within 1% of coefficient of power. The circulation distribution of the blade was found using Nelder-Mead simplex optimization. The results showed a 2.5% increase in power output for a downwind winglet with height of 2% of the rotor radius [100].

A summary of previous studies on the design and performance results for winglet designs for wind turbines is shown in Table 6-1.

Table 6-1 Previous studies of winglets for wind turbines.

Year	Authors	Method		Winglet Height % of Rotor Radius	Predicted % increase in Power	Experimental % increase in power
1980	Gyatt and Lissaman	VL-FW	downwind	5%	7%	0%
1998	Imamura et al.	FWLL	downwind	10%	21%	--
2007	Johansen and Sørensen	NS-CFD	upwind	1.50%	0.6-1.4%	--
2008	Gaunaa and Johansen	FWLL	downwind	2%	2.50%	verified with CFD

6.2 Winglet Design for a Small-Scale Wind Turbine

6.2.1 Baseline Blade Description

The winglet designed in this research is a modification to a small-scale wind turbine blade designed at the University of Waterloo. The baseline planar blade was designed at the University of Waterloo using the inverse blade-element momentum theory (BEMT) design code PropID [103,104]. The blade was designed around the S835, S834, and S833 airfoils [105]. Details of the design process are given by Gertz [89–91], the results of which are summarized in Table 6-2 and Figure 6-4.

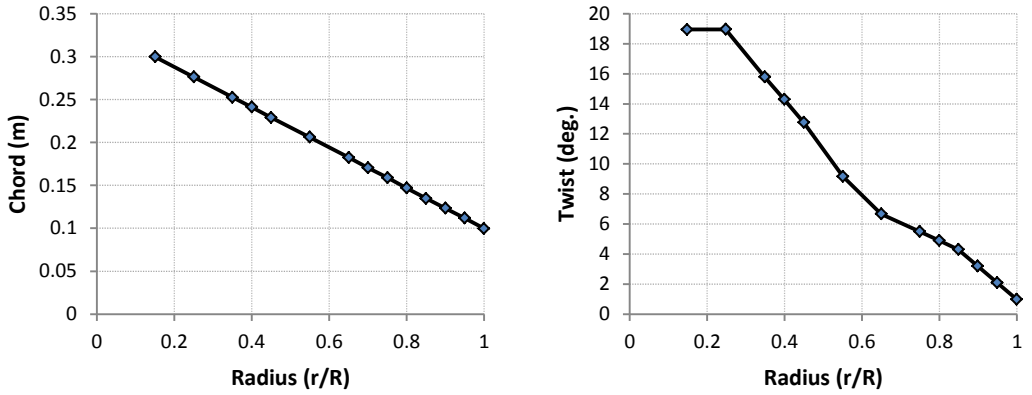

Figure 6-4 Planform definition of the baseline, planar blade [89].

Table 6-2 Baseline Blade Description.

Rated Power ~ 1.5 kW
1.6m radius rotor
Airfoil: S835 to 40% radius, S833 at 75% radius, S834 from 95% to the tip, with linear blends between the airfoil stations.
Chord and Twist: modification of optimum found using PropID [103,104]
Rotation rate: 200 rpm, constant

6.2.1.1 Airfoil Data for Baseline Blade

During the design analysis of the baseline blade, Gertz [89] used the S834 airfoil data along the entire blade span. The winglet design study of the present research used the airfoil distribution from the actual constructed blade; this distribution is summarized in Table 6-3.

Table 6-3 Baseline Blade Geometry and Airfoil Distribution.

r/R	c/R	Pitch (deg)	Alpha_zl (deg)	Airfoil #	Airfoil Data Description
0.15	0.1875	18.96	-0.925	1	S835 XFOIL
0.25	0.1728	18.96	-0.925	1	S835 XFOIL
0.35	0.1581	15.78	-0.925	1	S835 XFOIL
0.40	0.1508	14.27	-0.925	1	S835 XFOIL
0.45	0.1434	12.76	-1.00	4	S833 14.3%, S835 85.7%
0.55	0.1287	9.16	-1.40	5	S833 50%, S835 50%
0.65	0.1140	6.67	-1.30	6	S833 71.4%, S835 28.6%
0.75	0.0993	5.49	-1.20	2	S833 XFOIL
0.80	0.0919	4.89	-1.00	7	S834 25.0%, S835 75.0%
0.85	0.0846	4.29	-1.00	8	S833 50.0%, S835 50.0%
0.95	0.0699	2.07	-1.20	3	S834 XFOIL
1.00	0.0625	0.96	-1.20	3	S834 XFOIL

The S833, S834, and S835 airfoils were analyzed using XFOIL [88] for angles-of-attack between negative and positive stall. The XFOIL data was then extended to 90 degrees angle-of-attack using AirfoilPrep [86]. The blended airfoil data tables were created by applying the

blending routine in AirfoilPrep to the airfoil data using the ratios indicated in the airfoil data description in Table 6-3. The resulting airfoil data used for the winglet design analysis are plotted in Figure 6-5 through Figure 6-16.

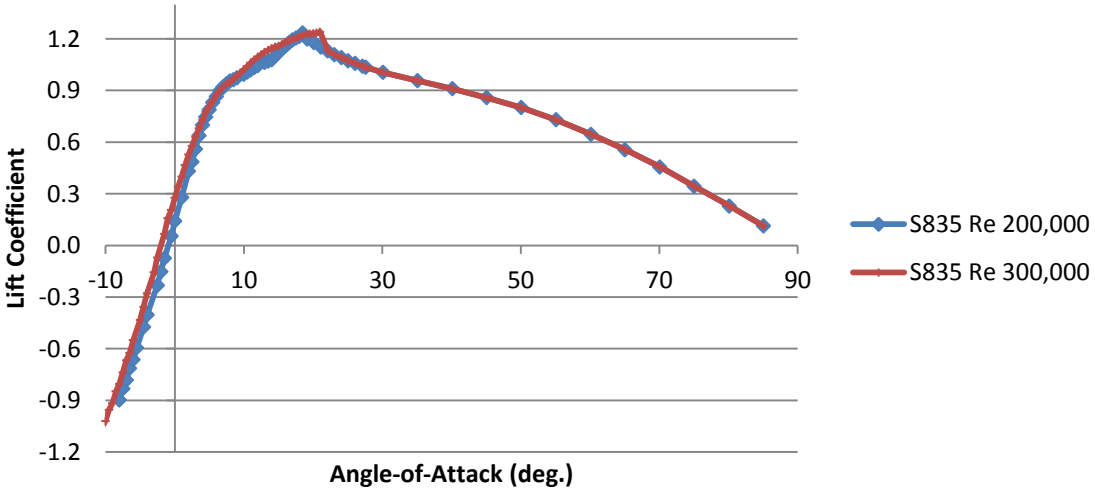

Figure 6-5 S835 airfoil data analyzed with XFOIL, lift coefficient.

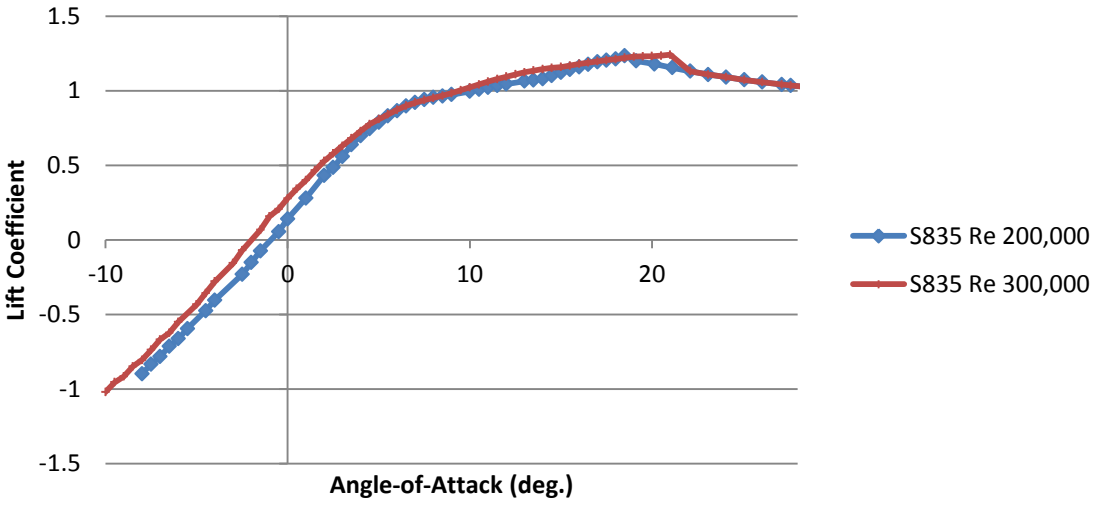

Figure 6-6 S835 airfoil data analyzed with XFOIL, lift coefficient.

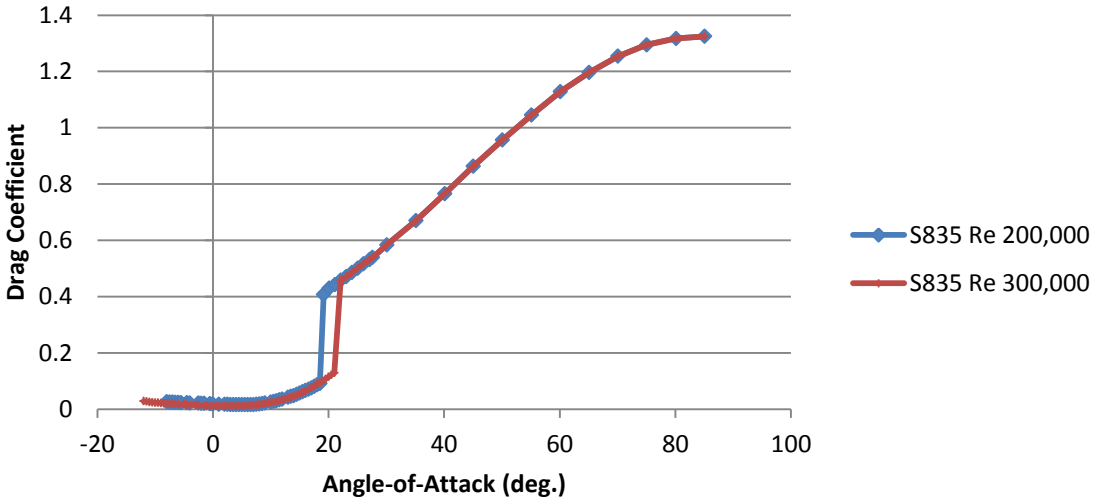

Figure 6-7 S835 airfoil data analyzed with XFOIL, drag coefficient.

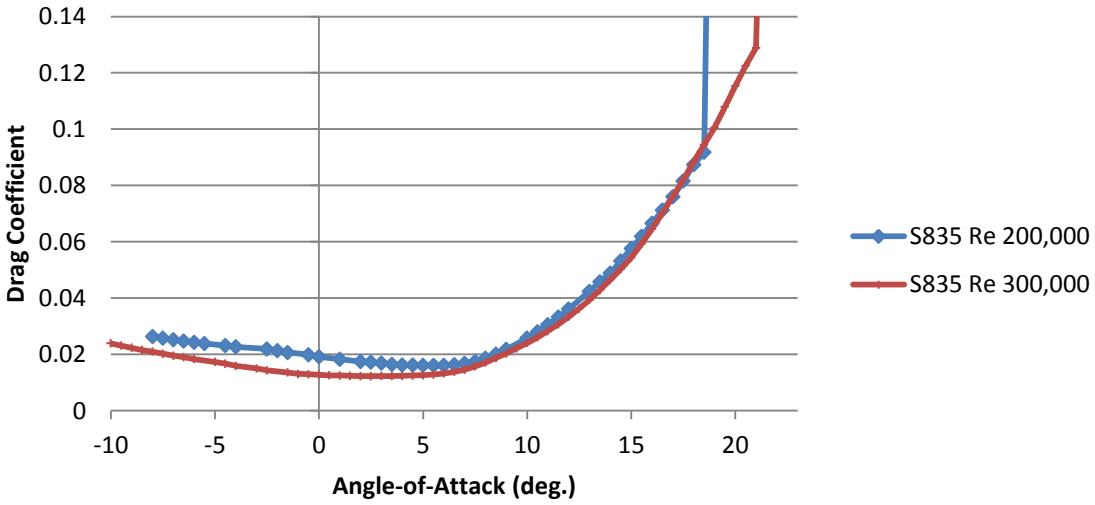

Figure 6-8 S835 airfoil data analyzed with XFOIL, drag coefficient.

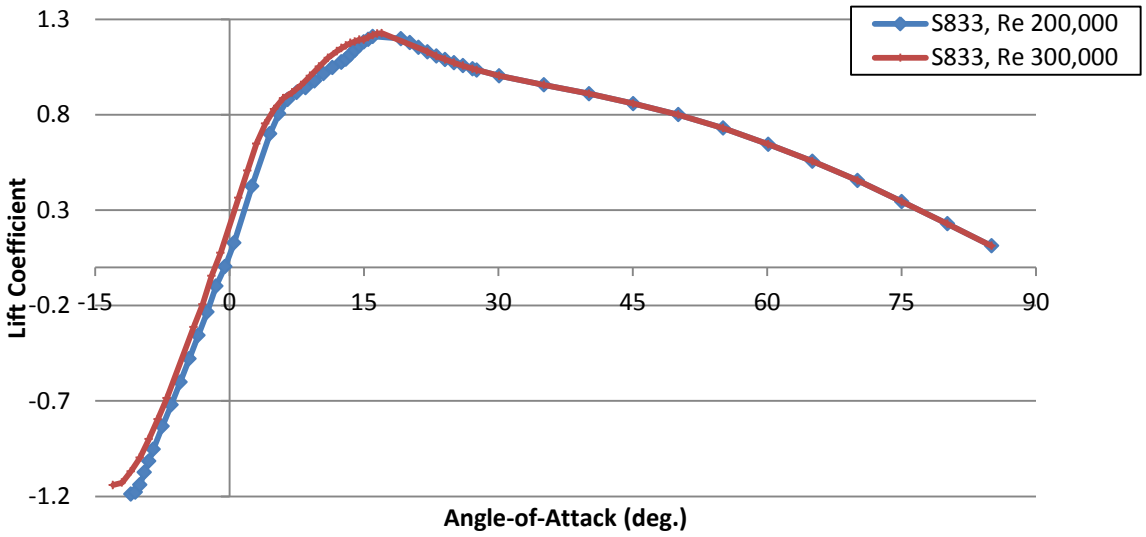

Figure 6-9 S833 airfoil data analyzed with XFOIL, lift coefficient.

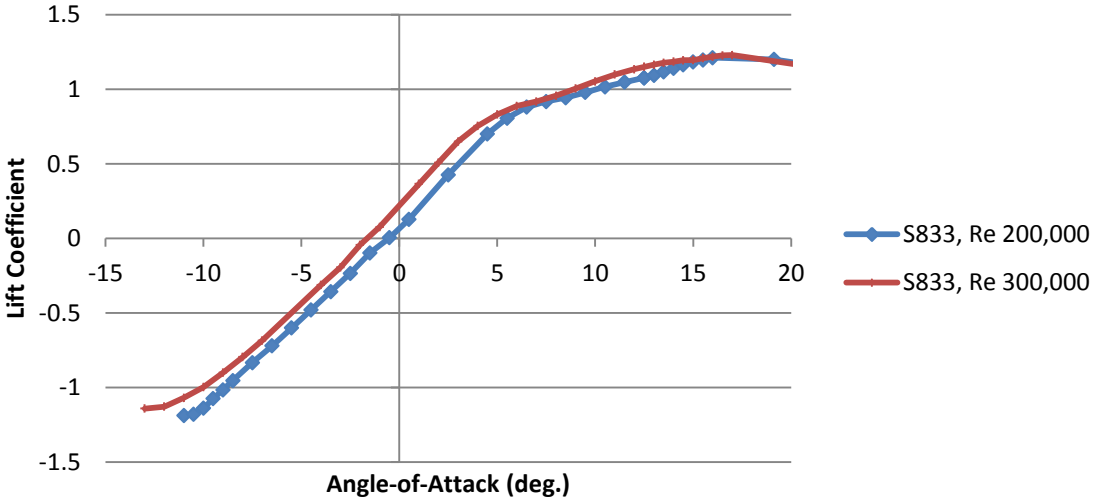

Figure 6-10 S833 airfoil data analyzed with XFOIL, lift coefficient.

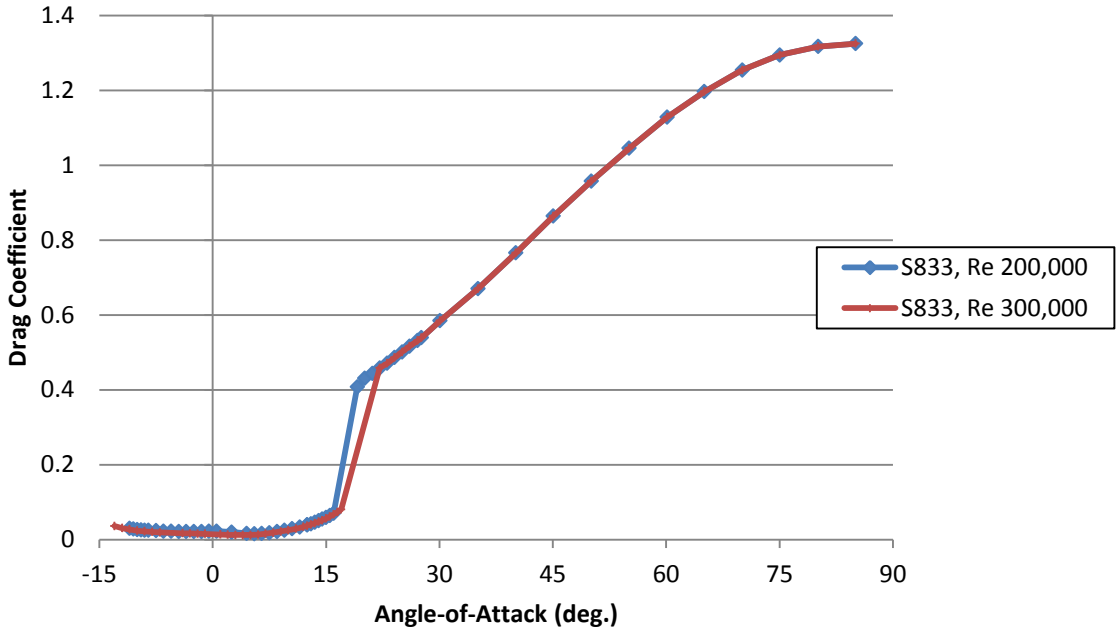

Figure 6-11 S833 airfoil data analyzed with XFOIL, drag coefficient.

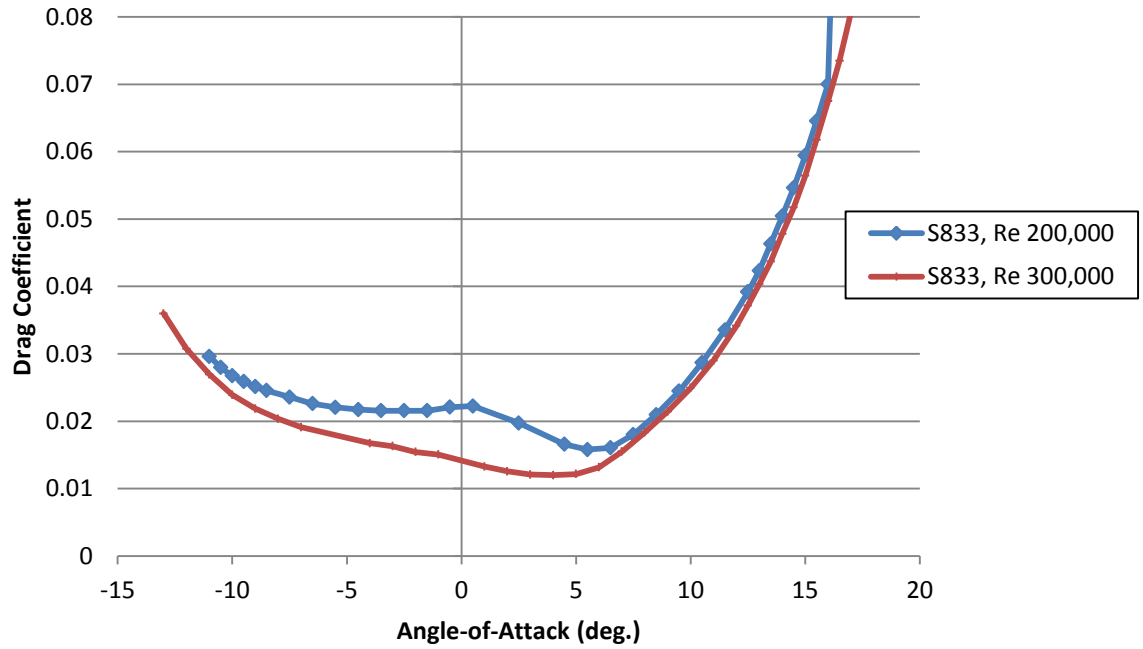

Figure 6-12 S833 airfoil data analyzed with XFOIL, drag coefficient.

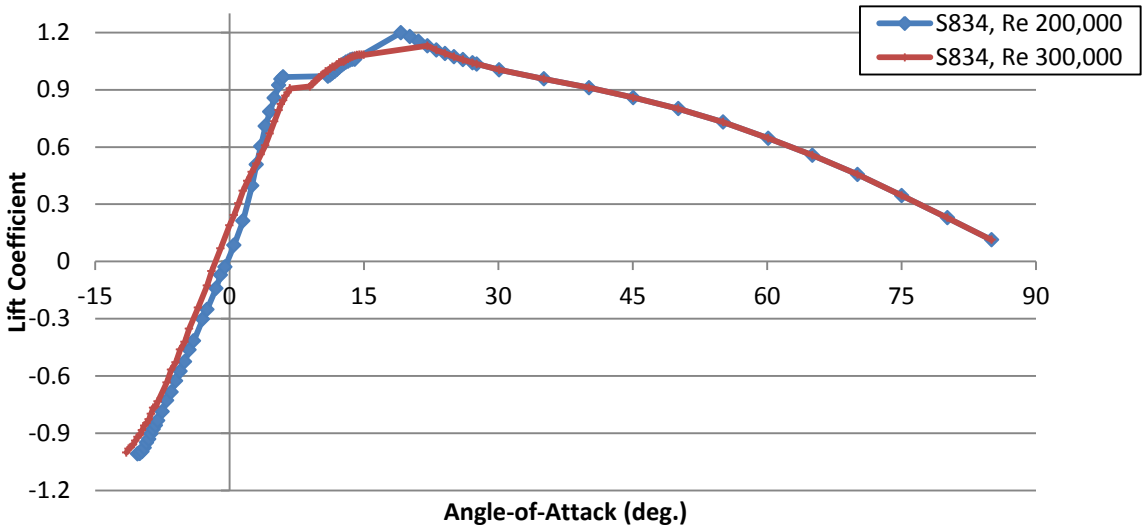

Figure 6-13 S834 airfoil data analyzed with XFOIL, lift coefficient.

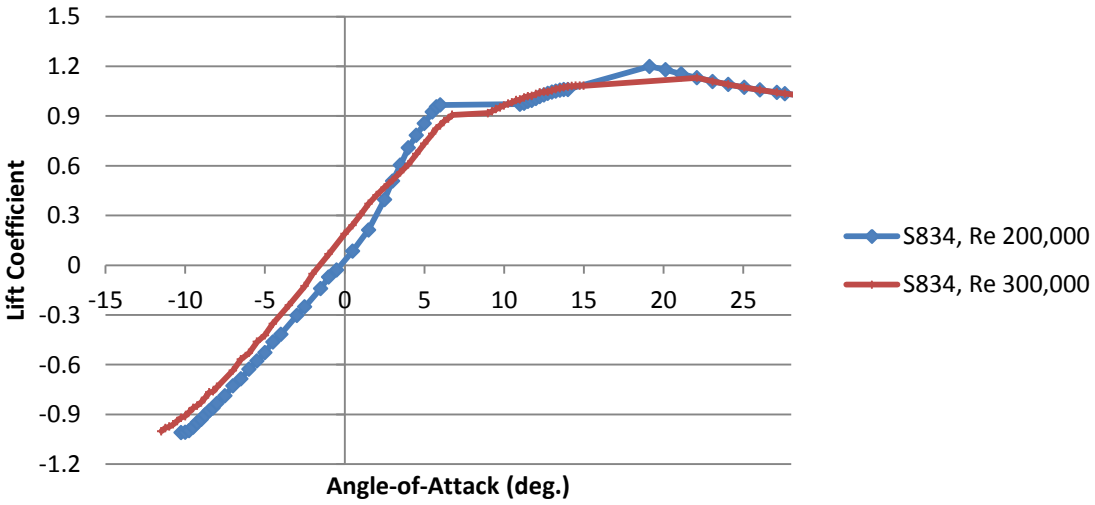

Figure 6-14 S834 airfoil data analyzed with XFOIL, lift coefficient.

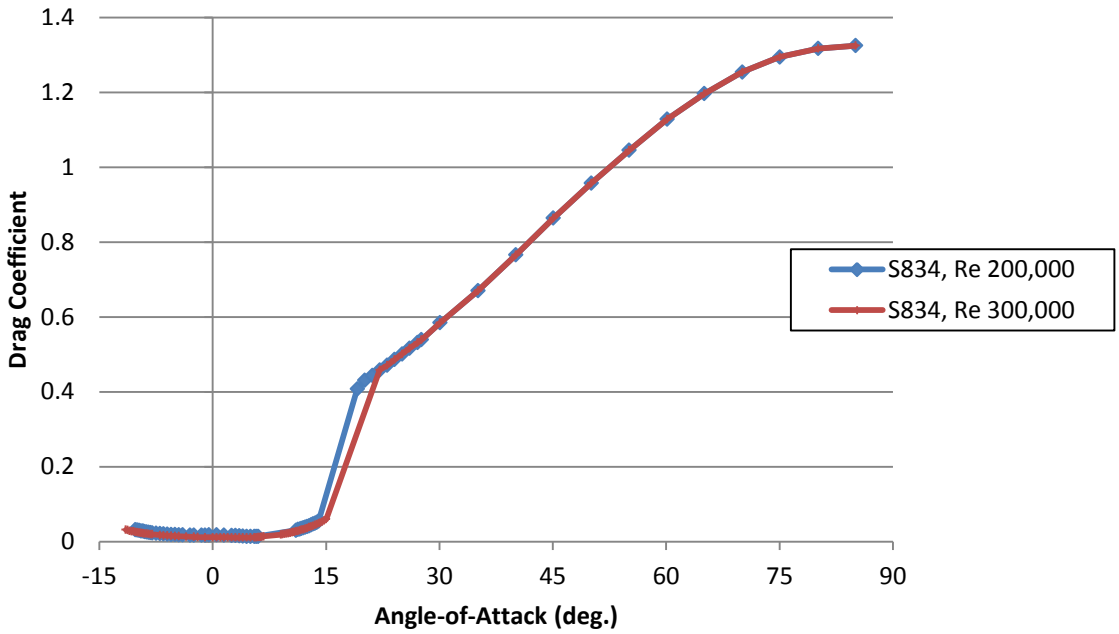

Figure 6-15 S834 airfoil data analyzed with XFOIL, drag coefficient.

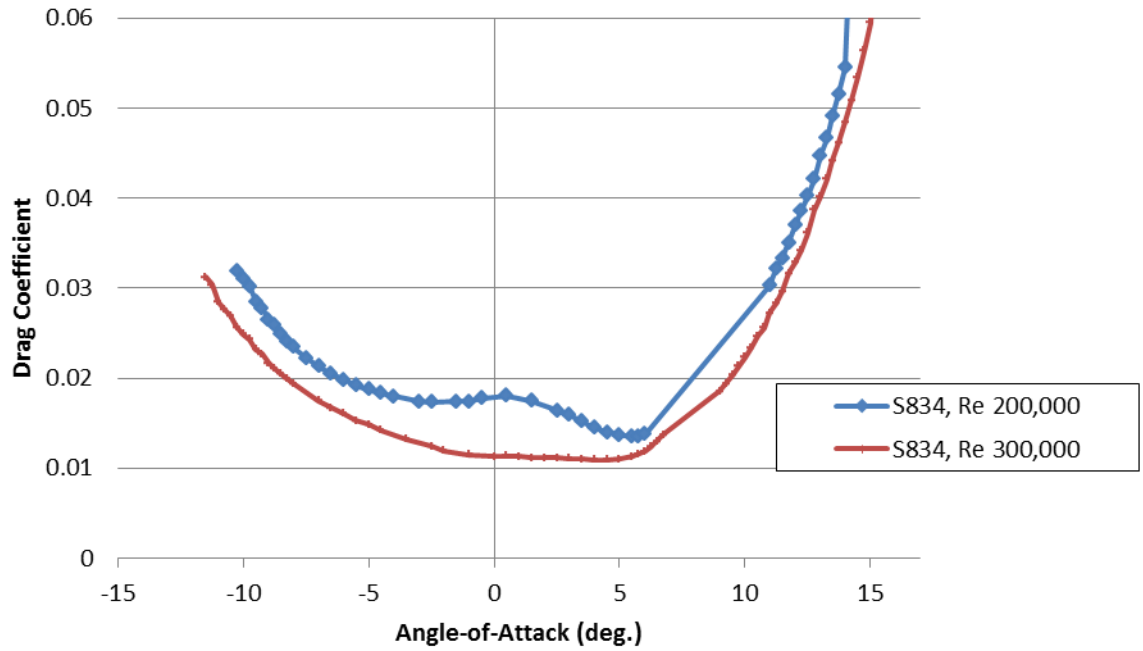

Figure 6-16 S834 airfoil data analyzed with XFOIL, drag coefficient.

6.2.1.2 Design Predictions Compared to Experimental Results for Baseline Blade

The predictions made by Gertz [89] during the baseline blade design process are compared to the experimental results in Figure 6-17 and Figure 6-18, which show the coefficient of power versus TSR and the power versus wind speed, respectively. These predictions were made using a blade element momentum theory (BEMT) analysis with the S834 airfoil data used to model the entire blade span [89]. Gertz reported an optimum predicted C_P for the baseline blade of 0.46 at a TSR of 5.3; the experimental results indicate a maximum C_P of 0.42 at 6.7 TSR. At a TSR of approximately 3, the experimental results indicate a slightly higher C_P than the predicted results from the BEMT code used in the baseline blade design process by Gertz. This increase in C_P accounts for the increase in power output shown in Figure 6-18 at a wind speed of 11 m/s [89]. Gertz found that the stall-delay model that was used for the BEMT analysis predictions could be adjusted in order to match the BEMT predictions with the experimental results. The experimental results for the baseline blade will be used for comparison of the performance gain due to the winglet; the "Predicted – Design" results from the BEMT analysis are shown for reference.

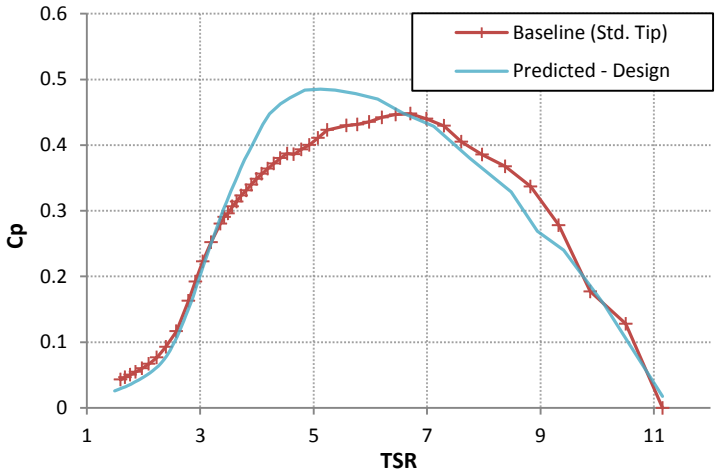

Figure 6-17 Coefficent of power vs. tip-speed ratio for the baseline blade with the standard blade tip, comparison of experimental results (Baseline) to the predictions made using blade-element momentum theory (Predicted) [89].

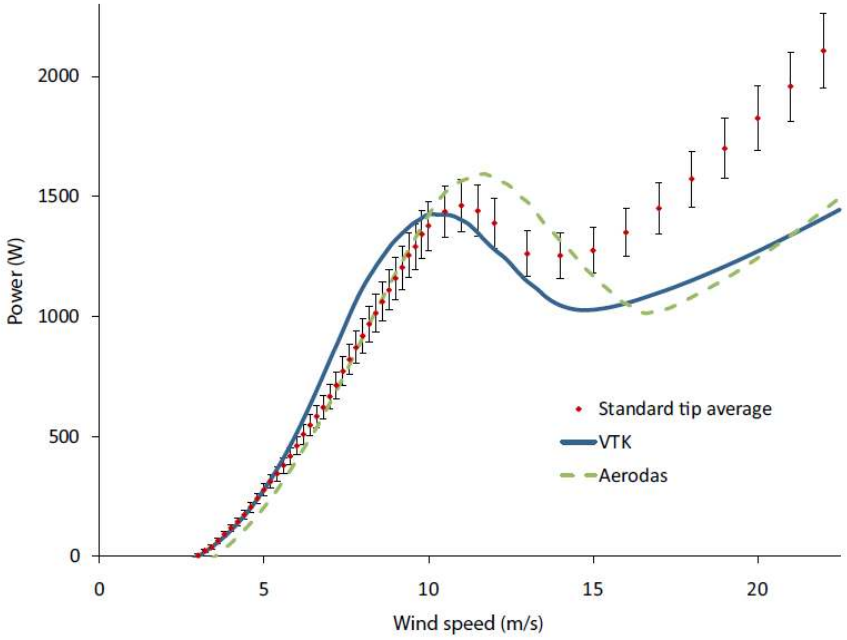

Figure 6-18 Power output of the baseline wind turbine (with a standard tip) from the experimental test (Standard tip average) compared to predictions from BEMT with VTK and Aerodas stall delay corrections [89].

6.2.1.3 Experimental Test Conditions

The wind tunnel used to take the experimental data had a range of mean flow speed between 3.7 m/s and 11 m/s. For test cases within this range, the rotational speed was held constant and the wind speed was changed, allowing both Reynolds number and tip-speed ratio to be matched to the design conditions. Analysis cases outside of this range were obtained by maintaining the mean flow speed at the high or low limit value and adjusting the rotational speed so that the tip-speed ratio was matched to the design conditions. This method resulted in the Reynolds number not being matched for the lowest and highest wind speed cases. The difference between the test and design conditions is shown in Figure 6-19, and is also listed in the Appendix. A detailed description of the wind tunnel and the test conditions is given by Gertz [89].

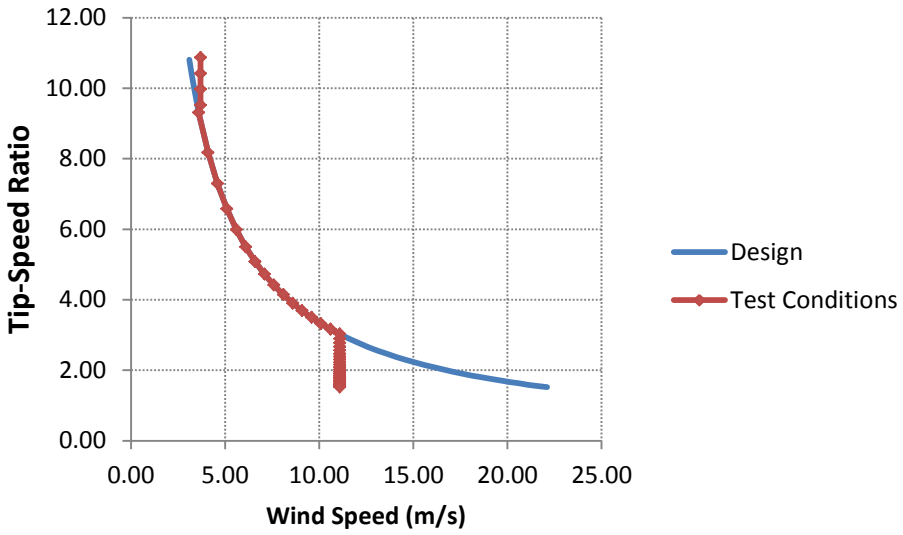

Figure 6-19 Design and wind tunnel test conditions for the wind turbine test at the University of Waterloo [89].

For most of the operating range of concern for design purposes (from 3.7 to 11.1m/s) the test conditions matched the desired design conditions. As the design wind speed moves further

outside of the range of matched conditions, there is more deviation in Reynolds number between the two. The maximum deviation is at the blade tip. The blade tip-speed was calculated for the entire range of design and test cases and is plotted in Figure 6-20.

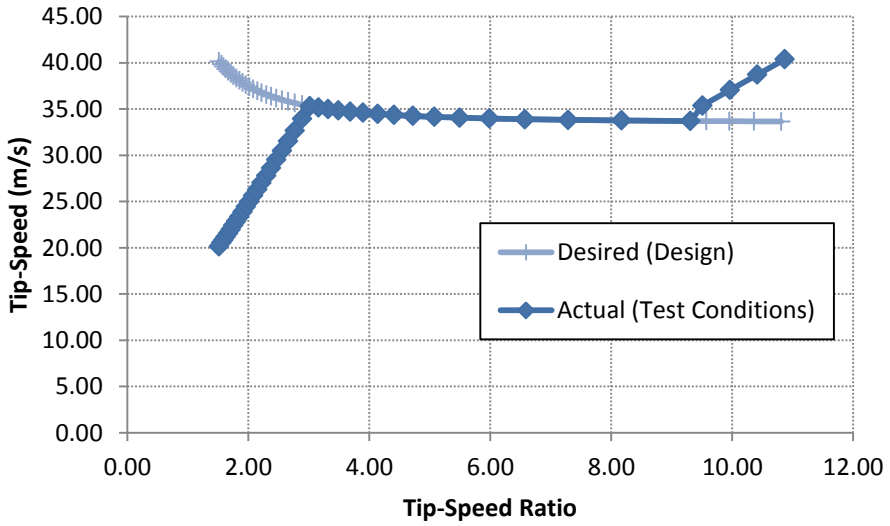

Figure 6-20 Tip-speed versus the tip-speed ratio of the design and test conditions of the small-scale wind turbine.

The deviation in Reynolds number at the blade tip between the test conditions and design conditions is shown in Figure 6-21. The maximum deviation at low wind speeds is 20%. The lower the Reynolds number, the stronger the influence of changes in Reynolds number on the airfoil lift, drag, and moment coefficients. Low Reynolds number conditions only occur at low wind speeds, and the portion of power generated at low wind speeds is small enough that these deviations in Reynolds number are not of a major concern for performance analysis. Design cases at higher wind speeds have higher Reynolds numbers, but at higher Reynolds numbers the airfoil forces and moments have a decreased dependence to changes in Reynolds number.

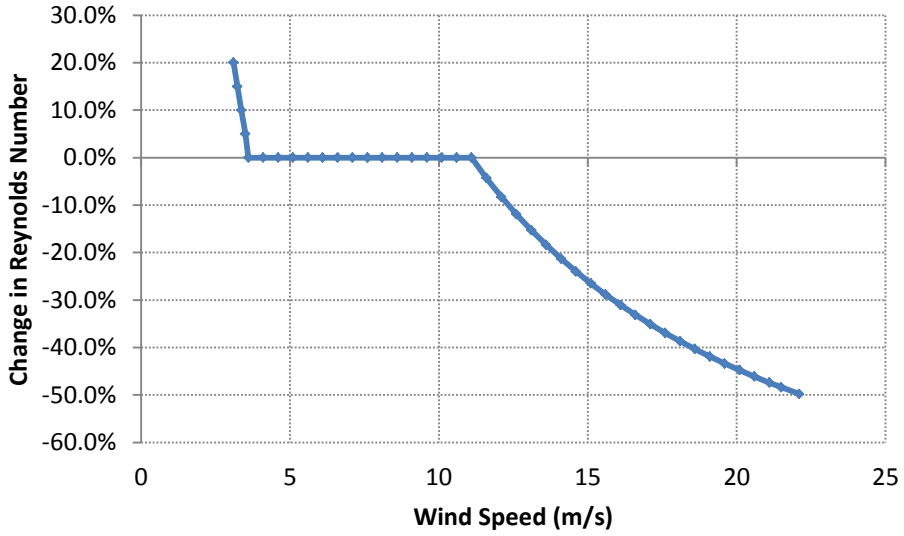

Figure 6-21 The deviation in the Reynolds number between the design and test conditions, computed at the blade tip.

In order to minimize the impact of these deviations in Reynolds number, the WindDVE analysis cases used for comparison with the experimental test results were performed at the test conditions, although results are plotted at the design condition wind speeds. This difference does not impact the initial winglet design study, since the design work was focused on the design TSR of 5.3, where the test and design conditions are equal.

6.2.2 Winglet Design

6.2.2.1 Winglet Airfoil

The PSU 94-097 airfoil was selected for the winglet, which is designed for sailplane winglet applications and applications with a similar Reynolds number range [106]. The Reynolds number for the winglet of the small-scale wind turbine ranges from 180,000 to 260,000, as shown in Figure 6-22, which shows Reynolds numbers at the 25% and 75% locations on the winglet height from the winglet root. The Reynolds number was found using the relative velocity

computed by the FW-DVE tool. The airfoil was only tested in a wind tunnel down to a Reynolds number of 240,000; therefore, airfoil data for lower Reynolds numbers was taken from predictions presented in reference [106]. The lift coefficient of the winglet varies from 0.28 to 1.21. At the design TSR of 5.3, the c_l has a range from 0.75 at 25% of the winglet load line to a c_l of 0.45 at 75% of the load line. This c_l range is below the design c_l range of the airfoil, which is from 0.5 to 1.0 in value. The theoretical and experimental characteristics of this airfoil at the lowest tested Reynolds number are shown in the left side of Figure 6-23, while the range of lift coefficient found by the FW-DVE tool are shown in the right side. The theoretical characteristics of the PSU-94-097 airfoil for a range of Reynolds numbers are shown in Figure 6-24.

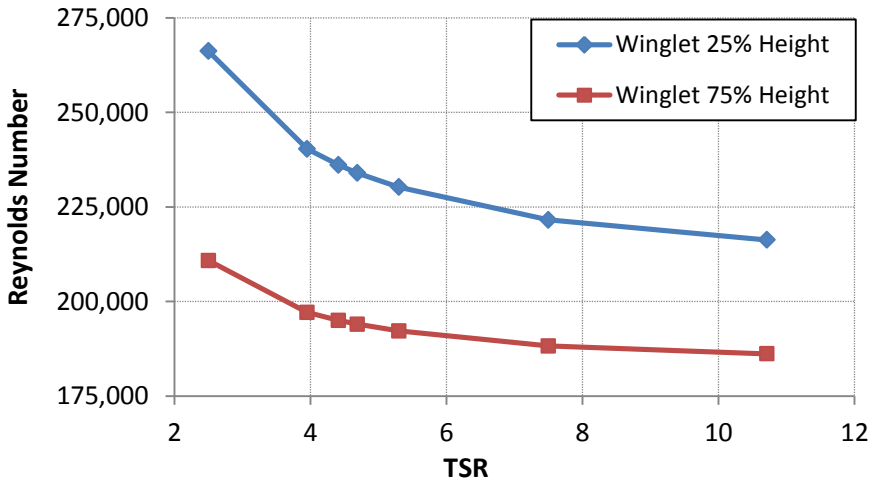

Figure 6-22 Reynolds number vs. TSR at the 25% and 75% of winglet height locations from the winglet root.

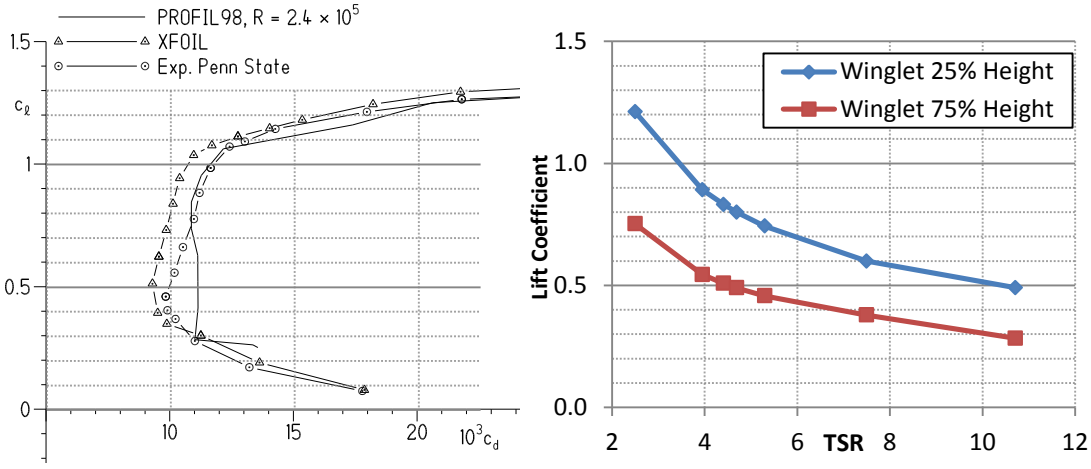

Figure 6-23 Theoretical characteristics of the PSU94-097 airfoil (right), and lift coefficient values at the 25% and 75% winglet height locations [106].

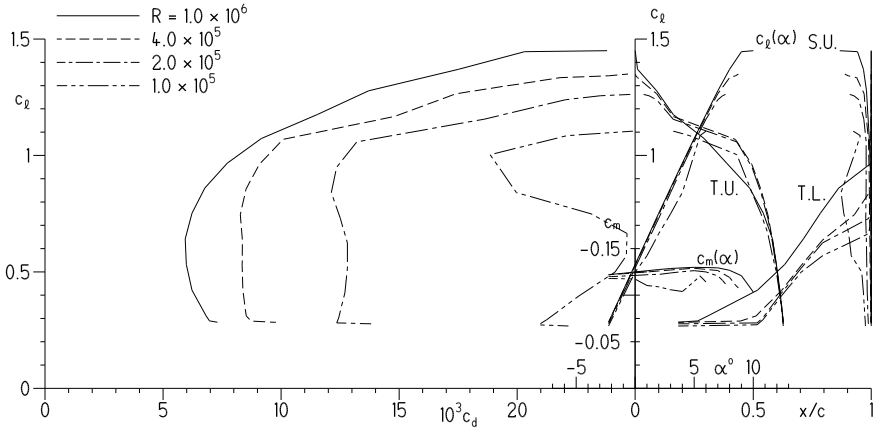

Figure 6-24 Theoretical characteristics of the PSU94-097 airfoil [106].

The zero lift angle-of-attack of the experimental airfoil data is between approximately -4.7 and -4.8 degrees, depending on the Reynolds number. These results show a trend of the zero-lift angle of attack decreasing slightly as Reynolds number decreases, so a value of -5 deg. was used for the initial winglet analysis. The multi-point design study presented later in this chapter used a zero-lift angle-of-attack of -4.8 degrees for the winglet airfoil.

The chord length of the winglet root and tip was initially selected in order to keep the airfoil in the laminar drag operation regime for as long as possible over the operating range of the

wind turbine, while ensuring that the winglet does not stall during normal operation [98,99]. At a Reynolds number of 100,000, there is a drastic change in the drag coefficient in the middle of the design c_l range due to the behavior of the laminar separation bubble. The winglet tip chord was lengthened in order to stay well above this range of Reynolds number to avoid the variability in drag. The penalty for lengthening the tip chord length is increased drag due to both the increase in wetted area and increased drag coefficient of the winglet tip region when the tip-speed ratio is greater than 7, as shown in Figure 6-23. It would have been interesting to also test a winglet with the same toe and twist angles, but a shorter tip chord length; however, only one model could be tested and so the more conservative approach was taken regarding the tip chord length.

6.2.2.2 Winglet Planform Design

The main design parameters of the winglet planform geometry are the cant angle, chord distribution, sweep angle, toe angle, and twist (which is defined by the tip angle), which are shown in Figure 6-25 for the conventions for fixed-wing aircraft. The winglet twist and toe angles were found by analyzing a range of possible winglet toe and tip angle combinations. For a winglet on the suction side (upper surface) of a wind turbine blade, a positive toe angle causes the winglet root to be pitched out in the radial direction, away from the blade. The tip angle is defined in the same way, with both angles being referenced to the un-pitched plane of the winglet. Winglet twist is defined as the difference between the winglet tip angle and root angle, such that positive twist along the winglet span will increase the angle-of-attack of the winglet tip.

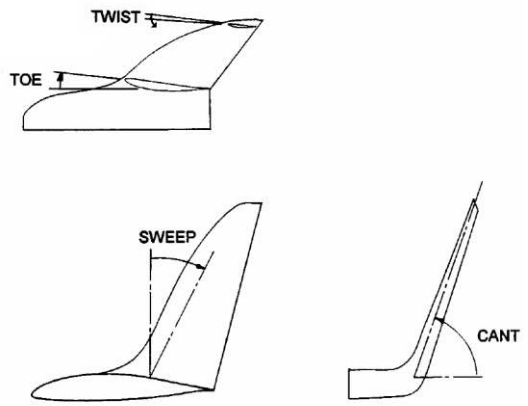

Figure 6-25 Winglet angle definitions [107].

The winglet cant angle was set at 90 degrees from the plane of the main blade in order to keep the maximum radius the same as the baseline blade. The winglet analysis in WindDVE used a cant angle slightly less than vertical, as 90.0 degrees of cant angle showed some numerical instability issues. The sweep angle was set as to maintain a straight trailing edge with the main blade, which simplified the manufacturing process.

The interference effects due to the juncture between the winglet and the main blade were ignored throughout the design process. Interference effects are challenging to model due to the interaction of the boundary layers and pressure distributions of multiple lifting surfaces. The interference of two lifting surfaces can produce drag (known as "interference drag" in aircraft performance models), but can cause a drag reduction (if designed correctly) due to favorable interactions between the pressure distribution of the winglet and the boundary layer on the tip region of the main blade.

The twist and toe angles were selected by analyzing the predicted power output from the FW-DVE code for a range of combinations of angles. For this study, the lifting surface and wake were modeled with the parameters presented in Table 6-4. Figure 6-26 shows the combination of winglet toe and twist angles that were explored.

Table 6-4 Lifting surface and wake modeling parameters used for the winglet design.

Main blade: 12 spanwise elements, cosine distribution, 1 lifting line
Winglet: 2 spanwise elements, linear distribution, 1 lifting line
Steady equation system solution and steady relaxation
Total wake length of 11 revolutions divided into three time intervals:
1.) 45 timesteps at 10 steps/rev.
2.) Transition region of 30 timesteps
3.) 90 timesteps at 20 steps/rev.

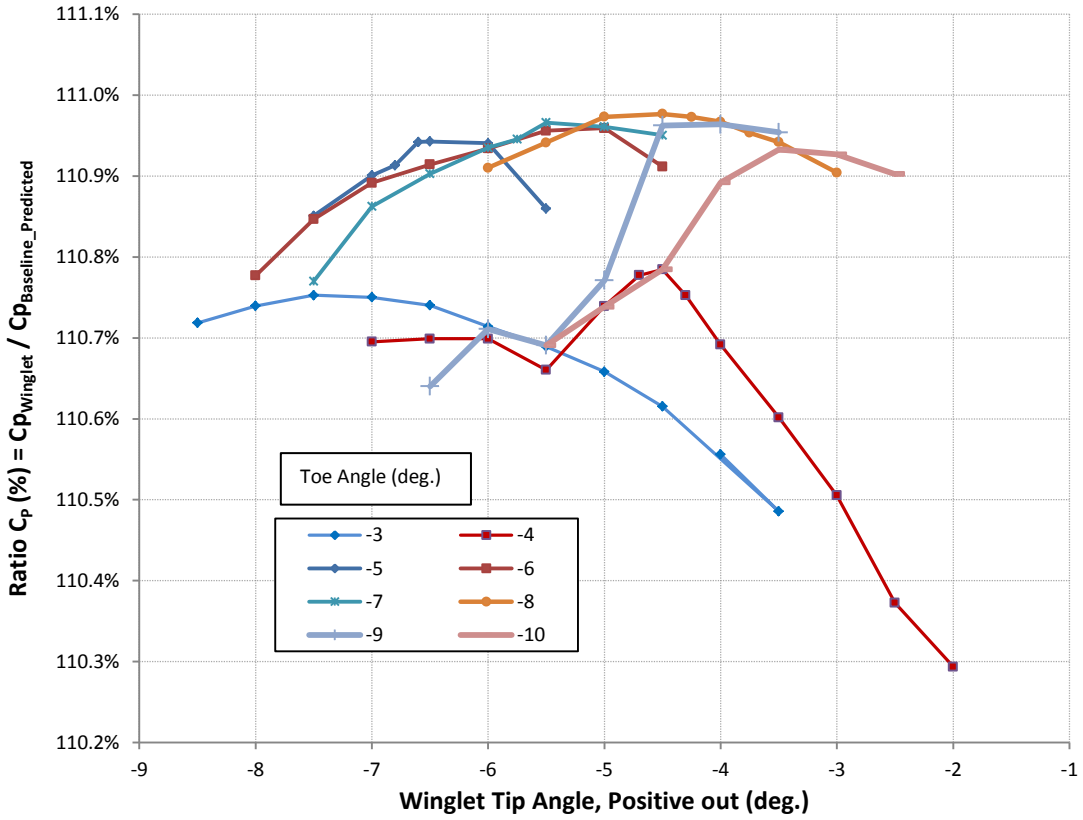

Figure 6-26 Effect of winglet toe and tip angles on the change in power due to winglet. The tip and toe angles are defined such that positive deflection angles the winglet out in the radial direction. $\text{Ratio}C_P(\%) = Cp_{Winglet} / Cp_{Baseline\_Predicted}$. Angles relative to zero lift line.

The optimum combination of winglet angles is at a toe angle of -8 deg. and a tip angle of -4.5 deg., giving a predicted increase in power output of 10.96% of the blade with winglet compared to the planar baseline blade. This combination results in a twist along the winglet of -3.5 degrees. These angles are used directly in the FW-DVE code, which does not account for airfoil camber effects. The zero-lift angle of attack of the airfoil must be added to the toe and tip angles of the winglet in order to find the final winglet angle geometry. As discussed earlier, a zero-lift angle of attack of -5.0 degrees was used for this design, resulting in the winglet angles used for manufacturing of -3 deg. toe angle and +0.5 deg. tip angle. The final winglet design is described in Table 6-5.

Table 6-5 Winglet Design Criteria and Planform.

Design for 1.6m radius rotor
Upper Surface winglet (Downwind)
Design TSR 5.3
Height 8% of rotor radius (0.128 m)
No sweep along winglet trailing edge
Airfoil: PSU 94-097, Zero Lift at -4.8 deg. AOA
Root: Chord: 0.095 m, Toe angle: -3 deg., relative to chord line
Tip: Chord: 0.075m, Tip angle: +0.5 deg., relative to chord line
Twist: -3.5 deg. (positive twist increases angle-of-attack of winglet tip)

6.2.3 Winglet Performance Results

The winglet design was shared with the wind turbine research group at the University of Waterloo which designed the baseline blade. As part of a thesis research project, the resulting winglet was fabricated and tested at the University of Waterloo small wind turbine test facility. The baseline blade is shown mounted in this facility in Figure 6-28. A description of the test facility, winglet and wind turbine construction, the testing method, and experimental results are

described in Ref. [89]. Figure 6-28 shows the fabricated winglet design that was fabricated and tested [89].

The turbulence intensity measured through the range of testing speeds was from 5.9% to 6.2%. In comparison, the turbulence intensity of atmospheric winds is on the order of 10% [89].

Figure 6-27 Baseline wind turbine blades mounted in the University of Waterloo wind turbine testing facility [89].

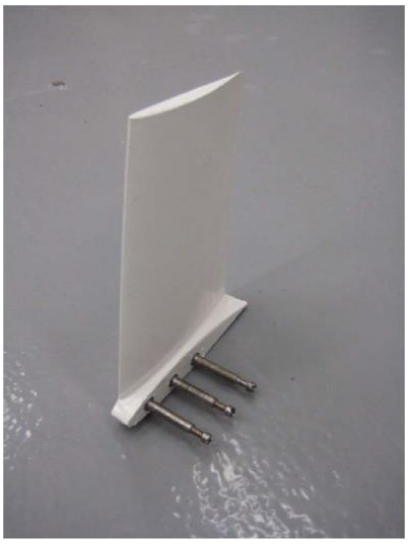

Figure 6-28 The fabricated winglet [89].

A comparison of the coefficient of power between experimental test and analysis predictions made with the version of WindDVE used for the initial winglet design process is given in Figure 6-29. During the initial design prcoess, the influence of profile drag was only included on the winglet The effect of stall was not included, but is investigated in the next section.

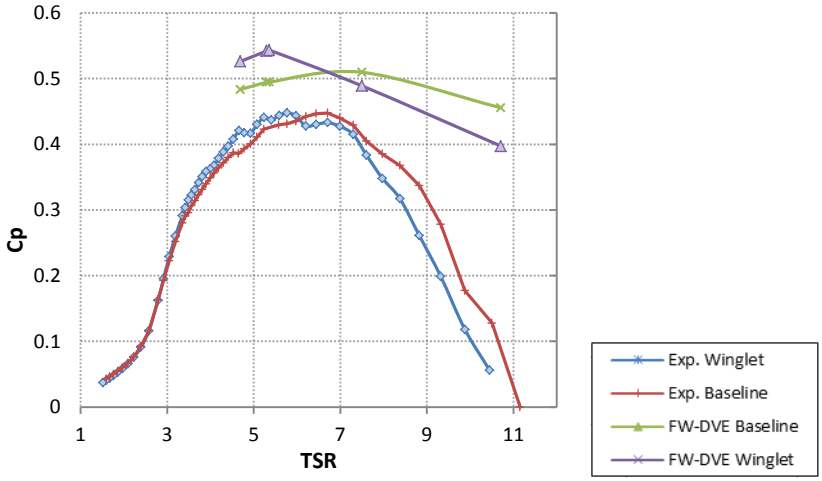

Figure 6-29 Effect on winglet coefficient of power for the initial winglet design analysis. Only the profile drag of the winglet is included in the FW-DVE results and the influence of stall was not included. Experimental ("Exp.") data from Ref. [89].

Figure 6-30 shows the change of the power coefficient due to the winglet for the experimental and FW-DVE predictions. The error range of the experimental test is also shown in this figure; the estimated error was taken from Ref. [91]. Almost the entire range of FW-DVE predictions of the change in power coefficient are within the error range of the experimental data. The correlation at a TSR of 4.69 and at 7.5 is very good. The model appears to over-predict the power coefficient at a TSR of 5.3, which is the TSR that the baseline wind turbine was designed for.

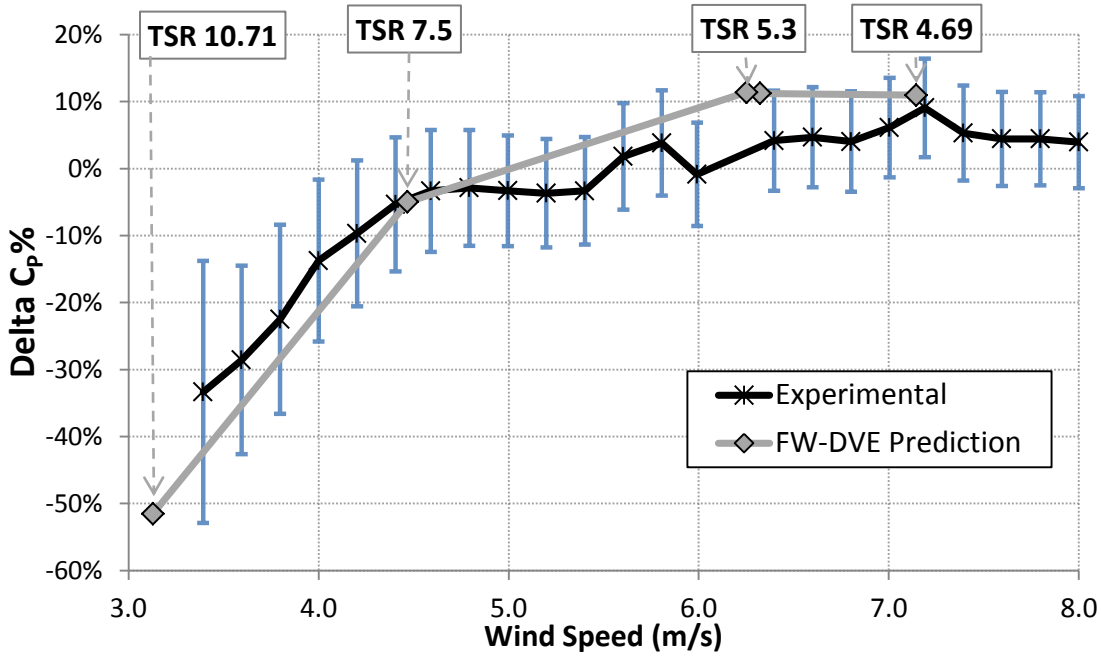

Figure 6-30 Coefficient of power difference between winglet and baseline rotor. $Delta\_Cp\ (\%) = (Cp_{Winglet} - Cp_{Baseline})/Cp_{Baseline\_Experimental}$. Experimental data and error bars from Ref. [89].

It should be noted that this winglet design is predicted to hurt performance at low wind speeds and help it at wind speeds equal to or above the wind speed for the design tip speed ratio of 5.3. A future design might be able to minimize the decrease in power at low speeds through a multi-point design process incoporating a low wind speed design point.

The local lift coefficient and circulation were found using the FVM analysis code, which are plotted along the blade span in Figure 6-31. Values below the design tip-speed ratio of 5.3 are not shown due to the lack of stall modeling in the FVM code. Below this tip-speed ratio, the lift coefficient along the blade begins to exceed the maximum lift coefficient of the airfoil (which is between 1.0 and 1.2 on the main blade). At a TSR of 5.3, the blade can be seen approaching the maximum lift coefficient at a radial station of 0.4 meters.

The circulation at the root of the winglet is shown to be much larger than that of the baseline blade. At the design TSR of 5.3, the circulation stays appromately constant along the

tip-region of the main blade. The value of circulation at the root of the winglet stays approximately constant for all of the tip-speed ratios. At low wind speed (TSR of 10.71), the constant value of circulation at the root of the winglet causes a "spike," which causes increased induced power losses for this case. The increased induced power losses could account for part of the decreased power output of the rotor with the winglet at low wind speed. The decreased power output at low wind speed could also be caused by increased profile drag in the tip region of the blade due to the increased lift coefficient there. For example, at a tip-speed ratio of 7.5, the tip lift coefficient increases from 0.4 to 0.6. For the S834 airfoil operating in rough conditions (transition fixed), this delta in c_l would result in a 10% increase in profile drag. For clean conditions, the predicted airfoil polar of the S834 indicates that the profile drag would not change significantly in this range of lift coefficient. The wind turbine test most likely falls somewhere between rough and clean airfoil conditions due to the turbulence intensity of the testing facility.

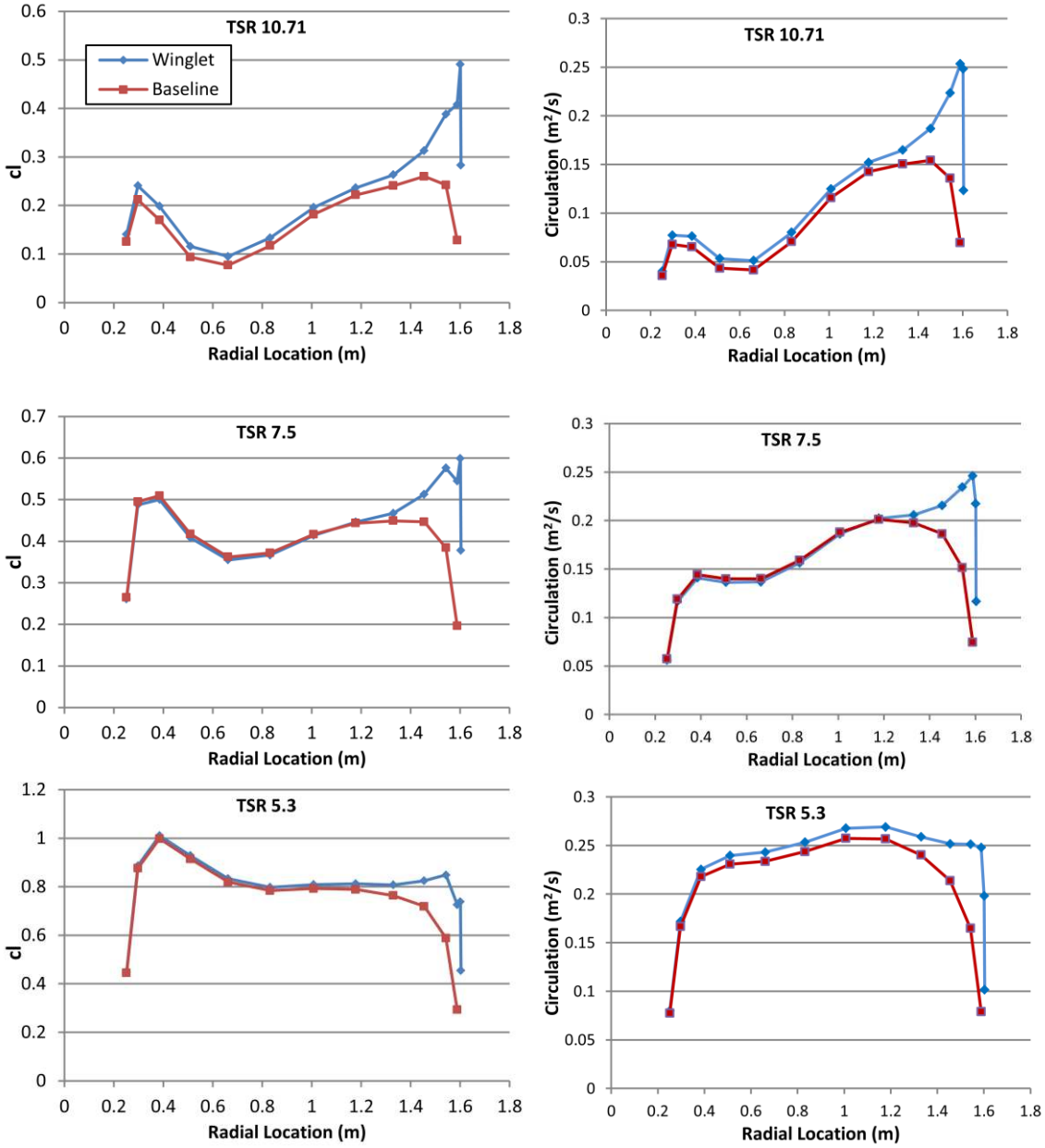

Figure 6-31 Results of winglet influence for low wind speed (TSR 10.7), through design wind speed (TSR 5.3) on lift coefficient (left) and circulation (right); results from the FVM analysis.

6.2.4 Power Predictions with Stall Modeling

The stall model presented in Chapter 3 was applied to the small-scale wind turbine in order to analyze the full range of wind speeds. The lifting surface and wake modeling parameters

for the stall modeling analysis are presented in Table 6-6. These parameters are similar to those used in the winglet design study, except that a shorter wake length was used and more spanwise panels were applied to the lifting surface. The stall model has shown increased sensitive to the number of spanwise panels, so more were used than in the design study. A shorter wake length was used to save computation time and because the influence on the predicted power relative to the experimental results was small for the higher wind speeds of concern for the stall model.

Table 6-6 Lifting surface and wake modeling parameters used for the small-scale wind turbine analysis with stall model.

Main blade: 18 spanwise elements, grid spacing factor 0.5, 1 lifting line
Winglet: 3 spanwise elements, linear distribution, 1 lifting line
Steady equation system solution and steady relaxation
Wake modeled with 2.7 revolutions over three time intervals:
1.) 15 timesteps at 10 steps/rev.
2.) Transition region of 10 timesteps
3.) 10 timesteps at 20 steps/rev.

The predicted power output is shown in Figure 6-32 for the experimental test as well as the analysis results from the FW-DVE method with and without the stall model. The influence of profile drag is included along the entire blade and winglet. The "Experimental" power curves are from the wind tunnel test at the University of Waterloo [89].

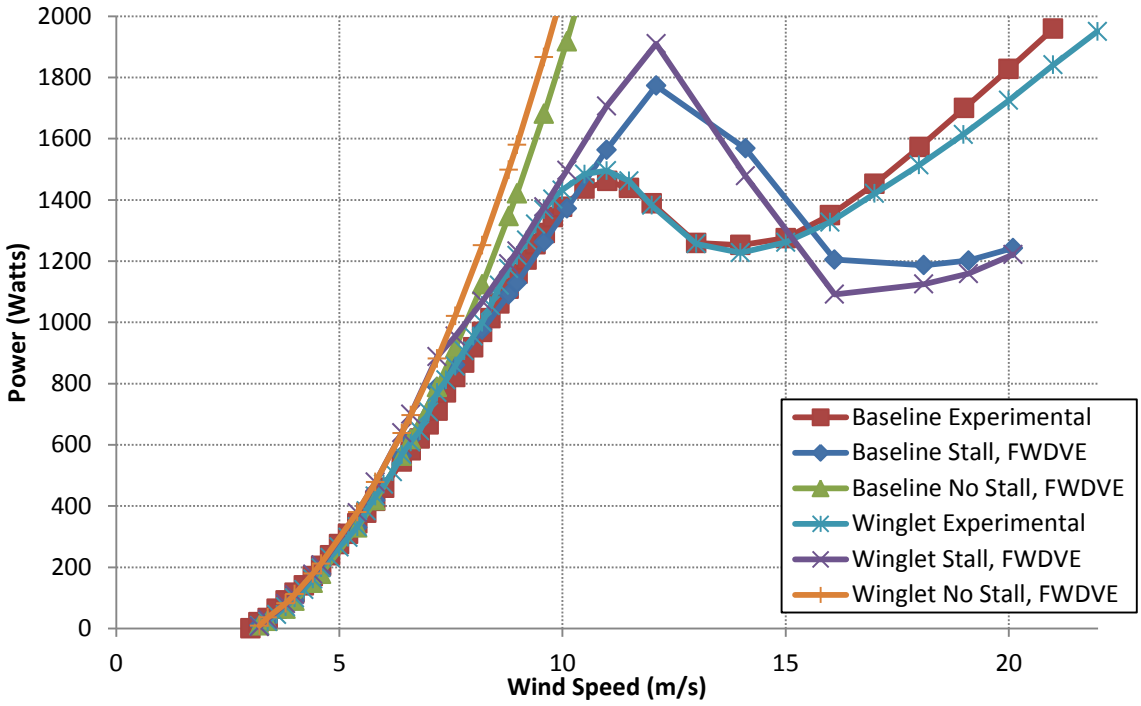

Figure 6-32 Power output of the baseline wind turbine (with a standard tip) and the wind turbine with winglet. Comparison between experimental results and predictions made using the free-wake distributed vorticity element (FWDVE) method with and without the stall model. Experimental results from Reference [89].

The FWDVE results are shown with and without the stall model. The specific models used from Table 3-1 are S03 (stall model) and S02 (without stall model). The operational region of interest for the winglet design is at the design tip-speed ratio of 5.3, which is an operating point where stall has a minimal impact. The initial winglet design study was only concerned with maximizing the power output below the wind speed for rated power, and so the stall model was not applied to the design analysis cases.

One concern with the addition of a winglet was that the rotor loads at high wind speeds would be increased. Since this is a stall regulated wind turbine, the stall model was required to predict the rotor loads for high wind speeds. Both the FWDVE predictions and experimental results indicate that at high wind speeds, the winglet slightly decreases power output. The FWDVE predictions with the stall model over predict the peak power output for both the baseline

and winglet cases; this error is most likely due to limitations in predicting the airfoil data for the baseline blade.

The winglet design was optimized for a TSR of 5.3 (wind speed of 6.32 m/s), corresponding to the TSR for maximum Cp of the baseline blade. This design increases Cp by about 10% at the design TSR and by a similar amount at wind speeds above the design wind speed. The difference in power output with and without the winglet is plotted in Figure 6-33 for both the FVM model predictions and the experimental results. The experimental results indicate that at wind speeds below 5 m/s, the winglet decreases performance. This performance decrease would hurt annual energy output in areas with low wind speeds. The design could be changed to increase performance at lower wind speeds, although the increase in power output at the design wind speed will not be as large as for the current design.

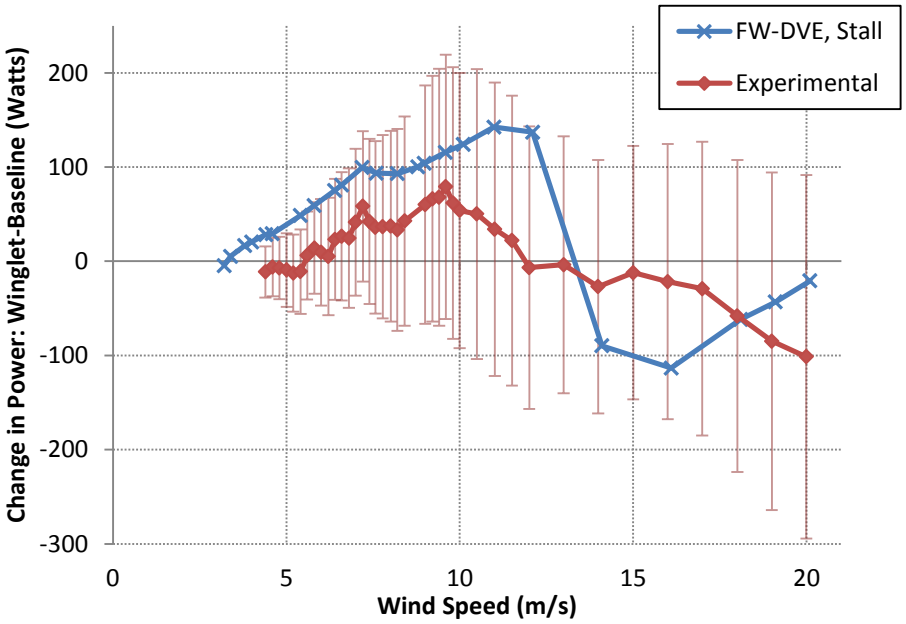

Figure 6-33 Difference in power between the baseline blade and the winglet blade. $DeltaPower = P_{Winglet} - P_{Baseline}$ for the respective experimental and FVM results. Experimental data and error bars from Ref. [89].

6.2.5 Summary of Initial Winglet Design

A design of a winglet for a small wind turbine was created using the FW-DVE vortex modeling code. The winglet was built and tested in a wind turbine testing facility at the University of Waterloo. The performance of the wind turbine with winglet was close to the predictions of the FW-DVE analysis code at the design tip-speed ratio and fell within the error bars of the experimental data; however, the performance increase due to the winglet did not fall over as broad of a range of wind speeds as was predicted. This data will be used to further develop the FW-DVE program and to improve future winglet designs for wind turbines.

6.3 Structural Considerations

The structural effect of the winglet was estimated by comparing the out-of-plane blade-root bending moment (BMOP_Root) of the baseline and winglet blade designs. Although a blade structural design ultimately depends on many possible load cases and combinations, the out-of-plane blade-root bending moment can give an estimate of the blade structural weight.

The power output and bending moment were estimated for the winglet and for scaled versions of the baseline blade, the results of which are shown in Figure 6-34. Two scaled baseline blades were analyzed: one scaled to match the increase in power due to the winglet at the design TSR (+5.2% radius) and the other scaled by the winglet height (+8% radius). For both scaled blades, the entire blade (including chord length) was scaled and the rotation rate was decreased to maintain the same tip-speed ratio as the unmodified baseline blade. The Reynolds number of the scaled blades also increased proportional to the increased rotor radius, but this increase is assumed to be negligible, allowing the same coefficient of power to be used for the scaled blades as the unmodified baseline blade. The power output of the scaled blades increased

by the square of the rotor radius scaling factor and the bending moment increased by the cube of the scaling factor.

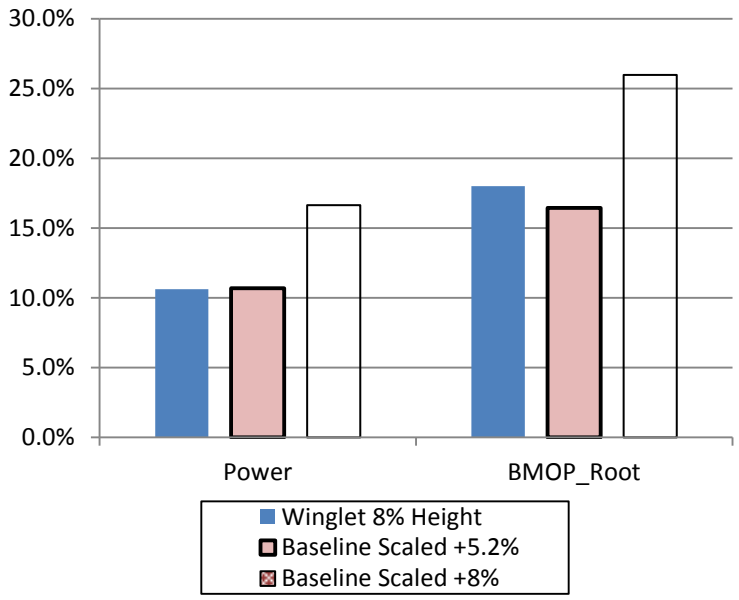

Figure 6-34 Power and BMOP_Root at TSR 5.3 (wind speed 6.3 m/s) for the winglet and the baseline, planar blade scaled to give an equivalent increase in power (+5.2%) and scaled by the winglet height (+8%).

For the initial winglet design with a height of 8% of the radius of the small scale wind turbine, the power increased by 10.6% relative to the planar baseline blade while the bending moment (BMOP_Root) increased by 18% at the design TSR of 5.3. The winglet produces about 8.5% higher bending moment for the same power increase as the power-scaled baseline rotor at 5.3 TSR. The blade scaled by the winglet height (+8% radius) shows a much larger increase in rotor power, but the bending moment increases significantly as well.

It is helpful to look at the spanwise distribution of differential power coefficient and bending moment in order to understand the difference between the winglet blade and the baseline. Figure 6-35 shows the incremental power coefficient per unit orthogonal length as a function of the orthogonal length along the blade for the baseline blade, winglet blade, and the baseline blade

scaled by the winglet height (+8%). The blade orthogonal location (s_0/R) and radial location (r/R) are the same as for a conventional blade; the orthogonal location is used for the blade with a winglet. The total rotor coefficient of power is found by integrating the incremental power coefficient along the blade orthogonal length and multiplying by the number of blades. The blade with a winglet actually produces negative power on the winglet, but increased power along the main blade.

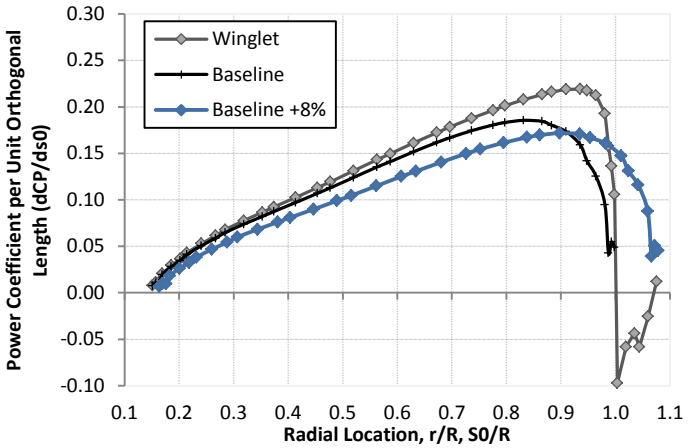

Figure 6-35 Incremental power coefficient per unit orthogonal length at TSR of 5.3.

Figure 6-36 shows the incremental BMOP_Root per unit orthogonal length, which when integrated gives the total out-of-plane blade root bending moment shown in Figure 6-34. The winglet itself adds little to the BMOP_Root; however, its effect on the main blade causes an overall increase in BMOP_Root. The spike in incremental BMOP_Root results in the increased BMOP_Root of the winglet relative to the scaled baseline blade.

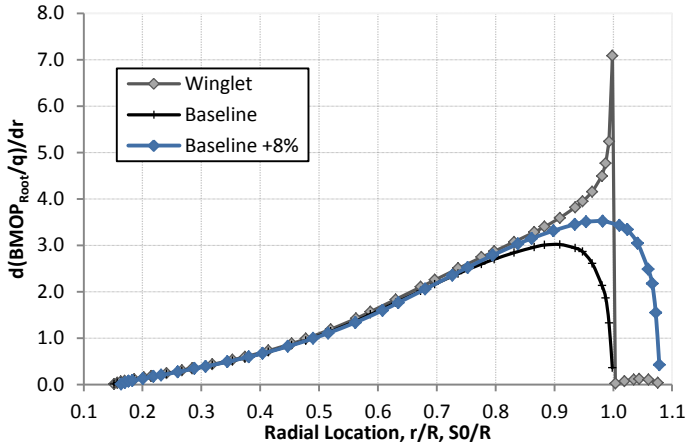

Figure 6-36 Incremental out-of-plane blade-root bending moment (BMOP_Root) per unit orthogonal length at TSR of 5.3.

It is important to note that the above structural results are only for the design tip-speed ratio. The next section will investigate the influence of a winglet on rotor forces for a range of tip-speed ratios.

6.3.1 Trade Space Exploration

The trade space exploration tool was used to visualize the effect of tip-speed ratio on the winglet geometry. The tip-speed ratio was varied as well as the tip-pitch angle of the winglet. The root-pitch angle was fixed, although the tool has been used to generate series of surface plots for a range of root-pitch angle. The coefficient of power for both the baseline and winglet cases is plotted in Figure 6-37 for a winglet root pitch angle of -8 degrees relative to the zero-lift line of the airfoil. The winglet case is represented by the higher surface. These data indicate that the benefit of the winglet with this root pitch angle peaks at a tip-speed ratio of about 6, which is slightly higher than the design TSR of 5.3 of the winglet design presented earlier in this chapter. This figure also indicates that the winglet benefit is fairly insensitive to the tip-pitch angle, which was also inferred from the data shown in Figure 6-26.

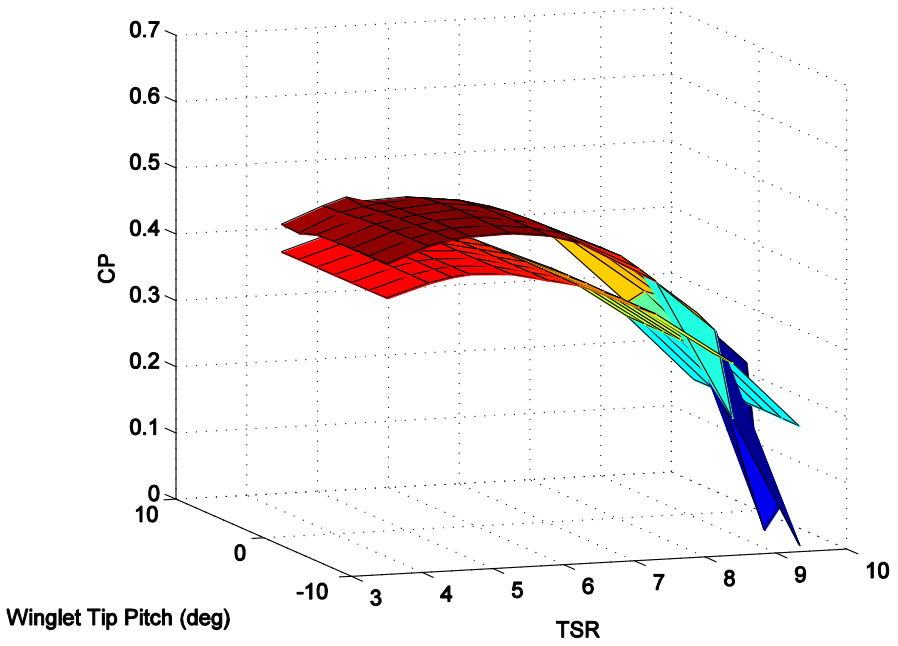

Figure 6-37 Surface plot of CP vs TSR and winglet tip-pitch angle for the winglet and baseline cases. The winglet case has higher CP values throughout most of the plot. Tip pitch relative to airfoil zero-lift line.

The difference in predicted coefficient of power (delCP) between the winglet and baseline cases is shown in Figure 6-38. The maximum delCP occurs at a TSR slightly less than 6 and at a winglet tip-pitch angle of about -5 degrees, which agrees with the choice of -4.5 degrees from Figure 6-26. The spike in delCP at high tip-speed ratio and negative tip-pitch angle is most likely caused by the wake modeling issues seen at high tip-speed ratios in the wake modeling studies.

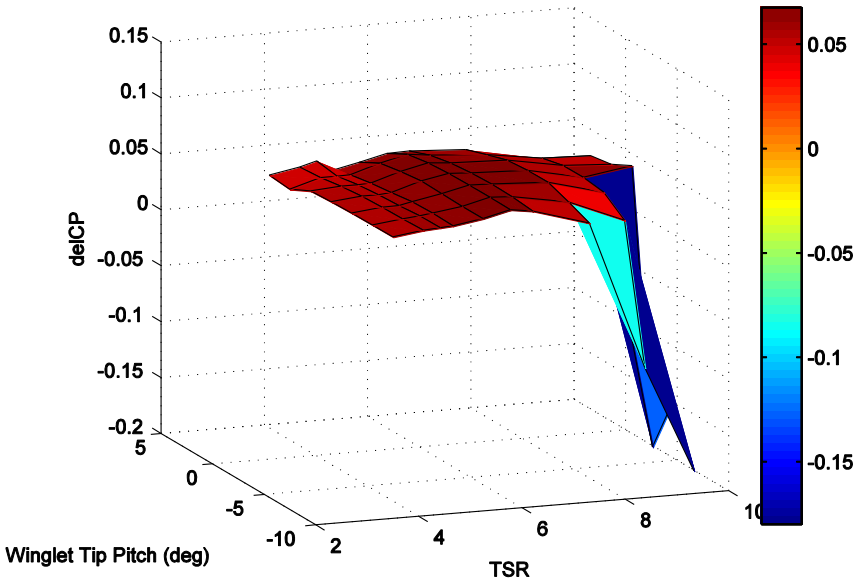

Figure 6-38 Surface plot of deltaCP vs TSR and winglet tip-pitch angle for the winglet and baseline cases.

The thrust coefficient of the winglet and baseline cases was also investigated, as shown in Figure 6-39. The winglet case is again the higher surface and shows a considerable increase in thrust coefficient at high tip-speed ratios, with a slight decrease as the tip-pitch is made more positive. The interesting trend with these data is that the increase in thrust coefficient of the winglet relative to the baseline blade decreases significantly as the tip-speed ratio decreases, or as the wind speed increases.

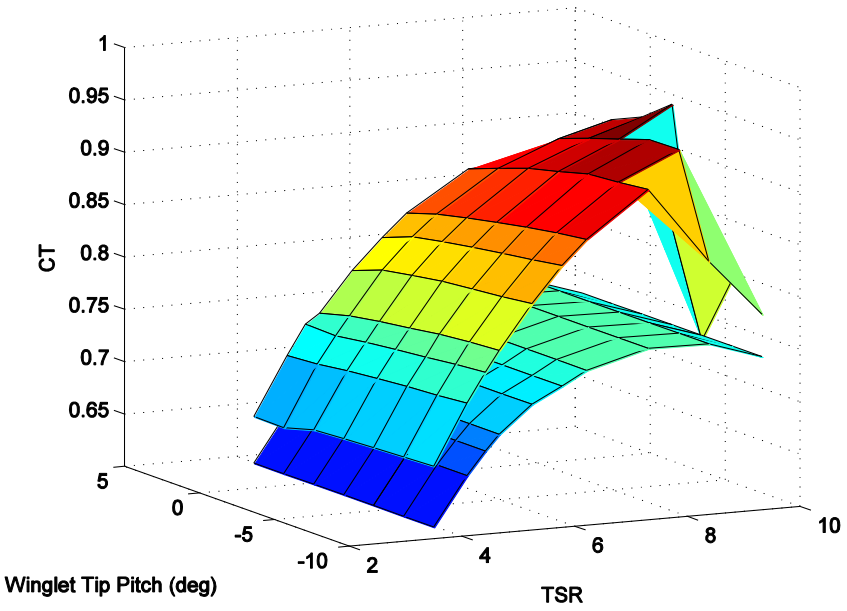

Figure 6-39 Surface plot of CT vs TSR and winglet tip-pitch angle for the winglet and baseline cases. The winglet case has higher CT values throughout most of the plot.

A similar surface plot as the ones shown in the preceding figures can be created for each root pitch angle of the winglet. A wind turbine blade design could be optimized for a site with a specific wind distribution by maximizing the annual energy output. This would allow the tip-speed ratio data points to be collapsed into a single value of annual energy output for each tip-pitch angle, so that a series of surface plots would collapse into one surface plot, giving an optimum design for the given wind distribution.

The previous study of the structural penalty of a winglet only focused on one tip-speed ratio. A wind turbine structure is typically sized for high wind speed load cases. The structural sizing of a wind turbine is proportional to the thrust it produces, so the lower predicted thrust in Figure 6-39 of the winglet at higher wind speeds indicates that the structural penalty of the winglet may be less than predicted by the previous, single point study.

In order to investigate the blade structural sizing at lower tip-speed ratio (higher wind speed), the bending moment of the winglet was calculated at a TSR of 3.95 (wind speed of 8.5 m/s) to verify that the bending moment of the winglet decreases as TSR increases, as indicated by Figure 6-39. The results for this TSR are shown in Figure 6-40.

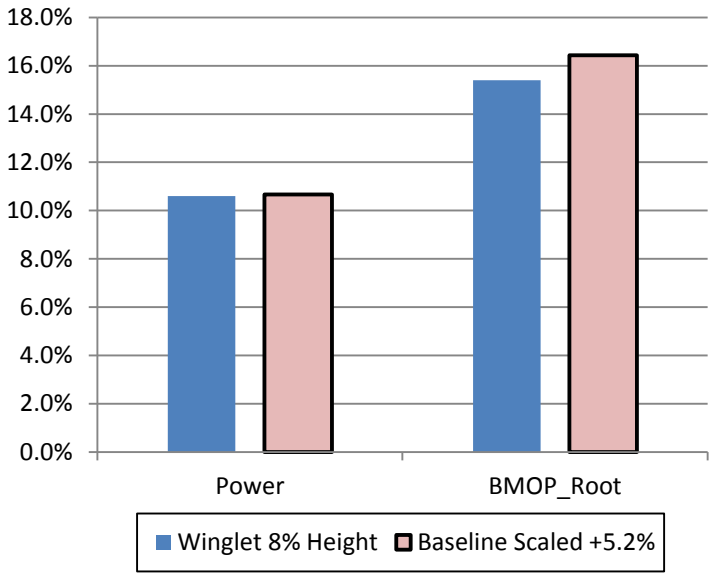

Figure 6-40 Power and BMOP_Root at TSR 3.95 (wind speed 8.5 m/s) for the winglet and the baseline blade scaled to give an equivalent increase in power (+5.2% radius).

The relative bending moment and power of the scaled blades does not change with tip-speed ratio, but the bending moment of the winglet blade decreases as predicted. The winglet blade coefficient of power did not change, resulting in the equivalent power, scaled baseline blade producing the same power as the winglet blade, but the winglet blade produces this power with a 6.3% reduction in integrated root bending moment relative to the scaled baseline blade.

The structural design loads of a wind turbine are typically at higher wind speeds, where the winglet blade has a decreased bending moment. If a blade spar is sized for tip deflection limits, than the winglet blade could have a structural advantage. Even if the bending moment of the winglet were equal to the scaled baseline blade, the winglet blade is shorter than the baseline

blade and has a correspondingly shorter chord length along its span, resulting in less required blade material and potentially lower blade production costs.

The structural advantage of the winglet is offset by the additional tower clearance required for the winglet. The trade-offs for a practical winglet design are inherently multi-disciplinary, since the decreased blade weight would be balanced against increased length and weight due to extending the rotor shaft for tower clearance of the winglet. A winglet may also reduce the tip-noise of a wind turbine, but noise is not trivial to predict and include in the design process [96].

The winglet designed and tested in this study is an initial design and can be improved upon. An upstream (lower surface) winglet has the potential for future investigation, since it would eliminate the tower clearance issue (on an upstream machine) of a downstream winglet and can create close to the same power benefit [95]. Designing the main blade concurrently with the winglet also has the potential for future work, since it would allow tailoring of the load distribution along the entire lifting surface, reducing the structural penalty of the winglet.

6.4 Design Differences of a Winglet for a Utility Scale Wind Turbine

A utility-scale wind turbine winglet design would be different than this small-scale design, partially due to the increased tip speed. The increased tip speed will cause a two to four fold increase in profile drag on the winglet of a utility-scale wind turbine relative to a small-scale wind turbine. For a moderately sized winglet, the profile drag is fairly small compared to the induced forces at the blade tip, so a utility-scale turbine will see an overall performance benefit from a winglet, but a detailed analysis is necessary to learn how the balance between profile drag and induced forces will affect the overall performance. The increased profile drag could potentially drive the design of a winglet for a large-scale wind turbine toward a shorter winglet

height in order to minimize the wetted area of the winglet. Potential future work includes further development of the FW-DVE analysis code for winglet design and the application of this tool to the exploration of the possible performance gains of a winglet on a utility-scale wind turbine.

Chapter 7

Concluding Remarks and Future Work

The research presented in this dissertation was focused on developing the inviscid free-wake distributed vorticity element (FW-DVE) analysis method into a design tool. This tool is capable of accurately modeling unconventional blade designs in a stable and computationally efficient manner as compared to other analysis methods. The FW-DVE method does not require the calibration of a vortex-core model, as is required for numerical stability by most filament and particle based free-wake vortex methods.

The two main contributions to the FW-DVE method were the addition of profile drag and stall effects to the rotor force predictions. The addition of profile drag was required to enhance the capability for design analysis; this capability was utilized in the winglet design study. The stall model is required to accurately model stall-regulated wind turbines, such as the National Renewable Energy Laboratory's Unsteady Aerodynamics Experiment Phase VI wind turbine, which was used for validation. The stall model is also required for detailed structural design analysis of pitch-regulated wind turbines, since wind gusts can cause the wind turbine blades to stall.

The angle-of-attack predictions with the modified FW-DVE method showed very good agreement with CFD predictions from another study. The local flow angle predictions did not show as good of an agreement with experimental measurements, although comparable discrepancies have been shown by similar analysis studies, including CFD predictions. The validation of the FW-DVE method using the NREL UAE Phase VI wind turbine showed good agreement for the normal force coefficient. Some of the angle-of-attack verification results were performed using a fixed wake analysis, which showed general agreement with the free-wake

analysis cases. For moderate tip-speed ratio analysis, the fixed-wake analysis shows the potential to be very useful for initial design, as it requires considerably less time than the free-wake analysis.

The effect of several of the modeling parameters was explored over a range of tip-speed ratios. At moderate to low tip-speed ratios, the FW-DVE method showed a general insensitivity to most modeling parameters beyond a certain threshold. High tip-speed ratio cases showed that the choice of surface and wake modeling parameters could lead to unrealistic wake shapes, although proper choice of the surface paneling and the wake modeling parameters produced stable, realistic results. A study was performed that compared the relative increase in power from a winglet as a function of the length of the wake model. The shortest wake was 8 rotor diameters and showed a 0.5% difference as compared to cases with much longer wakes (20+ diameters). The results indicate that shorter wakes may be useful for design studies, which would greatly reduce the required computation time or increase the number of cases that can be analyzed. Some of the validation and design study cases used shorter wake models for this reason. The extrapolation method has proven to be very useful for design analysis, as it significantly reduces computation time with a level of error that is more than acceptable for initial or even final design analysis.

A trade space exploration tool (TSET) was developed, which greatly aided in the design and validation of analysis cases. The tool reads a simplified geometry definition file and uses it as a basis for creating input files for WindDVE; it will then run WindDVE and perform post-processing of the results. It can also perform simple one or two variable parametric studies and create surface plots of the results. This tool enables the user to explore a much larger trade space than would otherwise be possible.

The design ability of the method was exercised during the design of a winglet for a small scale wind turbine. This winglet design was tested on a small-scale wind turbine test stand at the

University of Waterloo, producing the only experimental data of a winglet designed for a wind turbine using modern analysis tools. The FW-DVE method predicted a maximum benefit from the winglet of 11% for a wide range of tip-speed ratio, whereas the experimental results showed a maximum benefit of 9% for a narrower range of tip-speed ratio. The predictions were within the estimated error bars of the experimental results, indicating reasonable agreement. When the stall model was included in the analysis, the FW-DVE method under predicted the coefficient of power for the baseline planar case and slightly over predicted it for the winglet case. The cause of this error is not clear; as there are many sources of uncertainty including the airfoil data, stall delay corrections, wake modeling parameters, and the experimental data.

The numerical stability of the FW-DVE method is evidenced by its ability to model wakes of fifty or more revolutions downstream. This stability indicates that the method is a good candidate for modeling the interaction of a rotor with the wake from an upstream rotor. Future work could include coupling the FW-DVE method with a structural dynamics code to analyze the aeroelastic effects of rotors interacting with complex, time-varying flow fields such as occur during turbine-turbine interaction.

Other future work could include improving the numerical stability of the stall model developed for the FW-DVE method. The stall model will be important for analyzing unsteady cases where flow field conditions change rapidly. Dynamic stall and unsteady aerodynamics models will also be important for such cases and could be developed as part of a more complex stall model.

The computational requirements of the code could be improved through several methods. The FW-DVE method would benefit from parallel processing, as most of the computational time is spent solving the influence of the wake DVEs on each other, which is an inherently parallel process with a limited amount of overhead.

The trade space exploration tool has proven to be very useful for the initial winglet design study presented as part of this research, as well as for the validation studies. Future work could include adding an optimizer, which would enable exploration of a much larger trade space. If wind data is available, then the tool could be used to optimize the annual energy production of a turbine design for the specific site. Structural considerations could also be included in the optimization routine as a cost function, enabling multi-disciplinary design optimization of advanced blade designs. Blade-element momentum theory based optimizers are available, which can run thousands of cases in the time it takes to generate one free-wake vortex method solution, but they cannot model non-planar, swept, or other non-conventional blade geometries and they are less accurate at off-design conditions for conventional geometries. Computational fluid dynamics based optimizers can handle advanced blade geometries, but can take days to analyze a single case in a parallel processing environment. A FW-DVE based optimizer would fill the gap between these two, as it takes considerably less time to perform an analysis than CFD, but it can accurately analyze advanced blade geometries, as shown in this dissertation.

Appendix A

Example Airfoil Data File

Alpha	cl	cd	Re#	cm
S833_XFOIL		rows =	27	
-11.5	-1.1954	0.04103	100000	-0.0414
-11	-1.1718	0.03934	100000	-0.0381
-10	-1.1281	0.03565	100000	-0.0318
-4	-0.6675	0.02645	100000	-0.016
-3	-0.5849	0.02703	100000	-0.0136
-2	-0.5034	0.02838	100000	-0.0109
-1	-0.3109	0.03378	100000	-0.0253
0	-0.1934	0.0362	100000	-0.0265
1	-0.077	0.03777	100000	-0.0279
8	0.8003	0.02133	100000	-0.0229
9	0.8845	0.02308	100000	-0.0208
10	0.9271	0.02774	100000	-0.0157
11	0.9798	0.03392	100000	-0.0134
12	1.0484	0.04088	100000	-0.013
-14	-1.154	0.03972	400000	-0.0626
-13	-1.1227	0.03309	400000	-0.0649
-2	0.0266	0.01168	400000	-0.1002
0	0.3289	0.01018	400000	-0.1163
1	0.4482	0.00993	400000	-0.1174
2	0.5821	0.00977	400000	-0.1213
3	0.6815	0.00987	400000	-0.1181
4	0.771	0.01007	400000	-0.1128
5	0.8401	0.01065	400000	-0.1035
13	1.2142	0.03719	400000	-0.0341
14	1.239	0.04424	400000	-0.0292
15	1.2493	0.05343	400000	-0.0255
16	1.251	0.06416	400000	-0.0235

Appendix B

NREL UAE Phase VI Blade Geometry

Span (r/R)	Chord (c/R)	Twist (deg)	Thickness (%chord)	ZLL_Offset (deg)	Airfoil Number
0.250	0.14655	20.04	20.95	-1.228	809
0.267	0.14476	18.074	20.95	-1.228	809
0.300	0.14138	14.292	20.95	-1.228	809
0.328	0.1386	11.909	20.95	-1.228	809
0.388	0.13243	7.979	20.95	-1.228	809
0.449	0.12647	5.308	20.95	-1.228	809
0.466	0.12468	4.715	20.95	-1.228	809
0.509	0.1203	3.425	20.95	-1.228	809
0.570	0.11414	2.083	20.95	-1.228	809
0.631	0.10797	1.15	20.95	-1.228	809
0.633	0.10777	1.115	20.95	-1.228	809
0.691	0.10181	0.494	20.95	-1.228	809
0.752	0.09584	-0.015	20.95	-1.228	809
0.800	0.09087	-0.381	20.95	-1.228	809
0.812	0.08968	-0.475	20.95	-1.228	809
0.873	0.08352	-0.92	20.95	-1.228	809
0.934	0.07735	-1.352	20.95	-1.228	809
0.950	0.07576	-1.469	20.95	-1.228	809
0.994	0.07119	-1.775	20.95	-1.228	809
1.000	0.07079	-1.8447	20.95	-1.228	809

Rotor Radius	5.029 m
Rotor RPM	72.0
Cone Angle	0 deg.
Blade Tip Pitch Angle	3 deg.
Collective Blade Pitch	-4.8 deg.
Air density	1.2250 (kg/m^3)
Kinematic air viscosity	1.464E-05 (m^2/s)

The blade pitch of -4.8 degree gives a tip pitch angle of 3 degrees. Pitch is defined as positive toward feather (away from stall), referenced from the rotor disc plane. The blade geometry and the collective pitch angle come from NREL reports that describe the UAE Phase VI wind turbine [5,108].

Appendix C

Example WindDVE Input File: NREL Phase VI Turbine

Each panel side edge also has a boundary condition that is used to define the boundary conditions at the side-edges of the DVEs when solving the surface circulation equation system. The blade tip and root typically has a boundary condition of "100" and all inner panel side-edges will have a boundary condition of "220". The condition of "100" corresponds to an undefined slope of circulation and a magnitude of circulation of zero. The condition of "220" corresponds to the slope and magnitude of circulation being equal to the neighboring element.

The azimuth angle does not have any influence on panel geometry of the surface geometry generation routine developed by Basom [4], which was used in the present research. In the old version of surface geometry from the work of Bramesfeld [2] (such as FreeWake 2007), the azimuth angle input for each panel would rotate the vectors defining the panel geometry about the Y axis by the input angle; hence why the input is retained. The new surface geometry generation routine could be modified to use the azimuth angle as well, but this was not necessary for the present research since the input file tool input the X,Y,Z coordinates of each panel.

```
Please note that the program uses equal, number, ampersand, and : signs as special
recognizers!

******************************** OPERATIONAL PARAMETERS ********************************
This program allows for multiple timestep intervals.  For each interval set the
following parameters:
1)  'tsteps': max number of timesteps in interval
2)  'tsteps_per_rev': number of timesteps per blade revolution
                enter '-999.' to smoothly change the step size over the interval
3)  'lam': tip speed ratio
4)  'Uinf': freestream velocity magnitude
5)  'alpha': X-axis angle of attack [deg]
6)  'yaw': X-axis yaw angle [deg]
7)  'a':  Axial wake induction factor (a) - only applies when 'relax' is 0
8)  'relax': Wake relaxation option:
     0 - fixed, constant pitch     2 - fully relaxed
     1 - fixed, iterated pitch              3 - semi-relaxed
9)  'steady': steady operation option:
                0 - unsteady     1 - steady
10) 'extrp': extrapolate wake downstream of nD_extrp
                0 - no      1 - yes

num of timestep intervals:            nint = 3
```

```
interval #1:
 tsteps  tsteps_per_rev  lam     Uinf    alpha   yaw     a      relax   steady    extrp
    45           10    5.42     7.00    0.00    0.00    0.00     2       1        1

interval #2:
 tsteps  tsteps_per_rev  lam     Uinf    alpha   yaw     a      relax   steady    extrp
    30         -999    5.42     7.00    0.00    0.00    0.00     2       1        1

interval #3:
 tsteps  tsteps_per_rev  lam     Uinf    alpha   yaw     a      relax   steady    extrp
    90           20    5.42     7.00    0.00    0.00    0.00     2       1        1

num of Dref's downstream aft of which
   relaxed wake is extrapolated:          nD_Extrp  =   3.480
tsteps_per_rev for rows aft of extrp
              set to -999. to use orig. step sizes:   tpr_extrp  = -999.

tsteps between wake saves:                    saveStep  =     300
tsteps between force calcs:                   forceStep  = 1
timestep for 1st force calc:                 forceStart = 0

convergence delta-power coeff.:              dCP       = 0.     (0. if only time stepping)
num of consecutive forceSteps
              that must meet conv criteria:          nconv     = 5
Profile Force and Stall Option:                                          profStallOpt=    2
Profile Force and Stall Model Option, 1 cd,cm from cl,non-stall 2 cl,cd,cm from alpha, non-stall 3 stall model, cl,cd,cm from alpha.
NOTE Mode 1 requires airfoil profile data to be 1-1 and between negative and postiive stall
**********************************Fluid Properties**************************************
Note These properties are constant throughout the fluid space and time
              Density                  = 1.22500  //(kg/m^3)  //Note: not used in code since everything is output by 1/Uinf or 1/q
KinViscosity   = 0.0000150        //(m^2/s)  //Used to compute Reynolds Number for airfoil profile data lookup, units should be
relative to radius and coordinate inputs
@******************************** GEOMETRICAL PARAMETERS ********************************
reference radius:                Rref =    5.029
X-coord of rotation center:       Xrot =    0.000
Y-coord of rotation center:       Yrot =    0.000
Z-coord of rotation center:       Zrot =    0.000
blade collective pitch (deg):BetaCollective =   4.8000

symmetric geometry (yes 1, no 0):  sym    =     1
total number of blades:           blades =     2
number of panels entered:          panels =    18
number of chordwise lifting lines: m      =     1
No. of airfoils (max. 15)             airfoils =    12  //airfoil file numbers go from 1 to 15 max 500 data points

panel #:   1                number of spanwise elements: n = 1  airfoil no. = 12
Alpha_zl =  -1.2280
neighboring panels (0 for none)        left:   0  right:   2
azimuth angle of panel Y'=axis:        azi =    0.000
     Xout       Y'out      Z'out      chord      pitch    Bound.Cond.
   0.00000    1.25725    0.00000    0.73700   20.04000     100
     Xout       Y'out      Z'out      chord      pitch    Bound.Cond.
   0.00000    1.37635    0.00000    0.72456   17.30822     220

panel #:   2                number of spanwise elements: n = 1  airfoil no. = 12
Alpha_zl =  -1.2280
neighboring panels (0 for none)        left:   1  right:   3
azimuth angle of panel Y'=axis:        azi =    0.000
     Xout       Y'out      Z'out      chord      pitch    Bound.Cond.
   0.00000    1.37635    0.00000    0.72456   17.30822     220
     Xout       Y'out      Z'out      chord      pitch    Bound.Cond.
   0.00000    1.52366    0.00000    0.70951   14.03887     220

panel #:   3                number of spanwise elements: n = 1  airfoil no. = 12
Alpha_zl =  -1.2280
neighboring panels (0 for none)        left:   2  right:   4
azimuth angle of panel Y'=axis:        azi =    0.000
     Xout       Y'out      Z'out      chord      pitch    Bound.Cond.
```

```
   0.00000    1.52366    0.00000    0.70951   14.03887     220
    Xout       Y'out      Z'out      chord      pitch    Bound.Cond.
   0.00000    1.69789    0.00000    0.69204   11.27887     220

panel #:   4                number of spanwise elements: n = 1  airfoil no. = 12
Alpha_zl =  -1.2280
neighboring panels (0 for none)        left:   3  right:   5
azimuth angle of panel Y'=axis:        azi =    0.000
    Xout       Y'out      Z'out      chord      pitch    Bound.Cond.
   0.00000    1.69789    0.00000    0.69204   11.27887     220
    Xout       Y'out      Z'out      chord      pitch    Bound.Cond.
   0.00000    1.89694    0.00000    0.67158    8.68640     220

panel #:   5                number of spanwise elements: n = 1  airfoil no. = 12
Alpha_zl =  -1.2280
neighboring panels (0 for none)        left:   4  right:   6
azimuth angle of panel Y'=axis:        azi =    0.000
    Xout       Y'out      Z'out      chord      pitch    Bound.Cond.
   0.00000    1.89694    0.00000    0.67158    8.68640     220
    Xout       Y'out      Z'out      chord      pitch    Bound.Cond.
   0.00000    2.11793    0.00000    0.64970    6.52773     220

panel #:   6                number of spanwise elements: n = 1  airfoil no. = 12
Alpha_zl =  -1.2280
neighboring panels (0 for none)        left:   5  right:   7
azimuth angle of panel Y'=axis:        azi =    0.000
    Xout       Y'out      Z'out      chord      pitch    Bound.Cond.
   0.00000    2.11793    0.00000    0.64970    6.52773     220
    Xout       Y'out      Z'out      chord      pitch    Bound.Cond.
   0.00000    2.35734    0.00000    0.62561    4.63250     220

panel #:   7                number of spanwise elements: n = 1  airfoil no. = 12
Alpha_zl =  -1.2280
neighboring panels (0 for none)        left:   6  right:   8
azimuth angle of panel Y'=axis:        azi =    0.000
    Xout       Y'out      Z'out      chord      pitch    Bound.Cond.
   0.00000    2.35734    0.00000    0.62561    4.63250     220
    Xout       Y'out      Z'out      chord      pitch    Bound.Cond.
   0.00000    2.61108    0.00000    0.59981    3.20050     220

panel #:   8                number of spanwise elements: n = 1  airfoil no. = 12
Alpha_zl =  -1.2280
neighboring panels (0 for none)        left:   7  right:   9
azimuth angle of panel Y'=axis:        azi =    0.000
    Xout       Y'out      Z'out      chord      pitch    Bound.Cond.
   0.00000    2.61108    0.00000    0.59981    3.20050     220
    Xout       Y'out      Z'out      chord      pitch    Bound.Cond.
   0.00000    2.87461    0.00000    0.57319    2.05841     220

panel #:   9                number of spanwise elements: n = 1  airfoil no. = 12
Alpha_zl =  -1.2280
neighboring panels (0 for none)        left:   8  right:  10
azimuth angle of panel Y'=axis:        azi =    0.000
    Xout       Y'out      Z'out      chord      pitch    Bound.Cond.
   0.00000    2.87461    0.00000    0.57319    2.05841     220
    Xout       Y'out      Z'out      chord      pitch    Bound.Cond.
   0.00000    3.14312    0.00000    0.54603    1.24177     220

panel #:  10                number of spanwise elements: n = 1  airfoil no. = 12
Alpha_zl =  -1.2280
neighboring panels (0 for none)        left:   9  right:  11
azimuth angle of panel Y'=axis:        azi =    0.000
    Xout       Y'out      Z'out      chord      pitch    Bound.Cond.
   0.00000    3.14312    0.00000    0.54603    1.24177     220
    Xout       Y'out      Z'out      chord      pitch    Bound.Cond.
   0.00000    3.41164    0.00000    0.51852    0.62899     220

panel #:  11                number of spanwise elements: n = 1  airfoil no. = 12
Alpha_zl =  -1.2280
neighboring panels (0 for none)        left:  10  right:  12
azimuth angle of panel Y'=axis:        azi =    0.000
```

```
    Xout      Y'out     Z'out     chord     pitch    Bound.Cond.
   0.00000   3.41164   0.00000   0.51852   0.62899     220
    Xout      Y'out     Z'out     chord     pitch    Bound.Cond.
   0.00000   3.67517   0.00000   0.49242   0.16194     220

panel #:  12              number of spanwise elements: n = 1  airfoil no. = 12
Alpha_zl =  -1.2280
neighboring panels (0 for none)        left:  11  right:  13
azimuth angle of panel Y'=axis:        azi =    0.000
    Xout      Y'out     Z'out     chord     pitch    Bound.Cond.
   0.00000   3.67517   0.00000   0.49242   0.16194     220
    Xout      Y'out     Z'out     chord     pitch    Bound.Cond.
   0.00000   3.92891   0.00000   0.46675  -0.23803     220

panel #:  13              number of spanwise elements: n = 1  airfoil no. = 12
Alpha_zl =  -1.2280
neighboring panels (0 for none)        left:  12  right:  14
azimuth angle of panel Y'=axis:        azi =    0.000
    Xout      Y'out     Z'out     chord     pitch    Bound.Cond.
   0.00000   3.92891   0.00000   0.46675  -0.23803     220
    Xout      Y'out     Z'out     chord     pitch    Bound.Cond.
   0.00000   4.16832   0.00000   0.44244  -0.59797     220

panel #:  14              number of spanwise elements: n = 1  airfoil no. = 12
Alpha_zl =  -1.2280
neighboring panels (0 for none)        left:  13  right:  15
azimuth angle of panel Y'=axis:        azi =    0.000
    Xout      Y'out     Z'out     chord     pitch    Bound.Cond.
   0.00000   4.16832   0.00000   0.44244  -0.59797     220
    Xout      Y'out     Z'out     chord     pitch    Bound.Cond.
   0.00000   4.38931   0.00000   0.42012  -0.91854     220

panel #:  15              number of spanwise elements: n = 1  airfoil no. = 12
Alpha_zl =  -1.2280
neighboring panels (0 for none)        left:  14  right:  16
azimuth angle of panel Y'=axis:        azi =    0.000
    Xout      Y'out     Z'out     chord     pitch    Bound.Cond.
   0.00000   4.38931   0.00000   0.42012  -0.91854     220
    Xout      Y'out     Z'out     chord     pitch    Bound.Cond.
   0.00000   4.58836   0.00000   0.39999  -1.19889     220

panel #:  16              number of spanwise elements: n = 1  airfoil no. = 12
Alpha_zl =  -1.2280
neighboring panels (0 for none)        left:  15  right:  17
azimuth angle of panel Y'=axis:        azi =    0.000
    Xout      Y'out     Z'out     chord     pitch    Bound.Cond.
   0.00000   4.58836   0.00000   0.39999  -1.19889     220
    Xout      Y'out     Z'out     chord     pitch    Bound.Cond.
   0.00000   4.76259   0.00000   0.38248  -1.44725     220

panel #:  17              number of spanwise elements: n = 1  airfoil no. = 12
Alpha_zl =  -1.2280
neighboring panels (0 for none)        left:  16  right:  18
azimuth angle of panel Y'=axis:        azi =    0.000
    Xout      Y'out     Z'out     chord     pitch    Bound.Cond.
   0.00000   4.76259   0.00000   0.38248  -1.44725     220
    Xout      Y'out     Z'out     chord     pitch    Bound.Cond.
   0.00000   4.90990   0.00000   0.36725  -1.65203     220

panel #:  18              number of spanwise elements: n = 1  airfoil no. = 12
Alpha_zl =  -1.2280
neighboring panels (0 for none)        left:  17  right:   0
azimuth angle of panel Y'=axis:        azi =    0.000
    Xout      Y'out     Z'out     chord     pitch    Bound.Cond.
   0.00000   4.90990   0.00000   0.36725  -1.65203     220
    Xout      Y'out     Z'out     chord     pitch    Bound.Cond.
   0.00000   5.02900   0.00000   0.35600  -1.84470     100
```

Appendix D

University of Waterloo Wind Tunnel Test Conditions

The limits of wind speed of the tunnel at the University of Waterloo caused some high and low wind speed cases to be tip-speed ratio matched to the desired design conditions, so that the rotor RPM was varied to match tip-speed ratio. The design and test conditions are given in the table below; the data was compended from information by Gertz [89]. The minimum wind speed was set to 3.6 m/s and the maximum to 11.1 m/s in the wind tunnel. This caused an error in the Reynolds number calculation relative to the conditions in which the wind turbine was designed to operate. For most of the operating range of concern for design purposes (from 3.6 to 11.1m/s) the test conditions matched the desired design conditions.

Desired (Design)				Actual (Test Conditions)			
Vwind	RPm	Rad/s	TSR	Vwind	RPm	Rad/s	TSR
11.1	200	20.94	3.02	11.1	200	20.94	3.02
3.10	200	20.94	10.81	3.7	240	25.13	10.87
3.23	200	20.94	10.36	3.7	230	24.09	10.42
3.37	200	20.94	9.95	3.7	220	23.04	9.96
3.50	200	20.94	9.57	3.7	210	21.99	9.51
3.6	200	20.94	9.31	3.6	200	20.94	9.31
4.1	200	20.94	8.17	4.1	200	20.94	8.17
4.6	200	20.94	7.28	4.6	200	20.94	7.28
5.1	200	20.94	6.57	5.1	200	20.94	6.57
5.6	200	20.94	5.98	5.6	200	20.94	5.98
6.1	200	20.94	5.49	6.1	200	20.94	5.49
6.6	200	20.94	5.08	6.6	200	20.94	5.08
7.1	200	20.94	4.72	7.1	200	20.94	4.72
7.6	200	20.94	4.41	7.6	200	20.94	4.41
8.1	200	20.94	4.14	8.1	200	20.94	4.14
8.6	200	20.94	3.90	8.6	200	20.94	3.90
9.1	200	20.94	3.68	9.1	200	20.94	3.68
9.6	200	20.94	3.49	9.6	200	20.94	3.49
10.1	200	20.94	3.32	10.1	200	20.94	3.32
10.6	200	20.94	3.16	10.6	200	20.94	3.16
11.1	200	20.94	3.02	11.1	200	20.94	3.02
11.6	200	20.94	2.89	11.1	191.4	20.04	2.89
12.1	200	20.94	2.77	11.1	183.5	19.21	2.77
12.6	200	20.94	2.66	11.1	176.2	18.45	2.66
13.1	200	20.94	2.56	11.1	169.5	17.75	2.56
13.6	200	20.94	2.46	11.1	163.2	17.09	2.46
14.1	200	20.94	2.38	11.1	157.4	16.49	2.38
14.6	200	20.94	2.30	11.1	152.1	15.92	2.30
15.1	200	20.94	2.22	11.1	147.0	15.40	2.22
15.6	200	20.94	2.15	11.1	142.3	14.90	2.15
16.1	200	20.94	2.08	11.1	137.9	14.44	2.08
16.6	200	20.94	2.02	11.1	133.7	14.00	2.02
17.1	200	20.94	1.96	11.1	129.8	13.60	1.96
17.6	200	20.94	1.90	11.1	126.1	13.21	1.90
18.1	200	20.94	1.85	11.1	122.7	12.84	1.85
18.6	200	20.94	1.80	11.1	119.4	12.50	1.80
19.1	200	20.94	1.75	11.1	116.2	12.17	1.75
19.6	200	20.94	1.71	11.1	113.3	11.86	1.71
20.1	200	20.94	1.67	11.1	110.4	11.57	1.67
20.6	200	20.94	1.63	11.1	107.8	11.29	1.63
21.1	200	20.94	1.59	11.1	105.2	11.02	1.59
21.5	200	20.94	1.56	11.1	103.3	10.81	1.56
22.1	200	20.94	1.52	11.1	100.5	10.52	1.52

Appendix E

Derivation of the Total Induced Velocity due to a DVE

The term $\vec{\boldsymbol{w}}_{\boldsymbol{3j}}(x_0, y_0, z_0)_i$ represents the combined influence of the vortex filaments and vortex sheet of DVE "j" on the control point of DVE "i" (following the nomenclature of Appendix 3 of Bramesfeld) [2]. The induced velocity of the vortex filaments of DVE "j" on point $\vec{\boldsymbol{x}}_{\boldsymbol{0i}} = (\xi_0, \eta_0, \zeta_0)_i$ is given by:

$$\vec{\boldsymbol{w}}_{\boldsymbol{1j}}(\xi_0, \eta_0, \zeta_0)_i = \frac{-1}{4\pi}\begin{bmatrix} a_{1\xi ji} & b_{1\xi ji} & c_{1\xi ji} \\ a_{1\eta ji} & b_{1\eta ji} & c_{1\eta ji} \\ a_{1\zeta ji} & b_{1\zeta ji} & c_{1\zeta ji} \end{bmatrix}\begin{bmatrix} A_j \\ B_j \\ C_j \end{bmatrix} \tag{E-1}$$

The induced velocity of the vortex sheets of DVE "j" on point $\vec{\boldsymbol{x}}_{\boldsymbol{0i}} = (\xi_0, \eta_0, \zeta_0)_i$ is given by:

$$\vec{\boldsymbol{w}}_{\boldsymbol{2j}}(\xi_0, \eta_0, \zeta_0)_i = \frac{-1}{4\pi}\begin{bmatrix} 0 & 0 & 0 \\ 0 & b_{2\eta ji} & c_{2\eta ji} \\ 0 & b_{2\zeta ji} & c_{2\zeta ji} \end{bmatrix}\begin{bmatrix} A_j \\ B_j \\ C_j \end{bmatrix} \tag{E-2}$$

where the influence coefficients are given in the Appendix of Ref. [4] as a function of the local DVE geometry $(\eta_j, \Lambda_{j\_l.e.}, \Lambda_{j\_t.e.})$. The derivation in the appendix of Ref. [4] represents the point where the induced velocity is being calculated as $\vec{P}_A(\xi_A, \eta_A, \zeta_A)$ and the sweep of a DVE filament as Λ [4].

The sum of the induced velocity caused by the vortex filaments and vortex sheets of DVE "j" on the reference point of DVE "i" is given by:

$$\begin{aligned}\vec{\boldsymbol{w}}_{\boldsymbol{3j}}(\xi_0, \eta_0, \zeta_0)_i = {} & \vec{\boldsymbol{w}}_{\boldsymbol{1j_{le}}}(\xi_0 - \xi_j, \eta_0, \zeta_0, A_j, B_j, C_j, \Lambda_{j_{l.e.}}) + \vec{\boldsymbol{w}}_{\boldsymbol{1j_{te}}}(\xi_0 + \xi_j, \eta_0, \zeta_0, A_j, B_j, C_j, \Lambda_{j_{t.e.}}) \\ & + \vec{\boldsymbol{w}}_{\boldsymbol{2j\_le}}(\xi_0 - \xi_j, \eta_0, \zeta_0, B_j, C_j, \Lambda_{j\_l.e.}) + \vec{\boldsymbol{w}}_{\boldsymbol{2j\_te}}(\xi_0 + \xi_j, \eta_0, \zeta_0, -B_j, -C_j, \Lambda_{j\_t.e.})\end{aligned} \tag{E-3}$$

where $\xi_j$represents half of the mid-span chord length of the influencing DVE "j", $\Lambda_{j\_l.e.}$ is the leading-edge sweep, and $\Lambda_{j_t.e.}$is the trailing-edge sweep [2]. The resulting influence coefficients can then be written as:

$$\vec{\boldsymbol{w}}_{\boldsymbol{3j}}(\xi_0, \eta_0, \zeta_0)_i = \frac{-1}{4\pi}\begin{bmatrix} A_j a_{3\xi ji} + B_j b_{3\xi ji} + C_j c_{3\xi ji} \\ A_j a_{3\eta ji} + B_j b_{3\eta ji} + C_j c_{3\eta ji} \\ A_j a_{3\zeta ji} + B_j b_{3\zeta ji} + C_j c_{3\zeta ji} \end{bmatrix} \tag{E-4}$$

Appendix F

Integrated Circulation Method for Solving the Surface Circulation Distribution

The integrated circulation method is an alternative way to include the influence of stall on the surface circulation distribution. It was not applied to the WindDVE code, but is described here as it may be interesting to investigate as part of future research. The integrated circulation method applies the magnitude of circulation boundary condition by finding the value of the total circulation of an element based on external data; the integral of the parabolic circulation distribution is then set equal to this total value. The external force data can be taken from airfoil coefficient tables, a boundary layer solution, or from a semi-empirical unsteady aerodynamics method, such as that by Leishman and Beddoes.

The following derivation of this method is limited to one surface lifting-line (one chordwise surface DVE), although more could be used if a model of chordwise distribution of lift was included. The integrated value of the parabolic circulation distribution is by:

$$\boldsymbol{\Gamma_{i\_tot}} = \int_{-\eta}^{\eta} \boldsymbol{\Gamma(\eta)}\, \boldsymbol{d\eta} = \int_{-\eta}^{\eta} \boldsymbol{A_i} + \boldsymbol{B_i(\eta_i)} + \boldsymbol{C_i(\eta_i)^2}\, \boldsymbol{d\eta} \tag{F-1}$$

which results in:

$$\Gamma_{\mathrm{i\_tot}} = 2\mathrm{A_i}(\eta_\mathrm{i}) + \frac{2}{3}\mathrm{C_i}(\eta_\mathrm{i})^3 \tag{F-2}$$

and in matrix form the result is:

$$\left[\, \mathbf{2\eta_i} \quad \mathbf{0} \quad \mathbf{\frac{2}{3}\eta_i^3} \right] \cdot \begin{bmatrix} \mathbf{A_i} \\ \mathbf{B_i} \\ \mathbf{C_i} \end{bmatrix} = \mathbf{\Gamma_{i\_tot}} \tag{F-3}$$

Or one can find the average gamma across the panel (since gamma is per unit span). The span of a panel equals $2\eta_i$; dividing Γ_{i_tot} by $2\eta_i$ results in:

$$\Gamma_{i\_average} = A_i + \frac{1}{3} C_i (\eta_i)^2 \tag{F-4}$$

This value is referred to as "K" in the WindDVE code [4]. This method enables the circulation ($\Gamma_{i\_average}$) to be set from an external source, such as airfoil section data. The equation system can then be solved using this boundary condition rather than the kinematic flow condition. An example equation system is created in the next section using integrated circulation boundary condition.

Matrix Form of the Integrated Circulation Method

Similar to the kinematic flow condition, the integrated circulation method can be solved in matrix form. The solution is similar to the kinematic flow condition, except that the 2nd and 5th rows of the matrix are replaced with the integrated circulation boundary condition.

For a two element lifting surface the boundary conditions would be:

1. Side-edge, left (tip) of element 1.
2. Integrated circulation boundary condition of element 1.
3. Circulation equivalence between elements 1 and 2.
4. Vorticity equivalence between elements 1 and 2.
5. Integrated circulation boundary condition of element 2.
6. Side-edge, left (tip) of element 2.

The equation system for the two DVE element lifting surface using the integrated circulation method is represented in matrix form by:

$$\begin{bmatrix} 1 & \eta_i & {\eta_i}^2 & 0 & 0 & 0 \\ 2\eta_i & 0 & \frac{2}{3}{\eta_i}^3 & 0 & 0 & 0 \\ 1 & \eta_i & {\eta_i}^2 & -1 & -\eta_{i+1} & -(\eta_{i+1})^2 \\ 0 & 1 & 2\eta_i & 0 & -1 & -\eta_{i+1} \\ 0 & 0 & 0 & 2\eta_{i+1} & 0 & \frac{2}{3}{\eta_{i+1}}^3 \\ 0 & 0 & 0 & 1 & \eta_{i+1} & {\eta_{i+1}}^2 \end{bmatrix} \cdot \begin{bmatrix} A_i \\ B_i \\ C_i \\ A_{i+1} \\ B_{i+1} \\ C_{i+1} \end{bmatrix} = \begin{bmatrix} 0 \\ \Gamma_{i\_tot} \\ 0 \\ 0 \\ \Gamma_{i+1\_tot} \\ 0 \end{bmatrix} \tag{F-5}$$

Bibliography

[1] Basom B., and Maughmer M. D., 2011, “Inviscid Analysis of Horizontal-Axis Wind Turbines Using Distributed Vorticity Elements,” 49th AIAA Aerospace Sciences Meeting and Exhibit, AIAA 2011-539, Orlando, FL.

[2] Bramesfeld G., A Higher Order Vortex-Lattice Method with a Force-Free Wake, University Park, PA.

[3] Bramesfeld G., and Maughmer M. D., 2008, “Relaxed-Wake Vortex-Lattice Method Using Distributed Vorticity Elements,” Journal of Aircraft, **45**(2).

[4] Basom B. J., 2010, Inviscid Wind-Turbine Analysis Using Distributed Vorticity Elements, University Park, PA.

[5] Hand M. M., Simms D. A., Fingersh L. J., Jager D. W., Cotrell J. R., Schreck S., and Larwood S. M., 2001, "Unsteady Aerodynamics Experiment Phase VI : Wind Tunnel Test Configurations and Available Data Campaigns Unsteady Aerodynamics Experiment Phase VI : Wind Tunnel Test Configurations and Available Data Campaigns", NREL/TP-500-29955, Boulder, CO.

[6] McLean D., 2005, “Wingtip Devices: What They Do and How They Do It,” 2005 Boeing Performance and Flight Operations Engineering Conference, Article 4.

[7] McCormick B. W., 1995, Aerodynamics, Aeronautics, and Flight Mechanics, John Wiley and Sons, Inc., New York.

[8] Goldstein S., “On the Vortex Theory of Screw Propellers,” Proceedings of the Royal Society of London. Series A.

[9] Horstmann K. H., 1987, “Ein Mehrfach-Traglinienverfahren und seine Verwendung für Entwurf und Nachrechnung nichtplanarer Flügelanordnungen,” DVFLR, Institut für Entwurfsaerodynamik, Braunschweig, Germany, DFVLR-FB 87-51.

[10] Horstmann K. H., Engelbrecht T., and Liersch C., 2007, LIFTING _ LINE Version 2.2, Braunschweig, Germany.

[11] Burton T., Sharpe D., Jenkins N., and Bossanyi E., 2001, Wind Energy Handbook,, Wiley & Sons, New York.

[12] Glauert H., 1963, “Airplane Propellers,” Aerodynamic Theory, D. W.F., ed., Dover Publications, New York.

[13] Buhl Jr. M. L., Wright A. D., and Tangler J. L., "Wind Turbine Design Codes: A Preliminary Comparison of the Aerodynamics", NREL, Golden, CO.

[14] Hansen M. O. L., Sørensen J. N., Voutsinas S., Sørensen N., and and Madsen H. A., 2006, "State of the art in wind turbine aerodynamics and aeroelasticity," Progress in Aerospace Sciences, **42**(4), pp. 285–330.

[15] Wilson R. E., and Lissaman P. B. S., 1974, Applied Aerodynamics of Wind-power Machines, Corvallis, OR.

[16] Manwell J. F., McGowan J. G., and Rogers A. L., 2002, Wind Energy Explained: Theory, Design and Application, John Wiley & Sons, New York.

[17] Maniaci D., 2011, "An Investigation of WT_Perf Convergence Issues," AIAA Aerospace Sciences Meeting including the New Horizons Forum and Aerospace Exposition, AIAA, Orlando, Florida, p. AIAA 2011–150.

[18] Moriarty P. J., and Hansen A. C., AeroDyn Theory Manual, Golden, CO.

[19] Buhl M., 2011, "NWTC Design Codes (WT_Perf by Marshall Buhl)" [Online]. Available: http://wind.nrel.gov/designcodes/simulators/wtperf/.

[20] Gupta S., and Leishman J. G., "Comparison of Momentum and Vortex Methods for the Aerodynamic Analysis of Wind Turbines," Proceedings of the 24th ASME Wind Energy Symposium, AIAA 2005-594, Reno, NV.

[21] Leishman J. G., 2006, Principles of Helicopter Aerodynamics, Cambridge University Press, New York.

[22] Suzuki A., and Hanson A., 1999, "Generalized Dynamic Wake Model for Yawdyn," The 1999 ASME Wind Energy Symposium.

[23] Suzuki A., Application of Dynamic Inflow Theory to Wind Turbine Rotors.

[24] Maniaci D., and Li Y., "Investigating the Influence of the Added Mass Effect to Marine Hydrokinetic Horizontal-Axis Turbines Using a General Dynamic Wake Wind Turbine Code," Oceans 11 Conference, Kona, Kona, Hawaii.

[25] Maniaci D., and Li Y., 2012, "Investigating the Influence of the Added Mass Effect to Marine Hydrokinetic Horizontal-Axis Turbines Using a General Dynamic Wake Wind Turbine Code," MTS Journal, **46**(4), pp. 71–79.

[26] Laino D., and Hansen A. C., User's Guide to the Wind Turbine Dynamics Aerodynamics Computer Software AeroDyn, Windward Engineering, Salt Lake City, UT.

[27] Kecskemety K. M., and McNamara J. J., "Investigation into the Impact of Wake Effects on the Aeroelastic Response and Performance of Wind Turbines," 52nd AIAA/ASME/ASCE/AHS/ASC Structures, Structural Dynamics and Materials Conference, AIAA 2011-1948, Denver, Colorado.

[28] Sezer-Uzol N., and Long L. N., "3-D Time-Accurate CFD Simulations of Wind Turbine Rotor Flow Fields," 44th AIAA Aerospace Sciences Meeting and Exhibit, AIAA-2006-394, Reno, NV.

[29] Sprague M. A., Moriarty P. J., Churchfield M. J., Gruchalla K., Lee S., Lundquist L. K., Michalakes J., and Purkayastha A., "'Computational Modeling of Wind-Plant Aerodynamics'."

[30] Sørensen J. N., and Shen W. Z., 2002, "Numerical Modeling of Wind Turbine Wakes," Journal of Fluids Engineering, **124**, pp. 393–399.

[31] Xu G., and Sankar L. N., 2000, "Computational Study of Horizontal Axis Wind Turbines," Journal of Solar Energy Engineering, **122**(1), pp. 35–39.

[32] Schmitz S., and Chattot J. J., 2005, "A Parallelized Coupled Navier-Stokes/Vortex-Panel Solver," **127**, p. 475.

[33] Schmitz S., and Chattot J. J., 2006, "Characterization of Three-Dimensional Effects for the Rotating and Parked NREL Phase VI Wind Turbine," J. Sol. Energy Eng., **128**, p. 445.

[34] Bhagwat M. J., Moulton M. A., and Caradonna F. W., 2007, "Development of a CFD-based Hover Performance Prediction Tool for Engineering Analysis," Journal of the American Helicopter Society, **52**(3), pp. 175–188.

[35] Sezer-Uzol N., 2001, "High-Accuracy Wake and Vortex Simulations Using a Hybrid Euler/Discrete Vortex Method."

[36] Katz J., and Plotkin A., 2001, Low-Speed Aerodynamics, Cambridge, New York.

[37] Van Garrel A., Development of a wind turbine aerodynamics simulation module.

[38] Mortara K. W., and Maughmer M. D., "A Method for the Prediction of Induced Drag for Planar and Non-Planar Wings," AIAA Applied Aerodynamics Conference, AIAA Paper 93-3420 CP,, Monterey, CA.

[39] Palmiter S. M., and Katz J., "Evaluation of a Potential Flow Model for Propeller and," 48th AIAA Aerospace Sciences Meeting, Orlando, Florida.

[40] Baltazar J., and Falcao de Campos J. A. C., "Unsteady Analysis of a Horizontal Axis Marine Current Turbine in Yawed Inflow Conditions With a Panel Method," First International Symposium on Marine Propulsors, Trondheim, Norway.

[41] Cline S., and Crawford C., "Comparison of Potential Flow Wake Models for Horizontal-Axis Wind Turbine Rotors," 48th AIAA Aerospace Sciences Meeting, Orlando, Florida.

[42] Scully M. P., 1975, Computation of helicopter rotor wake geometry and its influence on rotor harmonic airloads.

[43] Gupta S., and Leishman J. G., "Stability of Methods in the Free-Vortex Wake Analysis of Wind Turbines," Proceedings of the 23rd ASME Wind Energy Symposium and the 42nd AIAA Aerospace Sciences Meeting, Reno, NV.

[44] Okulov V. L., 2004, "On the stability of multiple helical vortices," J. Fluid Mech., **521**, pp. 319–342.

[45] Betz A. L., and Prandtl, "Schraubenpropeller mit geringstem Energieverlust."

[46] Theodorsen T., 1948, Theory of Propellers, McGraw-Hill Book Company, Inc., New York.

[47] Okulov V. L., and Sørensen J. N., 2008, "An Ideal Wind Turbine with a Finite Number of Blades," Doklady Physics, Pleiades Publishing, Ltd., **53**(6), pp. 337–342.

[48] Jeng D. R., Keith, Jr. T. G., and Aliakbarkhanafjeh A., Aerodynamic Analysis of a Horizontal Axis Wind Turbine by use of Helical Vortex Theory.

[49] Kocurek J. D., and Tangler J. L., 1977, "A Prescribed Wake Lifting Surface Hover Performance Analysis," Journal of the American Helicopter Society, **22**(1), pp. 24–35.

[50] Kocurek J. D., 1978, A Lifting Surface Performance Analysis with Wake Circulation Coupled Wake for Advanced Configuration Hovering Rotors, College Station, TX.

[51] Kocurek J. D., Berkowitz L. F., and Harris F. D., 1980, "Hover Performance Methodology at Bell Helicopter Textron," 36th Annual Forum Proceedings, American Helicopter Society, Washington, D. C., p. Preprint No. 80–3.

[52] Kocurek D., 1987, Lifting Surface Performance Analysis for Horizontal Axis Wind Turbines.

[53] Simms D., Schreck S., Hand M., and Fingersh L. J., 2001, "NREL Unsteady Aerodynamics Experiment in the NASA-Ames Wind Tunnel : A Comparison of Predictions to Measurements", NREL/TP-500-29494, Boulder, CO.

[54] Tangler J. L., The Nebulous Art of Using Wind-Tunnel Airfoil Data for Predicting Rotor Performance: Preprint, Boulder, CO.

[55] Fisichella C. J., 2001, An Improved Prescribed Wake Analysis for Wind Turbine Rotors.

[56] Coton F. N., and Wang T., 1999, "The prediction of horizontal axis wind turbine performance in yawed flow using an unsteady prescribed wake model," Proc. Instn. Mech. Engrs, IMechE, **213, Part**.

[57] Currin H. D., Coton F. N., and Wood B., 2008, "Dynamic Prescribed Vortex Wake Model for AERODYN/FAST," Journal of Solar Energy Engineering, **130**(3).

[58] Jonkman J., and Buhl M., 2005, "NWTC Design Codes (FAST Verification by Jason Jonkman and Marshall Buhl)."

[59] Jonkman J., and Buhl M., "New Developments for the NWTC's FAST Aeroelastic HAWT Simulator," 23rd ASME / 42nd AIAA Wind Energy Symposium, Reno, NV.

[60] Jonkman J., 2010, "NWTC Design Codes (FAST)," NWTC Design Codes (FAST), NREL, Boulder, CO.

[61] Clark D. R., and Leiper A. C., 1970, "The Free Wake Analysis a Method for The Prediction of Helicopter Rotor Hovering Performance," Journal of the American Helicopter Society, **15**(1), pp. 3–11.

[62] Rosen A., and Grabe A., 1988, "Free Wake Model of Hovering Rotors Having Straight or Curved Blades," Journal of the American Helicopter Society, **33**(3), pp. 11–19.

[63] Felker F. F., Quackenbush T. R., Bliss D. B., and Light J. L., 1988, "Comparisons of predicted and measured rotor performance using a free wake method," Proc. 44th A. Nat. Forum, American Helicopter Society, Washtington, D.C.

[64] Leishman J. G., Bhagwat M. J., and Bagai A., 2002, "Free-Vortex Filament Methods for the Analysis of Helicopter Rotor Wakes," Journal of Aircraft, **39**(5).

[65] Emdad H., and Nikseresht A. H., 2003, "Application of Vortex Lattice and Quasi-Vortex Lattice Method with Free Wake in Calculation of Aerodynamic Characteristics of a Hovering Helicopter Rotor Blade in Ground Effect," Scientia Iranica, **10**(1), pp. 84–90.

[66] Kecskemety K. M., and McNamara J. J., 2011, "Influence of Wake Effects and Inflow Turbulence on Wind Turbine Loads," AIAA Journal, **49**(11).

[67] Baron A., and Boffadossi M., "Unsteady Free Wake Analysis of Closely Interacting Helicopter Rotors," Proc. 19th European Rotorcraft Forum, Cernobbio (Como), Italy.

[68] Duck Joo Lee. and Seon Uk Na, 1999, "Numerical simulations of wake structure generated by rotating blades using a time marching, free vortex blob method," European Journal of Mechanics - B/Fluids, **18**(1), pp. 147–159.

[69] Westware P. L., 1935, The Rolling Up of the Surface Discontinuity Behind an Airfoil of Finite Span.

[70] Rom J., 1992, “High Angle of Attack Aerodynamics,” Springer-Verlag, New York.

[71] Hackett J. E., and Evans M. R., 1971, “Vortex Wakes Behind High Lift Wings,” Journal of Aircraft, **8**(5), pp. 334–340.

[72] Cottet G. H., and Koumoutsakos P. D., 2000, Vortex Methods Theory and Practice, Cambridge University Press, New York.

[73] Kloosterman M. H. M., Development of the Near Wake behind a Horizontal Axis Wind Turbine, Including the development of a Free Wake Lifting Line Code.

[74] Almosnino D., 1985, “High Angle of Attack Calculations of the Subsonic Vortex Flow on Slender Bodies,” AIAA Journal, Vol. 23, No. 8, pp. 1150-1156., **23**(8), pp. 1150–1156.

[75] Krasny R., 1987, “Computation of vortex sheet roll-up in the Trefftz plane,” J. Fluid Mech., **184**, pp. 123–155.

[76] Voutsinas S., Belessis M., and Rados K., 1996, “Investigation of the Yawed Operation of Wind Turbines by Means of a Vortex.”

[77] Selle A., Rasmussen N., and Fedkiw R., “A vortex particle method for smoke, water and explosions,” ACM Transactions on Graphics (TOG) - Proceedings of ACM SIGGRAPH 2005, Volume 24 Issue 3, July 2005,, New York, NY.

[78] Simoes and Graham, J.M.R. F. J., 1992, “Application of a free vortex wake model to a horizontal axis wind turbine,” Journal of Wind Engineering and Industrial Aerodynamics, **39**, pp. 129–138.

[79] Roskam J., and Lan C.-T. E., 1997, Airplane Aerodynamics and Performance, DARcorporation, Lawrence, Kansas.

[80] Sant T., 2007, Improving BEM-based Aerodynamic Models in Wind Turbine Design Codes1.

[81] Sørensen N. N., Michelsen J. a., and Schreck S., 2002, “Navier-Stokes predictions of the NREL phase VI rotor in the NASA Ames 80 ft x 120 ft wind tunnel,” Wind Energy, **5**(2-3), pp. 151–169.

[82] Laino D. J., Hansen A. C., and Minnema J. E., 2002, “Validation of the AeroDyn Subroutines Using NREL Unsteady Aerodynamics Experiment Data,” Wind Energy, **5**(2-3), pp. 227–244.

[83] Sant T., Van Kuik G., and Van Bussel G. J. W., 2006, “Estimating the angle of attack from blade pressure measurements on the NREL Phase VI rotor using a free wake vortex model:axial conditions,” Wind Energy, **9**(6), pp. 549–577.

[84] Sant G. & van Bussel, G.J.W T. van K., 2006, "Estimating the Angle of Attack from Blade Pressure Measurements on the NREL Phase VI Rotor Using a Free Wake Vortex Model: Axial Conditions," Wind Energy, **9**, pp. 549–577.

[85] Johnson W., "Rotorcraft Aerodynamics Models for a Comprehensive Analysis," Heli Japan 98: AHS International Meeting on Advanced Rotorcraft Technology and Disaster Relief, Japan.

[86] Hansen C., "NWTC Design Codes, AirfoilPrep" [Online]. Available: http://wind.nrel.gov/designcodes/preprocessors/airfoilprep/. [Accessed: 28-Jun-2012].

[87] Du Z., and Selig M. S., 2000, "The Effect of Rotation on the Boundary Layer of a Wind Turbine Blade," Renewable Energy, **20**, pp. 167–181.

[88] Drela M., 1989, "XFOIL: An Analysis and Design System for Low Reynolds Number Airfoils," Lecture Notes in Engineering: Low Reynolds Number Aerodynamics, M. TJ, ed., Spring-Verlag, New York.

[89] Gertz D., 2011, "An Evaluation Testbed for Alternative wind Turbine Blade Tip Designs," University of Waterloo.

[90] Gertz D. P., and Johnson D. A., 2010, "The Design , Fabrication , and Testing of a Wind Turbine Blade with Interchangeable Tips," The Canadian Society for Mechanical Engineering Forum 2010, CSME, Victoria, British Columbia, Canada, pp. 1–8.

[91] Gertz D., and Johnson D. A., 2011, "An evaluation testbed for wind turbine blade tip designs – baseline case," INTERNATIONAL JOURNAL OF ENERGY RESEARCH, **35**(August), pp. 1360–1370.

[92] G. W. Gyatt, and Lissaman P. B. S., 1985, Development and Testing of Tip Devices for Horizontal Axis Wind Turbines, Cleveland, OH.

[93] Imamura H., Hasegawa Y., and Kikuyama K., 1998, "Numerical Analysis of the Horizontal Axis Wind Turibne with Winglets," JSME International Journal, **41**(Series B), pp. 170–176.

[94] Hasegawa Y., Kikuyana K., and Imamura H., 1995, "Application of Panel Method to Flow Around horizontal Axis Wind Turbines," Numerical Simulations in Turbomachinery; Proceedings of the Symposium, ASME/JSME Fluids Engineering and Laser Anemometry Conference and Exhibition, ASME, Hilton Head, South Carolina, pp. 59–65.

[95] Johansen J., and Sørensen N. N., 2007, Numerical Analysis of Winglets on Wind Turbine Blades Using CFD.

[96] Johansen J., Gaunaa M., and Sørensen N. N., “Increased Aerodynamic Efficiency on Wind Turbine Rotors using Winglets,” 26th AIAA Applied Aerodynamics Conference, AIAA, Honolulu, Hawaii, pp. 1–9.

[97] Coiro D. P., Nicolosi F., Scherillo F., and Maisto U., 2008, “Single Versus Multiple Winglets: Numerical and Experimental Investigation,” 26TH INTERNATIONAL CONGRESS OF THE AERONAUTICAL SCIENCES, ICAS, Anchorage, Alaska, pp. 1–11.

[98] Maughmer M. D., 2001, “The Design of Winglets for High-Performance Sailplanes,” The 19th Applied Aerodynamics Conference, AIAA 2001-2406, Anaheim, CA.

[99] Maughmer M. D., 2003, “Design of Winglets for High-Performance Sailplanes,” Journal of Aircraft, **40**(6), pp. 1099–1106.

[100] Gaunaa J. M. and J., “Can CP be Increased by the Use of Winglets? – or – A Theoretical and Numerical Investigation of the Maximum Aerodynamic Efficiency of Wind Turbine Rotors with Winglets,” 46th AIAA Aerospace Sciences Meeting and Exhibit, Reno, Nevada.

[101] Johansen Madsen, H, Aa., Gaunaa, M. and Bak C. J., 2009, “Design of a wind turbine rotor for maximum aerodynamic efficiency,” Wind Energy, **12**, pp. 261–273.

[102] Gaunaa Réthoré, P.E., Sørensen, N.N., and Døssing, M. M., 2011, “A Computational Efficient Algorithm for the Aerodynamic Response of Winglet Blades,” EWEA, Brussels.

[103] Ninham C., and Selig M., 1997, “An Interactive Windows 95/NT Version of PROPID for the Aerodynamic Design of Horizontal Axis Wind Turbines,” American Wind Energy Association WINDPOWER Conference, Austin, TX.

[104] Selig M. S., and Tangler J. L., 1995, “Development and Application of a Multipoint Inverse Design Method for Horizontal Axis Wind Turbines,” Wind Engineering, **19**(2), pp. 91–105.

[105] Somers D. M., 2005, "The S833 , S834 , and S835 Airfoils", National Renewable Energy Laboratory, NREL/SR-500-36340, Boulder, CO.

[106] Maughmer M. D., Swan T. S., and Willits S. M., 2001, “The Design and Testing of a Winglet Airfoil for Low-Speed Aircraft,” AIAA 19th Applied Aerodynamics Conference, AIAA 2001-2478, Anaheim, CA.

[107] Maughmer M. D., and Kunz P. J., “Sailplane Winglet Design,” The XXV OSTIV Congress, Saint Auban, France.

[108] Tangler J., and Bir G., "Evaluation of RCAS Inflow Models for Wind Turbine Analysis," NREL/TP-500-35109, Golden, CO.

VITA

David Maniaci was born in 1981 in Reading, Pennsylvania. He has previously been employed by the National Renewable Energy Laboratory (Golden, CO), Piasecki Aircraft Corporation (Essington, PA), Aereon Corporation (Princeton, NJ), and the Dramesi Design Corporation (Johnstown, PA). The Penn State Aerospace Engineering Department has employed him as a teaching assistant for the Sailplane class, teaching assistant for the Learning Factory, research assistant for the Penn State Low-Speed, Low Turbulence Wind Tunnel, graduate research assistant, and instructor of aircraft design.

EDUCATION

Pennsylvania State University, University Park, PA 2007- 2013
Doctoral Candidate, Department of Aerospace Engineering
Dissertation Topic: "Wind Turbine Design Using a Free-Wake Vortex Method with Winglet Application"

Pennsylvania State University, University Park, PA 2003-2007
Master of Science, Department of Aerospace Engineering
Masters Thesis: "Operational Feasibility Study of Liquid Hydrogen-Fueled Commercial Aircraft"

Pennsylvania State University, University Park, PA 1999-2003
Bachelor of Science, Department of Aerospace Engineering

PRESENTATIONS AND PAPERS

"Investigating the Influence of the Added Mass Effect to Marine Hydrokinetic Horizontal-Axis Turbines Using a General Dynamic Wake Wind Turbine Code", (with Li, Ye), July 2012. MTS Journal, 46(4), pg. 71-79.

"Winglet Design for Wind Turbines Using a Free-Wake Vortex Analysis Method", (with Maughmer, M.D.) 50th AIAA ASM, Nashville, Tennessee, Jan. 9-12, 2012. AIAA-2012-1158.

"An Investigation of WT_Perf Convergence Issues", 49th AIAA Aerospace Sciences Meeting, Orlando, Florida, Jan. 4-7, 2011. AIAA-2011-150.

"Relative Performance of a Liquid Hydrogen-Fueled Commercial Transport", 46th AIAA Aerospace Sciences Meeting and Exhibit, Reno, Nevada, Jan. 7-10, 2008. AIAA-2008-152

"Operational Performance Prediction of a Hydrogen-Fueled Commercial Transport", 45th AIAA Aerospace Sciences Meeting and Exhibit, Reno, Nevada, Jan. 8-11, 2007. AIAA-2007-34